Spray and combustion dynamics in an aero jet engine gas turbine model combustor

Titouan Moriniere

THÈSE

En vue de l'obtention du
DOCTORAT DE L'UNIVERSITÉ DE TOULOUSE

Délivré par l'Université Toulouse 3 - Paul Sabatier

Présentée et soutenue par

Titouan MORINIERE

Le 31 août 2023

Dynamique du spray et de la combustion dans une chambre de combustion de modèle de turbine à gaz de moteur à réaction

---

Ecole doctorale : **MEGEP - Mécanique, Energétique, Génie civil, Procédés**

Spécialité : **Energétique et transferts**

Unité de recherche :
IMFT - Institut de Mécanique des Fluides de Toulouse

Thèse dirigée par
Thierry SCHULLER et Thierry POINSOT

Jury

M. Aymeric VIé, Rapporteur
M. Wolfgang POLIFKE, Rapporteur
M. Yoann MéRY, Examinateur
M. Thierry SCHULLER, Directeur de thèse
M. Thierry POINSOT, Co-directeur de thèse
Mme Françoise BAILLOT, Présidente

Je hais les indifférents aussi parce que leurs pleurnicheries d'éternels innocents me fatiguent. Je demande à chacun d'eux de rendre compte de la façon dont il a rempli le devoir que la vie lui a donné et lui donne chaque jour, de ce qu'il a fait et spécialement de ce qu'il n'a pas fait. Et je sens que je peux être inexorable, que je n'ai pas à gaspiller ma pitié, que je n'ai pas à partager mes larmes. Je suis partisan, je vis, je sens dans les consciences viriles de mon bord battre déjà l'activité de la cité future que mon bord est en train de construire. Et en elle la chaîne sociale ne pèse pas sur quelques uns, en elle chaque chose qui se produit n'est pas due au hasard, à la fatalité, mais elle est l'œuvre intelligente des citoyens. Il n'y a en elle personne pour rester à la fenêtre à regarder alors que quelques uns se sacrifient, disparaissent dans le sacrifice ; et celui qui reste à la fenêtre, à guetter, veut profiter du peu de bien que procure l'activité de peu de gens et passe sa déception en s'en prenant à celui qui s'est sacrifié, à celui qui a disparu parce qu'il n'a pas réussi ce qu'il s'était donné pour but. Je vis, je suis partisan. C'est pourquoi je hais qui ne prend pas parti. Je hais les indifférents.

– Antonio Gramsci, *Je hais les indifférents, 1917*

Spray and combustion dynamics in an aerojet engine gas turbine model combustor

Abstract

Faced with more severe legislative constraints on polluting emissions, the architectures of the combustion chambers of aeronautical engines are more vulnerable to dynamic issues. Among them, combustion instabilities (CI) constitute a major issue. Progress must therefore be made to better prevent them. They first require identifying the precursor mechanisms that lead to their triggering. While many efforts have been devoted to their modeling for gaseous flames, similar investigations for two-phase flames remain marginal. In addition, the detection of CI precursor events with online monitoring would increase the engine lifespan and space preventive maintenances, and more generally the safety of aircraft engines. This thesis proposes to pursue these two objectives by studying the interactions between the acoustic field and the spray dynamics on the one hand, and by developing alternative techniques for the online monitoring of CIs on the other hand. Called TALISMAN, a new swirl stabilized spray burner has been designed and built for this purpose.

In the first part of the manuscript, the acoustic-spray interactions are examined. It is first shown that the velocity response of an isolated droplet to acoustic disturbances corresponds to a first-order low-pass filter with a cut-off frequency proportional to the Stokes number. The acoustic response of a perfectly monodisperse spray in a uniform flow gives rise to density waves of the number of droplets. Expressions are derived for these density waves using an eulerian formalism for the two phases. They feature two contributions with acoustic waves interfering with waves convected by the mean flow. The influence of particle velocity dispersion on these number density waves is also studied by analytical and numerical means. It is shown that a dispersion of the velocity of the injected particles induces a set of characteristic waves which result in a modification of the propagation and dispersion of these waves. Finally, the response of a hollow cone spray to acoustic disturbances is studied numerically and experimentally. The gas and liquid phase velocity profiles obtained in high fidelity Euler-Lagrange simulations are compared to phase Doppler laser anemometry measurements. Results agree very closely at steady state. However, while the air velocity profiles are correctly reproduced in a pulsating flow, the particle velocity profiles show large differences with experiments due to the lack of dynamic behavior of the numerical model for spray injection.

The second part of the manuscript investigates CI in the TALISMAN setup. A thermo-acoustic analysis is conducted for a configuration exhibiting large scale oscillations with a reduced order model of the burner acoustic response. The system dynamics is analyzed with an acoustic network and a flame describing functions (FDFs) measured experimentally. By considering that the OH^* emission signal from the flame well reproduces heat release rate disturbances, the resulting low-frequency limit of the FDF cannot be reproduced accurately for a spray flame. It is shown that fluctuations of the equivalence ratio need to be considered and modeled. Integrating them into the relationship between the OH^* signal and the heat release rate results into a better prediction of the low-frequency limit of the flame response. Coupling the acoustic model and the FDF, it successfully predicts the CI observed in the experiments. Finally, online monitoring of CI precursors is explored by considering the acoustic flux at the inlet of the combustor as an indicator of impending instabilities. It is successfully applied to the TALISMAN setup and shows better performance than other indicators commonly used without requiring measurements inside the combustion chamber. Finally, application of Deep-Learning to predict CI is discussed.

Keywords: swirl-stabilized spray combustion, combustion instabilities, online monitoring, acoustic-spray interactions, number density waves, hollow cone spray

Remerciements

Peu d'occasions nous sont données dans une vie pour remercier ceux qui nous ont accompagnés jusque-là, alors que sans eux, l'aboutissement de ces travaux n'aurait jamais eu lieu. Ainsi, je saisis l'opportunité qui m'est donnée de pouvoir témoigner de toute la gratitude et de l'affection que je porte à ceux qui m'ont entouré jusqu'ici.

En premier lieu, il convient de remercier les membres de mon jury, Wolfgang Polifke, Aymeric Vié, Françoise Baillot ainsi que Virginel Bodoc qui m'ont fait l'honneur de lire et de juger mon manuscrit. Comme tout jeune chercheur travaillant dans la solitude des trois années de thèse, il est précieux d'obtenir l'avis de pairs dont il estime particulièrement la qualité de leurs recherches. Connaissant l'emploi du temps et la quantité de travail auxquels les chercheurs sont souvent soumis, je vous remercie profondément du temps consacré à la lecture et à la soutenance de ses travaux.

Ensuite, je remercie mes encadrants de thèse, Thierry Schuller, Thierry Poinsot, Alain Cayre et Yoann Méry de m'avoir formé et guidé dans mes travaux pendant ces trois années. Je tiens à remercier particulièrement Thierry Schuller de sa disponibilité pour échanger sur mes travaux en laissant toujours ouverte la porte de son bureau, mais aussi de son réel investissement pour le devenir professionnel de ses étudiants, ma place aujourd'hui à l'ONERA tenant principalement à sa chaleureuse recommandation. Je suis reconnaissant de la confiance qu'il a toujours accordé à mon travail et à ma personne malgré les nombreuses difficultés qui ont pu être rencontrées au début de cette thèse. Je souligne que ces qualités n'ont rien à voir avec un quelconque traitement de faveur envers ma personne, mais bien avec la considération naturelle que Thierry a pour tous ses étudiants, qui découle de sa sincère éthique professionnelle. Aussi, je remercie Alain pour ses chaleureux retours sur mes travaux tout au long de ma thèse. Je lui souhaite une bonne retraite et un bon apprentissage de la guitare électrique. Merci aussi à Laurent Selle, mon co-encadrant de thèse officieux, pour l'aide occasionnelle, mais non moins importante, sur la partie numérique. Je le remercie également d'inviter annuellement tout le département chez lui pour un barbecue estival et pour se rafraîchir à l'aide de sa piscine et (quelques) boissons. Mais, avant tout, je le remercie pour les nombreux midis que nous avons pu gâcher ensemble grâce à nos échanges sur l'actualité, et je m'excuse pour les autres.

Evidemment, je ne peux pas oublier de remercier mes collègues de thèse qui m'ont maintes fois extirpé de la solitude de la thèse : Andrea, Pierre-Alexandre, Tarik, Sylvain, les Hugo, Hervé et bien sûr Antoine, mon camarade de combustion diphasique, et dont le travail tardif un soir de Saint-Patrick a été l'origine de nombreuses amitiés qui continuent de se nouer encore aujourd'hui. Je souhaite bon courage aux nouveaux arrivés : les Matthieu, Sébastien et Martin. Je précise ici que les travaux présentés dans ce manuscrit ont été réalisés avec un horaire de travail se limitant à du 9h-18h en semaine, débordant très rarement sur le week-end et les vacances. A eux de juger si la qualité et la quantité de ces travaux sont suffisantes pour considérer qu'une bonne thèse peut se faire sans excès de travail, mais aussi en préservant une vie personnelle hors du bureau que notre âge impose de développer.

Car, si aujourd'hui je suis évidemment fier de la rédaction de ce manuscrit, je le suis d'autant plus des nombreuses relations tissées en dehors du laboratoire. Elles continuent de me donner la force de perséverer dans ma vie et mon travail malgré les difficultés rencontrées. En premier lieu, merci

à ceux qui aujourd'hui accompagnent régulièrement mes soirées : Colin, Marine, Guilhem, Coline, Laurine, Marion, Anaëlle, Rachel, Charlotte, Romain Gasparini, Maxime, Marie-Diane et Francesco. Un écosystème toulousain où s'ancre une profonde fraternité composée de Yannis, mon camarade de musique et de basket, Romain Thieulen, dont la résilience face aux aléas de la vie m'impressionne encore, et, bien sûr encore et toujours, Antoine. Mais le cerveau derrière ce réseau est bien sûr mon (ex)-colocataire, mon camarade de combat (de salon), et mon meilleur ami, Romain Bielawski, en qui j'ai pu toujours trouver de l'aide et du réconfort face à toutes les adversités que peut rencontrer un jeune homme à notre époque (doutes dans ses amours et son travail, confinement et couvre-feu, deux mandats de Macron, ...). J'ai bien conscience tout ce que je lui dois dans la construction de ce que j'ai et de ce que je suis aujourd'hui. Je n'oublie pas Alexy, dont j'admire la détermination et le courage dans les efforts pour trouver une voie dans laquelle il se retrouve vraiment, n'hésitant jamais à quitter le confort matériel pour à affronter l'inconnu. Merci à Corentin Chesne, d'être mon ami depuis bientôt 20 ans. Tu es pour moi presque un frère adoptif, étant depuis tout ce temps au côté de ma famille à Guérande alors que je suis loin d'elle. Enfin, je ne peux pas oublier Sarah, que j'ai rencontré au début de ma thèse et qui aujourd'hui accompagne chacune de mes journées et de mes pensées. J'ai découvert avec elle le fait qu'on puisse aimer pleinement sans se consumer. Ayant souvent des doutes à propos de ce qui pourrait se passer et ne pas se passer dans le futur, je n'en ai cependant aucun concernant le nôtre.

Mais cette nouvelle famille toulousaine ne remplace pas celle qui m'accompagne depuis ma naissance. Merci à Corentin, qui a joué le rôle ingrat du frère ainé, mais qui m'a toujours intégré dans ses activités. Sans lui, je n'aurais jamais joué de la basse et découvert le monde de la musique. Merci à Morgane, ma jumelle, qui, toutes ces années, a toujours veillé sur moi et sur toute la famille. Merci à mon père d'être un modèle d'exigence et de persévérance dans son travail professionnel et associatif. Merci à ma mère, d'avoir toujours été là pour moi, à l'autre bout du téléphone quand je désespérais et qui, sans pour autant tout comprendre de ce qui m'animait, m'a toujours soutenu et aimé pour qui j'étais.

Enfin, je me dois de remercier ma grand-mère. Alors qu'elle ne comprenait pas tout ce que je faisais dans mes études et mon travail, elle avait l'habitude de les noter sur des post-its. Elle les utilisait pour mettre de côté les articles de journaux qui avaient un quelconque rapport avec ce que je faisais pour me les montrer lorsque je venais la voir. Ainsi, dans le meuble avec les photos de famille, on a pu retrouver un article de mars 1995 sur le radar Nostradamus de l'ONERA, qu'elle n'a jamais pu malheuresement me montrer en personne. Malgré la grande distance qui nous séparait, sa fierté dans ce que je faisais et de qui j'étais m'a porté pendant tant d'années. Malgré la mort qui nous sépare aujourd'hui, elle continue encore de me porter. J'aurais aimé avoir assez de temps pour qu'avec l'obtention du grade de docteur, je puisse encore la rendre fière, juste une dernière fois, autant que je le suis de l'avoir eu comme grand-mère.

Contents

Nomenclature

Reactive Fluid Mechanics

Δh_r^0	standard enthalpy of reaction per unit of mass [J/kg]
$\dot{m}$	mass flow rate [kg/s]
$\dot{Q}$	heat release rate [W]
$\dot{q}$	volumetric heat release rate [W/m^3]
γ	ratio of specific heat capacities [-]
λ	wavelength [m]
$\mathscr{D}$	period, spatial and spectrum averaged acoustic flux [W]
$\mathscr{E}$	period, spatial and spectrum averaged acoustic energy [W]
$\mathscr{F}$	Flame Transfer Function [-]
$\mathscr{R}$	period, spatial and spectrum averaged source term [W]
$\mathscr{U}$	Transfer function of the gas velocity [-]
μ	dynamic viscosity [Pa.s]
$\mathcal{D}$	period and spatial averaged acoustic flux [J]
$\mathcal{E}$	period and spatial averaged acoustic energy [J]
$\mathcal{R}$	period and spatial averaged source term [J]
$\mathcal{T}$	acoustic transfer matrix [-]
Φ	equivalence ratio [-]
ρ	mass density [kg/m^3]
A_F	flame surface area [m^2]
k_a	acoustic wave number [m^{-1}]
M	Mach number [-]
m	mass [kg]
P	Thermal Power [W]
p	pressure [Pa]
Re	Reynolds number [-]
S_F	flame speed [m/s]
S_L	laminar burning velocity [m/s]
S_T	turbulent flame speed [m/s]
St	Strouhal number [-]
T	Temperature [K]
U	amplitude of the velocity fluctuations u' [m/s]
u	velocity [m/s]
Y_k	mass fraction of the species k [-]
c	celerity of sound wave [m/s]

Geometry

$\mathscr{C}$	geometrical configuration i of the TALISMAN burner
A	area [m^2]
R	radius [m]
V	volume [m^3]

Notations

$\breve{(\cdot)}$	mesoscopic mass-weighted average
$(\cdot)'$	time fluctuating component
$(\cdot)''$	spatial fluctuating component
$\hat{(\cdot)}$	Complex amplitude of the Fourier Transform
$\bar{(\cdot)}$	time average component
$\tilde{(\cdot)}$	Fourier Transform
$\angle\cdot$ or arg	argument
$\cdot_c$	cut-off
$\cdot_g$	gaseous phase
$\cdot_l$	liquid phase
$\cdot_p$	particle
$\cdot_\theta$	tangential component
$\cdot_{cr}$	critical zone
$\cdot_{in}$	at the inlet
$\cdot_r$	radial component
$\cdot_{sf}$	safe zone
$\cdot_w$	warning zone
$\cdot_z$	axial component
$\frac{D_k}{Dt} = \frac{\partial}{\partial t} + \mathbf{u}_k \cdot \nabla(\cdot)$	Lagrangian derivative of the phase k
$\langle(\cdot)\rangle$	phase average
i	imaginary unit

Numerical

Δx	mesh cell characteristic length [m]
θ_S	mean half angle of the spray cone of the FIM-UR model [°]

Two-phase formalism

α_l	volume fraction of the liquid phase [-]
δq_p^2	uncorrelated particle kinetic energy [J/kg]
τ_p	particle time relaxation [s]
$\tau_{p,0}$	particle time relaxation in a Stokes flow [s]
c_l	celerity of the characteristic waves in the dispersed phase [m/s]
d_{10}	Mean diameter [m]
d_{32}	Sauter mean diameter [m]
d_p	particle diameter [m]
f_p	particle probability density function [-]

l_p	particle relaxation length [m]
N_A	amplitude of the acoustic particle clustering [m^{-3}]
N_C	amplitude of the convective particle clustering [m^{-3}]
n_p	particle number density [m^{-3}]
q	spread parameter of the Rosin-Rammler distribution [-]
St	Stokes number [-]
St_0	nominal Stokes number [-]
X	characteristic particle size of the Rosin-Rammler distribution [m]

Signal post-processing

$\Delta\varphi$	phase lag [-]
ω	angular frequency [s^{-1}]
φ	phase [-]
f	frequency [Hz]
I	Signal voltage of the light intensity [V]
S_{xx}	power spectral density of the signal $x(t)$
S_{xy}	cross power spectral density between the signals $x(t)$ and $y(t)$
t	time [s]
V_{sp}	amplitude of the speaker voltage V_{sp} [V]

Abbreviations

APC	Acoustic Particle Clustering
CAEP	Committee on Aviation Environment Protection
CFL	Courant–Friedrichs–Lewy number
CI	Combustion Instabilities
CORSIA	Carbon Offsetting and Reduction Scheme for International Aviation
CPC	Convective Particle Clustering
CPSD	Cross-Power Spectral Density
DAC	Dual Annular Combustor
DFT	Discrete Fourier Transform
EASA	European Aviation Safety Agency
EE	Euler-Euler
EL	Euler-Lagrangian
ENBW	Equivalent Noise BandWidth
EU-ETS	European Union - Emissions Trading System
FAA	U.S Federal Aviation Administration
FDF	Flame Describing Function
FTF	Flame Transfer Function
GE	General Electric
HIVD	Homogeneous Isotropic Velocity Dispersion
HW	Hot-Wire
ICAO	International Civil Aviation Organization
IPCC	Intergovernmental Panel on Climate Change
IRZ	Inner Recirculation Zone

LDA	Laser Doppler Anemometer
LES	Large Eddy Simulations
LPP	Lean Premixed Prevaporised
LTO	Landing and Take-Off
MLDI	Multi-point Lean Direct Injection
ORZ	Outer Recirculation Zone
PDA	Phase Doppler Anemometer
PDF	Probability Density Function
PDPA	Phase Doppler Particle Analyzers
PM	Photomultiplier
PRZ	Particle Relaxation Zone
PSD	Power Spectral Density
PVC	Precessing of central Vortex Core
RCP	Rayleigh Criterion Probe
RMS	Root Mean Square
RQL	Rich-burn Quick-quench Lean-burn
RR	Rosin-Rammler
RUE	Uncorrelated Particle Kinetic Energy
SAE	Safran Aircraft Engines
SAF	Sustainable Aviation Fuels
SN	Smoke Number
TAI	ThermoAcoustic Instabilities
TAPS	Twin Annular Premixing Swirler Combustors

Chapter 1

General Introduction

Trente, soixante, cent millions de morts ne vous détourneraient pas de votre idée fixe : « Aller plus vite, par n'importe quel moyen. » Aller vite ? Mais aller où ?[...] Dans la prochaine inévitable guerre, les tanks lance-flammes pourront cracher leur jet à deux mille mètres au lieu de cinquante, le visage de vos fils bouillir instantanément et leurs yeux sauter hors de l'orbite ! La paix venue vous recommencerez à vous féliciter du progrès mécanique. « Paris-Marseille en un quart d'heure, c'est formidable ! » Car vos fils et vos filles peuvent crever: le grand problème à résoudre sera toujours de transporter vos viandes à la vitesse de l'éclair.

– Georges Bernanos, *La France contre les robots, 1947*

The first chapter of this manuscript begins with a brief description of the current environmental context. After examining the contribution of the aviation to the global warming, regulations regarding local pollution and greenhouse gases emissions are presented. Then, a state of the art of combustor technologies used in aero-engines is drawn up. Among the different challenges to build the low-emission combustor architectures, combustion instabilities constitute a major issue. Hence, the fundamental mechanisms as well as the current methods to detect and prevent these instabilities are reviewed. Finally, the objectives and the outline of the present manuscript are presented.

Overview

1.1. Global context

1.1.1. At the dawn of a new geological era

In an article published in Nature, the atmospheric chemist and Nobel laureate Paul Crutzen popularized the concept of "Anthropocene". It designates a new geological epoch where human activities significantly alter the Earth's geology in a way that upsets the climate balance from the previous Holocene era [1]. According to him, this process would have started with the design of the steam engine in 1784 and then the use of combustion in an industrial process. While this concept has been largely discussed and criticized about its denomination, its origins or its history [2–4], there is large scientific consensus that we are confronted to a new ecological era induced by the industrial and economic growths of (some of the) human societies, where combustion of fossil fuel is playing a major role.

A quick review of that the human activity footprint on the ecological system over the three last centuries is reminded here: from 1750, the atmosphere has seen its the concentration of methane (CH_4) increased over 150%, 63% for nitrous oxides (N_2O) and 43% for carbon dioxide (CO_2). New kind of gases such as fluorinated gases (CFC and HCFC) have also appeared in the atmosphere. The accumulation of greenhouse gases in the atmosphere is responsible for the global warming, with already an increase of the Earth's mean temperature about 0.8°C from the middle of the XIXth century. Their simulated contribution in 2019 relative to 1750 are shown in Figure 1.1. According to the Intergovernmental Panel on Climate Change (IPCC), this temperature is projected to reach between 1.2 and 6°C by the end of the XXIth century. It will result into, on the one hand, the disappearance of actual climates covering between 10 and 48% of the Earth's terrestrial area, and on the other hand, the creation of climates that living organisms have never been confronted with covering over 12–39% of Earth's terrestrial area [5]. Absorbing a quarter of the CO_2 emissions, oceans are 26% more acid than the preindustrial era. With current rates of extinction about 1000 times than the normal, 20% of the current species will disappear by the end of 2030, while 97% of the biomass of all mammals on Earth are now constituted by humans and domestic animals [6, 7]. Aquatic life has been considerably reduced by the urea, phosphore and the nitrates released by the fertilizers in groundwater, rivers and oceans.

In 2009, a group of 28 international scientists have identified 9 keys processes that are affecting deeply the stability and the robustness of the whole planet [9]. They associate indicators to monitor them with threshold levels, named planet boundaries, which could lead to brutal and unknown environmental changes if a single one of them is crossed. As pictured in Figure 1.2, six of them have been already crossed in 2022 while already three of them were crossed in the initial study in 2009 [10]. Hence, succeeding an exceptional era of climate and ecological stability where human societies have developed, those latter are leaving the Holocene to enter irretrievably in a novel and unknown geological era.

1.1.2. Aviation in the Anthropocene

The contribution of aviation to the global warming has been recently examined by Lee et al. [11] and the referential Climate and Aviation of ISAE-SUPAERO [12]. Only key elements are reminded here. Different species emitted by planes are considered as source terms of radiative forcing (i.e absorbing more energy flux in the atmosphere than releasing it): carbon dioxide (CO_2), water vapor, soot, sulfate aerosols, and increased cloudiness from contrail formation. Although nitrogen oxides (NOx) do not contribute directly to the radiative forcing, they lead to the formation of ozone (O_3) in the atmosphere, which is an important greenhouse gas. Their action on climate system is depicted in Figure 1.3. With passenger revenue kilometers rising from 109 to 8269 billion km per year over the period 1960-2018, global aviation has experienced exponential growth in terms of activity, especially the two last decades

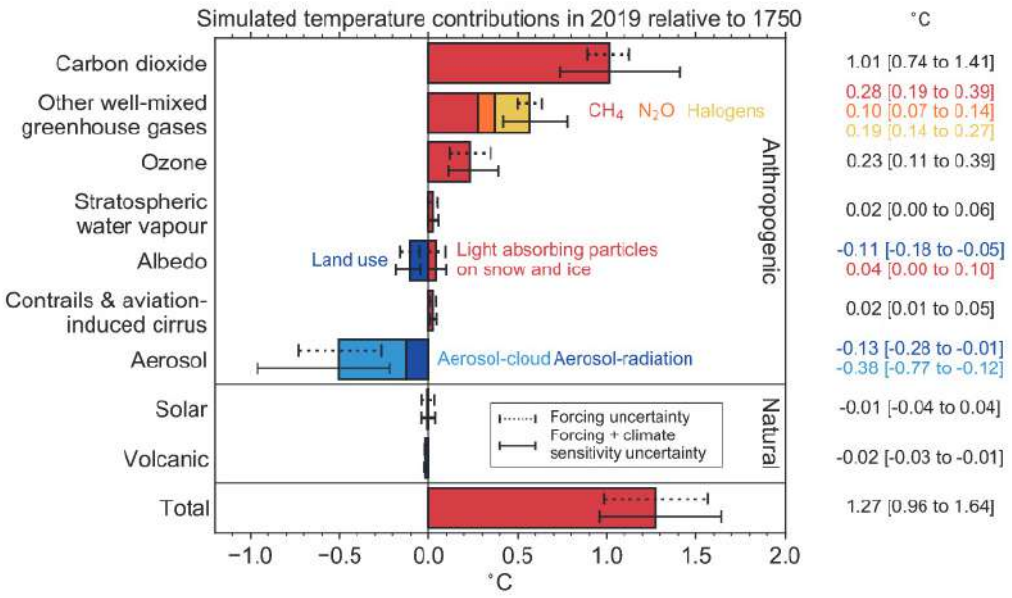

Figure 1.1. – The contribution of forcing agents to 2019 temperature change relative to 1750 produced. Figure reproduced from the chapter 7 of GIEC's 2021 report [8].

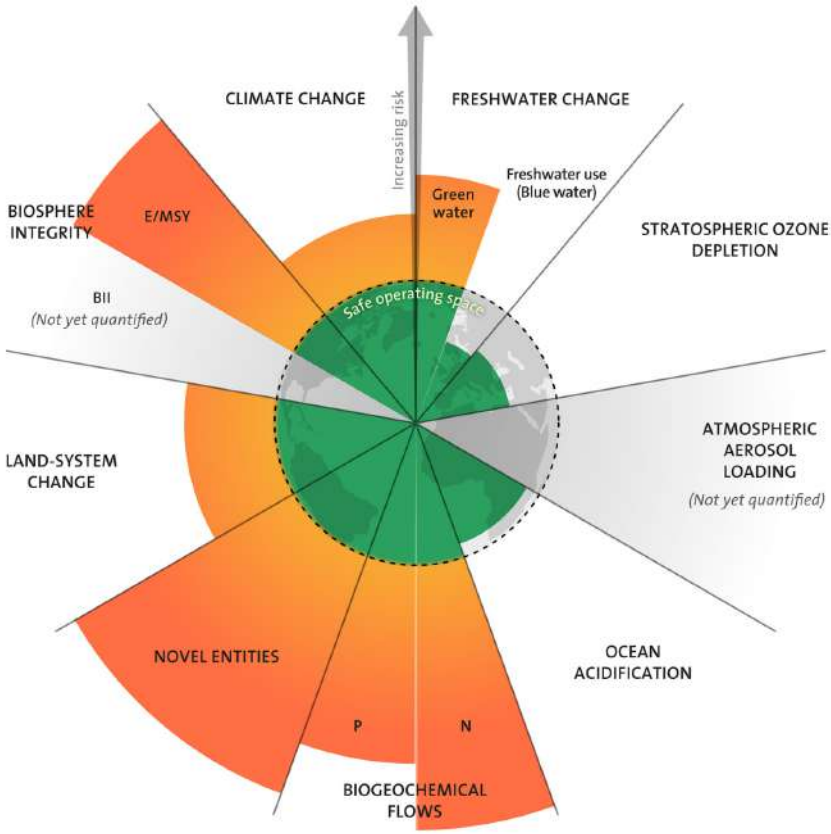

Figure 1.2. – Planetary boundaries diagram reproduced from [10]: orange sections indicate the excess of the fixed thresholds while green sections indicate measurements within the boundaries.

in Asia-Pacific region due to the expanding civil aviation sector which will represent around 41% of Airbus orders in next two decades. In parallel, CO_2 emissions have increased by a factor of 6.8 reaching

1034 Tg CO_2 per year as shown in Figure 1.4, overcoming the 1000 million tonnes for the first time. Between 1960 and 2018, the average annual rate of CO_2 emissions was 15 millions tonnes CO_2 per year, with a significant increase from 2013 to 2018 at 44 millions tonnes of CO_2 per year. The growth rate has increased by 27% between 2013 and 2018 and is now reaching a 5% annual growth rate. In 2018, the cumulative emissions from aviation since 1940 reached 32.6 billion tonnes of CO_2, half of which were released in the last two decades. These emissions account for approximately 2.4% of all anthropogenic CO_2 emissions in 2018 and contribute to 3.5 % of effective radiative forcing.

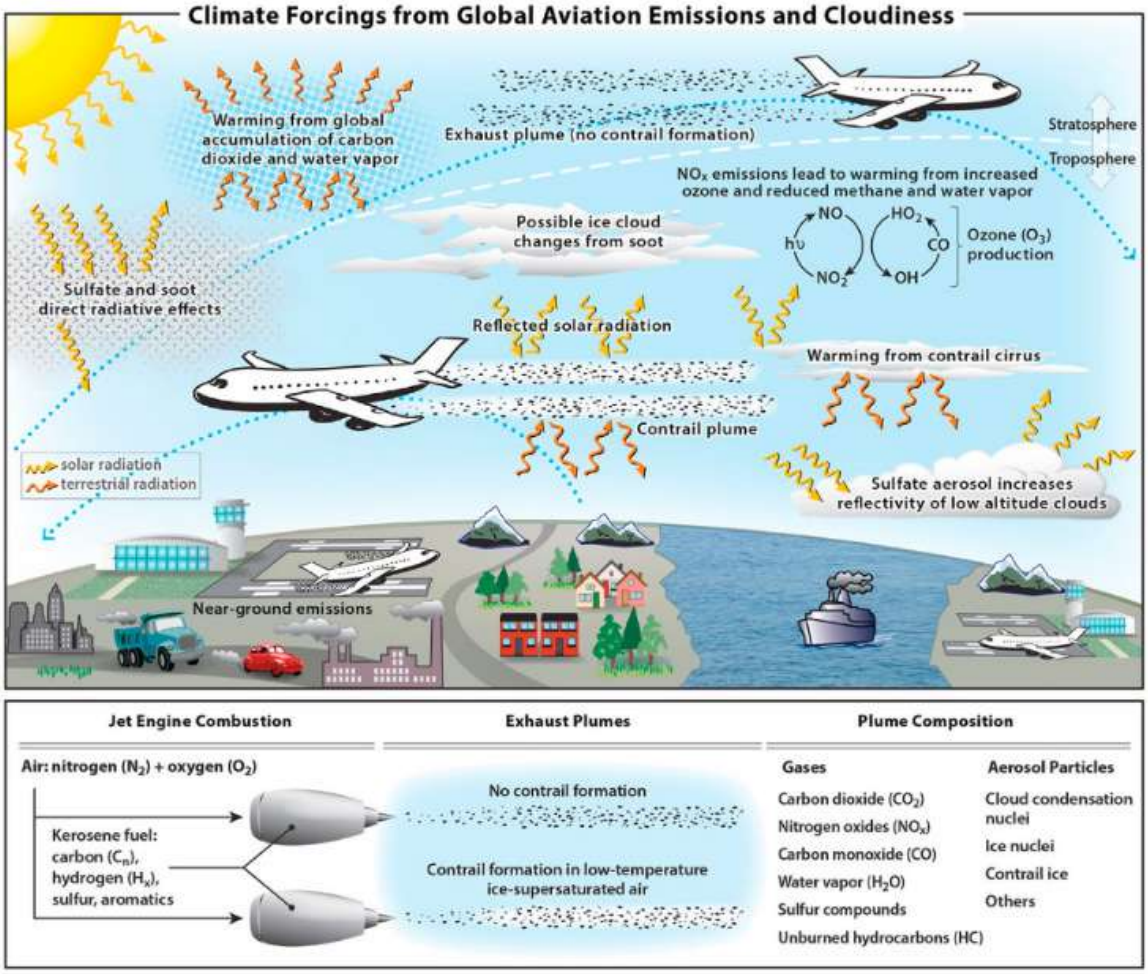

Figure 1.3. – Schematic overview of the processes by which aviation emissions and increased cirrus cloudiness affect the climate system. Reproduced from [11]

To limit the global warming under 1.5°C, 195 delegations at the COP21 signed the Paris Agreement in 2015. Translating by the IPCC in terms of greenhouse gases emissions reductions, it does not specify emissions by sector or country. Each signatory country is required to establish and plan a list of their own contributions to meet the reduction goal, with regular reporting. The European Union, including France, committed to reduce the greenhouse gas emissions by 40% by 2030 compared to 1990. In December 2019, this target was updated to 55%. Regarding aviation, only domestic flights are covered by the Paris Agreement while international flights are not considered because no agreement has been reached regarding which country should be responsible for these emissions (the departure, the registration or the destination country). However, international aviation accounts for approximately 60% of commercial aviation emissions. To address this issue, the UN delegated the International Civil Aviation Organization (ICAO). In 2010, the ICAO set an aspirational goal to stabilize international aviation emissions from 2020 and achieve carbon-neutral growth from that date. Furthermore, in 2016,

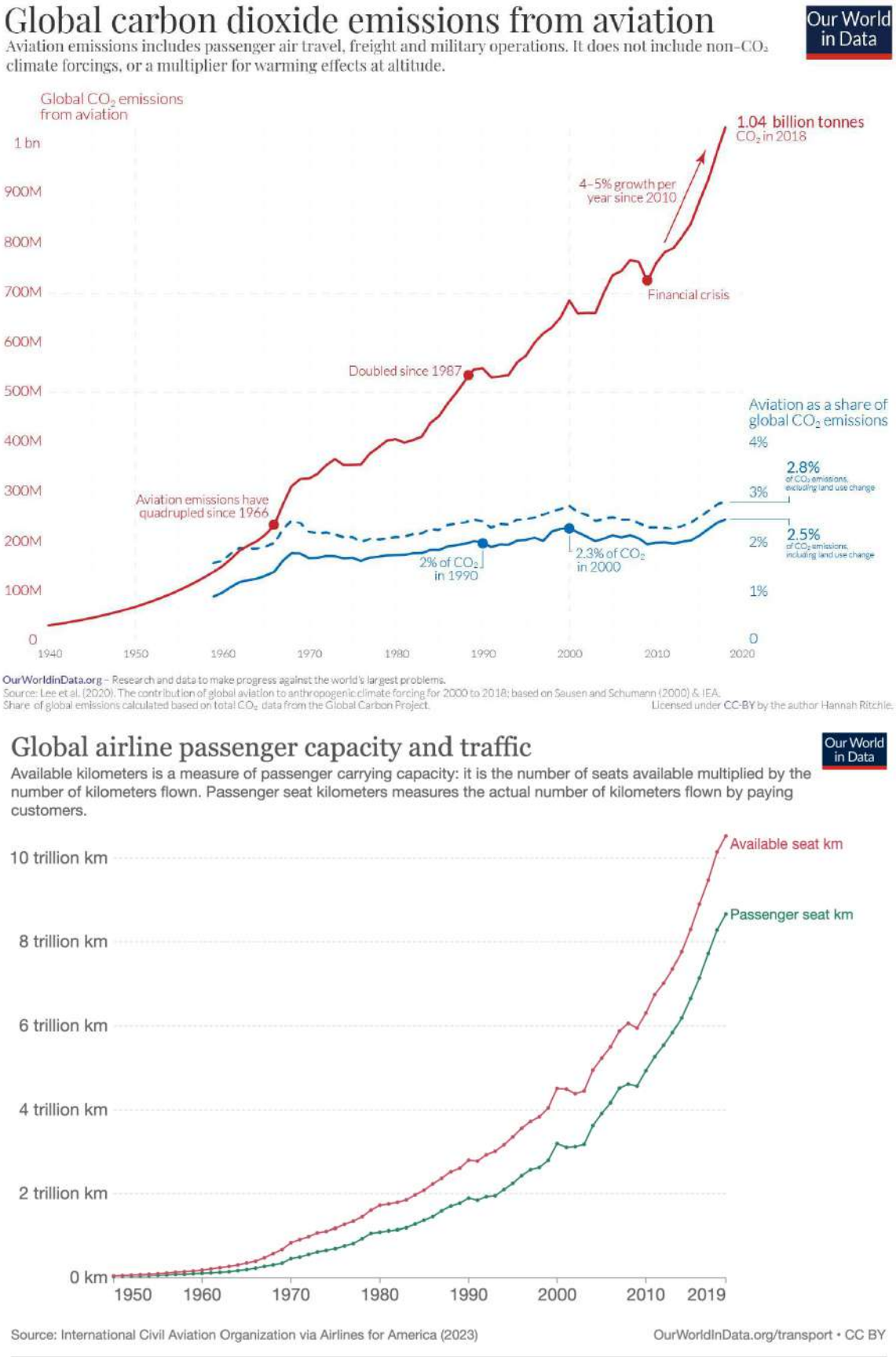

Figure 1.4. – (Top) Global CO_2 emission in tonnes from aviation and (Bottom) global airline traffic and aviation efficiency. Data from [11] and adapted by Hannah Ritchie of Our World in Data.

the ICAO adopted the Carbon Offsetting and Reduction Scheme for International Aviation (CORSIA) system for emissions above the 2019 level. Under this system, aircraft operators must purchase carbon credits, the value of which is determined by a financial carbon market. The European Union goes further in its reduction objectives and includes intra-European flights in its EU-ETS (European Union - Emissions Trading System) carbon quota system, which has been in place since 2013. However, extra-European flights have been excluded from EU-ETS to allow the ICAO to implement CORSIA. Since 2013, a free quota of 38 million tons of CO_2 per year has been allocated to intra-European aviation. However, CO_2 emissions from aviation have increased from 53.5 million tons in 2013 to 67 million tons in 2018, leading airlines to purchase around 100 million carbon credits at the value of 1.3 billions euros. To align with the objective of 90% reduction of greenhouses gas in the transport sector, this free quota for aviation will be gradually reduced by 2.2% each year until 2030. Not considered by CORSIA and EU-ETS, the impact of non-CO2 gases on the climate will eventually be addressed with associated regulations integrated into the EU-ETS framework at a later stage.

Until now, regulations determined in the CORSIA or EU-ETS system rather concern the activities of airline operators and are not restrictive but incentive-based, paying proportionally to their CO_2 emissions (polluter-pay principle). When it comes to aero-engine manufacturers, the Committee on Aviation Environment Protection (CAEP), a technical committee of the ICAO Council, issues restrictive regulations about noise and emissions of pollutants and associates technical recommendations to reach these global standards. They are agreed through some international meetings every three years and subsequently adopted into domestic regulations by each ICAO Member State. The certification process of engines according to these standards is ensured by aviation safety authorities such as European Aviation Safety Agency (EASA) or the U.S Federal Aviation Administration (FAA). Described in ICAO Annex 16 Volume II, the engine certification process involves evaluating the performance of an engine during a landing and take-off (LTO) cycle, simulating the engine's operation around an airport on a test bench and measuring its impact on local air quality. The cycle consists of four distinct operating modes with specific thrust settings and durations.

The gas concerned by the ICAO emissions standards are unburnt hydrocarbons (UHC), sulfur dioxide (SO_2), carbon monoxide (CO), nitric oxide (NO) and NOx. To consider the engine size, their limits are expressed on the mass of each of these gaseous species divided by the maximum sea level static rated thrust of the engine. They do not apply to subsonic aircraft engines with a rated thrust below 26.7 kN, neglecting the contribution of smaller engines to total emissions. Aircraft particulate matter emissions have been measured through Smoke Number (SN), since 2020, with nvPM Mass and Number. Standards are measured to take into account ultrafine soot particles. NOx emissions have been targeted by CAEP and their limit values have been more and more binding. Adding a third volume to the ICAO Annex 16 in 2016, CO_2 emissions of aero-engines have now to be certified to take into account their contribution to global warming. It concerns new designs from 2020 and designs which are already in-production as of 2023 for subsonic jet airplanes over 5,700 kg and propeller-driven airplanes over 8,618 kg. CO_2 emissions are measured at three different loads (low, medium, high) for optimal speeds and altitudes and evaluated through a specific air range (SAR), i.e a typical measure of cruise fuel burn in km/kg, adjusted to take into account fuselage size. The evaluated value is the average of these three measured emissions. Hence, confronted to more and more stringent limitations, engine manufacturers need to develop low emissions combustion technologies in the next years.

1.2. Combustion in Aeronautical Engines

Fundamental mechanisms and considerations governing the design of a gas turbine propulsion systems in aircraft have been exhaustively covered by Oates [13], Mellor [14], Lefebvre et al. [15], Mat-

tingly et al. [16] and Soares [17]. Recently, Palies [18] provides a complete overview of the aeronautical propulsion science and engineering, as well as of the current challenges the field is facing nowadays, with particular attention to premixed swirled combustion. This section describes the basic elements of the principle of an aero-engine, with a specific focus on the combustion chamber.

1.2.1. Principle of an aero-engine

Designed to generate either power or propulsion, a gas turbine engine aims at giving momentum to a fluid at rest. The momentum given to the fluid is then extracted by a ground gas turbine to generate electricity. Even if an aero-engine attributes a part of the momentum to power the aircraft electrical system, it mainly uses it to generate thrust from the rotation of aerodynamic blades and the expulsion of a gaseous exhaust jet. The contribution of each source depends on the architecture of the aircraft engine. In a turboprop engine as used in the ATR regional and A400M military transport aircraft, the thrust is only generated by a propeller for its lightweight and good performances at slow flying speed. In a turbojet as used for fighter aircraft, the exhaust jet is used as the only source of thrust to reach efficiently very high speed that can go beyond the sound speed. Finally, most commercial aircraft use turbofan engines where the main part of the thrust is provided by the inlet fan through the by-pass stream, while the remainder is generated by the exhaust gas through the core stream. This configuration aims to maximize overall efficiency with a balanced trade-off between the high propulsive efficiency of the turboprop and the thermal efficiency of the turbojet [18].

A typical architecture of a turbofan engine is shown in Figure 1.5. This example is the 2-spool aero-engine CFM56 from General Electric (GE) and Safran Aircraft Engines (SAE). A simplified explanation of its operation principle can be given with the help of the Brayton cycle, which is commonly used to describe the thermodynamic cycle of gas turbines. The air flow enters the inlet duct which has an divergent shape, known as subsonic diffuser inlet. It ensures that the flow remains in a subsonic regime throughout the fan. Being compressed by the fan, the air is then decelerated and split into a core flow and a by-pass flow. The by-pass flow goes through a large duct named fan nozzle to be ejected to create thrust. The core flow, on the other hand, undergoes further compression by the low-pressure and the high-pressure compressors. It is then directed into the combustion chamber, where fuel is injected into the air. Here, the air-fuel mixture is ignited in order to add thermal energy to the flow. The hot gases resulting from combustion pass through the high-pressure and low-pressure turbines, where the rotating kinetic energy is sequentially extracted by the turbine blades. The extracted energy powers the on-board systems and, most importantly, drives the rotation of the fan and compressors, ensuring a continuous airflow into the aero-engine. Finally, the hot gases exit the turbines and are expelled through a core nozzle at a flow velocity close to the airflow velocity exiting the fan nozzle.

1.2.2. Combustion chamber

The combustion chamber is a crucial element of a turbofan engine: through the conversion of chemical energy into thermal energy, it generates thrust indirectly through the rotation of the fan and directly through the hot exhaust gas. Additionally, it powers all the onboard systems. Combustion then needs to perform efficiently and safely across various operating conditions encountered during different flight phases (taxi, take-off, climb, cruise, descent, landing). It must also minimize environmental impact and meet thermal and mechanical constraints. From the perspective of a combustion engineer, the flame must be stabilized within the most compact combustor possible over a given region without knowing any flashback or blowout during its operation, being able to be reignited if this occurs. The thermal energy provided by combustion must result in temperature profiles uniform

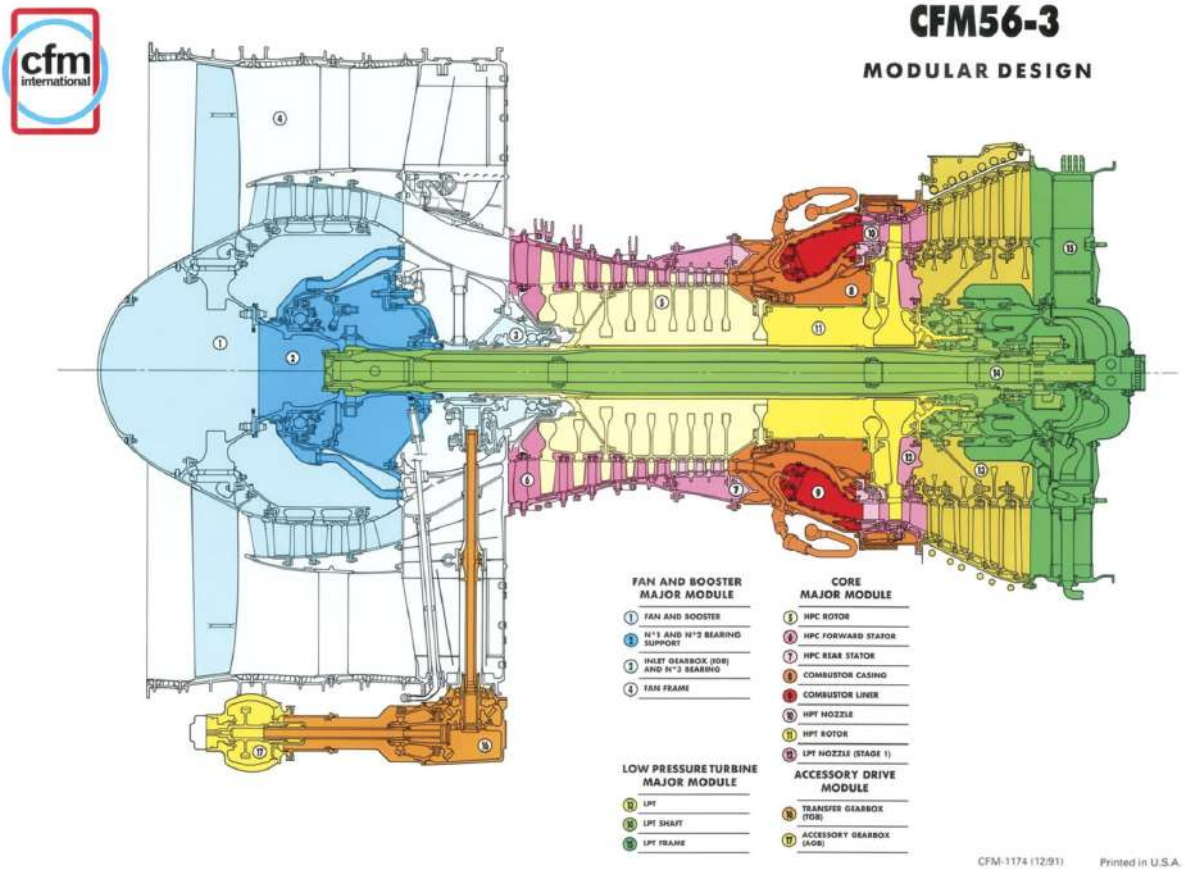

Figure 1.5. – Longitudinal cutaway of the turbofan CFM-56 engine developed by SAE and GE

throughout the flow delivered to the turbine while remaining within the temperatures limits tolerated by the combustor walls and turbine blades. Appropriate air cooling methods are employed for such purposes. Noise and pollutants generated by combustion must be limited as much as possible. Finally, the design of the combustor must prevent acoustic-flame interactions that could lead to combustion instabilities. This latter phenomenon will be the main focus of the manuscript. Its fundamental mechanisms and its modelling will be addressed in Section 1.3.

Apart from some aero-engines that used can-annular combustor decades ago (e.g GE J79 turbojet, Pratt & Whitney JT8D or Rolls-Royce Tay turbofans), single annular combustors are now the preferred geometry due to their uniform combustion and reduced volume. An example of an annular combustor is pictured in Figure 1.6. Air-fuel injection is evenly distributed over nearly 20 sectors without any walls separating them. These sectors are equally spaced along the azimuth of a single ring-shaped combustion chamber located between an inner and outer casing. Details of the geometry of a single sector for the CFM56-3 are depicted in Figure 1.7. The combustion process in a single sector of a conventional combustor occurs as follows: the compressed air from the compressor is slowed through a divergent section known as a diffuser. It is then divided into a primary air flow and a dilution flow with a "snout" or a splitter. The primary air flow goes through an air spray nozzle, which consists of air swirlers and pressure atomizers. Fuel is injected into the primary airflow, and the air-fuel mixture is burned in the first part of the combustion chamber named primary zone. The flame is anchored in this zone, where most of the fuel is burnt. Through secondary holes, a portion of the dilution air flowing through the annulus is injected into the region downstream the primary zone, named intermediate zone, to complete the combustion process. Another part of the dilution air protects the combustion

chamber walls with a film of cool air flowing through perforated liners and cooling slots which isolates the walls from the hot gases (1800-2000°C). The remaining part is dumped into the hot gas stream through drilled holes to uniformly cool it to the temperature required at the turbine inlet.

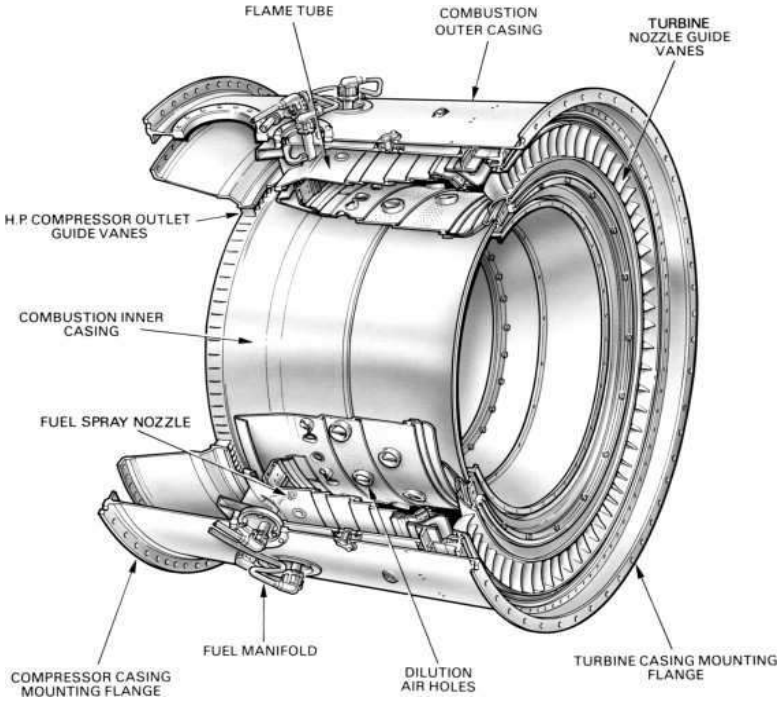

Figure 1.6. – Description of an annular combustion chamber (reproduced from [17])

1.2.3. Air-fuel injection system

Due to their high power density without requiring any pressurization, liquid fuels are still the privileged physical state of hydrocarbons for aeronautical transport. With a low freezing point (~ -50 °C), kerosene, also known as Jet-A1, is mostly used by the aircraft. It is mainly composed from 70% to 85% of C_8-C_{16} hydrocarbons. For a comprehensive overview of commercial jet aviation fuels and the potential future of Sustainable Aviation Fuels (SAF) along with their technical challenges, several recent reviews are available [19–21].

Exhaustive review about the fuel injection in the combustion chamber has been provided by Lefebvre's book [22]. Only key elements specific to aero-engines are briefly reminded here. In aero-engines, an airspray nozzle is the the combination of air swirlers, where primary air flow goes through, and a fuel injection unit, where liquid fuel is injected at a relative much lower velocity than the air flow. This combination is commonly referred to as an airblast atomizer when the air velocity is relatively low (typically below 100 m/s), or an air-assist atomizer where the air velocity is higher. Through the action of aerodynamic forces distorting the liquid fuel at the fuel-air interfaces, the bulk fuel is transformed into a fuel spray composed of small droplets dispersed in the surrounding swirling airflow. The atomization occurs in two stages. Referred to as primary atomization, the liquid fuel jet is firstly disintegrated into ligaments and then into droplets. It results from the amplified oscillations occurring at the surface of the fuel jet caused by disruptive forces that overcomes the cohesive forces. The second stage, known as secondary atomization, occurs when variations in air pressure along the droplet surface cause local deformation. If the internal pressure cannot compensate for the local external aerodynamic pressure, the deformation may increase the internal pressure deficit at other points on the surface of the droplet. The further deformation can ultimately lead to the breakup into smaller

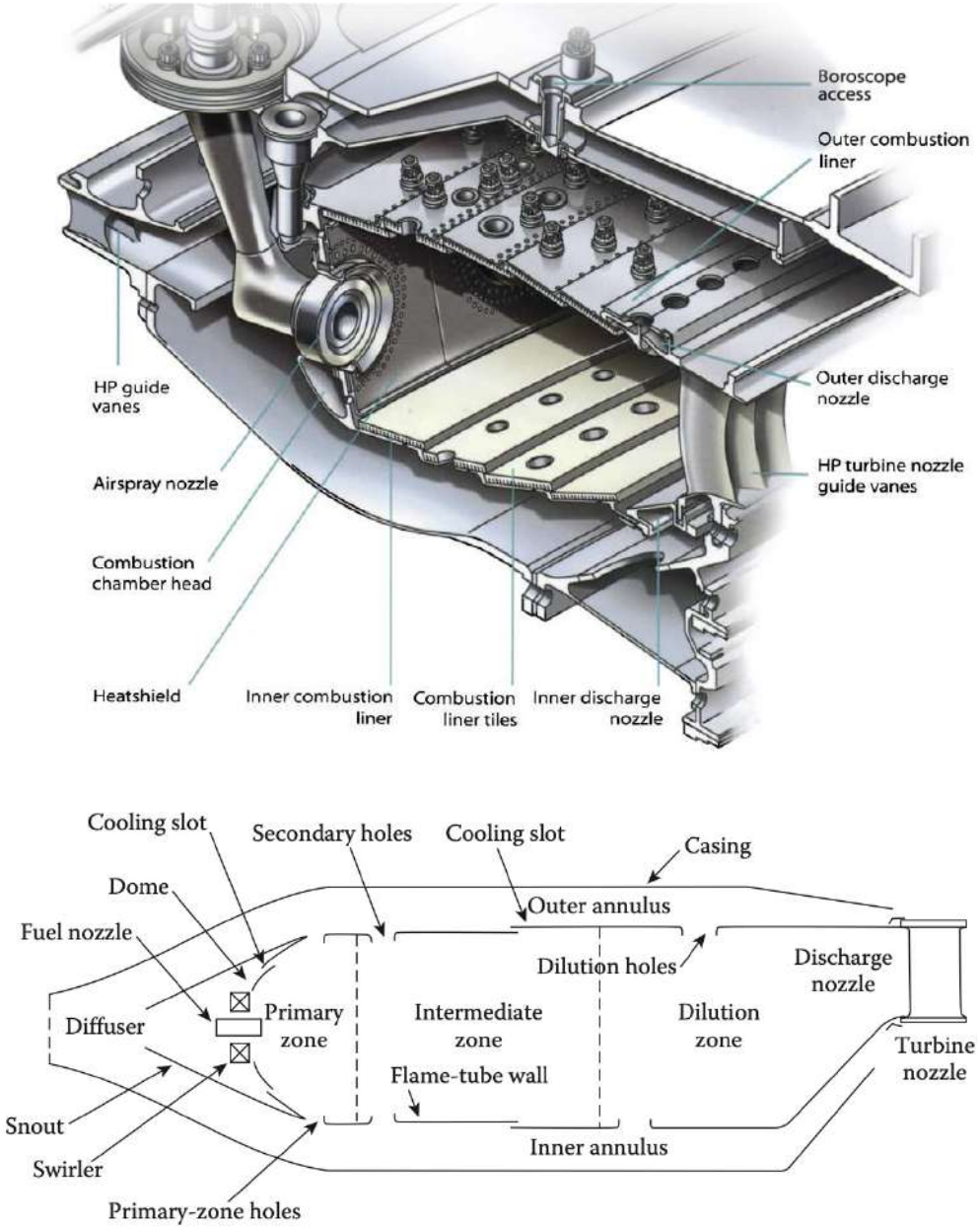

Figure 1.7. – (Top) 3D and (bottom) 2D views of a single sector of an annular combustion chamber. Reproduced from [17] and [15] respectively.

droplets. Currently, airblast atomizers are widely used in a prefilm configuration as pictured in Figure 1.8.(a). In this configuration, fuel from the pressure atomizer impinges on the convergent lips of the injection system to form a continuous liquid sheet. This film is then atomized by the action of the inner and outer swirling air flows on both sides of the fuel film.

The transformation of fuel into a spray can be achieved by pressure atomizers which can be simple plain orifices or pressure-swirl atomizers, also known as simplex atomizers. Both types of atomizers convert the accumulated pressure energy from the small orifice (about a few hundred micrometers) into kinetic energy. However, a simplex atomizer incorporates a swirler with tangential holes upstream of the outlet orifice, as shown in Figure 1.8.(b). This additional swirl movement of the liquid fuel creates a hollow-cone spray, where the fuel forms the outer contour and the air forms its core. This type of

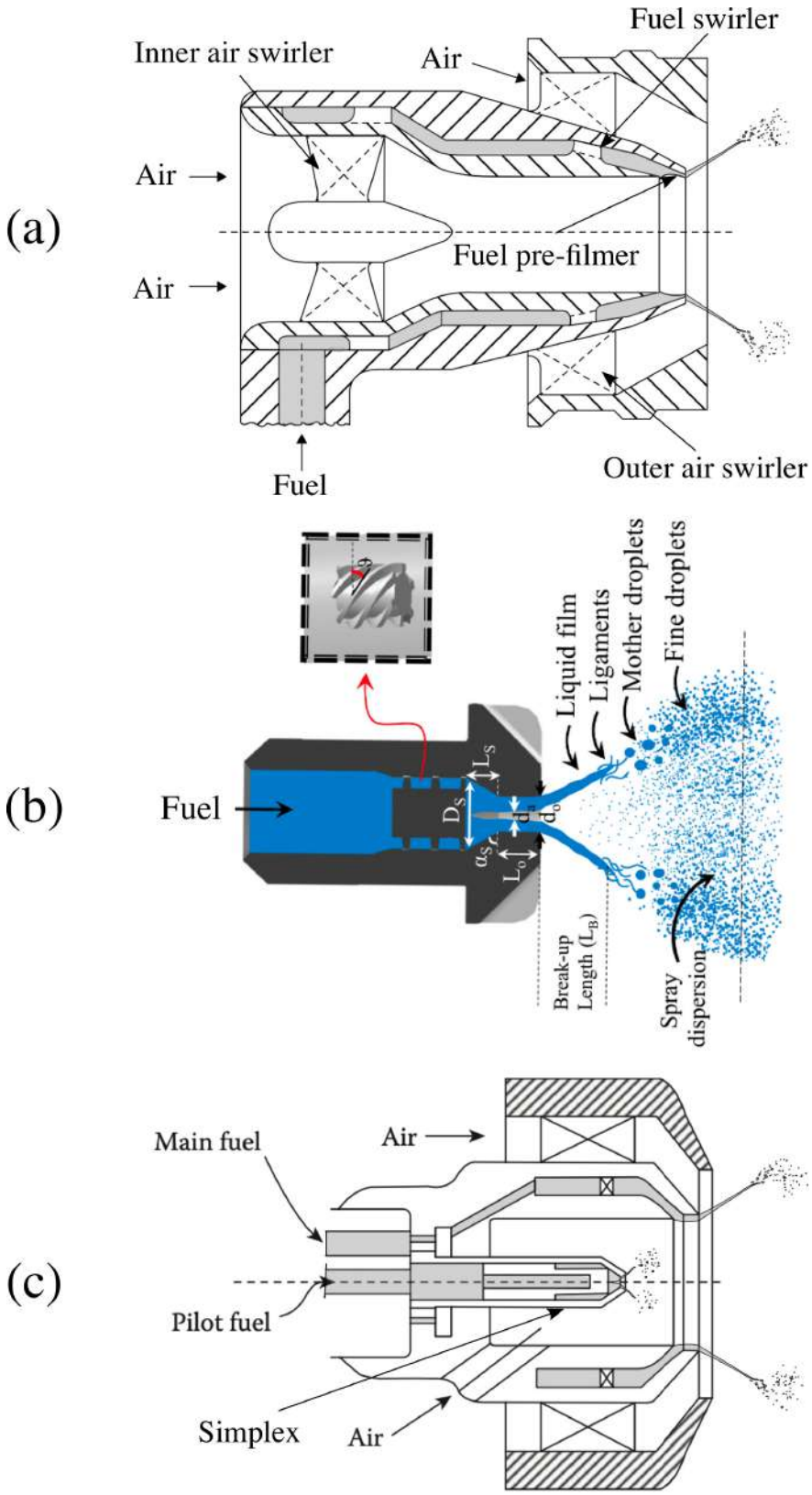

Figure 1.8. – (a) Prefilming Airblast (b) Pressure swirl atomizer and (c) piloted or hybrid airblast. (a) and (c) are adapted from [22] and (b) is reproduced from [23].

spray provides very fine atomization, with droplet diameter ranging from a few dozen micrometers, and a spray angle varying between 30° and 180°. Due to the difficulty of simplex and air-blast atomizers to provide respectively proper atomization at low pressure drop through the orifice and low air velocity, they can be coupled with a surrounding swirling air to enable proper atomization and reignition at low power and/or high pressure operations. Denoted as piloted or hybrid atomizers and shown in Figure 1.8.(c), this combination uses the simplex as a pilot injection at low power operation and the air-blast prefilming at higher power operations. These technologies are currently employed in certain aircraft engines. Another approach is to remove the prefilming part and to keep the central simplex for the fuel injection. Known as airblast simplex (ABS), this configuration is cheaper and easier to manufacture. It exhibits good reignition and mixing proprieties but faces challenges in atomizing at high pressure operations.

1.2.4. Flow and combustion dynamics of the primary zone

Depicted in Figure 1.9, the role of swirlers of the air-fuel injection systems is to provide a tangential velocity component to the primary air flow by deflecting it through a set of axial or radial vanes. The level of swirl induced in the air flow is quantified by the swirl number S, which is commonly used for high Reynolds number flows [24]. The swirl number S is defined as the ratio of the axial flux of tangential momentum to the product of the axial momentum flux and a characteristic radius of the air injector [24]. The additional tangential velocity component generated by the swirler leads to positive radial pressure gradient, resulting in a decrease in pressure along the axis of the air-fuel injection. As the air flow expands and homogenizes in the primary zone, the tangential component gradually decreases, and the pressure increases along the axis of the combustion chamber. If the tangential component provided by the swirler is high enough, the pressure drop across the combustion chamber axis reverses the flow downstream of the swirler. This phenomenon is known as vortex breakdown [25]. The threshold of the swirl number S required to induce flow reversal is specific to each air injection and combustion chamber architecture. It also depends on the velocity profiles upstream of the primary zone [26].

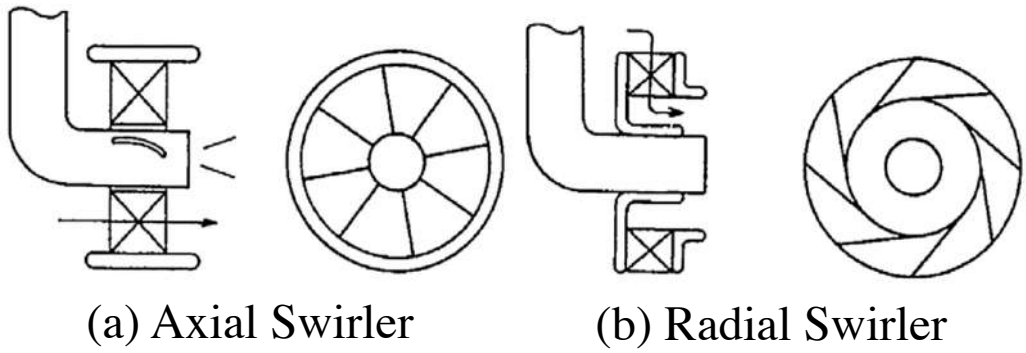

Figure 1.9. – Schematics of axial and radial air swirlers. Reproduced from [27].

Pictured in Figure 1.10.(a), the flow structure observed in the primary zone of a gas turbine is of primary importance for flame stabilization in high power combustion devices. The dynamics of swirling flows and their interaction with combustion have been widely studied by several authors [24, 27, 32]. Their interactions with fuel spray injection (see e.g. [28–30, 33–37]) have been recently reviewed by Menon and Rajan [38]. Here, only key elements will be briefly described. As shown in Figure 1.10.(b), flame stabilization is provided by inner (IRZ) and outer (ORZ) recirculation zones that are respectively generated in the center and the corners of the primary zone. When a flame is ignited in this zone, these regions with low speed and reverse flow regions are filled with hot gas

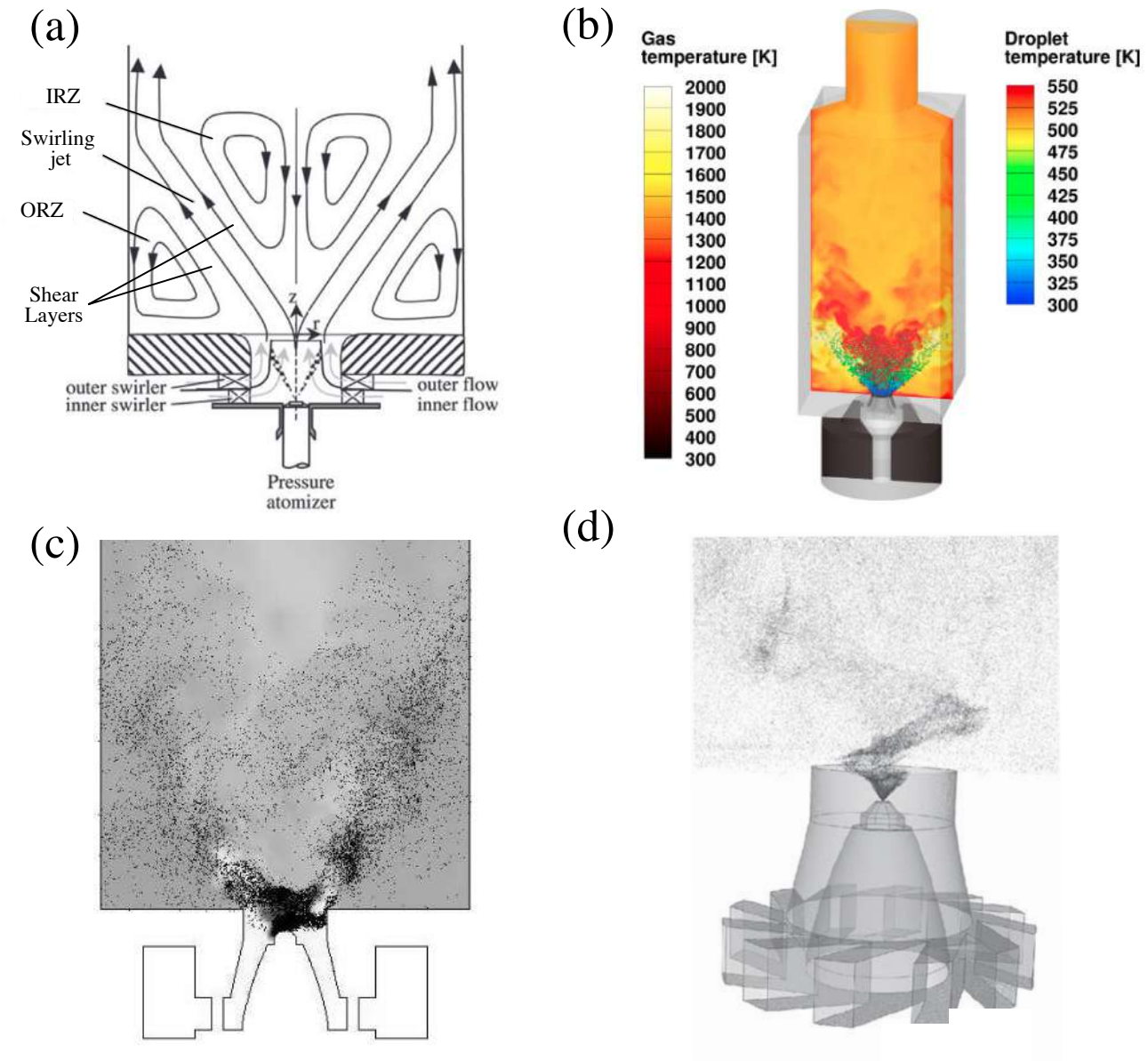

Figure 1.10. – (a) Characteristic flow features of a swirling flow (adapted from [28]) (b) Swirl-stabilized spray flame (reproduced from [29]) (c) Instantaneous droplet distribution in swirling flow (reproduced from [30]) (d) Structure of the PVC highlighted by the presence of droplets (reproduced from [31]).

products. They act as steady heat sources and contain entrained fuel which continuously feeds the exothermic reactions with active chemical species. In the case of spray injection, only the smaller particles representing a minor fraction of the fuel are trapped in the recirculation zones where they are vaporized and mixed with the hot combustion products, as depicted in Figure 1.10.(c). Meanwhile, dense pockets of fuel particles are convected by the high-speed swirling jets that enter the combustion chamber. Fuel vaporization mainly occurs in these latter regions, resulting into the intertwining of rich mixtures spots and particle clusters. Characterized by the highest temperatures and mixture fractions close to stoichiometry, the swirling jets roughly correspond to the flame zone in reacting flow. These jets creates strong shear layers on both sides with high velocity gradients due to the velocity difference with the recirculation zones. Finally, swirling flows often feature a three-dimensional unsteady helical flow structure originating from a hydrodynamic instability. This structure is caused by the precession

of central vortex core (PVC) around the injector axis. The spiraling flow motion occurs at a well defined frequency and develops near the shear layers and the IRZ. As shown in Figure 1.10.(d), the PVC participates to the spatial dispersion of fuel particles in the combustion chamber, allowing smaller particles to penetrate into the recirculation zones while heavier particles remain in the swirling jets due to their higher inertia. Hence, the PVC enhances mixing with air and improves flame static stability, but it also introduces periodic fuel vapor inhomogeneities and helical wrapping of the flame reaction layer around the vortex tube, which can deteriorate flame dynamic stability. These large vortical structures break into smaller ones and are further dispersed downstream.

1.2.5. Dry low-NOx combustor architectures

Various combustor architectures have been developed over the last decades to reduce gas emissions, particularly NOx emissions, produced by aero-engines. Modern dry low NOx emissions combustion technologies have already been the topic of several reviews (see e.g. [39–42]). Only the most privileged designs in future aero-engines are briefly presented here:

- **Rich-burn Quick-quench Lean-burn (RQL)**: Introduced by Mosier et al. [43], the RQL concept is shown in Figure 1.11.(a). In the primary zone, an excess amount of fuel is injected with an overall equivalence ratio between 1.2 and 1.8. It enhances static and dynamic flame stability while reducing flame temperature, which results in lower NOx production at the detriment of higher emissions of UHC, CO and soot. To address this issue, large jets of air are injected into the vitiated air to oxidize these carbon-based pollutants to near stoichiometric proportions. This mixing occurs rapidly in a small volume known as the quick quench zone, which minimizes the residence time of hot gases and lowers their temperature to limit NOx production. Finally, the remaining dilution air is injected into a final lean burn zone. The UHC and CO from the primary zone are consumed at equivalence ratios between 0.5 and 0.7. Additionally, the temperature profile is homogenized to levels acceptable for the turbine. RQL combustors have been popularized by Pratt & Whitney with its TALON (Technology for Advanced Low NOx) combustor family for commercial aircraft. These technologies successfully reduce NOx emissions without encountering flame dynamic stability issues that lean combustors may experience. However, RQL technologies require careful air distribution and mixing design to achieve proper reduction of NOx emissions without increasing UHC and CO emissions.
- **Dual Annular Combustor (DAC)**: The DAC design is pictured in Figure 1.11.(b). In comparison to a single annular combustor, the DAC incorporates two airspray nozzles that share a common feed-arm but have their respective primary zones separated by a center body. This configuration allows for double the fuel-air injection along the radial direction. The goal of DAC is to reduce the overall operating equivalence ratio and, consequently, the flame temperature in order to limit NOx production. The air and fuel are split between these two stages based on power conditions. During low-power operation (startup, altitude relight, and engine idle conditions), the pilot stage located in the outer dome operates at low-air velocity and with an equivalence ratio around 0.8 to achieve high combustion efficiency and low emissions of CO and UHC. At higher power levels, both the inner and outer stages operate at low equivalence ratio ($\sim$0.6), but the inner stage has higher air velocity and a higher percentage of fuel burned. This reduces the residence time and NOx emissions. The DAC technology has been implemented in models such as the CFM56-5B and GE90 models. However, there are some drawbacks to these technologies. They require an increased number of injectors and complex control systems to accommodate different operating conditions. Achieving a homogeneous temperature profile downstream of the combustor can be challenging, and the increased combustion chamber volume requires efficient cooling mechanisms.

- **Lean Premixed Prevaporised Combustors (LPP)**: the LPP combustion concept aims to perform lean premixed combustion with early fuel injection for achieving very low pollutant emissions and high combustion efficiency. In this design, fuel is atomized, mixed homogeneously with air, and vaporized in a tube upstream of the primary zone of the combustion chamber. A recent and popular application of the LPP concept is the Twin Annular Premixing Swirler Combustors (TAPS), depicted in Figure 1.11.(c). The airspray nozzle of TAPS consists of a fuel pilot injection surrounded by concentric outer air channels known as cyclonic mixers. Similar to the DAC design, TAPS optimizes combustion efficiency by injecting fuel in a rich proportion at low power operations. At higher power levels, the fuel is split between the pilot and the cyclonic mixers, with most of the fuel injected upstream in the latter through circumferentially drilled fuel orifices. This configuration enables lean premixed combustion. TAPS have been implemented in LEAP engines that power aircraft such as the COMAC 919, Airbus A320 NEO and Boeing 737 MAX. While the premixed combustion mode provides very low-NOx emissions according to the latest ICAO standards, it raises many challenges in terms of combustion safety with flashback, auto-ignition, lean blowout (LBO) and combustion instabilities issues.
- **Multi-point Lean Direct Injection (MLDI)**: Being the focus of developments in the United States by the NASA, the fuel is injected direct in the flame zone at lean proportions to avoid the safety issues associated with premixing chamber as in LPP designs [44]. This injection technology requires excellent atomization, air-fuel mixing and vaporization over a short length in order to avoid formation of CO, UHC and soot. To do so, the air-fuel injection is distributed over multiple small injectors instead of a single one as shown in Figure 1.11.(d). The high number of injectors increases fabrication costs and poses challenges in terms of compactness, although recent advancements in modern manufacturing have helped mitigate these challenges. Since the injection is located close to the reaction zone, the atomizers are more exposed to fuel coking than other designs. Even though this concept has demonstrated its potential for very low-NOx emissions in combustion tests simulating only a single sector of annular combustion chambers, it is still in the early stages of design, and further studies are required before its implementation in real aero-engines.

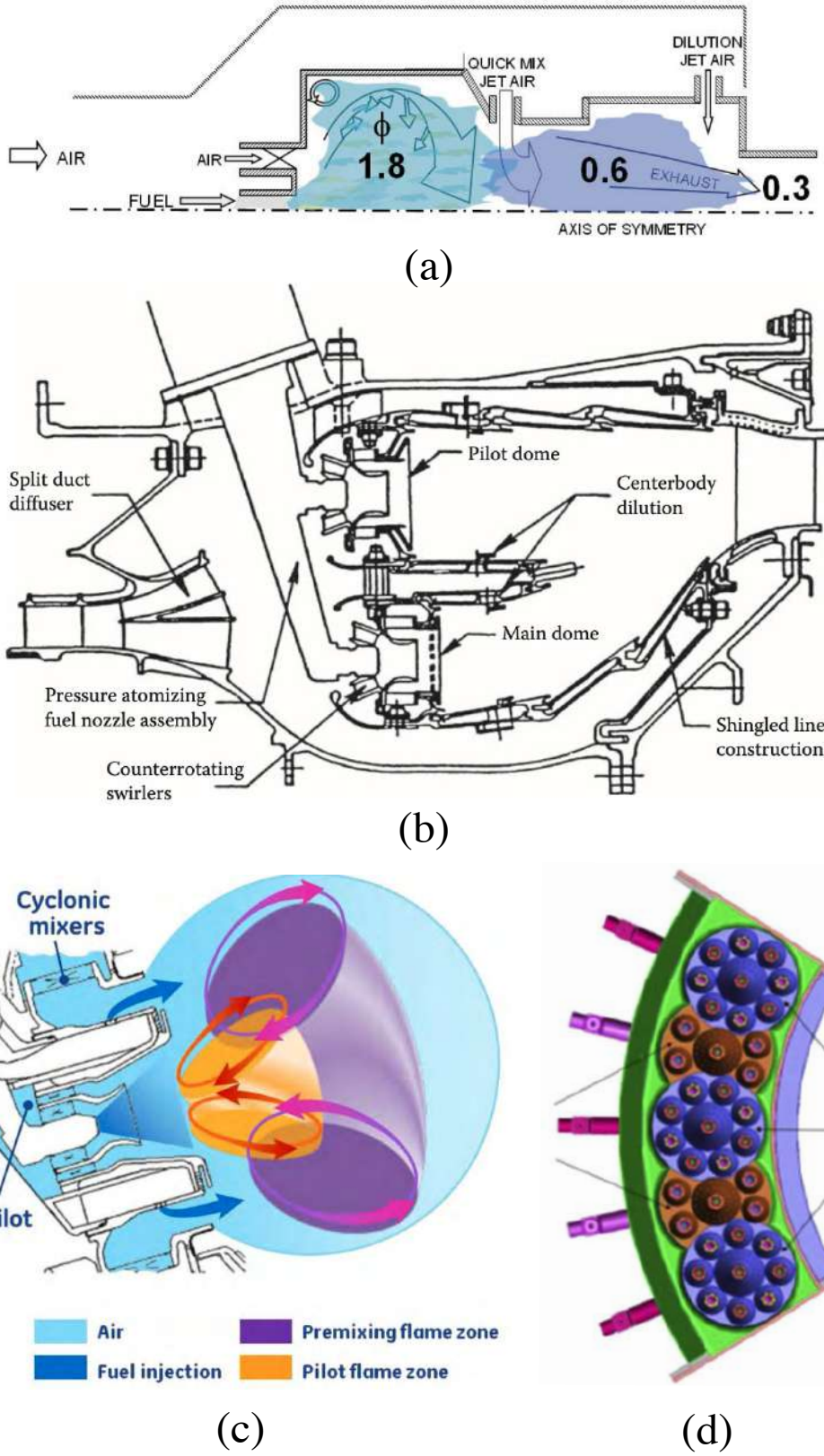

Figure 1.11. – (a) Rich-burn Quick-quench Lean-burn combustor (reproduced from [45]) (b) General Electric dual-annular combustor (reproduced from [15]) (c) TAPS Mixer Concept (reproduced from [46]) (d) Example of MLDI concept for NASA N+3 performance targets (reproduced from [44])

1.3. Combustion Instabilities in Aero-Engines

Most of the combustion technologies for dry low-NOx aero-engines are following a major trend. The main objective is to design new air-fuel injection systems in order to achieve globally lean (partially or totally) premixed combustion in the primary zone of the combustor. Unfortunately, this mode of combustion raises new and numerous challenges regarding auto-ignition, flashback, lean-blow off and thermoacoustic instabilities [27, 47, 48]. This latter issue will be investigated in the rest of the manuscript. Combustion instabilities (CI) or thermoacoustic instabilities (TAI) in industrial devices have been extensively reviewed by many authors. For instance, the reader could refer to Candel [49], Mongia et al. [50], Lieuwen and Yang [51] or Poinsot [52].

1.3.1. Basic concepts about thermoacoustic instabilities

Combustion or thermoacoustic instabilities (CI or TAI) can lead to high amplitude pressure and velocity oscillations at well-defined frequencies that can seriously damage the system in many different ways: flame blowoff or flashback, vibrations that wear out the mechanical parts of the aero-engine or disturb the acquisition and control systems, thermal flux overload over combustor walls or turbine blades... An example of damages caused by CI is pictured in Figure 1.12.

Figure 1.12. – An injector of a Safran Aircraft Engines Lean Premixed Prevaporized combustor damaged by a thermoacoustic instability. Reproduced from [53].

These oscillations are the result of the resonant coupling between heat release rate disturbances of the flame and the acoustic field inside the burner as commonly illustrated in Figure 1.13. Heat release rate fluctuations $\dot{Q}'$ create acoustic energy in the combustion chamber, leading to gas pressure and velocity perturbations p' and u', propagating throughout the combustion chamber and inside the air injectors. [1] If these acoustic fluctuations excite the flow and/or mixture oscillations in such manner that they create new heat release rate fluctuations in phase with the pre-existing ones, they add up and create higher acoustic perturbations. The closed feedback loop becomes a feedback amplifier, making the amplitude of perturbations in the system to grow until their reach saturation, resulting in a distinctive noise at one or several well-defined frequencies.

The condition for CI to happen is commonly expressed through the Rayleigh criteria derived firstly by Lord Rayleigh [54], and later extended by many authors, as for example by Polifke et al. [55] and

1. When the subscript is not specified, u' refers to the velocity fluctuations of the gas phase. In two-phase flow, the ambiguity is removed with the subscript u'_g to differ from the particle velocity fluctuations u'_p

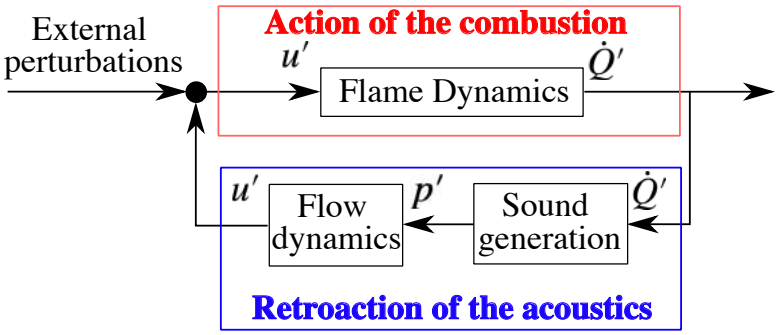

Figure 1.13. – Feedback loop of thermoacoustic instabilities

Nicoud and Poinsot [56] to include acoustic losses. The criteria are written as follows:

$$\mathcal{R} > \mathcal{D} \tag{1.1}$$

where $\mathcal{R}$ is the acoustic energy source term due to combustion averaged over the volume V of the combustion chamber and over a period T of instability cycle

$$\mathcal{R} = \frac{1}{T}\int_T \iiint_V \frac{\gamma - 1}{\gamma \overline{p}} p' \dot{q}' dV dt \tag{1.2}$$

and $\mathcal{D}$ is the period and spatial averaged acoustic flux leaving the combustor through its inlet and its outlet, through the boundary surface area A

$$\mathcal{D} = \frac{1}{T}\int_T \iint_A p' u' dA dt \tag{1.3}$$

In these equations, γ is the specific heat capacity ratio, p is the average pressure over the system control volume while p', q' and u' are respectively the pressure, and volumetric heat release rate and velocity fluctuations. A CI may develop when Equation 1.1 is satisfied. This condition states that (1) the phase lag between the pressure and heat release rate fluctuations must be between $-\pi/2$ and $\pi/2$ to have the product $\mathcal{R} > 0$ (necessary condition), and (2) the amount of acoustic energy created by the flame/acoustic interaction has to be larger than the acoustic losses across the boundaries ($\mathcal{R} > \mathcal{D}$). When these conditions are fulfilled, $\mathcal{R}$ will grow non-linearly with the amplitude of the fluctuations, until reaching a limit cycle where the damping mechanisms are compensating the driving mechanism: $\mathcal{R} = \mathcal{D}$). Nonetheless, this formulation is only valid for isentropic flows where diffusion and viscosity effects are neglected. For non-isentropic flows, the expression for $\mathcal{R}$ has to include other entropy fluctuations [56, 57].

1.3.2. Mechanisms of flame/acoustic coupling

As pictured in Figure 1.13, when investigating TAI in a system, it is mandatory to study how p' produces $\dot{Q}'$ (Action of the combustion in the coupling loop) on the one hand, and conversely how $\dot{Q}'$ produces p' on the other hand (Retroaction of the acoustics in the coupling loop). Many physical mechanisms are involved in those processes and have been reviewed for instance by Ducruix et al. [58] and De Goey et al. [59] for gaseous fueled premixed systems, by Huang et al. [27] and Candel et al. [60] for swirling flames, by Connor et al. [61] and Vignat et al. [62, 63] for annular combustors, by Gajan et al. [64] for liquid fuel flames. Figure 1.14 illustrates a non-exhaustive list of the elementary processes that need to be taken into account when describing TAI in a spray burner. Hence, among

those many various mechanisms, it is necessary to determine the dominating ones for the studied system.

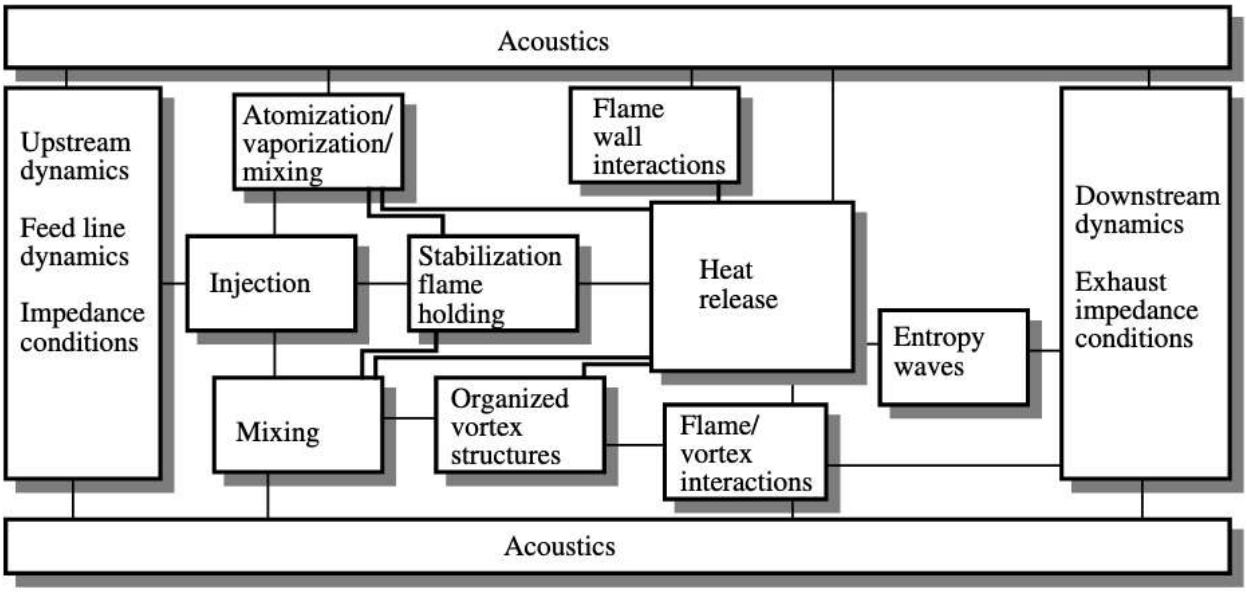

Figure 1.14. – Basic interactions leading to combustion instabilities. Reproduced from [49].

1.3.2.1. Acoustics in a confined burner

The retroaction block in Figure 1.13 is now analyzed. The turbulent flame generates pressure fluctuations p' through variations in heat release rate $\dot{Q}'$, and this phenomenon is known as combustion noise. This topic has been reviewed for example in Candel et al.[65], Duran et al.[66] and Dowling et al.[67]. Only key elements are described. When TAI occur, the spectrum of combustion noise exhibits both broadband noise and discrete tones at resonant frequencies. As illustrated in Figure 1.15, contribution to the global noise can be direct or indirect.

The generation of the acoustic disturbances by unsteady gas expansion due to the exothermic reaction is called direct combustion noise. Assumed in the classical theory [68] and demonstrated in the modern one [69], its source can be considered as a set of monopoles distributed over the flame zone in a far-free field environment, whose local source strength is proportional to its volumetric heat release fluctuations $\dot{q}'$. Considering the direct noise of a compact flame, i.e. the characteristic length over which the combustion takes place is much smaller than the acoustic wavelength λ_a, the pressure radiated at a distance R far away from the flame and an instant t from the combustion zone is:

$$p'(R,t) = -\frac{\gamma - 1}{4\pi R c^2} \frac{d}{dt} \left[\int_V \dot{q}' dV \right]_{t-R/c} \tag{1.4}$$

where c is the sound celerity and $\dot{q}'$ is integrated all over the volume V of the flame containing all heat release sources. This expression requires to model the term $\dot{Q}' = \int_V \dot{q}' dV$ to determine the pressure radiated by the combustion. For premixed combustion, it can be linked to the fluctuations of the flame surface area [70].

The confinement of the flame will have two main consequences on p' generated by $\dot{Q}'$. Firstly, the boundary conditions at the limits of the studied domain will cause reflection of the generated acoustic waves and interferences with the incident ones. Only at certain frequencies, known as resonant

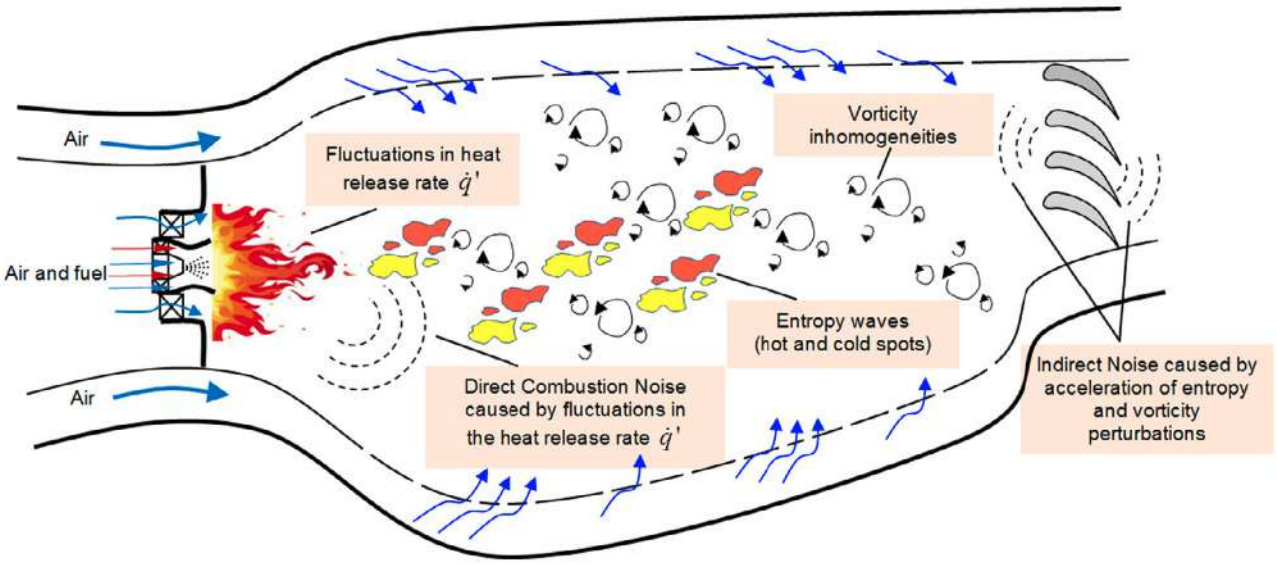

Figure 1.15. – Generation of direct combustion noise and indirect combustion noise in aero-engines. Reproduced from [67].

frequencies mainly determined by the geometry of the combustor and the distribution of speed of sound, standing waves will settle in the system, while at other frequencies, the acoustic disturbances are damped [71]. A modal structure is then imposed to p', where it can expressed as the sum of harmonic oscillators forced at different excitation frequencies f_i that need to be determined [72]. Secondly, if the exit of the combustor accelerates the flow like the exit nozzle or the turbines blades of a gas turbine, indirect noise can be generated downstream the combustion zone. Vorticity and temperature inhomogeneities generated by $\dot{Q}'$ result respectively in vorticity and entropy waves. Their acceleration at the exit of combustor provoke vortex stretching [73] and a volume contraction in the regions of fluid with different densities [74] in the stream-wise direction creating additional acoustic waves propagating upstream and downstream, the former ones interacting with the flame triggering potentially thermoacoustic instabilities at very low-frequencies ("rumble") and the latter one generating exhaust noise [75]. Nonetheless, the local hot spots inducing local increase of viscosity tend to dissipate the large vortical structures downstream of the combustion zone. Thereby, the contribution of vorticity waves in the generation of indirect noise is reduced. Hence, while the term "indirect noise" includes the generation of noise through vorticity and entropy waves, it designates mainly entropy noise. More information about indirect combustion noise can be found for example in Morgans and Duran [76].

1.3.2.2. Flame dynamics of a swirl-stabilized spray flame

The action block in Figure 1.13 is now analyzed. In many combustors, the flame thickness is much smaller than the acoustic wavelength. It results in the flame being insensitive to pressure disturbances p' or temperature fluctuations, regardless of their amplitude. The action of p' is generally indirect through the generation of gas velocity fluctuations u', equivalence ratio fluctuations Φ' or entropy waves. Here, we will only detail the main mechanisms that can create heat release rate fluctuations $\dot{Q}'$ in a single swirl-stabilized spray flame without an exit nozzle (interactions of neighbouring flames and entropy waves are discarded). In two-phase flows, the mechanisms disturbing the flame dynamics can be divided into two main groups: those resulting directly from the interactions with the gas phase, and those resulting indirectly through the interactions between the gas phase and the liquid phase. There are summarized in Figure 1.16.

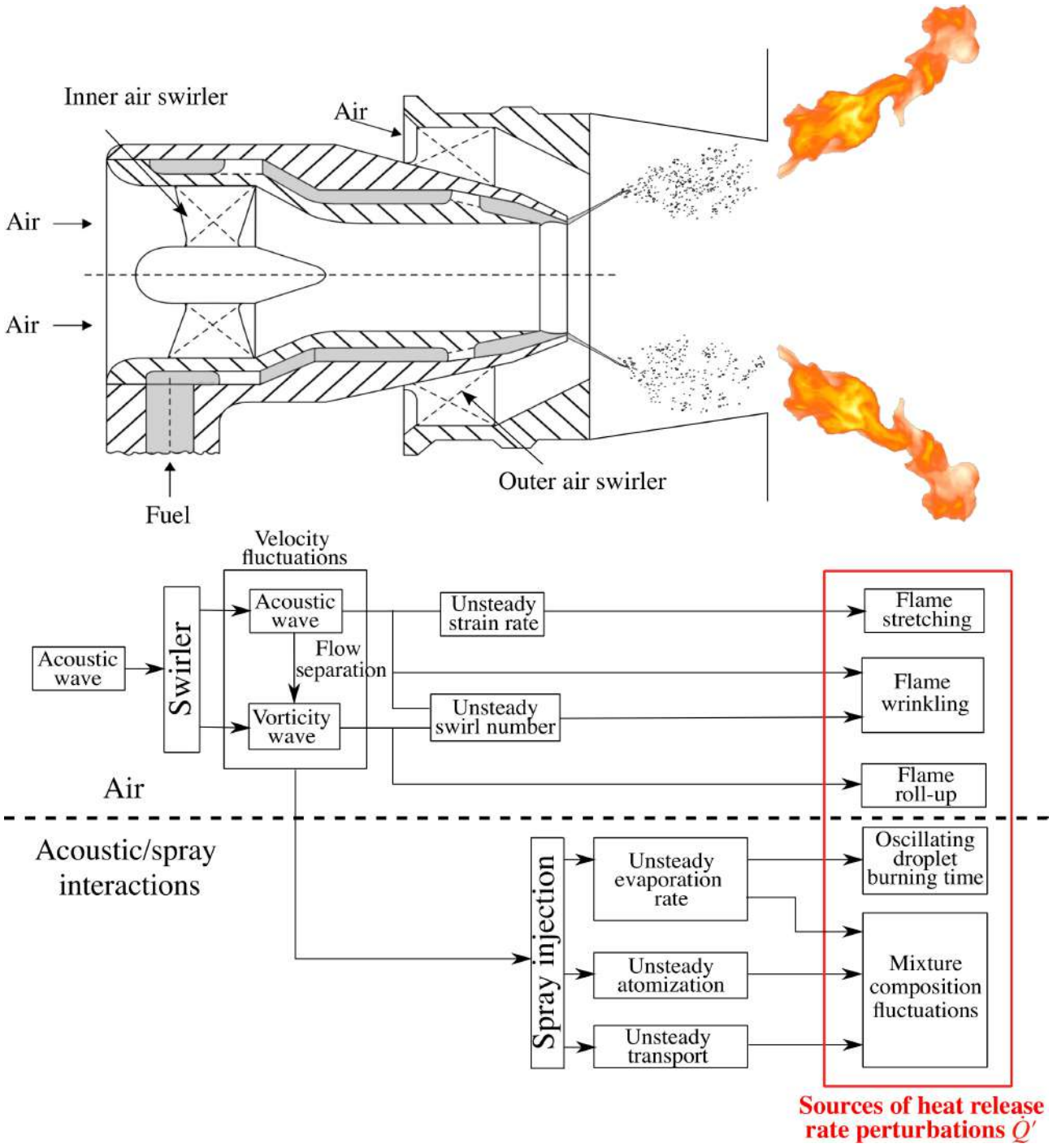

Figure 1.16. – Block diagram representing the mechanisms generating heat–release rate fluctuations $\dot{Q}'$ in a swirl-stabilized spray flame obtained with an airblast injector.

To understand how $\dot{Q}$ is affected by these different mechanisms, one can use its expression for a laminar premixed flame [77]:

$$\dot{Q} = \rho_u S_L A_F Y_f \Delta h_r^0 \tag{1.5}$$

where ρ_u is the density of the unburnt gas, S_L the laminar flame speed, A_F the flame surface area, Y_f the fuel mass fraction, Δh_r^0 is the standard enthalpy of reaction (also called heat of reaction) per unit mass of fuel. Hence, fluctuations of the release rate of a flame $\dot{Q}'$ are induced by the acoustic disturbances through the perturbations of these parameters. At low Mach number, fluctuations of the cold gases density ρ_u' can be neglected. Assuming that the turbulent flame front can be assimilated to a set of wrinkled laminar flame in the thin flamelet regime, this formulation can be extended to turbulent premixed flames by replacing the laminar burning velocity S_L in Equation 1.5 by a turbulent flame speed S_T, higher than S_L, due to the surface wrinkling. The actual flame speed is denoted here as S_F.

The perturbations resulting from the direct interactions with the gas phase are addressed first. A kinematic balance between the flame speed S_F and the gas velocity u_n normal to the flame is required to reach a steady state. A local flame angle α can be defined as the angle between the main direction of the gas velocity u and the normal to the flame front. A perturbation of the gas velocity u' breaks this local kinematic equilibrium. The flame angle α then fluctuates at the excitation frequency as u' in order to find a new equilibrium between u and S_F. This process results in the wrinkling of the flame surface A_F, which is convected downstream from the flame base to its tip. The increase in flame curvature associated to the modification of flame surface A_F will increase the local flame speed S_F, further enhancing the flame wrinkling through kinematic restoration. This phenomenon has been observed and studied extensively by several authors (see e.g. [78–81]).

For a swirl-stabilized flame, azimuthal velocity fluctuations are generated by the swirler, adding a convective vorticity wave to the incident acoustic wave. Their combined action creates swirl number fluctuations and resulting in flame wrinkling due to the modulation of the flame angle and burning velocity [82–84]. Acoustic disturbances also lead to unsteady stretch on the flame surface A_F and to an unsteady heat release rate $\dot{Q}$. In diffusion flames, an unsteady strain rate will also generate fluctuations of species gradients at the flame and alter the local reaction rate. In the case of premixed flames, it will rather directly act on the burning velocity S_F [85–87]. Finally, vortices from the swirler and convected downstream wrap flames around them (flame roll-up) causing a distortion of the flame surface A_F. The vortices also mix the pockets of fresh reactants with hot gases [88]. Rapid variations of the flame surface area and delayed sudden ignitions of reactive pockets can lead to high $\dot{Q}'$.

Heat release rate perturbations $\dot{Q}'$ also result from interactions between velocity perturbations and the liquid injection dynamics. These interactions are mainly caused by fluctuations of the equivalence ratio Φ', which lead to modifications in the flame speed S_F and reactions rates. In this manuscript, particular attention will be given to these interactions. Acting on the liquid phase dispersion and evaporation, Halle et al. [89] have shown that external acoustic forcing can significantly alter the structure of a turbulent spray flames, which can be characterized by three dimensionless parameters. Two of these parameters are relative to the liquid phase: the Strouhal number of the velocity perturbations, the Stokes number of the fuel droplets, and the ratio between the droplet evaporation time and the acoustic characteristic time.

Fundamental research in liquid rocket engines has demonstrated that the vaporization rate of fuel droplets can be altered by acoustic waves, leading to thermoacoustic instabilities, even for steady propellant injection [90]. For a single fuel droplet injected in a standing acoustic field, Saito et al. [91, 92] observed different combustion behaviors, ranging from stable combustion to violent oscillating flame regimes, correlated with an increase of evaporating/burning rate. Several other works have reported

an increase in the evaporation rate due to axial acoustic oscillations for single droplets maintained in a quasi-zero mean flow velocity [93–95]. This effect is mainly attributed to the enhancement of heat transfer and the reduction of the terminal velocity (i.e increase of the residence time) due to the increased relative velocity between the droplets and the surrounding gas, thereby increasing the drag force acting on the droplets. Consequently, large droplets, being less influenced by flow oscillations compared to small droplets, exhibit a greater mass transfer enhancement, which increases with droplet diameters, pressure amplitudes, and frequencies. This increased evaporation rate leads to two driving mechanisms of thermo-acoustic instabilities: oscillations of mixture fraction and burning droplet consumption rate, resulting in shorter and pulsating flames [96–100]. These mechanisms have been highlighted in the context of solid propulsion, where individual aluminum particles burn, but they are also present for liquid fuel sprays in aero-engines.

For fuel sprays submitted to airflow perturbations, the transport of the droplets is strongly modified. In oscillating swirling flows, Giuliani et al. [101] observed the formation of non-sinusoidal convected droplet concentration zones, which are correlated to the convection of vortex rings created in the jet shear layers as shown in Figure 1.17. When the fluctuating velocity component is negative, a dense spray is formed in the near injection zone, and it is ejected when the fluctuating velocity component becomes positive. This results in successive sparse and dense droplets fronts, which are referred as droplet density waves, Gajan et al. [102] have shown that they were the result of the response of a single droplet to oscillating convective velocity wave. They showed that the convection velocity of these waves is related to the size of the captured droplets and the wave amplitude increases with the distance to the spray angle, especially for small droplets. These concentration waves lead to equivalence ratio fluctuations creating thermoacoustic instabilities. This destabilizing mechanism was also considered by Eckstein et al. [103] as the origin of self-excited flame oscillations in a RQL combustor. Number density waves as a mechanism leading to thermoacoustic instabilities has been evidenced experimentally in a kerosene spray flame by de la Cruz Garcia et al. [104], and numerically by Pera and Reveillon [105] for a laminar conical premixed spray flames and by Fratolocchi and Wok [106] for ethanol turbulent spray flames. Finally, Baillot et al. [107] and Patat et al. [108] analyzed the spray impact on the dynamics for a swirling spray flame of n-heptane and dodecane located in the basin of a pressure antinode of a transverse acoustic wave. When subjected to a transverse acoustic wave, the envelope of the sprays radially oscillates. A very few large and slow droplets were detected near the injection exit of the burner when the acoustic pressure is positive, while numerous small and rapid droplets were detected when the acoustic pressure is negative. These number density waves are detrimental to fuel mixing and evaporation. They have then attributed the saturation of the fluctuations of the CH^* signal I' emitted by the flame, which occurs at high pressure amplitude, to these density waves. The density of droplets was found to oscillate at a higher amplitude in the inner region of the spray than in its outer region, suggesting that the heat release disturbances of the spray flame are mainly induced by the perturbation of the spray dynamics in the inner region. Containing bigger particles, the amplitude of the number density waves was found to be less important for a dodecane spray than for a n-heptane spray. This resulted in attenuated heat release perturbations observed for a swirling dodecane spray flame compared to a swirling n-heptane spray flame. Patat et al. [109] also observed the formation of these number density waves for a swirling spray flame located at the maximum surface acoustic flux. They showed that these number densities were occurring for low radial fluctuations but high axial fluctuations of the particle velocity.

Furthermore, particle concentration waves are also generated by the unsteady atomization process of the fuel liquid sheets in airblast atomizers, which is highly sensitive to the surrounding airflow velocity [97, 103, 110, 111]. The oscillations of the spray angle cone have been observed in the pulsated airflow of a TAPS injection system during a thermoacoustic instability cycle by Apeloig et al. [112]. For a liquid jet injected into an air crossflow and subjected to acoustic disturbances, Bodoc et al. [113]

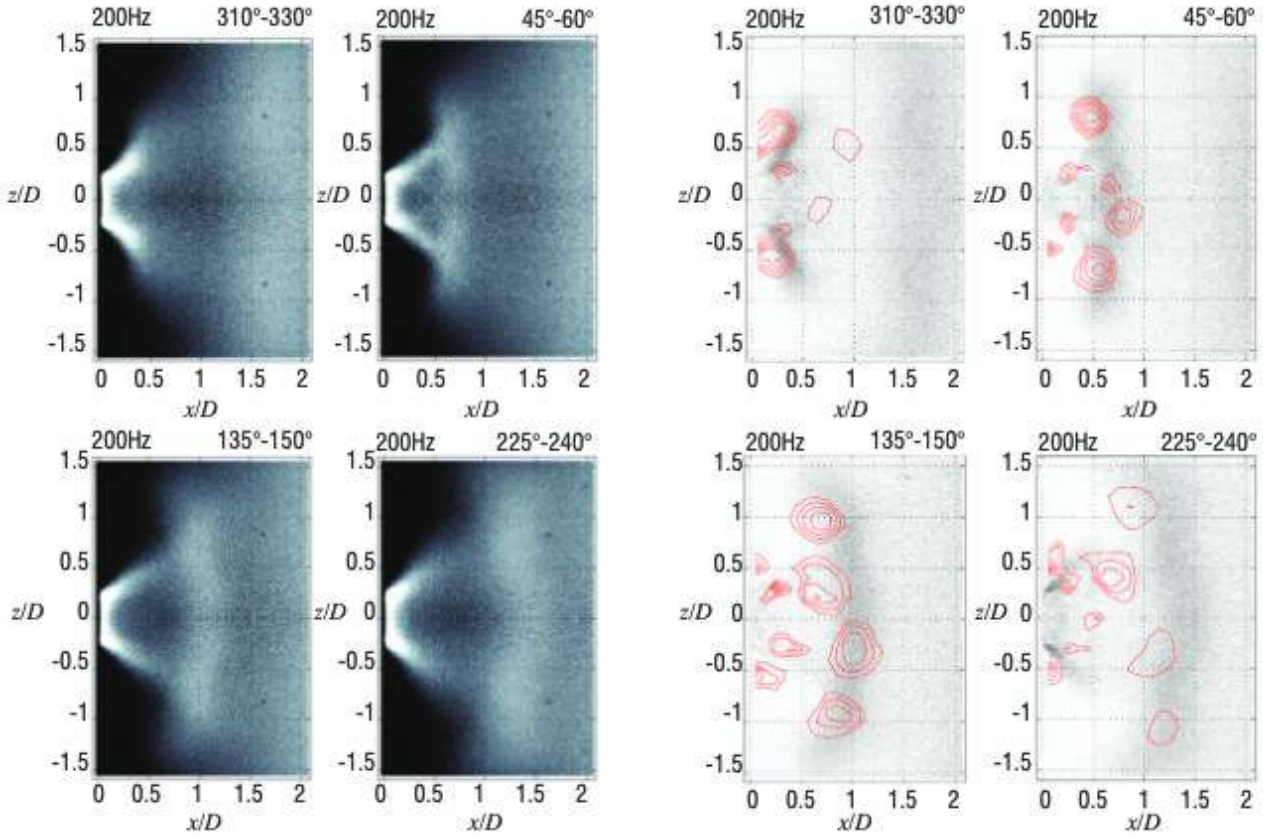

Figure 1.17. – Phase averaged images obtained of a spray subjected to upstream air pulsation: Left: Maximum post-processing of the Mie scattering images illuminated by a stroboscopic lamp, Right : Interaction between the spray (grey zones) with vortical structures shed from the fuel air injection system. Reproduced from [64].

observed a cyclic swinging of the liquid jet column, periodically impinging on the wall, and resulting in oscillating droplet atomization. Particle number density waves were observed to be generated near the modulated atomization and propagate downstream. In a numerical study, Lo Schiavo et al. [114] have shown that at certain cone angle value, the proportion of fuel film formed on the injector lips can lead to self-excited oscillations. Particle clustering can alter the evaporation rate, but the question of whether it is beneficial or detrimental remains open [115, 116].

The interaction between the fuel droplets and the surrounding airflow can lead to complex phenomena, and the understanding of these processes is crucial in mitigating thermoacoustic instabilities and improving the stability of combustion systems. Further research is needed to explore these mechanisms and their effects on combustion stability in various conditions and designs.

1.3.3. Low-order modelling of thermoacoustic instabilities

In the perspective of predicting TAI in aero-engines during their design phase, conducting test campaigns or performing numerical simulations on prototypes in this iterative process are time-consuming and costly. The data from thermoacoustic experimental tests or high-fidelity numerical simulations can be used to inform and calibrate the parameters of analytical model of the feedback loop pictured in Figure 1.13. Instead of solving the full Navier-Stokes equations in the real geometry of an aero-engine, a low-order model of the thermoacoustic problem is often used, considering the frequency-domain

Helmholtz equation when assuming linear acoustics [77]:

$$\nabla \cdot \left(\frac{1}{\overline{\rho}} \vec{\nabla} \tilde{p} \right) + \frac{\omega^2}{\gamma \overline{p}} \tilde{p} = \mathrm{i}\omega \frac{\gamma - 1}{\gamma \overline{\rho}} \tilde{\dot{q}} \tag{1.6}$$

where ω the angular frequency and $\tilde{\cdot}$ denotes the Fourier transform as $\tilde{p} = \int_{-\infty}^{+\infty} e^{-\mathrm{i}\omega t} p' dt$ of the signal.

In Equation 1.6, the acoustic propagation inside the system and the flame dynamics are decoupled, respectively represented by the left and the right hand terms. Hence, the widespread method to predict thermoacoustic instabilities in a system is to model, on the one hand, its acoustic response through acoustic model of the combustor, and on the other hand, the flame response to acoustic disturbances. By also identifying the right boundary conditions of the acoustic model, it is possible then to compute the frequencies and the growth rates of each thermoacoustic mode which can be potentially triggered in the system. In complex geometries, this may be done with a Helmholtz solver (see e.g. [71]) or a low-order acoustic network model (see e.g [117]). This framework is now applied in the design of industrial burners [51].

1.3.3.1. Acoustic network modelling

Acoustic network modeling consists of representing the burner as a set of elementary acoustic components which are connected between them, each component representing an element of the burner [118, 119]. When investigating longitudinal modes, the burner is decomposed as series of one-dimensional ducts as shown in Figure 1.18. The propagation of acoustic waves in the system is determined by expressing the so-called Acoustic Transfer Matrices $\mathcal{T}_{ij}$ between the sections i and j of the acoustic network. The matrix $\mathcal{T}_{ij}$ relates the Fourier transform of the pressure and velocity fluctuations between those sections as:

$$\begin{pmatrix} \tilde{p}_j / (\overline{\rho c}) \\ \tilde{u}_j \end{pmatrix} = \mathcal{T}_{ij} \begin{pmatrix} \tilde{p}_i / (\overline{\rho c}) \\ \tilde{u}_i \end{pmatrix} \tag{1.7}$$

Gaudron [120] and Polifke [121] provide exhaustive reviews of the expressions for $\mathcal{T}_{ij}$ associated to different acoustic elements (straight duct, compact area change, compact flame, ...) that could be met in a burner. Once defined for each element, a global acoustic transfer matrix is obtained as the product of the elementary acoustic transfer matrices and its eigenvectors correspond to the thermoacoustic modes of the burner. This formulation can be extended to take into account the propagation of equivalence ratio waves [122, 123], entropy waves [124] or azimuthal modes in annular chamber [125, 126].

1.3.3.2. Flame Transfer Function (FTF)

A compact flame can be described as a discontinuity at a section j in the acoustic domain. Assuming that pressure is constant through the flame, the jump conditions across the flame fronts are [77]

$$\tilde{p}_j = \tilde{p}_{j+1} \tag{1.8}$$

$$S_{j+1} \tilde{u}_{j+1} = S_j \tilde{u}_j + \frac{\gamma - 1}{\gamma \overline{p}} \tilde{\dot{Q}} \tag{1.9}$$

To model the acoustic transfer matrix of the flame in order to compute the thermoacoustic modes, it is then necessary to link the total unsteady heat release $\tilde{\dot{Q}}$ of the flame to the gas velocity $\tilde{u}_j$ fluctuations

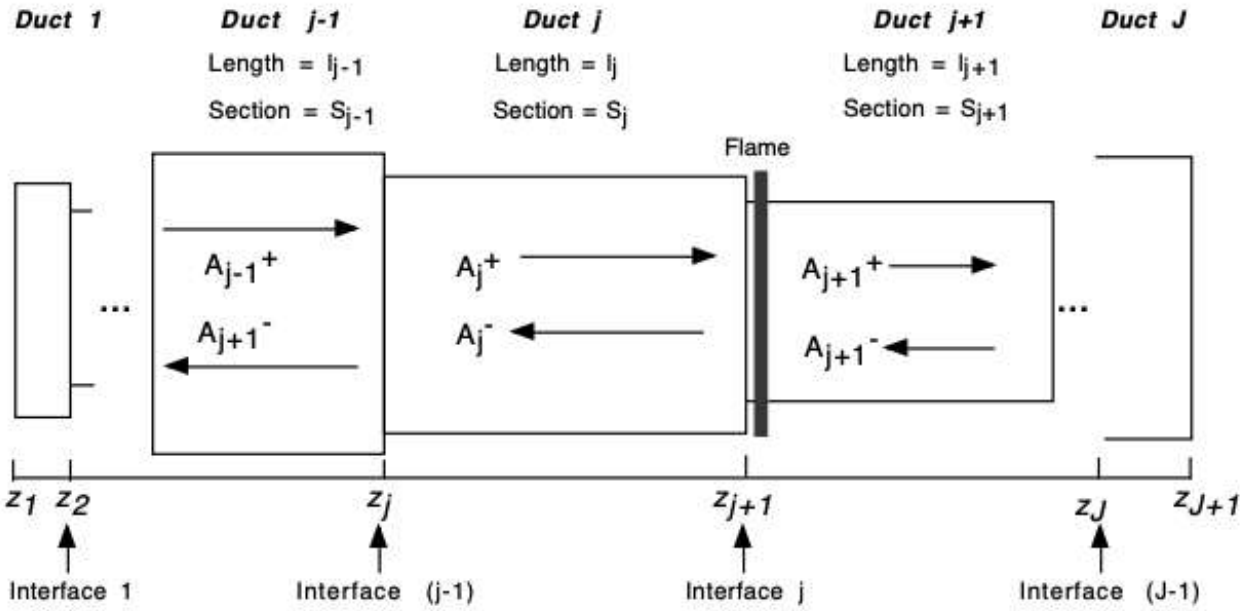

Figure 1.18. – Decomposition of a system into one-dimensional sections. Reproduced from [77].

right upstream the flame . It was firstly done by Crocco and Cheng [127] by introducing a $n-\tau$ model in a time domain representation, n and τ measuring respectively the gain and the delay between $\dot{Q}$ and $u'_{g,j}$:

$$\frac{\dot{Q}'}{\overline{\dot{Q}}} = n\frac{u'_j(t-\tau)}{\overline{u}_j} \tag{1.10}$$

From this pioneer work, a frequency domain formulation has emerged with the so called Flame Transfer Function (FTF) $\mathscr{F}$ defined as [58]

$$\mathscr{F}(\omega) = \frac{\tilde{\dot{Q}}/\overline{\dot{Q}}}{\tilde{u}_j/\overline{u}_j} \tag{1.11}$$

To take into account the non linear nature of the flame response to acoustic disturbances, an extended formulation named Flame Describing Function (FDF) has integrated the dependence of FTF to the amplitude of relative fluctuations $\tilde{u}_j/\overline{u}_j$ [128, 129]. Assuming that the flame response to acoustic disturbances generated by self-excited combustions instabilities as those produced by an external actuator, many derivations and measurements of FTFs through numerical simulations and experiments have been possible the last decades. They have been recently reviewed for premixed combustion systems by Schuller et al. [130]. Similar works were performed in the time domain and are reviewed by Polifke et al. [131].

In many gas powered or aeronautical engines, flames can also be submitted to equivalence ratio modulations (i.e mass fuel fraction modulations), [132, 133]. Hence, to distinguish the contribution to each perturbation, the FTF can be written as follows:

$$\frac{\tilde{\dot{Q}}}{\overline{\dot{Q}}} = F_u(\omega)\frac{\tilde{u}_j}{\overline{u}_j} + F_\Phi(\omega)\frac{\tilde{\Phi}_j}{\overline{\Phi}_j} \tag{1.12}$$

where Φ_j is the upcoming equivalence ratio at the flame front and $F_u(\omega)$ and $F_u(\Phi)$ are the gas velocity and equivalence ratio transfer functions respectively.

To respect the compactness assumption [134], the distance between the flame front and the reference position, where the perturbations $\tilde{u}_j$ and $\tilde{\Phi}_j$ are recorded, needs to be (i) very small compared to the acoustic wavelength, and (ii) also small compared and to the convective wavelength. Condition (i) is generally satisfied but condition (ii) is more difficult to ensure in many systems due to instrumentation difficulties close to the burner. When these conditions are not fulfilled, it leads to misunderstanding about the FTF obtained, which will depend in these cases on the location of the measurements but also on the downstream and upstream acoustic boundary conditions.

However, measurements close to the burner outlet are often impossible to do. The problem is illustrated with the diagram shown in the Figure 1.19. It is a simplified representation of a laboratory spray burner. Fuel is injected in a pulsated air flow and burnt through a planar flame sheet stabilized at section (2). Measurements are generally only possible in the fresh gas away from the inlet of the combustor chamber, here at section (1). Hence, one needs to extend the FTF method by expressing the relative fluctuations $\tilde{u}_2/\overline{u}_2$ and $\tilde{\Phi}_2/\overline{\Phi}_2$ just upstream the flame according to the relative velocity fluctuations $\tilde{u}_1/\overline{u}_1$ and the pressure fluctuations $\tilde{p}_1/\overline{p}_1$ recorded at section (1) inside the air injection unit [134].

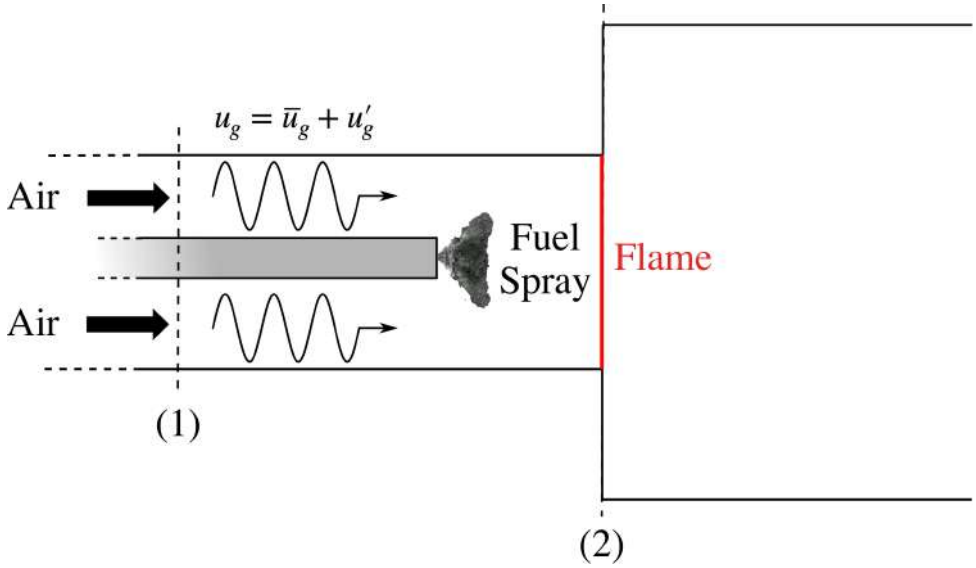

Figure 1.19. – Simplified representation of an air-fuel injection unit of a spray burner

This approach has been retained for example by Gaudron et al. [135] to study the response of a CH_4/air premixed swirled flame, where relations between FTFs were established for three different reference recorded signals .

1.3.4. Monitoring combustion instabilities

During the conception phase of a given gas turbine, engineers use low-order models and numerical simulations to optimize a design that aims to avoid thermoacoustic instabilities. Nonetheless, these tools are not mature enough to rely only on them. Hence, the design phase of aero-engines is still an iterative trial and error process highly depending on bench testing of engine prototypes where online monitoring of the combustion dynamics is performed. These multiple investigations have to raise dynamic issues as early as possible during this design phase. In most of systems, if an operating point with dynamic issues is detected lately, a change of the operating parameters is attempted to avoid these dynamic issues. But, in the worst cases, the system has to be redesigned by the manufacturer in order to be retrofitted to fix the problem, which can lead to very high costs [50, 136].

Obviously, even if a large range of input parameters is studied, every operating conditions that the gas turbine will meet through day to day operation along with ageing and degradation of its components cannot be entirely covered. Hence, an online monitoring of the combustion state is performed in order to watch for potential occurrence of combustion instabilities during operation for power gas turbines and during maintenances for aero-engines. Using a pressure measurement inside the combustion chamber, the online monitoring of combustion dynamics enable to detect as early as possible abnormal operation linked to a failure component and then has considerably decreased the number of accidents and increased the lifetime of power gas turbines [51]

Finally, online monitoring opens the possibility of applying an active control in the combustion chamber to deal with undesired phenomena [137]. This is a very active field of investigation with a large number of innovations. Making a list of all these strategies is out of the scope of this work, restricting itself to two recent examples among others. For instance, a pilot diffusion flame was shown to successfully extend the stability margins through modulation of the phase of the unsteady heat release rate to decouple the acoustic/combustion process [138, 139]. Recently, as an alternative to fuel injection, nanosecond repetitively pulsed discharges (NRPD) is gaining interest to also enhance the dynamic stability of a combustion chamber [140–145]. Nonetheless, active control requires in general large modification of the existing systems and remains today at the state of research topic, being very rarely experienced in real power systems [136, 146, 147].

1.4. Motivations and objectives of the thesis

In order to reach very low NOx emissions to meet international regulations, the major trend for the aero-engines design is to achieve lean premixed combustion which increases the probability to trigger TAI during operation. Low-order models and numerical simulations coupled with online monitoring of combustion dynamics are used by manufacturers to prevent CI to occur in combustion chambers throughout its entire life i.e. from its design to its end of operation. New combustion technologies are more prone to develop combustion technologies, these tools have to be strengthened.

Mechanisms underlying the heat release perturbations due to acoustic disturbances have been widely studied for laminar and swirling premixed gas flames. These studies have led to analytical expressions of FTF modelling the flame dynamics. Such analytical expressions are essential for manufacturers because they give insightful guidelines to help designing a system free of TAI. Furthermore, low order models of the flame dynamics reduce greatly the time and cost when evaluating the thermoacoustic behavior of burners because they do not require to measure numerically or experimentally the FTF at the desired operating points. Regarding the analysis of the acoustic response of spray flames, the two-phase nature of the flow adds supplementary complexities to the description of the flame destabilizing effects, originating from the interactions between the acoustic field, the gaseous flow field and the spray dynamics. Unfortunately, even if these effects have been observed numerically and experimentally, only the consequence of oscillating evaporation rate has been described analytically [100]. In particular, the impact of particles clustering and unsteady atomization on flame dynamics are ones of the missing stones to build analytical models of the FTF for spray flames. Recently, Kulkarni et al. [148] derived analytical expressions from the Euler-Lagrange formalism, describing the formation and propagation of number density waves for an evaporative monodisperse population of droplets in pulsated air flow. However, the transfer functions of spray flames are mainly determined from the experiments [149–155].

Online monitoring relies so far on pressure fluctuations measured in the combustion chamber to identify precursors of TAI. However, the increase of combustion noise prior to impending combustion instabilities is a necessary condition of TAI but not a sufficient one. Hence, better and more robust precursors and monitoring tools have to be defined in order to use them and in addition to pressure measurements for a better prevention of combustion instabilities.

The present thesis proposes tackle TAI in aero-engines by meeting the two following objectives:

- **Objective 1:** To improve the modelling of the response of spray to acoustic disturbances. A particular attention is addressed to the formation of particles clustering and the angle oscillations of hollow-cone spray. Modelling such acoustic-spray interactions will greatly help the development of low-order models and numerical tools of the combustion of a swirl-stabilized spray flames.
- **Objective 2:** To elaborate new techniques to perform online monitoring of combustion dynamics. Their performance to predict incoming TAI has to be evaluated against those of existing monitoring tools.

1.5. Outline of the manuscript

The manuscript is organized as follows;

Chapter 2 presents the experimental setup named TALISMAN that has been built in Institute of Fluids Mechanics of Toulouse to tackle objectives 1 and 2. Designed to reproduce a single sector of an annular combustor chamber at a laboratory scale, this swirl stabilized spray burner has a modular geometry and a description of the geometrical configurations that have been retained are given. The experimental diagnostics performed on these configurations are also reported. Finally, the numerical setup used to perform Large Eddy Simulations of the TALISMAN burner with the AVBP solver is described.

The manuscript is then divided in two parts, each one associated with the objectives of the thesis. The first part of this manuscript is devoted to the interactions between a fuel spray and an acoustic field.

Chapter 3 details the different models elaborated to study the spray/acoustic interactions in a 1D configuration for an isothermal spray in a laminar flow field. The simplifications made allow to focus only on the particle velocity and number density responses of spray and more specifically on the particle clustering phenomenon. The response of a single droplet is studied first through an Euler-Lagrange formalism. It will help to determine cases studies with different strengths of coupling between the droplet and gas velocity field. The Euler-Euler formalism is then presented and a model is elaborated to analyze the response of a perfectly monodisperse spray submitted to sound waves. Numerical simulations show that the intensity of the particle clustering is weakly correlated to the response of a single droplet. Finally, a model including a homogeneous and isotropic particle velocity dispersion is presented.

Chapter 4 shows how to express analytically the particle velocity and number density waves propagating when a perfectly monodisperse spray is injected in a pulsed laminar flow field. The equations obtained in the Euler-Euler formalism are linearized and are solved in the case where fuel droplets are injected with the same velocity as the gaseous phase. The case with different injection velocities is then explored. The empirical observations about particle clustering found in the literature are now interpreted with the help of these analytical expressions which are for the first time derived in an Euler-Euler formalism and linked to adimensional quantities such as a Stokes and a Mach number. These expressions are validated against numerical simulations at the end of the chapter.

Chapter 5 studies the influence of the particle velocity dispersion on the number density waves. While the polydispersion of particles at the injection is often modelled through different distribution laws, the particle velocity dispersion is often neglected or modelled with rough approximations. A characteristic analysis is performed on the system of equations derived in Euler-Euler framework for a homogeneous and isotropic particle velocity dispersion. This analysis shows that the particle velocity dispersion introduces characteristic waves linked to its level of dispersion, that influences the amplitude and the velocity of the number density waves propagating in the system. These theoretical results are validated against numerical simulations.

Chapter 6 finally studies the response of a hollow cone spray submitted to acoustic disturbances. The validity of the FIM-UR model of unsteady sprays is tested for numerical simulations against PDPA measurements. The structure of the spray and in particular the response of injection angle are closely examined.

The second part of this manuscript is dedicated to the investigation of thermoacoustic instabilities in the TALISMAN setup.

Chapter 7 details the characteristics of self-excited oscillations reported in the TALISMAN setup for a specific geometrical configuration. The methodology presented in Section 1.3.3 is used to predict the occurrence of such natural TAI. Acoustic and FTF measurements are conducted.These measurements are combined with low-order model simulated by the solver OSCILOS. The relationship between the OH^* signal emitted by a spray flame and its heat release rate is also examined and discussed.

Chapter 8 deals with the online monitoring of a TAI observed in the TALISMAN setup. A new precursor based on the acoustic energy flux at the burner inlet is used to predict impending TAI. The methodology to measure this acoustic flux in a robust way is presented. Its performances are compared to other precursors commonly used to monitor combustion dynamics in combustion chamber. For online monitoring purposes, the application of Deep-Learning techniques is finally discussed for this burner configuration in particular and for gas turbines in general. The pre-requirements to use DL tools are listed.

The outline of the manuscript is illustrated in Figure 1.20.

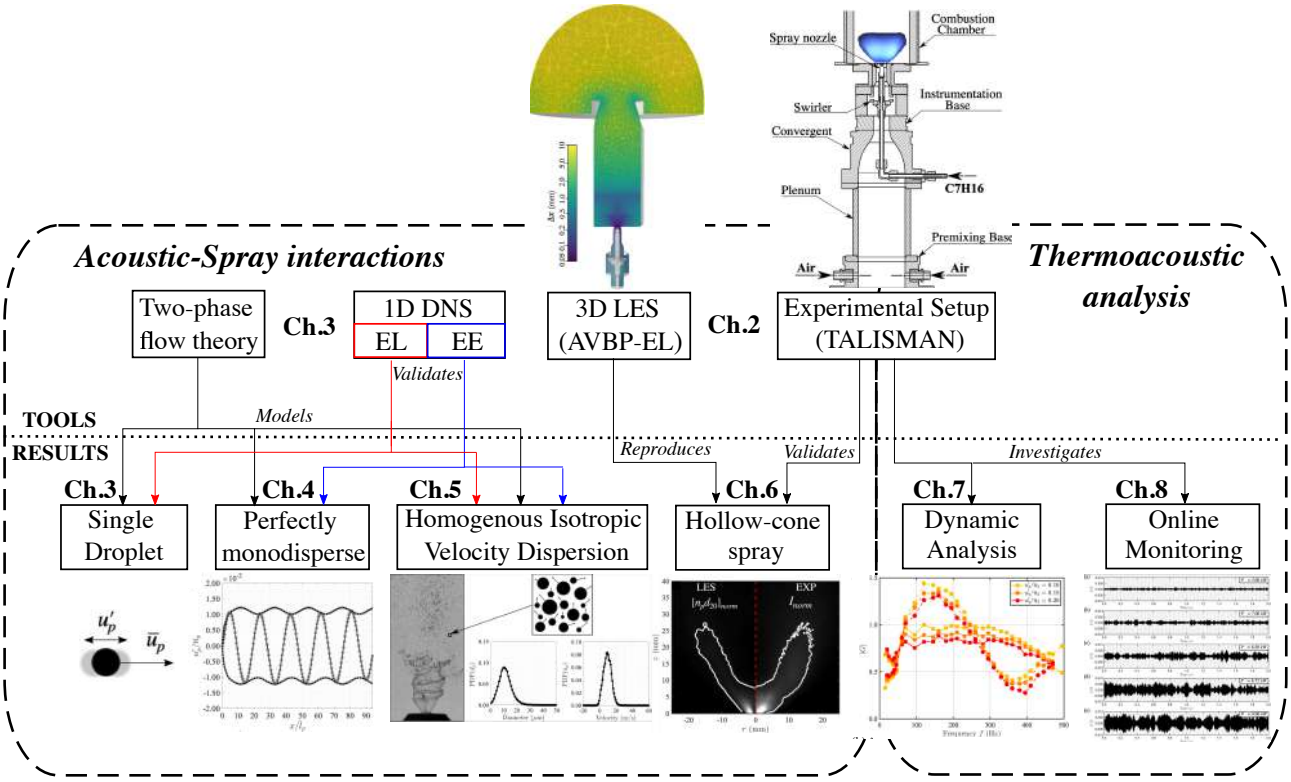

Figure 1.20. – Outline of the manuscript

1.6. Publications during the thesis

The work presented in this manuscript has led to the following publications:

- **T. Morinière**, L. Selle, T. Poinsot and T. Schuller (2023), A thermoacoustic instability precursor based on the acoustic flux at the combustion chamber inlet, *Combustion Science and Technology, 195:14, 3357-3371*
- **T. Morinière**, D. Laera and T. Schuller (2023), Influence of the particle velocity dispersion on the acoustic response of a 1D non-evaporating monodisperse fuel spray, *International Journal of Multiphase Flow, to be submitted*
- **T. Morinière** and T. Schuller (2023), Analytical study of the linear acoustic response of a monodisperse spray in a uniform laminar gas flow,*Journal of Fluid Mechanics, to be submitted*
- **T. Morinière** and T. Schuller (2023), The relationship between the OH^* signal and the heat release rate for spray flames: consequences on the Flame Describing Function, *Symposium on Thermoacoustics in Combustion, to be submitted*
- **T. Morinière**, D. Laera, L. Selle and T. Schuller (2023), Experimental and numerical investigations of the hollow-cone spray response to acoustic disturbances, *International Journal of Spray and Combustion Dynamics, to be submitted*

Chapter 2

Experimental setup

C'était là le jour qu'il attendait depuis des années, le commencement de sa vraie vie. Pensant aux journées lugubres de l'Académie militaire, il se rappela les tristes soirées d'étude, où il entendait passer dans la rue les gens libres et que l'on pouvait croire heureux ; il se rappela aussi les réveils en plein hiver, dans les chambrées glaciales où stagnait le cauchemar des punitions, et l'angoisse qui le prenait à l'idée de ne jamais voir finir ces jours dont il faisait quotidiennement le compte. Maintenant enfin, tout cela était du passé, il était officier, il n'avait plus à pâlir sur des livres, ni à trembler à la voix du sergent. Tous ces jours, qui lui avaient paru odieux, étaient désormais finis pour toujours et formaient des mois et des années qui jamais plus ne reviendraient. Oui, maintenant, il était officier, il allait avoir de l'argent, de jolies femmes le regarderaient peut-être, mais, au fond, il s'en rendit compte, ses plus belles années, sa première jeunesse, étaient probablement terminées

– Dino Buzzati, *Le désert des Tartares, 1940*

This chapter presents the swirl-stabilized spray burner that has been designed in this thesis and used for the experiments conducted. Being modular, the different configurations of the burner are described together with the diagnostics retained to realize the different investigations presented in the manuscript. Finally, the computational setup and methodology to perform a companion numerical study on the burner are also provided.

Overview

2.1. Introduction

When designing a laboratory combustor simulating an aero-engine, the reproduction of a whole engine can not be considered. In addition to obvious space and economic reasons, an aero-engine is not originally designed to easily welcome various sensors in its flow field and, in particular, to have an optical access on the combustion to probe the flow with advanced optical diagnostics. The data provided by these diagnostics are crucial to understand and model the structure of the flow field inside the combustion chamber, the combustion dynamics or the fuel spray behavior released from the injectors. Hence, laboratory scale burners are designed with simplified and scaled down geometries and operating conditions. Example of combustion test rigs for aero-engines studies used in research centers across the world and in particular in France (ONERA, CORIA and EM2C) are listed in [156, 157] and in [158–160], respectively.

The simplifying process of an aero-engine design to a laboratory scale burner depends on the different flow characterizations that the laboratory aims to perform. With only a few simplifications, the data provided aim at providing geometry guidelines for optimized geometries and predictions for the global combustor performance by these experiments. When the burner aims at focusing on the fundamental mechanisms underlying physics phenomena for modeling purpose, the burner design and the operating conditions should be simplified compared to the real designs of the combustion chamber. Still, the downsizing and simplifying process need to represent at best the characteristics of the aeronautical combustion chamber reproduced. The parameters influencing the combustion dynamics are given in the Table 2.1 for aero-engines and similar high performance systems [161]. During this process, it is then essential to fit at best some adimensional parameters (e.g the Reynolds Number, the Damkhöler Number, the Swirl Number, the Stokes number) and operating conditions (e.g the equivalence ratio, the inlet pressure and temperature, the air injection velocity, fuel) encountered for the real engines.

System	Aero-engines
Power density	High ≈ 1 GW.m^{-3}
Chamber pressure	High 3 to 5 MPa
Combustion mode	Partially premixed
Chamber Geometry	Annular
Upstream Boundary	High pressure compressor
Downstream Boundary	Turbine distributor
Injection	Swirling injectors, Hollow cone or multipoint atomizers
State of fuel and oxidizer	Liquid fuel and air / Nitrogent diluent in air stream

Table 2.1. – General characteristics of aero-engines of importance for their combustion dynamics analysis [161].

The Institute of Fluid Mechanics of Toulouse (IMFT) has developed laboratory scale burner with gaseous fuel injection such as MIRADAS [162] and HYLON [163]. No similar burner with liquid fuel injection had been developed yet before this thesis. In the next section, a new experimental setup named TALISMAN integrating a spray fuel injection is presented. The burner configurations used in the following chapters are also enumerated. Then, the diagnostics and post-processing tools that were used are presented. Finally, the numerical setup for LES computations of the TALISMAN burner is detailed.

2.2. Presentation of the TALISMAN set-up: a swirl-stabilized spray burner

2.2.1. General Description

As shown in Figure 2.1, the TALISMAN (ThermoAcoustic instabiLities Investigation for Spray flaMe in Aero engiNes) test rig is a swirl-stabilized spray burner. It aims at mimicking the flow dynamics in a single injector of an annular combustion chamber. Filtered air is delivered to the base of the burner in a section called "premixing base" by a Bronkhorst F202AV massflow regulator at a 15 $Nm^3.h^{-1}$ maximum normal volumetric flowrate, which corresponds to a massflow rate about 19.4 $kg.h^{-1}$. It then flows through a plenum with a 65 mm diameter to obtain a nearly uniform laminar flow. After being accelerated by a converging nozzle, the air flow enters a short annular tube of 12 mm internal diameter called "base instrumentation" where a set of sensors including microphones, a hot wire and K thermocouples can be plugged to characterize the air injection. Air goes then through a radial swirler with 8 feed channels with 4.5 mm diameter, oriented with an angle 25^o off the swirler axis as described in Figure 2.2. Finally, this swirled air stream is injected into the combustion chamber at the ambient pressure through an annular channel with a slightly converging nozzle.

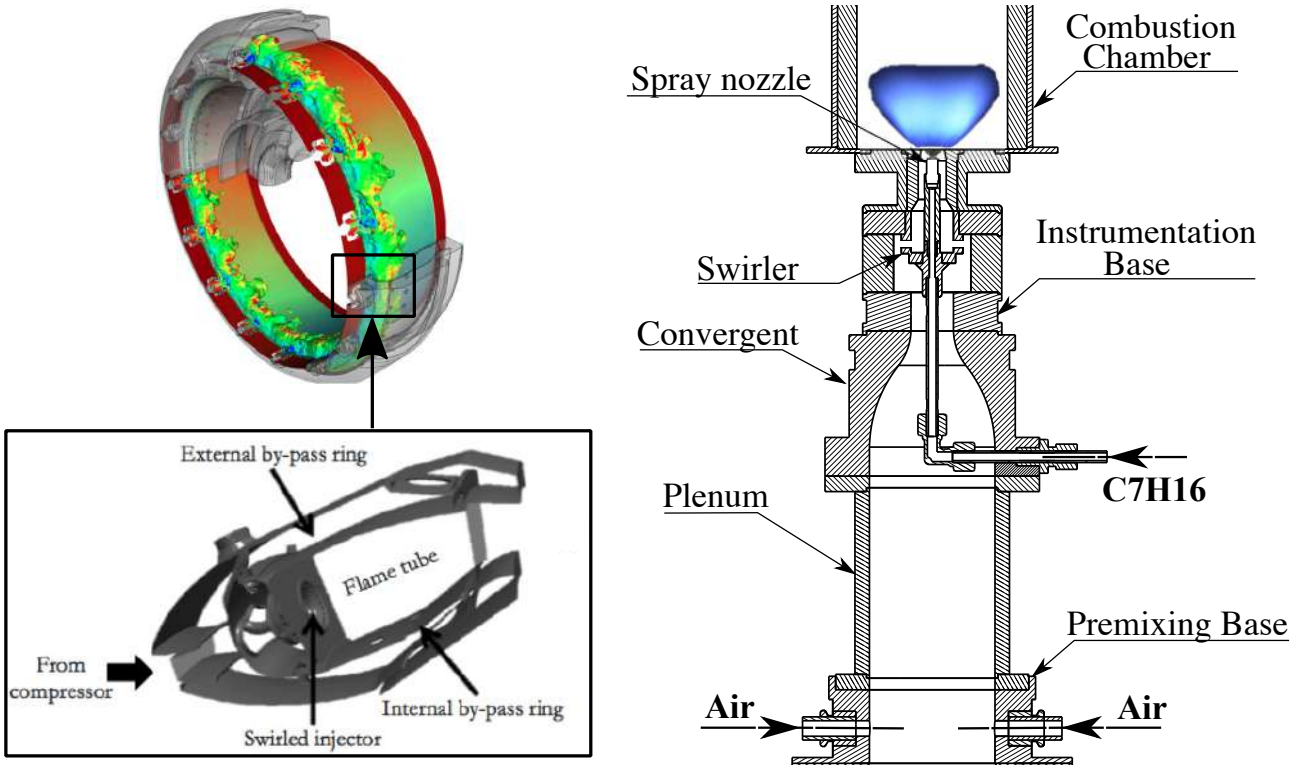

Figure 2.1. – General Description of (left) a single sector of an annular combustion chamber and (right) the generic configuration of the TALISMAN burner. Images of the annular combustion chamber and the single sector on the left are respectively taken from [52] and [164].

Meanwhile, stored in a 2L tank pressurized by N_2 gas at a maximum of 15 bar, liquid n-heptane (C_7H_{16}) is injected through a central tube equipped with a LECHLER hollow cone spray injector into the combustion chamber thanks to a Bronkhorst M13V14i Coriolis massflow regulator. The pressure swirl LECHLER (simplex) injector is set with a small recess distance from the combustion chamber backplane and is pictured in Figure 2.4. It is a stainless steel 316L axial-flow nozzle with an internal swirler and a 100 μm bore diameter that provides a hollow-cone spray with very fine and uniform atomization and a 60^o mean spray angle. Its range of volumetric flow rate with a proper atomization

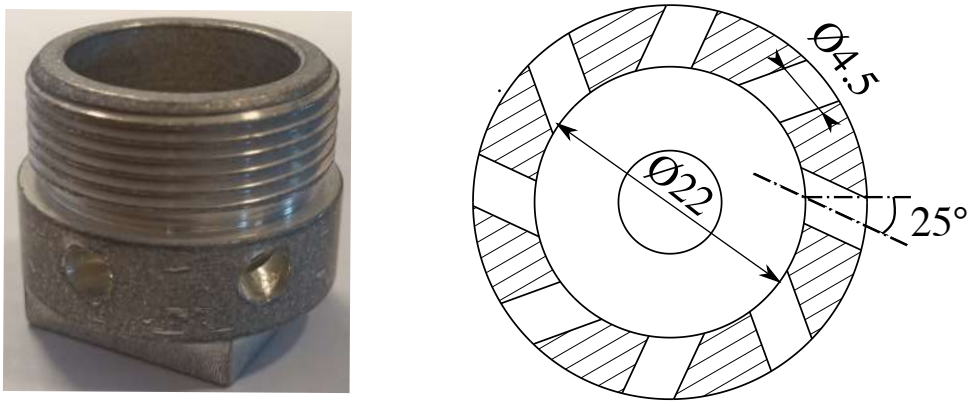

Figure 2.2. – (left) Snapshot and (right) technical drawing of the radial swirler used in TALISMAN. The dimensions are in millimetres.

goes from a minimum of 10 mL/min for a 5 bar tank pressure to a maximum 23 ml/min for a 16 bar tank pressure, corresponding to the thermal power range going from 5 to 12 kW. A strainer insert is integrated to the nozzle in order to prevent any potential clogging of the nozzle, thereby ensuring a long service life. The air-fuel injection system and the resulting flame obtained with it are detailed in Figure 2.3.

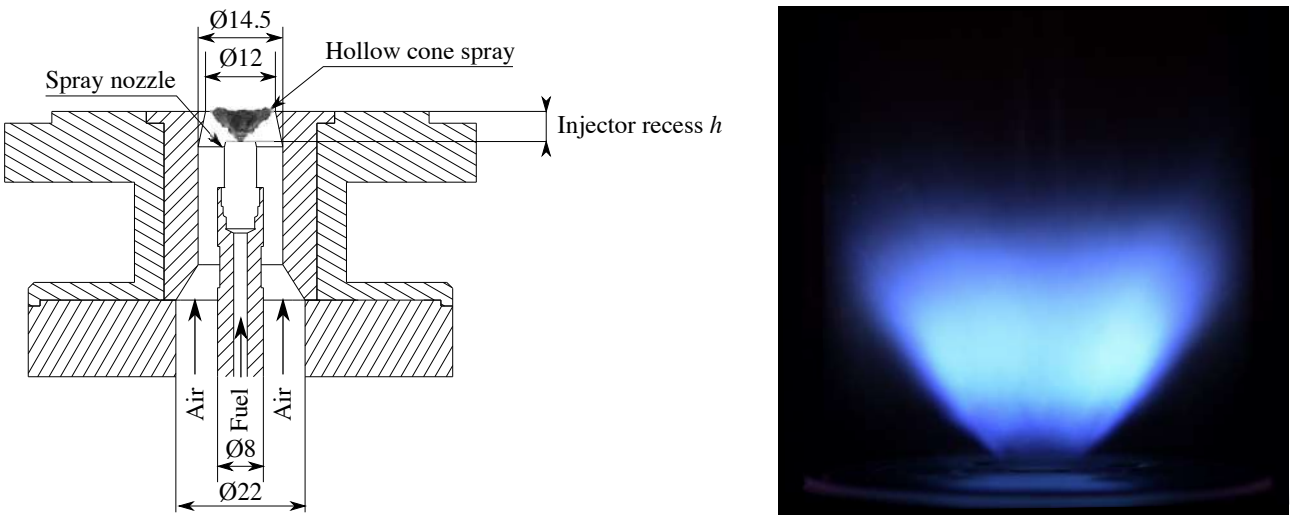

Figure 2.3. – (left) Air-fuel injection system used in TALISMAN. (right) Snapshot of a spray flame stabilized in the TALISMAN setup. The dimensions are in millimetres.

2.2.2. Configurations explored

The burner has been designed to provide a complete modularity of its components and of the flow characteristics. For instance, the length of the plenum and of the combustion chamber, the angle of swirl, the recess of the injector from the combustion chamber back plane can be easily changed to explore up to 20 different configurations. Only 2 main geometrical configurations have been retained. They are presented without their instrumentation in Figures 2.5 and 2.6 respectively. Their characteristics are summarized in Table 2.2.

The configuration named $\mathscr{C}_1$ shown in Figure 2.5 has a long quartz cylinder with a length of 300 mm and a diameter of 83 mm. This tube serves as a combustion chamber. It also features a long plenum

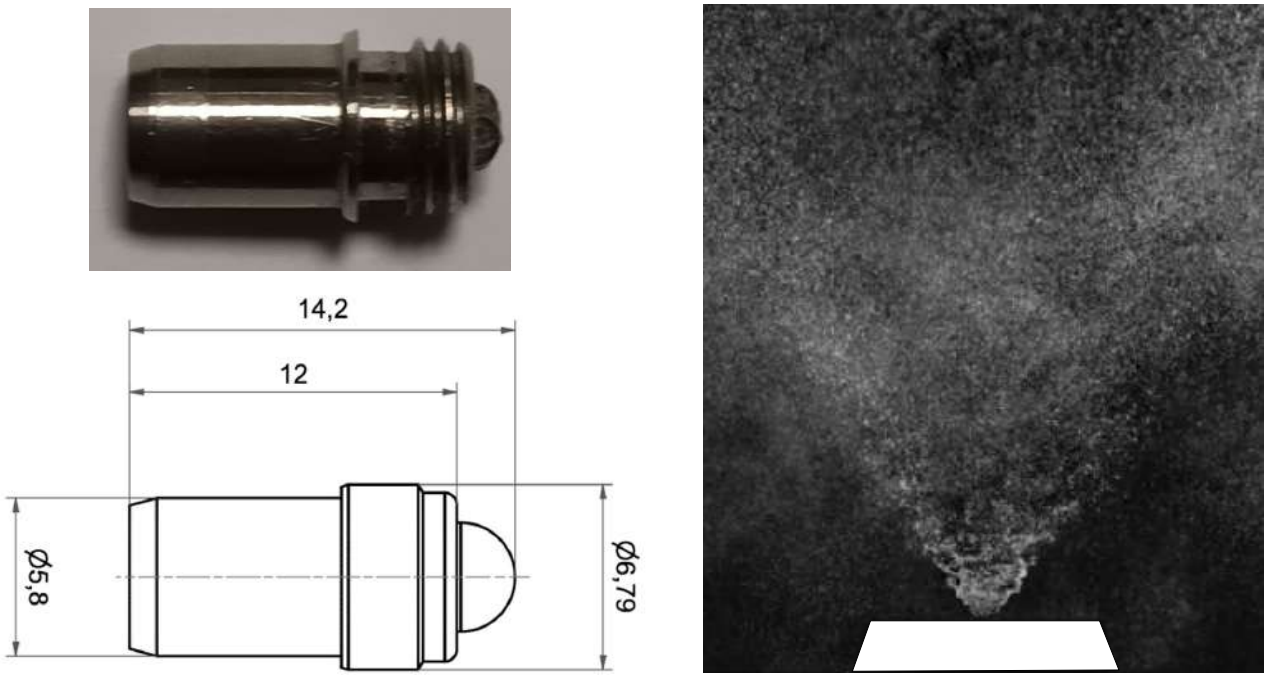

Figure 2.4. – (left) Snapshot and associated technical drawing of the LECHLER nozzle used in TALISMAN and (right) recolorized instantaneous snapshot of the resulting hollow cone spray obtained without co-flow recorded by a high-speed camera.

Configuration Name		$\mathscr{C}_1$	$\mathscr{C}_{20}$	$\mathscr{C}_{21}$
Operating points	Thermal power P (kW)	[5-10]	7	
	Equivalence ratio Φ	[0.45-0.80]	[0.70-0.80]	[0.50-0.80]
Plenum Length (mm)		200	100	
Tube recess h (mm)		3.35		
Swirl angle (°)		25		
Combustion Chamber	Type	Quartz Tube	Square Chamber	Square Chamber + Steel Tube
	Length (mm)	300	190	190 + 430
	Diameter or Side (mm)	Ø83	78	78 + Ø70
Diagnostics		Online monitoring	Acoustic, FTF, PDPA	Online monitoring
Chapters		8	3,6	3,8

Table 2.2. – List of the configurations studied in this work

with a length of 209 mm. This setup features a large operating range with stable, intermittent and unstable operating points as the power P and global equivalence ratio Φ are varied. It also offers the possibility to perform an online monitoring of the flame dynamic stability when approaching thermo-acoustic instability. This configuration is studied in Chapter 8.

Compared to $\mathscr{C}_1$, the configuration named $\mathscr{C}_{20}$ shown in Figure 2.5 is stable over its whole operating range. It features a shorter plenum with a length of 99 mm and a combustion chamber with a square

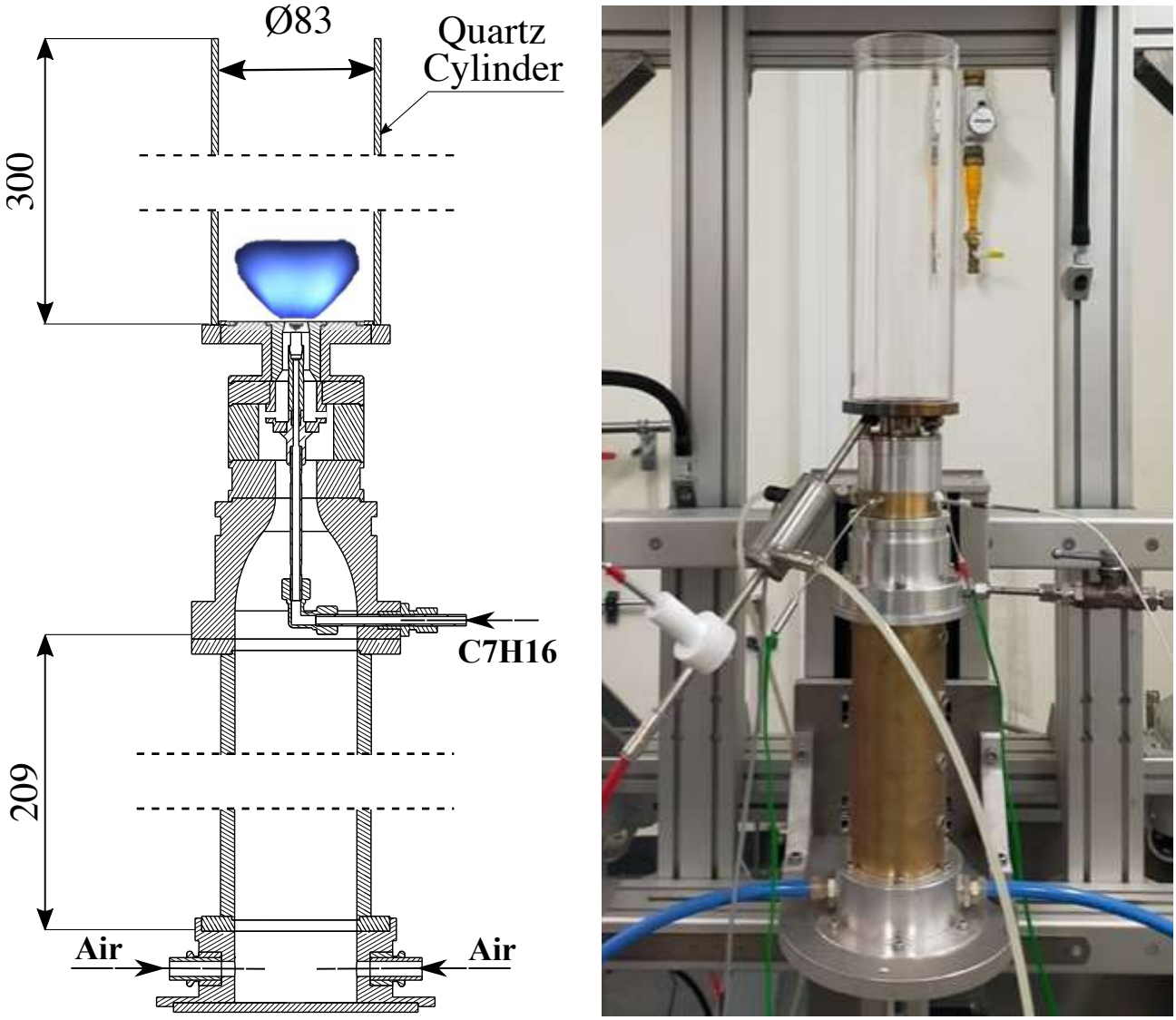

Figure 2.5. – (left) Drawing and (right) snapshot of the TALISMAN configuration named $\mathscr{C}_1$ used in this work

cross section area. The width of the chamber is 78 mm on each side and has 150 mm long quartz walls. It is ended by a 40 mm long nozzle making the combustion chamber 190 mm long. In order to make $\mathscr{C}_{20}$ unstable, a steel tube 430 mm long is added on the top of the combustion chamber. This configuration, which is a derivative of $\mathscr{C}_{20}$, is designated as $\mathscr{C}_{21}$. The natural thermoacoustic stability occurring in $\mathscr{C}_{21}$ is studied in Chapter 7. Flame Transfer Functions measurements are performed on configuration $\mathscr{C}_{20}$ for the flow operating conditions leading to thermoacoustic instabilities in $\mathscr{C}_{21}$. $\mathscr{C}_{20}$ is also used to study the interactions between the acoustic field and the hollow-cone spray in Chapter 6 at a frequency close to the instability frequency that develops in $\mathscr{C}_{21}$.

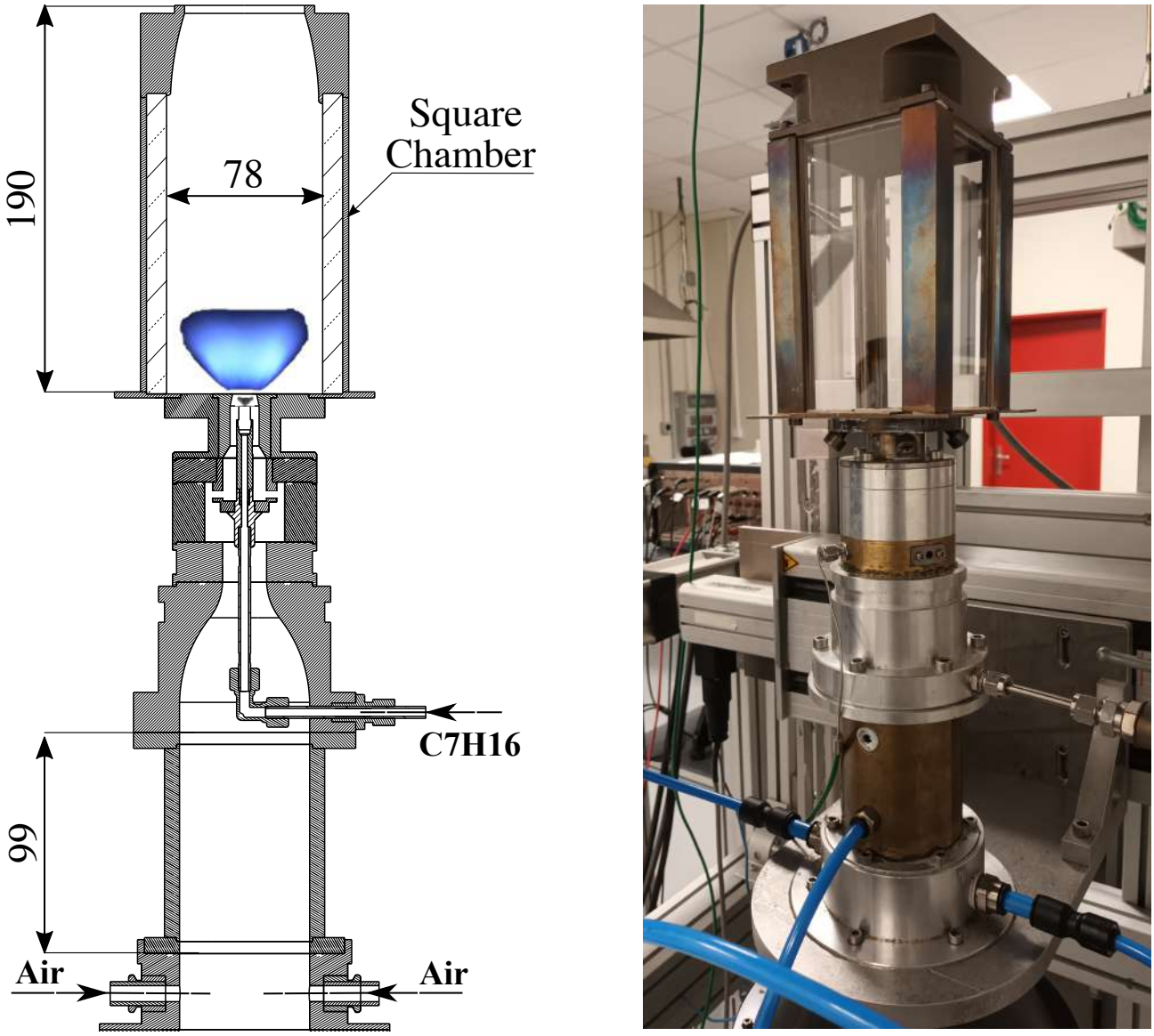

Figure 2.6. – (left) Drawing and (right) snapshot of the TALISMAN configuration $\mathscr{C}_{20}$

2.3. Diagnostics

This section describes the diagnostics used in this work which are summarized in Table 2.2. It also describes how they are implemented in the TALISMAN burner.

2.3.1. Online monitoring implementation

The test rig is instrumented with optical and acoustic diagnostics as pictured in Figure 2.7. A photomultiplier, labelled **PM**, with an interferometric filter centered on 310 ± 2 nm and a half width at half maximum of 10 ± 2 nm is used to record the OH^* radical emissions from n-heptane flames. The temperature T_{RZ} in the outer recirculation zone (ORZ) of the flow is also recorded with a K thermocouple. This information is used to determine the thermal state of the setup.

A miniature DANTEC Dynamics hot wire probe 55P16, labeled **HW**, is mounted below the radial swirler to measure the instantaneous air velocity in an annular channel where the flow is laminar

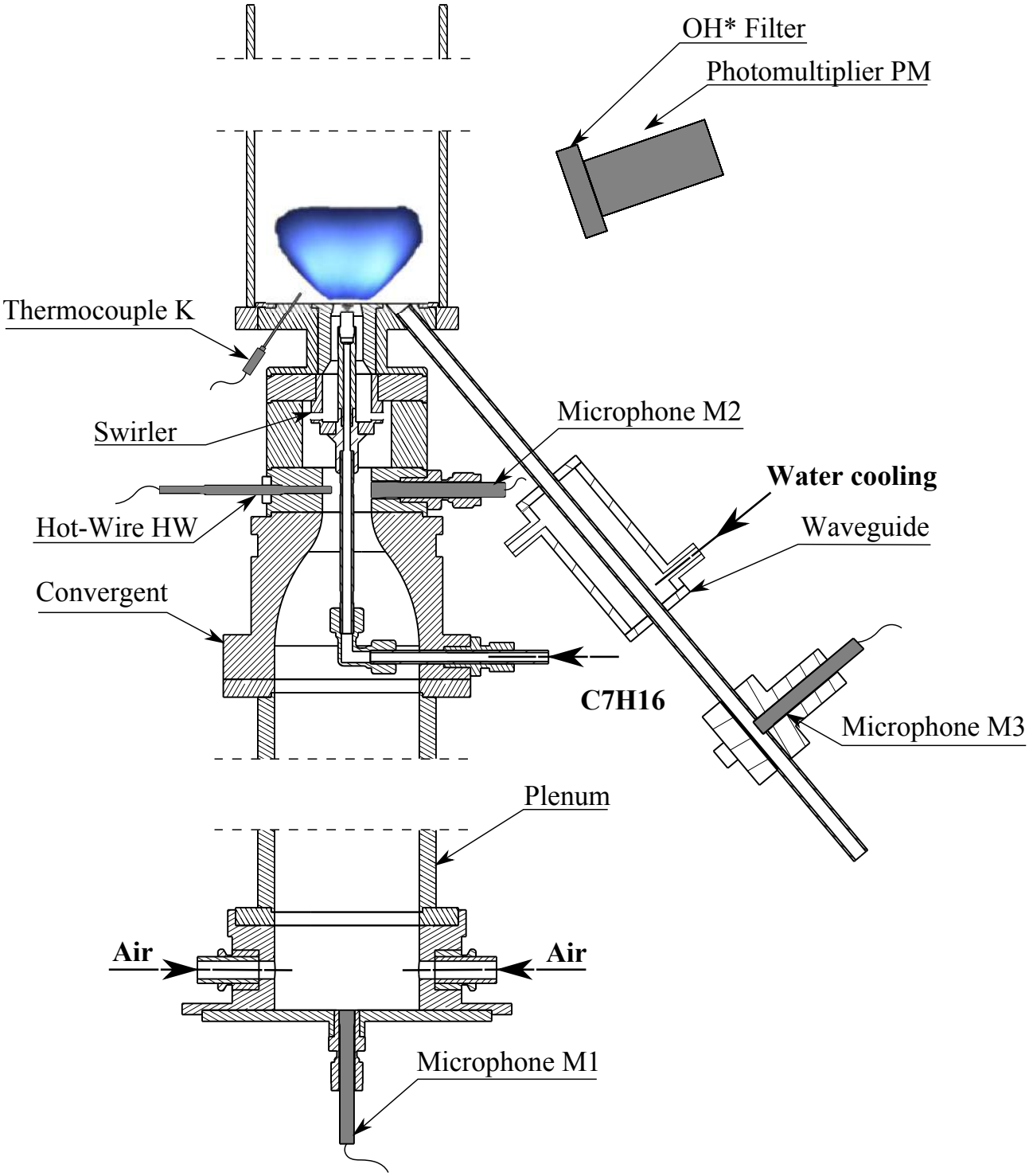

Figure 2.7. – Instrumentation of the burner for online monitoring purpose in the configuration $\mathscr{C}_1$

with an almost top hat profile. The hot-wire probe is very thin wire about 5 μm and is connected to two gold plated stainless steel support where electrical current is flowing through it. Hot-Wire anemometry in a constant temperature configuration consists of measuring the required current to maintain the thin wire in a given air flow field at a constant temperature. It is then possible to link the velocity of the flow field U to the resulting voltage E at the Wheatstone bridge constituting the hot wire thanks to King's law [165]

$$E^2 = A + BU^{0.5} \tag{2.1}$$

where A and B are two constants obtained by a calibration of the hot-wire. Example of a calibration performed in this work is presented in Figure 2.8.

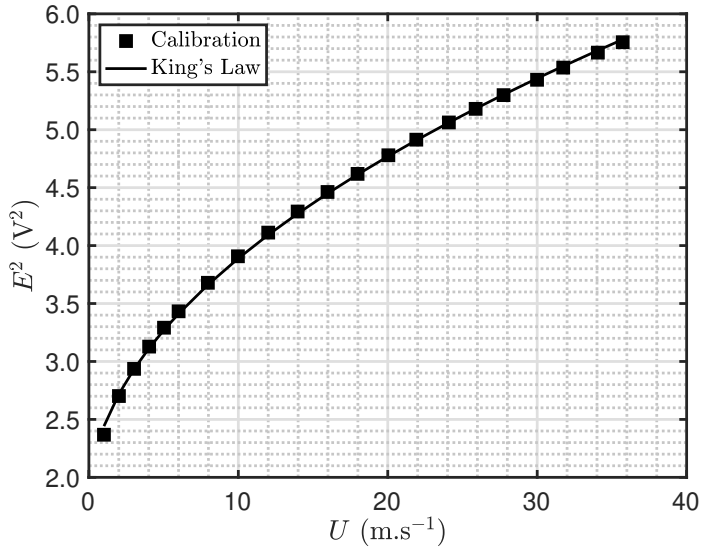

Figure 2.8. – A calibration of a hot-wire miniature probe 55P16.

The microphones **M1**, **M2** and **M3** are Brüel & Kjaer pressure field microphones type 4938-A-011 externally polarized and powered by a 2690-A Nexus signal conditioner. The microphone **M2** shown in Figure 2.7 is installed in front of the hot wire probe **HW** to record the acoustic pressure and air flow velocity. The acoustic flux can then be deduced in this burner section and is used as an indicator of impending TAI in Chapter 8. The acoustic pressure is also recorded at the bottom of the plenum by microphone **M1** and inside the combustion chamber by microphone **M3**. Microphones **M1** and **M2** are flush connected to the wall. Due to the hot burnt gases in the combustion chamber, microphone **M3** is connected on a water-cooled waveguide linked to the combustion chamber. The waveguide is shown in Figure 2.9.(a). To avoid any spurious reflection or sound interference, the waveguide is extended by a 25 m polyamide tube plugged at its end. Sweeping the frequency from 50 to 1000 Hz with a loudspeaker, the transfer function of the waveguide was determined between the acoustic pressure at the waveguide outlet inside the combustion chamber recorded by a microphone named **MC** and the acoustic pressure recorded by **M3** with the experimental setup pictured in Figure 2.9.(b), where the distance between **M3** and **MC** is l_W= 240 mm. At the extremity plugged to the backplane of the combustion chamber, a loudspeaker is driven by a harmonic voltage signal in order to have a constant amplitude of pressure fluctuations when sweeping the forcing frequency from 50 Hz to 1000 Hz. There is no flow in the waveguide in these experiments. For each forcing frequency, the microphone signals are recorded over a duration t_{ac} = 10 s at a sampling frequency f_s = 16384 Hz. The gain G and phase $\Delta\varphi$ of the transfer function between the pressure fluctuations recorded by microphone **MC** and microphone **M3** are presented in Figure 2.9.(b). Measurements are plotted against the theoretical gain and phase values as if the waveguide would be perfect, i.e. a tube without loss or any reflection:

$G = 1$ and $\Delta\varphi = 2\pi f l_w/c$. While the phase lag $\Delta\varphi$ recorded is consistent with the theory, the waveguide reduces the amplitude of the pressure fluctuations recorded inside the combustion chamber along the length l_w. This transfer function is used to deduce the actual acoustic pressure signal inside the combustion chamber from the one recorded by M3 for experiments with combustion. It is assumed that the calibration of the waveguide does not change with combustion.

2.3.2. Transfer Functions measurements

2.3.2.1. Acoustic measurements without flow

The experimental setup presented in Figure 2.10 is used to determine the acoustic modes of the TALISMAN burner for a given configuration. An external excitation of the burner is provided over the frequency range [20 Hz-800 Hz] by a loudspeaker set at the outlet of the combustion chamber with a microphone **M4** put just in front of it. The microphones **M1**, **M2** and **MC** are respectively located at the bottom of the plenum, at the instrumentation base and inside the combustion chamber. Microphone **M4** serves as a reference. The pressure fluctuations recorded by **M1**, **M2** and **MC** are normalized with respect to the signal recorded by **M4**. These data are used to determine the acoustic response of the burner and to infer the nature of each mode detected. This work is done in Section 7.3.

2.3.2.2. Acoustic measurements with non reacting cold flow

To measure the Flame Transfer Function (FTF), it is mandatory to determine the velocity fluctuations at the flame location. Since it is difficult to perform these velocity measurements in reactive flow conditions, they are determined in this work with a low-order acoustic model of the burner which links the velocity fluctuations at the flame location to those recorded upstream. To validate the low-order model, measurements of transfer functions for axial velocity fluctuations are performed with the experimental setup shown in Figure 2.11. Acoustic forcing is generated upstream the combustion chamber over the frequency range [15-500] Hz. An ATOHM LD230CRA08 loudspeaker with a 300 W nominal power is connected to the bottom of the plenum through a convergent. The loudspeaker is put into an airtight box which is connected to the plenum in order to avoid static pressure difference across the membrane of the loudspeaker. Two hot wires are used to measure the velocity in the flow: one, named **HW2**, in a section between the convergent and the swirler, and another, named **HW3**, located at the radius of 3 mm in section 3 at the inlet of the combustion chamber pictured in Figure 2.3. Microphone **M2** is also added in front of **HW2** to measure the pressure fluctuations at this location. Hence, it is possible to measure the transfer function $\mathscr{U}$ between the axial velocity fluctuations $u'/\overline{u}$ recorded by **HW3** and those recorded by **HW2** at given pressure fluctuations $p'/\overline{p}$ detected by **M2** for several levels of velocity fluctuations provided by the loudspeaker located at the base of the burner. These measurements are presented in Section 7.4.1.

2.3.2.3. Flame Transfer Function measurements

The FTFs are measured using the experimental setup pictured in Figure 2.12. Compared to the setup shown in Figure 2.11, the hot-wire inside the combustion chamber is removed and the photomultiplier coupled with the OH^* filter is set to record the OH^* signal emitted by the spray flame. The flame is forced by the upstream excitation provided by the ATOHM's LD230CRA08 loudspeaker over the frequency range [20-500] Hz for several forcing levels $u'/\overline{u}$ at the burner outlet. The OH^* intensity is a good estimate of the instantaneous heat release rate for lean premixed gaseous flames [166]. It is also often considered to be an indicator of heat release rate $\dot{Q}$ for n-heptane hollow cone spray flames operating at globally lean conditions [167]. The relationship between the OH^* chemiluminescence

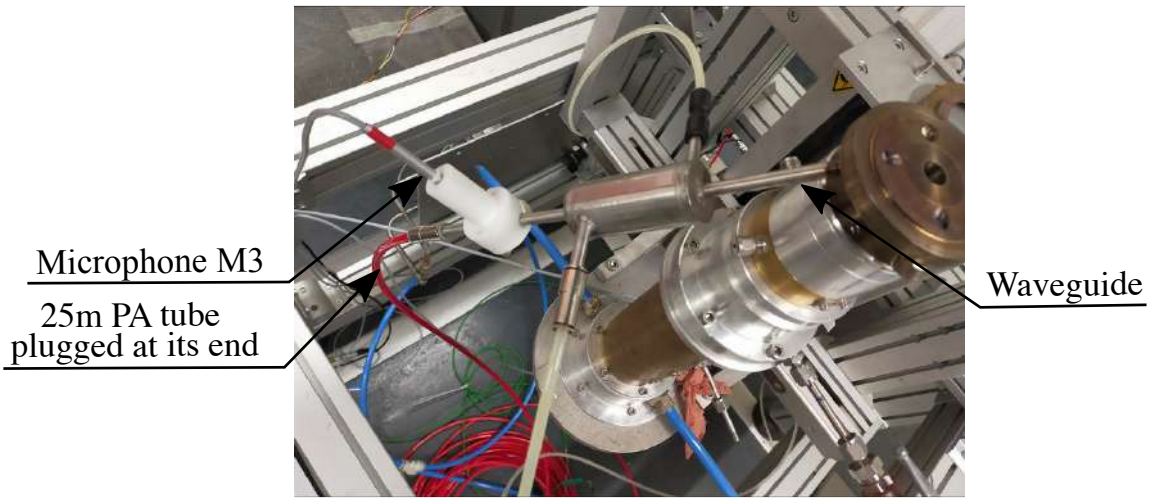

(a)

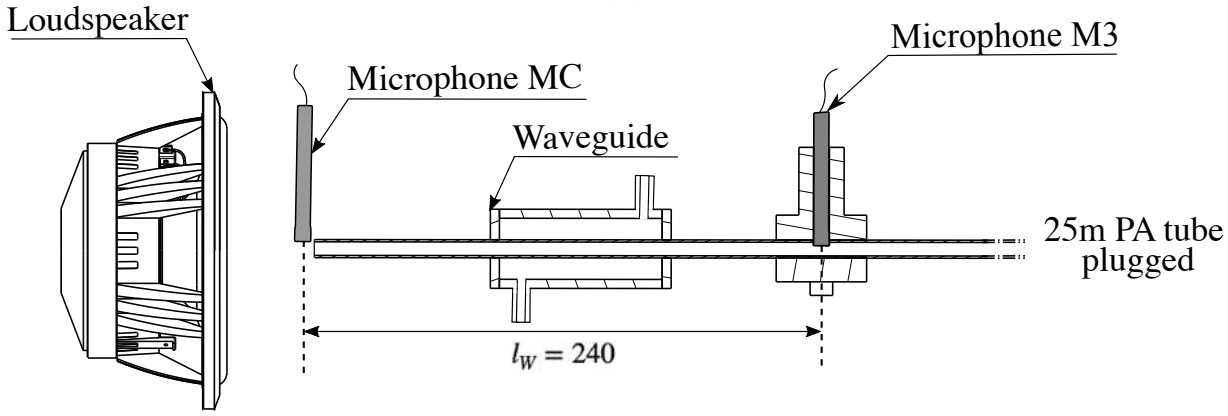

(b)

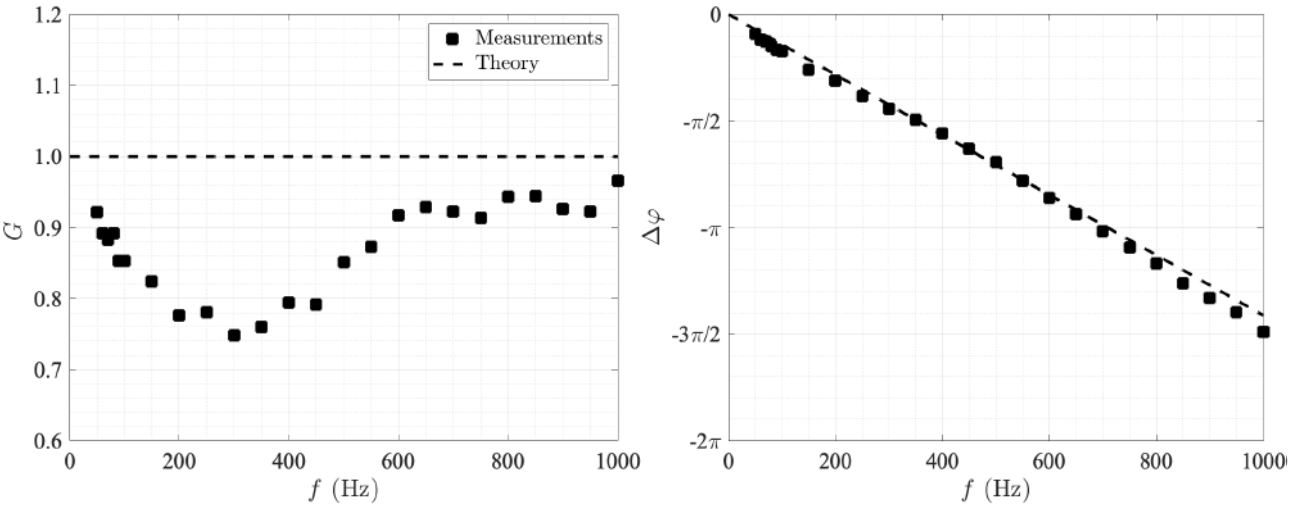

(c)

Figure 2.9. – (a) Snasphot of the waveguide mounted to the combustion chamber backplane. (b) Sketch of the experimental setup used to measure the transfer functions between the pressure fluctuations recorded by **MC** and **M3**. (c) Gain G and phase $\Delta\varphi$ of the measured transfer function compared to theory when the waveguide is considered as a tube without any loss and any reflection ($e^{-\mathrm{i}\omega t}$ convention).

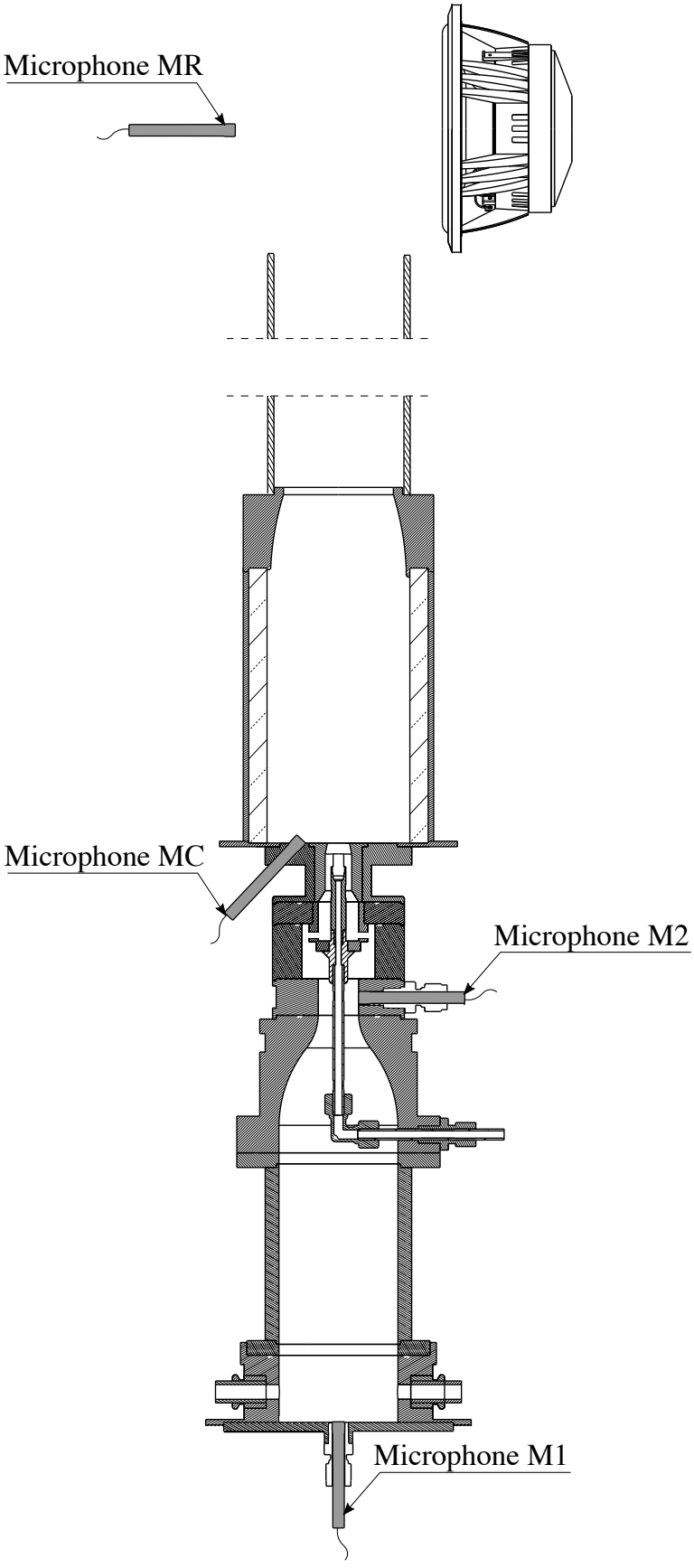

Figure 2.10. – Experimental setup used to determine the acoustic modes of the TALISMAN test rig

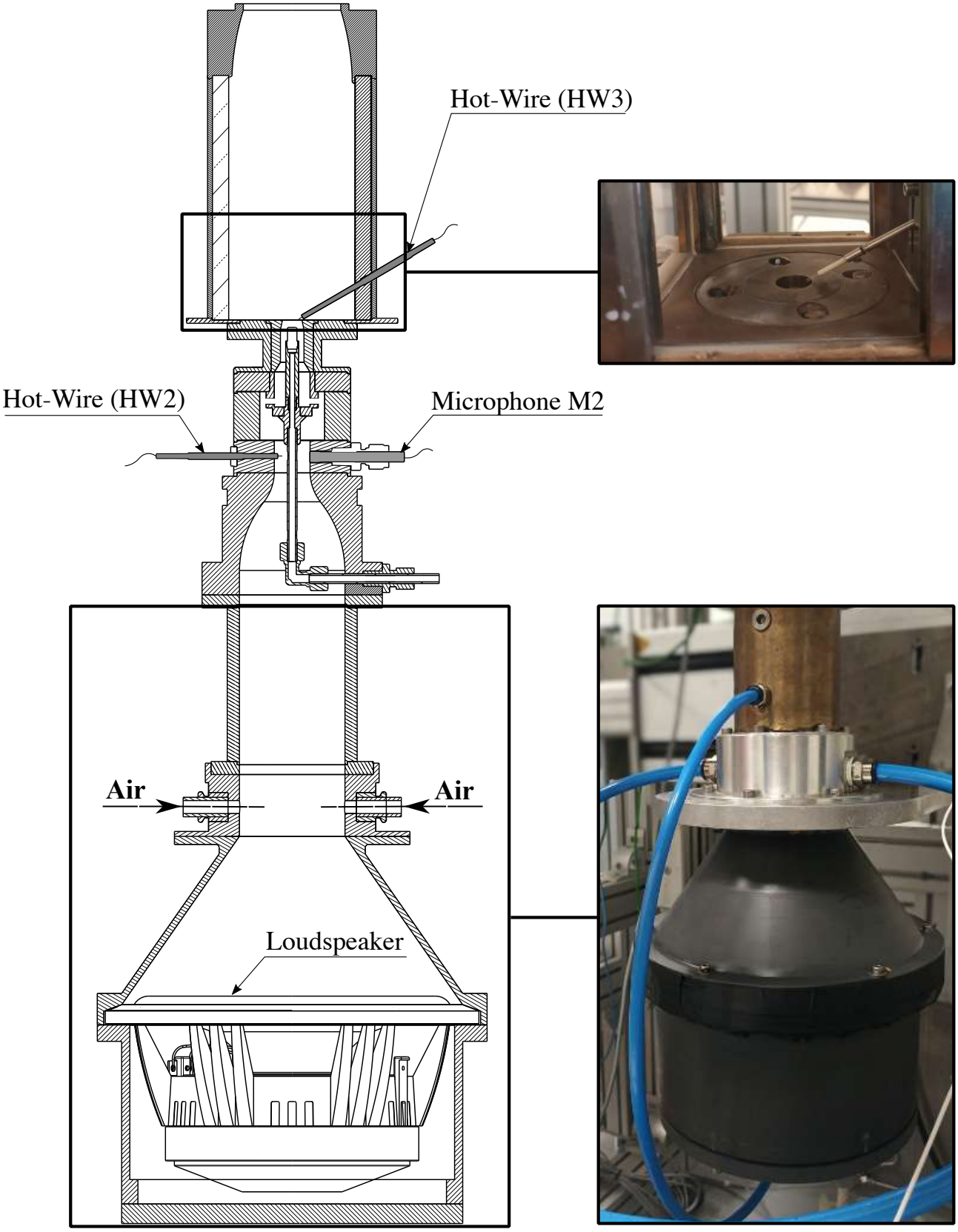

Figure 2.11. – Experimental setup used to determine the transfer function between the velocity fluctuations measured by **HW3** and **HW2**.

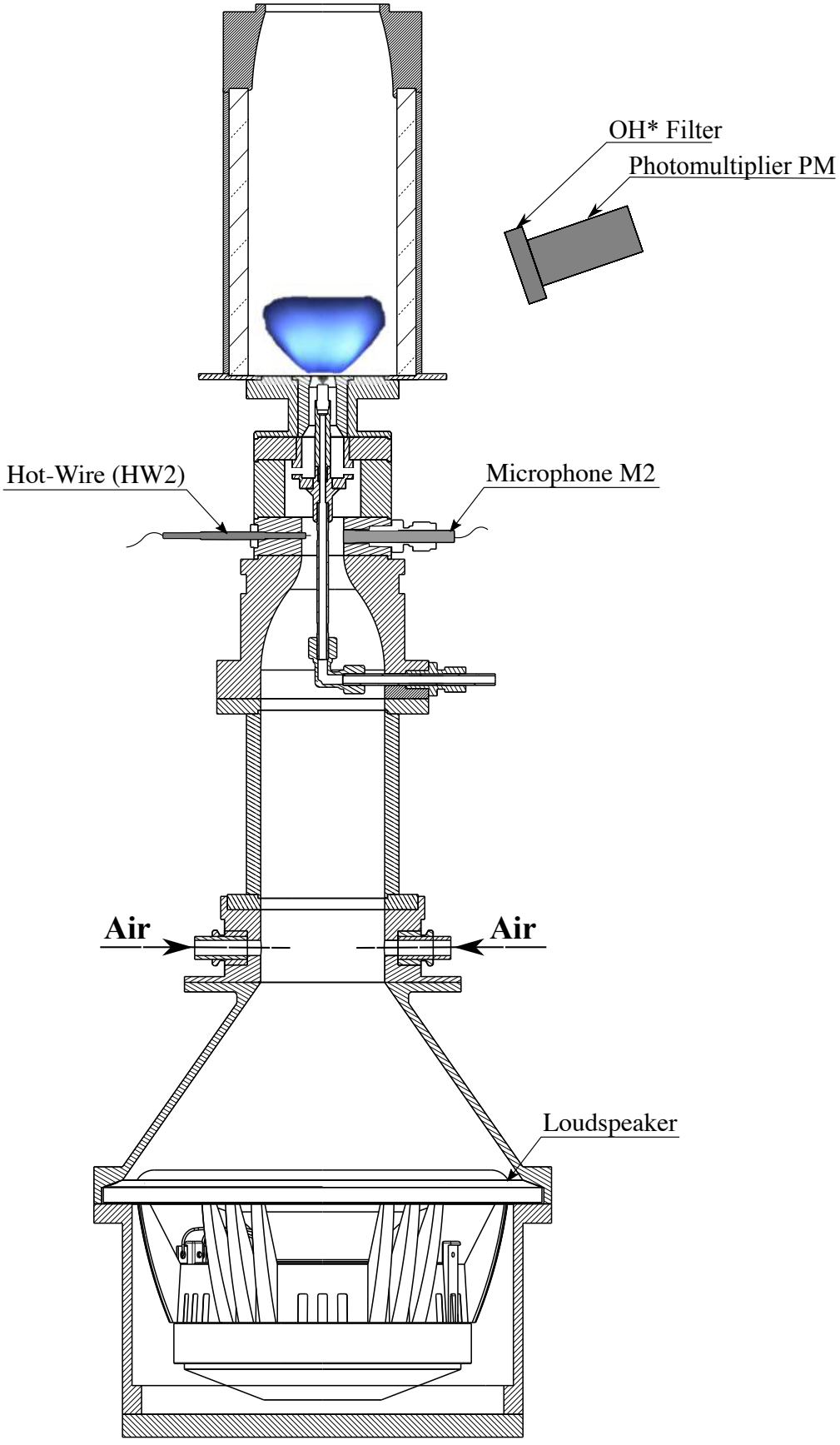

Figure 2.12. – Experimental setup used to determine the Flame Transfer Function.

signal and the heat release rate is investigated in Section 7.4.2. The velocity fluctuations $u'/\overline{u}$ at the air injection outlet are deduced from the low-order acoustic model of the burner developed in Section 7.3 with the pressure $p'/\overline{p}$ and velocity $u'/\overline{u}$ fluctuations recorded respectively by **M2** and **HW2**. The FTFs recorded for the TALISMAN burner are analyzed in Section 7.4.3.

2.3.3. Flow and spray characterization

2.3.3.1. Phase Doppler Particle Analyzer

A Phase Doppler Particle Analyzer (PDPA) is used to measure simultaneously the velocity and diameter of droplets from the spray produced inside the TALISMAN burner by combining a Laser Doppler Anemometer (LDA) and a Phase Doppler Anemometer (PDA). Extensive description of the principle of these measurement devices can be found in [168]. A brief summary is given below.

As illustrated in Figure 2.13, LDA relies on a laser light scattered by the droplets at a certain location with a monochromatic incident light at a wavelength λ_i. The scattered light at wavelength λ_r is detected by a receiver. The particle velocity is inferred from the difference between λ_i and λ_r using the Doppler effect. The Doppler frequency shift remains very small compared to the laser frequency and the direction of projection of the velocity depends on the receiver position. Hence, as illustrated in Figure 2.14, a dual laser beam configuration is used to overcome these issues. The source laser is split through a beam splitter in order to have two incident waves intersecting at the measurement volume. Hence, when a particle crosses the measurement volume, a wave with a Gaussian envelope named Doppler burst is recorded by the photodetector. Analyzing this fringe pattern, the projection of the particle velocity in the dual laser beam plan is computed from the Doppler frequency shift and the angle intersection of the two beams Θ. In order to determine if the velocity direction along the projection axis is positive or negative, one of the incident waves is slightly shifted positively and the other negatively by making use of Bragg Cells.

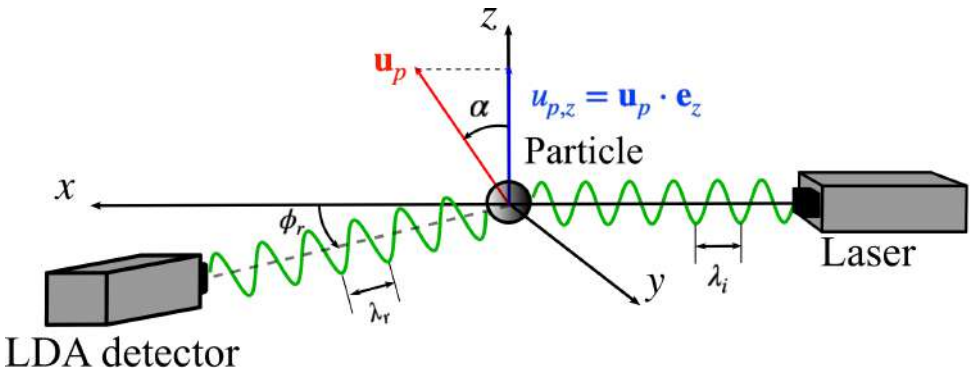

Figure 2.13. – Laser Doppler Anemometer (LDA) principle.

Assuming that particles are spherical, two photo detectors are positioned in the plan orthogonal to the direction studied by the LDA as illustrated in Figure 2.15. They are positioned respectively at an angle $\phi_r + \psi_r$ and $\phi_r - \psi_r$ out of the plane of incident beams, where ϕ_r is the off-axis angle. PDA relies on the phase difference between the signals recorded on the two detectors due to their respective path lengths which are linked to the diameter of the particle detected.

In this study, PDPA measurements are carried out with configuration $\mathscr{C}_{20}$ with a single laser at the wavelength $\lambda_i = 532$ nm and a dual beam splitter. The particle axial velocity along the z-axis and diameter are determined from the signals detected by three separate photo detectors located into a single optical fiber receiver probe with an off-axis angle $\phi_r = 30^o$. Air flow velocity measurements are

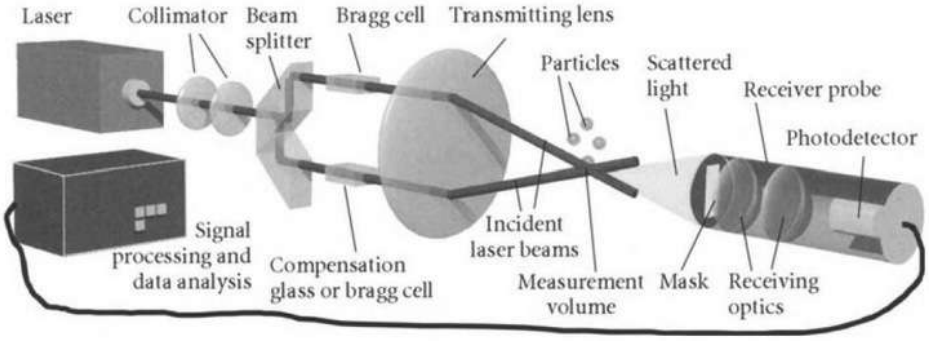

Figure 2.14. – Sketch a Dual Beam Laser Anemometer [168].

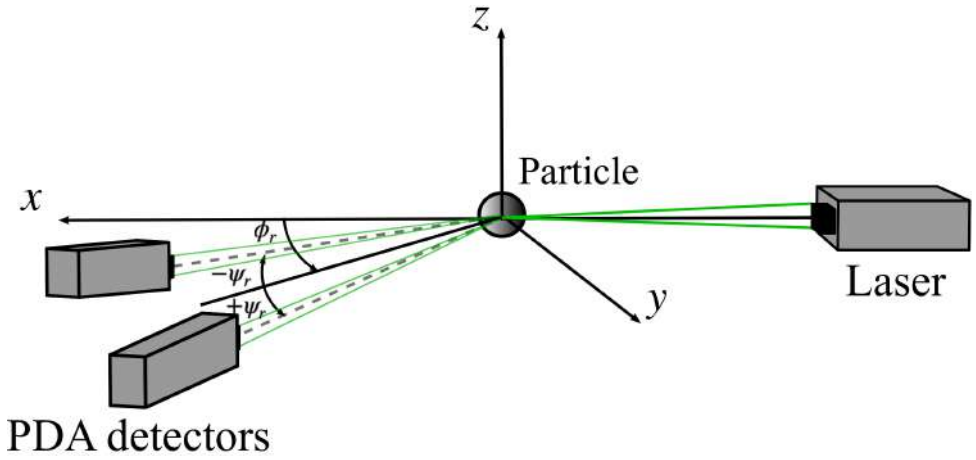

Figure 2.15. – Phase Doppler Anemometer (PDA) principle

also carried by a prior gas seeding the air stream with fine droplets ($< 5\ \mu m$) of Edwards Ultra Grade 15 Vacuum Pump Oil featuring a refractive index $n_r = 1.476$. Velocity and diameter measurements for the liquid phase are performed directly on the n-heptane droplets featuring a refractive index $n_r = 1.389$ at ambient temperature. As illustrated in Figure 2.16, measurements are performed in the transverse (r,z) plane of the combustion chamber at different heights z. The height z is controlled with a manual endless screw motion system with a precision of ± 0.2 mm while the displacement in the radial direction r is provided by an automated axis motion with a precision of ± 0.01 mm. Quartz walls of the square chamber receiving the dual laser beam are not orthogonal to its plan but are $21^o \pm 1^o$ out of it in order to ease collection of the scattered signal with the receiver probe.

2.3.3.2. Planar laser Mie scattering imaging

Laser tomography is also performed on the fuel particles as shown in Figure 2.17. Coupled with a laser sheet generator, a laser Coherent Verdi G18 produces a planar laser sheet at the wavelength $\lambda_i = 532 \pm 2$ nm at the nominal power of 10 W, which is normal to the quartz wall of the combustion chamber and illuminates the fuel droplets in a axial plane of the fuel injection. The light scattered by the particles is recorded by a PCO edge sCMOS camera equipped with a NIKON 105 mm f/4 camera lens, its line of sight being normal to the illuminated plane. The scattered signal being proportional to the square particle diameter, the image signal is biased in favor of the largest particles [169]. The spray base being dense and the particles having high velocity, the exposure time is reduced to 100 μm to avoid blurry images and damages to the camera.

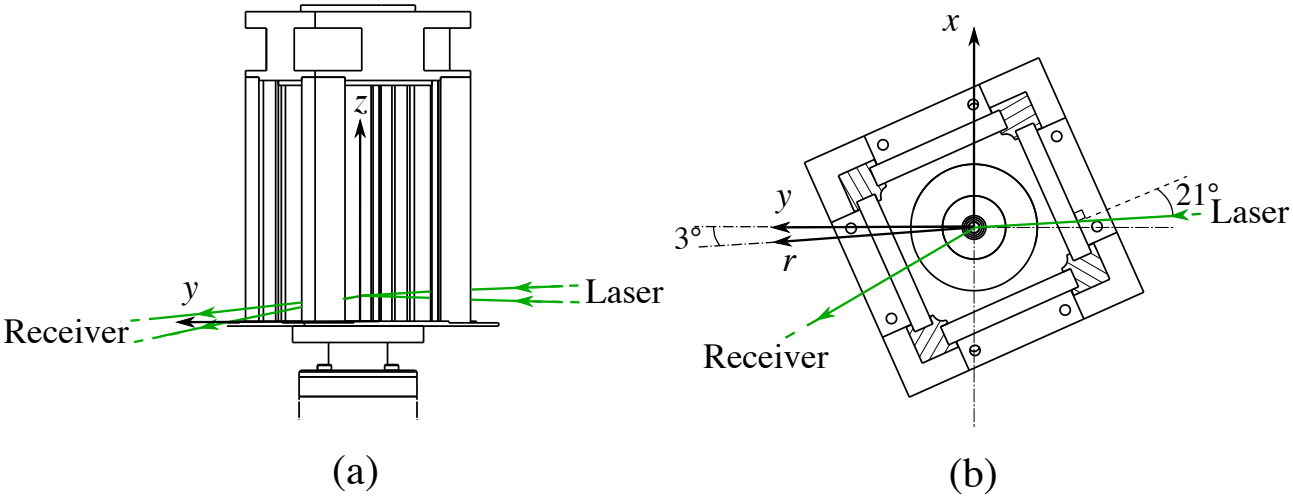

Figure 2.16. – (a) Side and (b) top views of the combustion chamber on which PDPA is performed. Axes and angles used throughout the study are indicated directly on the figure

Planar Mie scattering imaging is also realized on the spray for the steady and pulsed regimes as described in Section 2.3.3.2 to infer the spray structure. These images give insightful information about the spray structure. The light intensity I scattered by a group of particles in the volume observed by a pixel of the camera can be roughly considered as proportional to the sum of the square particle diameter d_p^2 [169]. Hence, the volume of observation being the same for each pixel, I is roughly proportional to the product $n_p d_{20}^2$ where n_p is the particle number density and d_{20}^2 the mean square diameter in the observed volume.

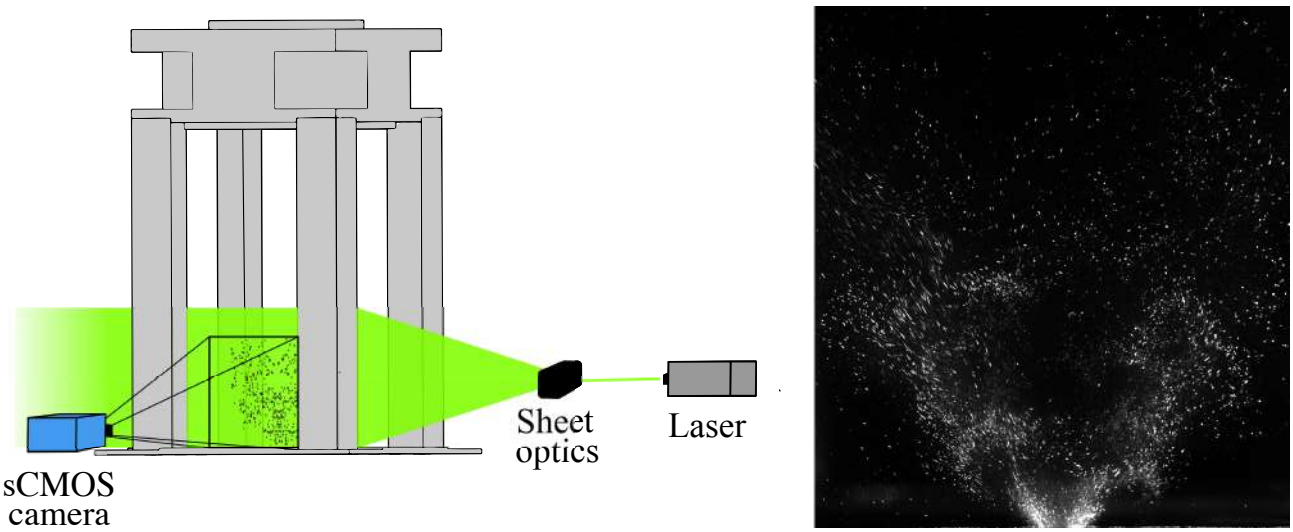

Figure 2.17. – (Left) Sketch of the experimental setup for planar laser Mie scattering imaging. (Right) Instantaneous image recorded of the fuel spray.

2.4. Numerical setup for Large Eddy Simulations of the TALISMAN burner

The interactions between the acoustic field and a hollow-cone spray is investigated in Chapter 6. Numerical flow simulations are performed with the Large Eddy Simulations (LES) framework in cold

reacting conditions for the configuration $\mathscr{C}_{20}$ [170]. The numerical methodology and the computational domain are presented in Section 2.4.1. The modeling of hollow cone spray injection in the computational domain is detailed in Section 2.4.2.

2.4.1. Numerical methodology

Numerical flow simulations are performed with the AVBP multi-phase compressible flow solver from CERFACS (www.cerfacs.fr/avbp7x/) [171–173]. The reader is referred to the Paulhiac's [174] thesis for a full description of the Euler-Lagrangian (EL) flow model used in this work. Only the main elements are briefly described. The compressible Navier Stokes equations are solved using a second-order accurate in time and space, Lax and Wendroff scheme [175] with an acoustic CFL = 0.7. Turbulent terms used in the LES model for the sub-grid stress tensors are computed with the Sigma model [176, 177]. The liquid fuel phase is modelled with the Lagrangian approach. Fuel droplets are modeled as rigid isolated evaporating spherical droplets: droplet deformation or break-up, internal circulation and interactions between droplets are not considered. Mass, momentum and energy coupling terms between the gaseous and the liquid phases are considered only through steady drag force and droplet evaporation. The steady drag force is modelled with the Schiller-Neumann correlation [178]. The Abramzon-Sirignano correlation is applied for the droplet vaporization model using a Schmidt Number $Sc = 1.3431$ and a Prandtl Number $Pr = 1.3431$ [179]. The two-way coupling terms are interpolated from the number of droplets inside a nodal control volume by considering their distance from the nodes [174].

Multiple cuts of the computational domain are shown in Figure 2.18. The numerical domain reproduces the experimental setup from the upstream plenum convergent to the downstream combustion chamber. Two meshes, named "COARSE" and "FINE", are used for the steady and pulsed regimes with respectively 28 M and 69 M tetrahedral cells. An hemisphere with a 150 mm radius representing the atmosphere is added at the top of the numerical domain to avoid managing wave reflection issues at the outlet. The mesh is identical for the steady and pulsed regimes with a total of 28 M tetrahedral cells. In Figure 2.18, mesh cell characteristic lengths are given using the local time step and CFL number. For the COARSE mesh, Δx is about 2.0-5.0 mm at the TALISMAN injector inlet, 0.10-0.20 mm in the radial cavities of the air swirler and goes from 1.0 to 0.5 mm along the convergent downstream the swirler. In order to properly capture the structure of the swirling flow field injected in the combustion chamber, mesh is refined up to 50 μm in the inner recirculation zones and along the fuel injection cone. Δx is then progressively decreased radially and axially to 0.8 mm and 0.5 mm respectively. For the FINE mesh, the mesh is refined to 0.10 mm from the feed-channel swirler to the inlet of the combustion chamber and in the jet shear layers of the swirling flows to better capture the vortical structures.

Static pressure is relaxed towards the atmospheric pressure $p_{out} = 101325$ Pa on the spherical surface of the atmosphere. A small co-flow inlet velocity of 0.5 m.s^{-1} is applied on the planar side of the exit plenum to avoid localized inlet speeds on the outlet patch. Inlet and outlet boundaries conditions are imposed following the NSCBC (Navier-Stokes characteristic boundary condition) formalism [180]. The wall boundary conditions of the computational domain are considered as no slip with a heat resistance of 1.0×10^{-4} K.m^2.W^{-1} and at the ambient temperature $T_a = 293.15$ K. Conditions in which the air is injected in the computational domain are given in Section 6.3.

2.4.2. Hollow cone spray modelling

The fuel is injected following the FIM-UR strategy, which reproduces the hollow cone spray injection realized by a pressure-swirler atomizer without requiring a numerical model for the primary atomiza-

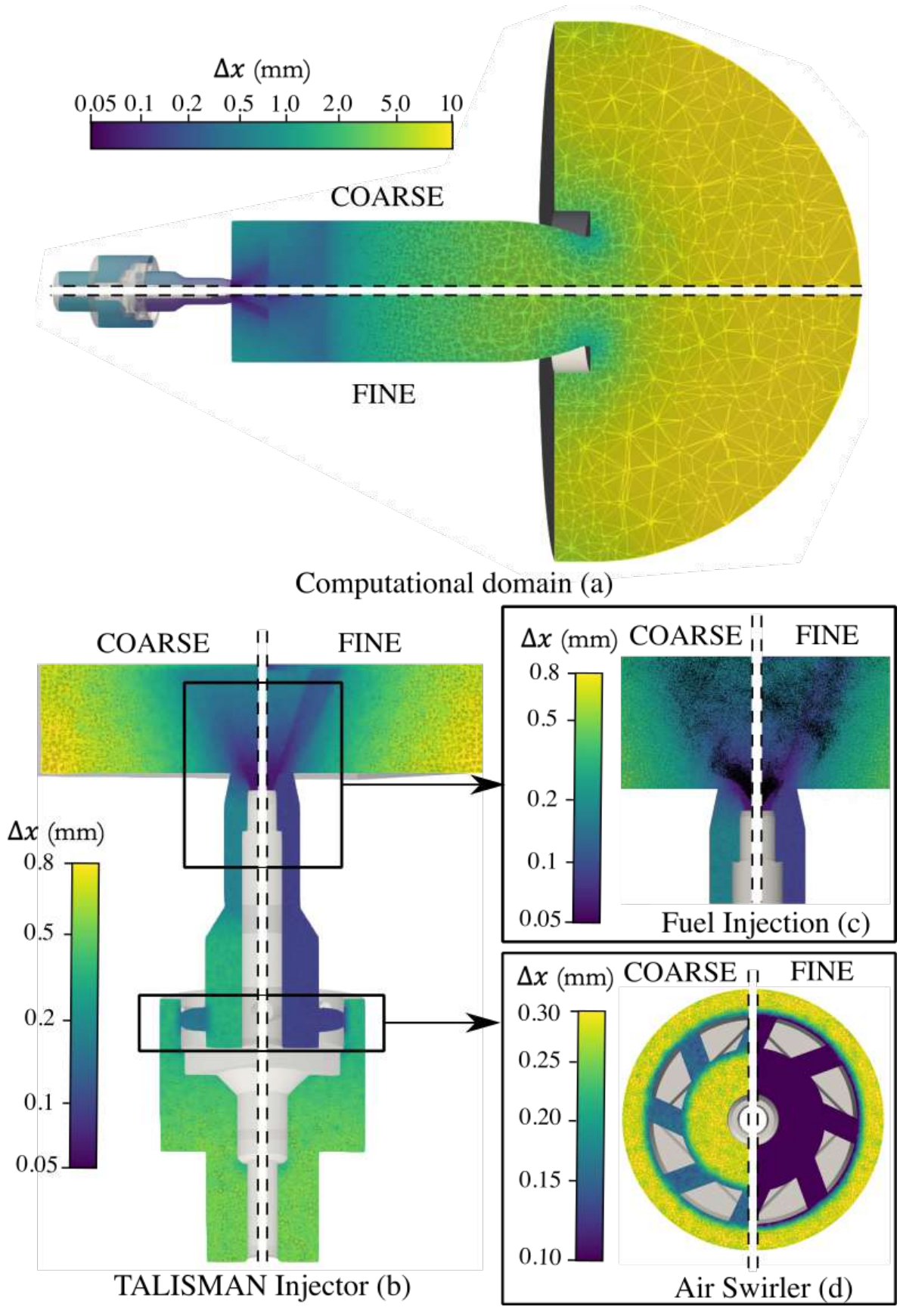

Figure 2.18. – Characteristic sizes Δx of the tetrahedral mesh elements used for the numerical simulations of the TALISMAN burner for the COARSE and FINE meshes.

tion [31]. Its principle is illustrated in Figure 2.19. FIM-UR uses correlations from the spray angle and replaces all the near injector physics by a model injecting the spray a few millimetres downstream of the real injector (Position x_0 in Figure 2.19). From the injector diameter hole R_0 and the mean half angle of the spray cone θ_s, FIM-UR injects the particles at the desired mass flow rate $\dot{m}_f$ over a ring with an outer radius R_0 and an inner radius R_a. In FIM-UR, R_a corresponds to the radius of the inner air core created by the swirler of the atomizer. The radius R_a is determined with the empirical formula of Rizk and Lefebvre [181]:

$$X = \frac{A_{air}}{A_{exit}} = \frac{R_a}{R_0} = \frac{\sin^2\theta_S}{1+\cos^2\theta_S} \tag{2.2}$$

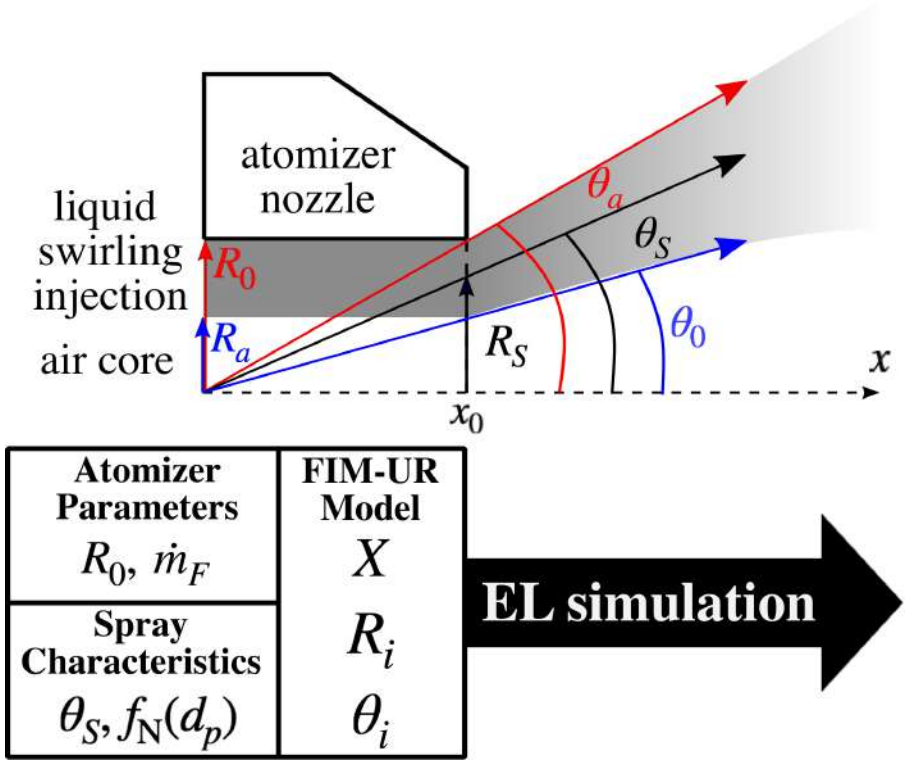

Figure 2.19. – Definition of parameters and schematic of the FIM-UR methodology [31]

As illustrated in Figure 2.19, θ_s corresponds to the half angle of the midpoint radius $R_S = (R_0 + R_a)/2$. The injection radius r_i and angle θ_i of each particle are uniformly distributed over the respective intervals $[R_a, R_0]$ and $[\theta_a, \theta_0]$ where:

$$\tan(\theta_a) = 2\frac{R_a}{R_0 + R_a}\tan(\theta_s) \tag{2.3}$$

$$\tan(\theta_0) = 2\frac{R_0}{R_0 + R_a}\tan(\theta_s) \tag{2.4}$$

The injection radius r_i of each particle is uniformly distributed. In the implementation of the original FIM-UR model in AVBP, each fuel particle with a density ρ_F is injected with an axial velocity equal to the bulk velocity of the liquid phase flowing through the atomizer hole:

$$u_{p,x} = \frac{\dot{m}_F}{\pi\rho_F(R_0^2 - R_a^2)} \tag{2.5}$$

The radial velocity is set to zero to take into account the wall constraint of the orifice at the injection outlet. Finally, swirl of of the atomizer creating an injection angle is reproduced by setting the tangential velocity as:

$$u_{p,\theta} = \tan\theta_i u_{p,x} \tag{2.6}$$

The initialization of the FIM-UR parameters for the fuel injection is detailed in Section 6.3.

Part I.

Interactions between acoustic field and spray

Chapter 3

Modelling an isothermal spray in a laminar flow field

Il y faut seulement une pensée injuste, c'est-à-dire logique. Cela n'est pas facile. Il est toujours aisé d'être logique. Il est presque impossible d'être logique jusqu'au bout. [...] Karl Jaspers [...] évoque après bien d'autres ces lieux déserts et sans eau où la pensée arrive à ses confins. [...] Le véritable effort est de s'y tenir, autant que cela est possible et d'examiner de près la végétation baroque de ces contrées éloignées. La ténacité et la clairvoyance sont des spectateurs privilégiés pour ce jeu inhumain où l'absurde, l'espoir et la mort échangent leurs répliques.

– Albert Camus, *Le mythe de Sisyphe, 1942*

The interaction between an acoustic field and a spray is modelled in a one-dimensional configuration for an isothermal spray in a laminar flow field. The objective is to examine the various models that can be used to determine the response of the particle velocity and number density response of the spray to acoustic disturbances. The response of a single droplet is examined with an Euler-Lagrange formalism. Three configurations are examined with varying degrees of coupling between the droplet and gas velocity field. Next, an Euler-Euler formalism is introduced, and a model is derived to analyze the response of a monodisperse spray. Numerical simulations demonstrate that the intensity of particle clustering is only weakly correlated with the response of a single droplet. Lastly, a model that incorporates homogeneous and isotropic particle velocity dispersion is presented.

Overview

Modelling of interactions between an acoustic field and groups of droplets is important for many engineering applications fields. Several studies have shown that acoustic waves can alter the atomization process of the fuel liquid sheets in airblast atomizers [111]. Additionally, acoustic forcing can impact the droplet evaporation rate. Studies have demonstrated that axial acoustic oscillations can enhance the evaporation rate of fuel droplets. This effect is attributed to the increase in relative velocity between the droplets and the surrounding gas, leading to enhanced heat and mass transfer [93, 182]. Moreover, the transport of the dispersed phase (i.e., fuel droplets) in the gas flow can be significantly affected by external acoustic forcing, leading to the formation of droplet number density waves with convected droplet clusters [101, 102, 110, 183, 184]. This latter phenomenon has been identified as a key mechanism triggering undesirable combustion oscillations in spray flames [101, 104–108, 185]. Particles clusters induced by acoustic perturbations of the gas flow can ease grouping and trapping of aerosols which can be seen as an opportunity for gas filtration purposes in exhaust gas and air filtration devices [186].

One mechanism leading to droplet clustering has been envisaged with a combined numerical and experimental approach in [187, 188]. The authors examine the dynamics of an acoustically forced laminar air jet interacting with a polydispersed evaporating spray. Large vortical structures are created in the shear layer of the gaseous jet at the burner outlet when it is submitted to acoustic forcing. Interactions of these vortical structures with the spray lead to a segregation of the droplets with the apparition of periodic patterns of dense and less dense zones along the burner axis. In these studies, droplet clustering is explained by the inertia of the droplets. They preferentially group together on the external sides of the eddies of the acoustically perturbed flow.

However, theoretical and numerical studies covering different technical fields have also identified droplet clustering phenomena for one dimensional sprays submitted to sound waves [115, 116, 189–195]. These authors have shown that droplet clustering does not need to be supported by interactions with a 2D or 3D unsteady flow structures. It already takes place in a 1D unsteady two phase flow when a monodisperse or a polydisperse spray is submitted to an harmonic acoustic modulation.

Katoshevski et al. [115, 190] attributed the creation of convecting clustering nodes and anti-nodes to the local acceleration or deceleration sustained by the particles. These waves originate from the local change of the particle relative velocity to the gas and depend on the relative position in the acoustic velocity wave. These local accelerations or decelerations are possible due to the relaxation time of the particles which creates a drag force to bring the particle velocity to the gas flow velocity.

Mahapatra et al. [191] studied the grouping and segregation phenomenon for an evaporating polydisperse group of droplets injected in pulsed flow. Numerical simulations have shown that, small droplets being more sensitive to the acoustic perturbation than large droplets, a phase lag appears between the convected clusters that are produced by the pulsating flow field. But evaporation also tends to damp the oscillations of the particle number density for small droplets while it does not seem to have an effect on the oscillations of the particle number density for large droplets.

Li et al. [193] have identified two kinds of particle clustering with two number density waves that are superposing. The first one is a convective particle clustering (CPC) where the corresponding wavelength is equal to the product of the mean gas velocity and the period of the excitation. The clustering develops in a zone near the injection named particle relaxation zone (PRZ) defined as the region where the particle travels during a period equal to its relaxation time after its injection. It is caused by the relaxation process of the initial particle velocity that relaxes to the instantaneous gas velocity, generating dense or sparse particle groups depending on the phase of the acoustic wave at the injection location. Hence, CPC occurs whatever the acoustic response of the particle to the gas excitation. The second one is the acoustic particle clustering (APC) propagating at the sound

speed of the gas and oscillating at the excitation frequency. It is only caused by the modulation of particle velocity by the acoustic wave. This phenomenon takes place over large distances. However, the authors have shown that the oscillations caused by CPC are much larger than those caused by APC.

Achury et al. [192] also identified these two regimes. They have classified the spray response in terms of two mechanisms. The first one is an acoustic agglomeration (AA) to describe the attraction of initially inert droplets to the nodes of the standing acoustic velocity wave. The second mechanism is the generation of propagating number density waves where the excitation of gas velocity is now a propagating acoustic wave with a non-zero mean velocity. The latter phenomenon is explained in the same way as in Li et al. [193]. Numerical simulations show that particle diameter polydispersion in a spray introduces a stretch of the global number density waves [196]. It has been attributed to the sum of the phase lags between the different number density waves for each particle size class present in the spray. Consequently, the distribution of diameter size is modulated along the channel.

From a numerical modelling perspective, unsteady simulations of two-phase flow and flame dynamics can be performed with Eulerian-Eulerian models ([116, 185, 191, 192, 195]) or more recently with Eulerian-Lagrangian ([197–200]) frameworks for the gaseous and disperse phases. Efforts to develop Eulerian-Lagrangian models for Large Eddy Simulations led to impressive progress made over the past ten years in the simulation of thermo-acoustic instabilities for combustors powered by spray flames (see for example [201]). Describing both spatial and temporal evolution of a two-fluid field with a set of conservation equations for each phase, the Eulerian-Eulerian framework remains attractive for the development of low order models to analyze the interactions between an acoustic field and a spray.

In the following sections, a preliminary study is carried out to analyze the response of an isolated particle submitted to an acoustic excitation of the surrounding gas. This analysis is used to determine the cut off frequency of the response of the particle velocity with respect to acoustic forcing. The balance equations constituting the Eulerian-Eulerian two-phase flow model for a isothermal spray in a laminar gas flow are presented. They are first given for a perfectly monodisperse spray. The numerical results given by the corresponding Eulerian-Eulerian model are validated against Euler-Lagrange flow simulations. Finally, the impact of the particle velocity dispersion present in turbulent sprays on the spray response is integrated in the Eulerian-Eulerian two-phase flow model when the dispersion is assumed homogeneous and isotropic.

3.1. Single Droplet model

3.1.1. Model Description

The response of an isolated spherical liquid particle in a homogeneous gaseous flow submitted to acoustic forcing is considered first as illustrated in Figure 3.1. The objective is to examine its harmonic response and identify cases of interest for the Eulerian-Eulerian analysis that will be developed for dense sprays. This problem has already been studied analytically and validated experimentally in [202]. The present analysis aims at deriving a simplified model in order to deduce an analytical expression able to reproduce the results obtained in [202].

The analysis is restricted to 1D flows. In a Lagrangian framework, the motion of a single isolated particle is tracked in the carrier flow. Particle deformation and rotation are neglected in the following. Considering here only sprays in diluted flows ($\rho_g/\rho_l \ll 1$) the drag force of the carrier phase on the

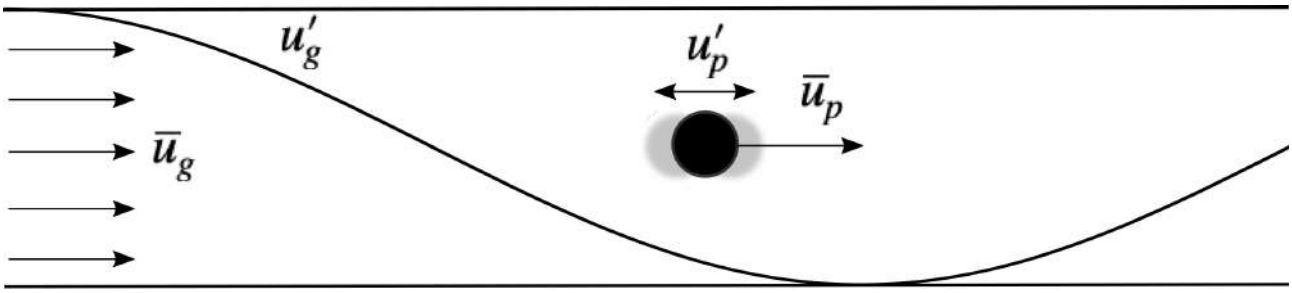

Figure 3.1. – Single droplet model configuration: a particle is injected with a mean velocity $\overline{u}_p$ in an oscillating gas flow with a mean velocity $\overline{u}_g$ and a fluctuating velocity u'_g. The particle is submitted to the acoustic field and has a fluctuating velocity u'_p which has to be determined.

particle, the momentum balance for a non-evaporating and isothermal droplet leads to:

$$\frac{du_p}{dt} = -\frac{u_p - u_g}{\tau_p} \tag{3.1}$$

where u_p and u_g are respectively the particle velocity and gas velocity. The quantity τ_p is the particle relaxation time, which is modeled here with the Schiller's correlation for a non evaporating spherical droplet [178]:

$$\tau_p = \frac{\tau_{p,0}}{\left(1 + 0.15 Re_p^{0.687}\right)} \quad \text{with} \quad \tau_{p,0} = \rho_l d_p^2/(18\mu_g) \tag{3.2}$$

In this expression, $\tau_{p,0}$ Re_p, ρ_l, d_p and μ_g are the nominal particle relaxation time, the particle Reynolds number, the liquid density, the particle diameter and the gas dynamic viscosity, respectively.

Equation (3.1) is an approximation of the momentum balance on the liquid particle, in which acceleration forces were neglected. The general equation of a single droplet in a unsteady and non uniform flow was derived by Max and Riley [203]. The general equation includes many terms that can be simplified depending on the problem considered. In an oscillatory flow, Hjelmfelt and Mockros [204] showed that the drag force appearing in Equation (3.1) largely dominates when $N_s = \sqrt{\nu/(\omega d_p^2)} > 6$ and the gas to liquid density ratio $\rho_g/\rho_l \approx 10^{-3}$ like in fuel-air two-phase flow investigated in this work. The quantities appearing in N_s are ν the gas kinematic viscosity and ω the angular frequency of the excitation. For $2 < N_s < 6$, the results obtained with Equation (3.1) and the general equation begin to differ, requiring to add the Basset force in order to retrieve a better agreement. However, differences between remain small, especially for the amplitude of u'_p, until $N_s < 4$. In general, Tchen force and added mass force can be ignored when the density ratio $\rho_g/\rho_l \ll 1$ [205, 206]. When ρ_g/ρ_l decreases, the acceleration forces can be neglected over a larger frequency range and particle diameter range. Hence, in liquid fuel sprays submitted to acoustic perturbations, Equation (3.1) for the particle diameters d_p = 10, 25, 50 and 100 μm are valid (i.e $N_s < 4$) for excitation frequencies respectively lower than f = 10000, 1500, 400 and 100 Hz.

At low forcing frequencies, the droplet is compact with respect to the acoustic wavelength and one may consider a harmonic fluctuation of the gas velocity $\tilde{u}_g = |\tilde{u}_g| \exp(-\mathrm{i}\omega t)$, where $|\tilde{u}_g|$ is the modulation amplitude. Assuming a constant relaxation time τ_p by fixing the particle Reynolds number

Re_p, the response of the particle velocity $\tilde{u}_p = |\tilde{u}_p| e^{-\mathrm{i}\omega t+\varphi}$ is governed by a first order low-pass filter:

$$\frac{|\tilde{u}_p|}{|\tilde{u}_g|} = \left(1 + (\omega/\omega_c)^2\right)^{-1/2} \tag{3.3}$$

$$\varphi = \arctan(\omega/\omega_c) \tag{3.4}$$

where φ is the phase lag between the flow and particle velocities. The angular cut-off frequency of the harmonic response $\omega_c = 1/\tau_p$ corresponds to the inverse of the mean particle relaxation time.

The harmonic response of the particle velocity in Equations (3.3) and (3.4) only depends on a Stokes number $St = \omega/\omega_c = 2\pi\tau_p/T$ that compares the relaxation time with respect to the pulsation period T of the gaseous flow disturbances. The time lag τ_p depends on the particle Reynolds number $Re_p = \rho_l |u_p - u_g| d_p/\mu_g$ where $|u_p - u_g|$ is the relative velocity of the particle with respect to the gaseous flow velocity.

As a consequence, the dynamics of a spray injected in a uniform gaseous flow submitted to acoustic forcing will be affected by its transient response due to the unbalance between the particle and gaseous flow velocities and by acoustic forcing. In order to unveil solely the effects of acoustics on the spray response, one considers in the following only cases with sprays injected at the same mean velocity as the gaseous stream without relative mean velocity difference $|\overline{u}_p - \overline{u}_g| = 0$, i.e. for a mean particle Reynolds number $\overline{Re}_p = 0$, where $\bar{\cdot}$ denotes here a time averaged quantity. In these conditions, the transient response of the particle velocity u_p is removed.

3.1.2. Numerical results

In the previous section, Equation (3.1) was integrated by assuming a constant particle Reynolds number Re_p. But the particle Reynolds number also slightly varies with time during acoustic forcing and consequently the relaxation time τ_p varies as well.

If τ_p is not constant, there is no simple analytical solution for Equation (3.1), which is here solved with an explicit 4-5th order Runge-Kutta algorithm [207]. In the following calculations, air is taken at ambient pressure $p = 1$ bar and ambient temperature $T_g = 293$ K. N-heptane particles are considered with density $\rho_l = 688$ kg/m^3. The free air stream air velocity is excited according to $u_g(t) = \overline{u}_g + U_g \sin(2\pi f t)$. The initial particle velocity is set to $u_p(0) = \overline{u}_g$. These conditions satisfy $\overline{Re}_p = 0$. Numerical simulations are determined for frequencies covering 1 to 1000 Hz and a set of particle diameters $d_p = 10$, 25, 50 and 100 μm.

The magnitude $|\tilde{u}_p|/|\tilde{u}_g|$ is determined by computing the square root of the ratio between the Power Spectral Density (PSD) of the particle velocity time series divided by the PSD of the gas velocity examined at excitation frequency f. The phase shift φ is deduced by taking the argument of the Cross Power Spectrum Density (CPSD) of the two signals at the excitation frequency f. The PSD and CPSD are calculated by windowing the signals with the Welch periodogram method [208].

The Bode plots are presented in Figure 3.2. They are drawn here for $\overline{u}_g = 40$ m/s and $U_g = 0.4$ m/s. Nonetheless, when $u_p(0) = \overline{u}_g$, these diagrams are independent of the mean component $\overline{u}_g$ and of the amplitude U_g in agreement with Equations (3.3) and (3.4). The analytical model relies on a constant particle relaxation time τ_p, which is equal here to the one in a Stokes flow $\tau_{p,0} = \rho_l d_p^2/(18\mu_g)$ where $u_p \approx u_g$. It matches well with the numerical results at low forcing frequencies and corroborates the results observed in [202]. Differences increase when the particle diameter and frequency increase. The cut-off frequency f_c of the response is defined here as the frequency above which the magnitude has dropped by 30%. Note that the numerical solution always has a larger frequency bandwidth than the

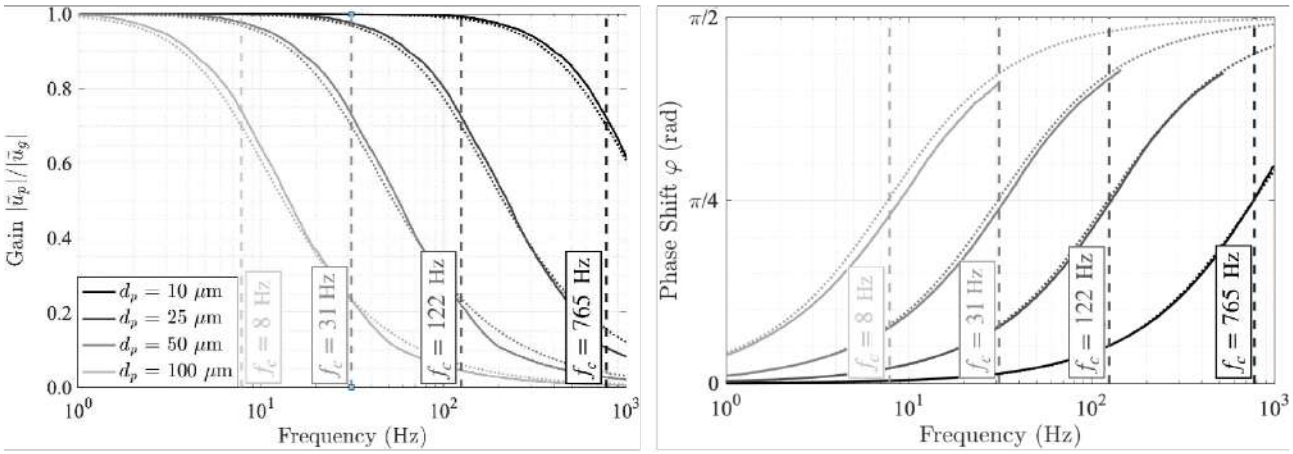

Figure 3.2. – Bode magnitude $|\tilde{u}_p|/|\tilde{u}_g|$ (left) and phase shift (right) plots of the frequency response of the fluctuating particle velocity $\tilde{u}_p$ with respect to the fluctuating gas velocity $\tilde{u}_g$ for particle diameters $d_p = 10$, 25, 50 and 100 μm. Dotted lines represent the harmonic response deduced with Equations (3.3) and (3.4). The full lines represent the solution of Equations 3.1 and 3.2. The cut-off frequencies $f_c = \omega_c/(2\pi)$ are indicated by the dashed lines.

one deduced from the simplified analytical model, meaning that the cut-off frequency f_c can safely be deduced from Equation (3.2).

In the following, simulations are carried out for sprays with a forcing frequency $f = 250$ Hz and particle diameters $d_p = 10$, 25 and 50 μm to analyze the cases where the particle are respectively very, moderately and little responsive to the acoustic field as shown in Figure 3.2. One could intuitively assume that if the velocity of a single fuel particle is only weakly altered by the acoustic perturbation with a significant phase lag, then the spray will not be strongly altered by the acoustic field. One will however show in the following that under these excitation conditions the structure of a dense fuel spray could still be deeply affected.

3.2. Euler-Euler spray model

3.2.1. Mesoscopic Eulerian equations

The response of dense fuel sprays to acoustic perturbations imposed to the gaseous flow is now considered with an Eulerian framework to model both the gaseous and liquid phase dynamics. A spray is defined here as a group of droplets conveyed by the air flow. When studying particle laden-flows, two different Eulerian-Eulerian descriptions are possible. The first approach is based on the quantities computed for each phase through volume, time or ensemble averages weighted by a phase indicator function. These quantities follow Navier-Stokes type equations written for each phase. They are coupled by transfer terms at gaseous and liquid interfaces [209, 210]. The main drawback of this formalism is that the system of equations are generally not hyperbolic which lead to difficulties to solve them numerically [211]. It often requires to determine closure laws for interfacial terms closure purposes, in particular the interfacial pressure, in order to make the system hyperbolic [212, 213]. The choice of a specific closure law among the numerous ones available is often justified by numerical considerations rather than physical based considerations [214].

In dilute two-phase flows, when the total volume of the particles represents less than 1% of the fluid

in the control volume that is considered, the two-phase flow can also be described using the mesoscopic Eulerian formalism (MEF) introduced by Simonin [215] and adopted later to monodisperse sprays by Février et al. [216–218]. Coupling the Multifluid Approach [219] with the MEF, Vié et al. [220, 221] extended the MEF to sprays with polydisperse droplet size. The MEF relies on a statistical description using a particle probability density function (PDF) f_p for the dispersed phase. The PDF f_p is defined such as $f_p\left(\mathbf{c}_p, \xi_p, \mu_p; \mathbf{x}, t\right) \delta\mathbf{c}_p \delta\xi_p \delta\mu_p \delta\mathbf{x}$ corresponds to the probability of the number of particles, whose centre of mass at time t is located in the volume $[\mathbf{x}, \mathbf{x}+\delta\mathbf{x}]$ with a translation velocity $\mathbf{u}_p \in [\mathbf{c}_p, \mathbf{c}_p+\delta\mathbf{c}_p]$, a temperature $T_p \in [\xi_p, \xi_p+\delta\xi_p]$ and a mass $m_p \in [\mu_p, \mu_p+\delta\mu_p]$. The PDF f_p is obtained by performing an ensemble averaging of the position and characteristics in time of any given particle over a very large number of two-phase flow realizations conditioned by one carrier-phase realization. Since, in dilute flows, the influence of the particles on the carrier phase is negligible and their spatial properties are only governed by direct interactions with the carrier phase, the present formalism assumes that f_p is only conditioned to the local and instantaneous carrier phase properties. Hence, it is possible to derive local and instantaneous dispersed phase properties from f_p and to have an Eulerian description for both phase.

The evolution of f_p obeys the Boltzmann transport equation. In order to switch from a microscopic to a macroscopic description of the dispersed phase flow, the general Enskog equation is written from the PDF equation:

$$\frac{\partial}{\partial t}\left(\alpha_l \rho_l \breve{\psi}\right) + \frac{\partial}{\partial x_i}\left(\alpha_l \rho_l \langle u_{p,i}\psi\rangle_l\right) = \mathcal{C}\left(\mathrm{m}_p\psi\right) + \alpha_l\rho_l\langle\frac{\mathrm{d}u_{p,\mathrm{i}}}{\mathrm{d}t}\frac{\partial\psi}{\partial u_{p,i}}\rangle_l + \alpha_l\rho_l\langle\frac{\mathrm{d}T_p}{\mathrm{d}t}\frac{\partial\psi}{\partial T_p}\rangle_l + \alpha_l\rho_l\langle\frac{\mathrm{d}m_p}{\mathrm{d}t}\left[\frac{\partial\psi}{\partial m_p} + \frac{\psi}{m_p}\right]\rangle_l \tag{3.5}$$

where $\mathcal{C}\left(\mathrm{m}_p\psi\right)$ is the mean collisional rate of change of the particle property and $\breve{\psi} = \langle\psi\rangle_l$ is the dispersed phase mass weighted averaged of the any function $\psi\left(\mathbf{c}_\mathrm{p}, \xi_\mathrm{p}, \mu_\mathrm{p}\right)$ defined as:

$$\breve{\psi} = \langle\psi\rangle_l = \frac{1}{\alpha_l\rho_l}\int \mu_\mathrm{p}\psi\left(\mathbf{c}_\mathrm{p}, \zeta_\mathrm{p}, \mu_\mathrm{p}\right) \mathrm{f}_p\left(\mathbf{c}_\mathrm{p}, \xi_\mathrm{p}, \mu_\mathrm{p}; \mathbf{x}, \mathrm{t}\right) \mathrm{d}\mathbf{c}_\mathrm{p}\mathrm{d}\xi_\mathrm{p}\mathrm{d}\mu_\mathrm{p} \tag{3.6}$$

where $\alpha_l = n_p\breve{m}_p/\rho_l$, m_p and n_p are the liquid volume fraction, the particle mass and the particle number density, respectively. Like the Favre decomposition used for compressible turbulent flows, any dispersed quantity y_p can be written as $y_p = \breve{y}_p + y_p''$. The local statistical dispersion y_p'' is the fluctuation of the quantity y_p at a the location $\mathbf{x}$ and the time t from one dispersed phase realization to another for a unique gas flow realization.

In this chapter, a dispersed liquid phase composed of an unique species, the liquid fuel, evolving in a laminar air flow is considered. The liquid phase is assumed to be diluted with a liquid volume fraction $\alpha_l = n_p\breve{m}_p/\rho_l < 10^{-4}$. Furthermore, it is assumed that droplets are perfectly spherical. Collisions between particles are also neglected. Only the steady drag force is considered in the momentum balance of the liquid particle. The effect of gas pressure gradient on the particles is supposed to remain small compared to the drag force, meaning that the momentum balance for each fluid particle is modeled with Equation (3.1). Fuel droplets are considered isothermal, evaporation and heat transfer being discarded. Finally, transport by all diffusion processes is neglected. Hence, the governing equations of an isothermal spray evolving in laminar air flow are given by:

– Population balance equation when $\psi = 1/m_p$:

$$\frac{\partial n_p}{\partial t} + \frac{\partial n_p\breve{u}_{p,i}}{\partial x_i} = -\frac{\partial}{\partial x_i}\left(\alpha_l\rho_l\langle\frac{u_{p,i}''}{m_p}\rangle_l\right) \tag{3.7}$$

– Liquid fraction balance equation when $\psi = 1$:

$$\frac{\partial}{\partial t}\left(\alpha_l \rho_l\right) + \frac{\partial}{\partial x_i}\left(\alpha_l \rho_l \breve{u}_{p,i}\right) = 0 \tag{3.8}$$

– Particle Momentum balance equation when $\psi = u_{p,i}$:

$$\frac{\partial}{\partial t}\left(\alpha_l \rho_l \breve{u}_{p,i}\right) + \frac{\partial}{\partial x_j}\left(\alpha_l \rho_l \breve{u}_{p,i} \breve{u}_{p,j}\right) = -\frac{\partial}{\partial x_j}\left(\alpha_l \rho_l \langle u''_{p,i} u''_{p,j} \rangle_l\right) - \alpha_l \rho_l \frac{\breve{u}_{p,i} - u_{g,i}}{\breve{\tau}_p} \tag{3.9}$$

– Particle energy balance equation when $\psi = h_p = c_{p,l} T_p$:

$$\frac{\partial}{\partial t}\left(c_{p,l} \alpha_l \rho_l \breve{h}_p\right) + \frac{\partial}{\partial x_i}\left(\alpha_l \rho_l \breve{u}_{p,i} \breve{h}_p\right) = -\frac{\partial}{\partial x_i}\left(\alpha_l \rho_l \langle u''_{p,i} h''_p \rangle_l\right) \tag{3.10}$$

The mean particle relaxation time $\breve{\tau}_p$ appearing in Equation 3.9 is modeled with Eq. (3.2) which is adapted to take into account the net effect of the instantaneous relative particle velocity at the mesoscopic scale [215].

When using the adjective "monodisperse" to qualify a spray, it commonly refers to the size distribution of the fuel droplets in the spray. However, n the equations (3.7), (3.9), and (3.10), there are terms on the right-hand side that involve the particle velocity and temperature distributions. Hence, the particle velocity and temperature distributions need to be described in order to express the first terms on the right-hand side of Equations (3.7), (3.9) and (3.10). They are respectively representing the change in the particle number density due to turbulent mixing of fuel particles featuring different diameters (or densities in multispecies flows), the transport of momentum by the velocity fluctuations and the transport of enthalpy by the velocity fluctuations. If one wishes to take dispersion into account for a particle property, supplementary equations describing the transport of this dispersion need to be written.

3.2.2. Perfectly monodisperse spray model

One considers here the spray to be perfectly monodisperse. All droplets are supposed to have the same size, the same velocity and the same temperature and made of the same species. Then, in this case, for every quantity x_p of the particles, one has $\breve{x}_p = x_p$ and $x_p'' = 0$.

The non-conservative transport equations for gas phase and dispersed phase quantities in a laminar compressible gas flow are:

$$\frac{D_g \rho_g}{Dt} = -\rho_g \frac{\partial u_{g,i}}{\partial x_i} \tag{3.11}$$

$$\frac{D_g Y_{F,g}}{Dt} = 0 \tag{3.12}$$

$$\frac{D_g u_{g,i}}{Dt} = -\frac{1}{\rho_g}\frac{\partial p}{\partial x_i} + \frac{\alpha_l \rho_l}{\rho_g}\frac{u_{p,i} - u_{g,i}}{\tau_p} \tag{3.13}$$

$$\frac{D_g p}{Dt} = -\gamma_g p \frac{\partial u_{g,i}}{\partial x_i} \tag{3.14}$$

$$\frac{D_p \alpha_l}{Dt} = -\alpha_l \frac{\partial u_{p,i}}{\partial x_i} \tag{3.15}$$

$$\frac{D_p u_{p,i}}{Dt} = -\frac{u_{p,i} - u_{g,i}}{\tau_p}\frac{D_p T_p}{Dt} = 0 \tag{3.16}$$

$$\frac{D_p n_p}{Dt} = -n_p \frac{\partial u_{p,i}}{\partial x_i} \tag{3.17}$$

where $\frac{D_g \cdot}{Dt} = \frac{\partial \cdot}{\partial t} + u_{g,i}\frac{\partial \cdot}{\partial x_i}$ and $\frac{D_P \cdot}{Dt} = \frac{\partial \cdot}{\partial t} + u_{p,i}\frac{\partial \cdot}{\partial x_i}$ are respectively the gas and the particle Lagrangian derivatives. Properties referring to the gaseous flow are ρ_g, $Y_{F,g}$, $u_{g,i}$, p and γ_g denoting the gas density, fuel mass fraction, the velocity component along the i-axis, pressure and the heat capacity ratio of the gas, respectively. Quantities describing the disperse phase are α_l, $u_{p,i}$, T_p and n_p corresponding to the liquid volume fraction, the particle velocity along direction i, the particle temperature and particle number density, respectively.

3.2.2.1. Numerical model

In order to validate the Euler-Euler monodisperse spray modelled by the Equations 3.11-3.17, numerical simulations with the Eulerian-Eulerian model and an Eulerian-Lagrangian reference model are compared on the same computational domain. This computational domain shown in Figure 3.3 corresponds to a $L = 0.4$ m long 1D channel. The inlet and outlet boundaries are treated with the Navier-Stokes Characteristic Boundary Condition algorithm from [180] for both Euler-Euler and Euler-Lagrange numerical models.

At the inlet, the air velocity is modulated by imposing $u_g(t) = \overline{u}_g + U_g \sin(2\pi f t)$, where $\overline{u}_g = 10$ m/s, $U_g = 1$ m/s and $f = 250$ Hz. Air is at ambient pressure $p = 1$ bar and ambient temperature $T_g = 293$ K. Non-evaporating fuel droplets are injected at a mass flow rate $\dot{m}_F = 0.1$ g/s, with a temperature $T_p = T_g$, an initial mean velocity $\breve{u}_p(0) = \overline{u}_g$ equal to the mean air flow velocity with a mono-disperse spray with particle diameter $d_p = 50$ μm at a point located at the middle of the inlet of the computational domain. The particle Reynolds number is in this case equal to $\overline{Re}_p = 0$.

Eulerian-Lagrangian simulations are performed with the AVBP multi-phase compressible flow solver from CERFACS (www.cerfacs.fr/avbp7x/). AVBP requires at least 2D meshes. To conduct the 1D simulations, the computational domain shown in Figure 3.3 corresponds to a 10 mm large two

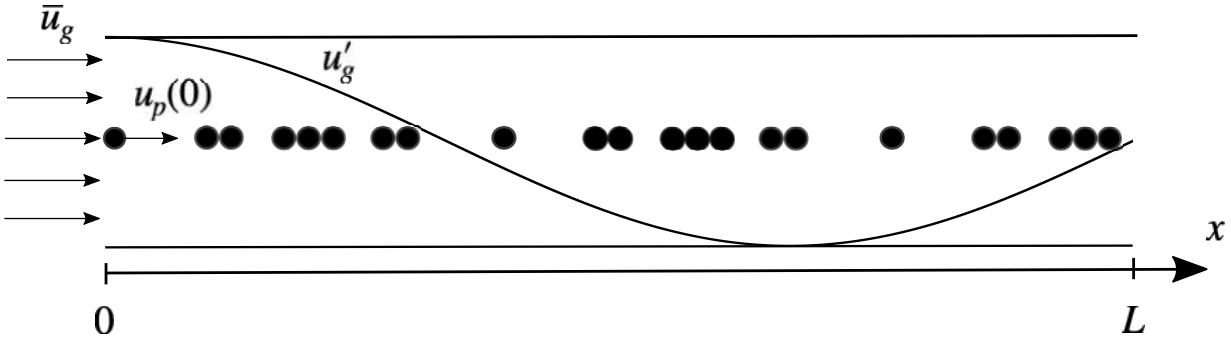

Figure 3.3. – Euler-Euler model configuration: groups of particles are injected in the domain at $x = 0$ with an initial velocity $u_p(0)$ in an oscillating gas flow with a mean velocity $\overline{u}_g$ and a fluctuating velocity u'_g. The acoustic field makes the particles to fluctuate at velocity u'_p but the whole population is also segregated into dense and sparse groups of particles in the flow field, creating particle number fluctuations n'_p around their mean number density $\overline{n}_p$.

dimensional channel and is discretized by 400 identical rectangular elements of length $\Delta x = 1$ mm and width $\Delta y = 10$ mm equal to the computational domain width. Periodic boundary conditions are used for the top and bottom boundaries of the domain. The second-order accurate Lax and Wendroff scheme is adopted for the numerical resolution [175].

Liquid fuel phase is modelled with a Lagrangian approach, where interactions between droplets are neglected. The interactions between the gaseous and the liquid phases are considered through mass, momentum and energy coupling terms due to droplet evaporation and steady drag force. The steady drag force is modelled with the correlation from [178]. The two-way coupling terms are interpolated from the number of droplets inside a nodal control volume by considering their distance from the nodes as in [174].

Eulerian-Eulerian simulations are conducted on the same computational domain shown in Figure 3.3 discretized by 1000 identical elements of length $\Delta x = 0.4$ mm. The system of equations 3.11-3.17 is solved with a finite difference numerical method relying on second-order centered schemes and a fourth-order Runge-Kutta scheme for the temporal resolution.

3.2.2.2. Numerical Results

For the AVBP simulations performed with an Euler-Lagrange model, the dispersed phase quantities are interpolated on the Eulerian grid in a similar manner as the two-way coupling terms are evaluated for the Lagrangian simulation [174]. Numerical results which are presented below are sampled on 16 equally-spaced phases in a forcing cycle and are averaged at least over 10 periods of oscillation.

Figure 3.4 compares the results obtained with Euler-Euler simulations and Euler-Lagrange simulations. Results from both simulations i.e the solid and dashed lines, match very closely in the three graphs. The top plot confirms that the oscillation of the gas velocity imposed at the inlet boundary propagates well in the numerical domain and reaches the correct limits. The envelopes of this signal are shown as dashed lines at 10±1 m/s. The wavelength of this oscillation $\lambda_a = (\overline{u}_g + c_g)/f = 1.41$ m confirms that it is an acoustic wave travelling from left to right in the gas stream.

In the middle plot in Figure 3.4, the oscillation of the gas stream leads to small velocity particle fluctuations characterized by short wiggles close to the droplet injection point which are superimposed

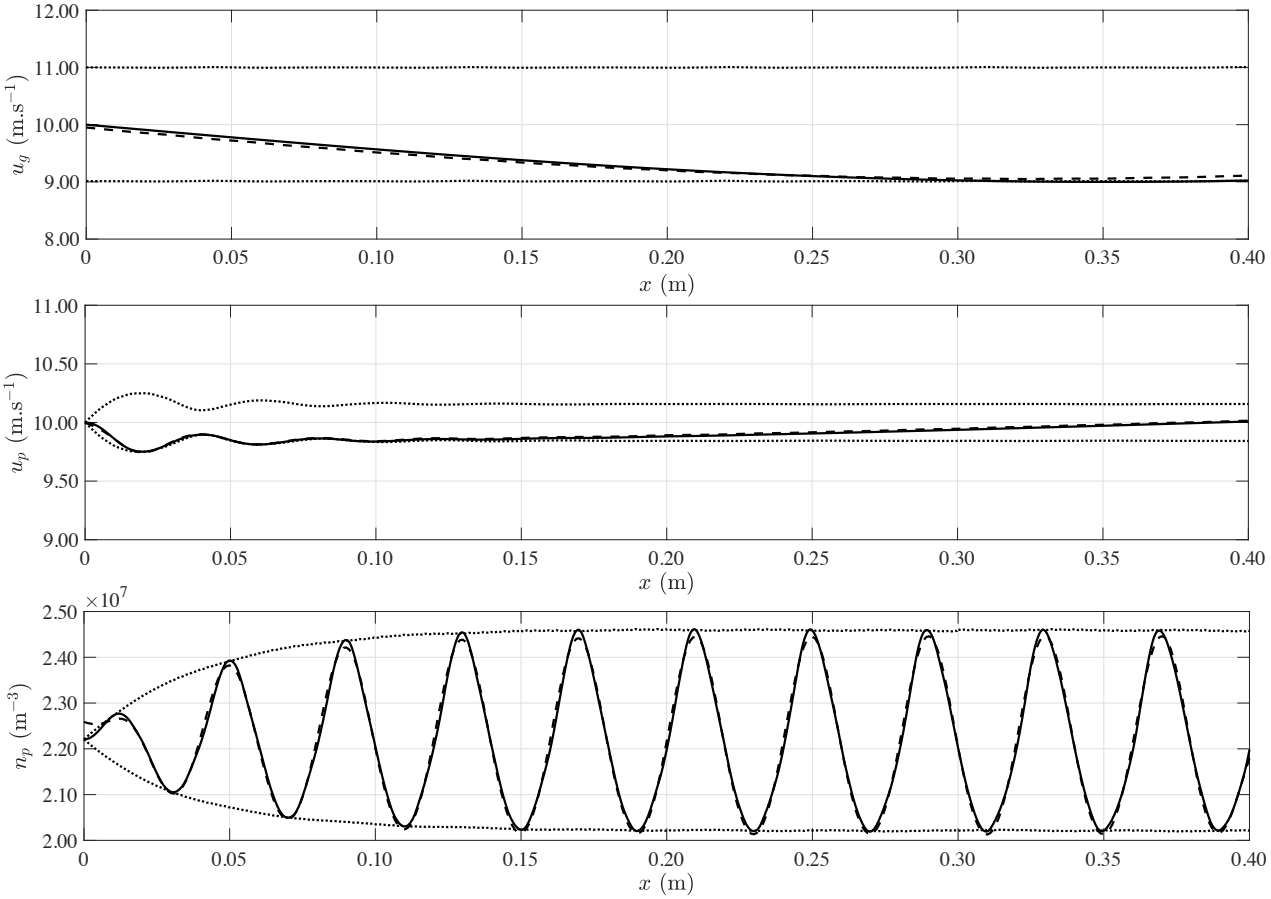

Figure 3.4. – Snapshots at some instant in the forcing cycle of the gas velocity u_g (top), the particle velocity u_p (middle) and particle number density n_p (bottom) for $d_p = 50$ μm, $u_p(0) = 10$ m/s, $\overline{u}_g = 10$ m/s, $U_g = 1$ m/s, $f = 250$ Hz. Envelopes of the oscillations are indicated in black dotted lines. Solid lines correspond to Euler-Euler simulations and dashed lines represent Euler-Lagrange AVBP simulations.

to a more global oscillation taking place in the entire numerical domain. The short wiggles correspond to transient oscillations advected by the mean flow with a wavelength $\lambda_c = \overline{u}_p/f = 0.04$ m, which are damped over a distance of about 110 mm. Further downstream, the particle velocity oscillation only takes place at the acoustic wavelength $\lambda_a = (c_g + \overline{u}_g)/f = 1.41$ m imposed by the gas velocity. The envelope of the signal well delineates the regions of influence of the acoustic and advected disturbances. The oscillation amplitude of the velocity particle u_p reaches $\pm$ 0.15 m/s in the purely acoustic regime away from the inlet. This value corresponds to that expected in Figure 3.2 for a forcing frequency $f = 250$ Hz and fuel droplet with a diameter $d_p = 50$ μm.

The bottom plot in Figure 3.4 shows that these small particle velocity oscillations create in turn droplet number density waves that are growing over a distance around 110 mm before reaching a limit cycle. The oscillating pattern now takes place at the convective wavelength $\lambda_c = \overline{u}_p/f = 0.04$ m over the entire numerical domain. The amplitude of envelope at limit cycle is again quite large $\pm$ 0.21 $\times 10^{-7}$ m^{-3}.

As a conclusion, an acoustic wave propagating in the gas stream with a 10 % relative fluctuation of the gas velocity u_g at a forcing frequency above the cut off frequency f_c leads to reduced oscillations of the liquid particle velocity u_p. The motion of the liquid particles is dominated by an acoustic wave

with a reduced relative fluctuation level of 1.5% that corresponds to that predicted for a single isolated particle. Close to the spray injector, the acoustic oscillation of the liquid particle is also altered by an additional wave which is advected at the mean particle velocity $\overline{u}_p$ and damped further downstream over a distance of about 110 mm. The particle number density only exhibits the advected wave that grows with the distance to the injector to reach a limit cycle 110 mm away from the inlet. Despite the small particle velocity fluctuations, the particle density wave reaches a relative oscillation level of 10%, which roughly corresponds to the oscillation level of the imposed acoustic wave in the gas stream.

This mode transition from acoustic to advected disturbances is well reproduced by the Euler-Euler and Euler-Lagrange simulations and has already been described in [193] for laminar uniform gaseous flows with sprays. Note that in the Euler-Lagrange simulation, transport by diffusion processes are taken into account in the gaseous and liquid phases, meaning that they have no influence on the propagation and amplitude of these waves for the conditions explored.

The mechanisms leading the particles segregation are further investigated in the Chapter 4.

3.2.3. Homogeneous Isotropic Velocity Dispersion (HIVD) spray model

In reality, sprays are rarely monodisperse. This problem is considered here for cases where a particle velocity dispersion is taken into account ($u_p'' \neq 0$) but the particle diameter and temperature distributions are still considered monodisperse ($d_p'' = 0$ and $T_p'' = 0$). Hence, a supplementary equation is required to the system of Equations (3.7)-(3.10) for the particle kinetic stress tensor $\psi = u_{p,i}u_{p,j}$:

$$\frac{\partial}{\partial t}\langle u_{p,i}''u_{p,j}''\rangle_l + \breve{u}_{p,m}\frac{\partial}{\partial x_m}\langle u_{p,i}''u_{p,j}''\rangle_l = -\langle u_{p,i}''u_{p,m}''\rangle_l\frac{\partial \breve{u}_{p,j}}{\partial x_m} - \langle u_{p,j}''u_{p,m}''\rangle_l\frac{\partial \breve{u}_{p,i}}{\partial x_m} \tag{3.18}$$

$$- \frac{1}{\alpha_l\rho_l}\frac{\partial}{\partial x_m}\alpha_l\rho_l\langle u_{p,m}''u_{p,j}''u_{p,j}''\rangle_l + 2\frac{\langle u_{p,i}''u_{p,j}''\rangle_l}{\breve{\tau}_p} \tag{3.19}$$

A new variable $\delta q_p^2 = \frac{1}{2}\langle u_{p,k}''u_{p,k}''\rangle_l$ named RUE for Uncorrelated Kinetic Energy introduced in [222]. It is related to the droplet velocity spatial dispersion of turbulent sprays, which is equivalent to the turbulence kinetic energy but applied here to the liquid phase. As usually done for isotropic turbulence in gaseous flows, a Homogeneous and Isotropic Velocity Dispersion (HIVD) model is retained with $u_{p,i}''u_{p,i\neq j}'' = 0$ and $u_{p,i}''u_{p,i}'' = u_p''^2$. Hence, neglecting the transport of the kinetic stress tensor by velocity fluctuations $\dfrac{\partial}{\partial x_m}\alpha_l\rho_l\langle u_{p,m}''u_{p,j}''u_{p,j}''\rangle_l = 0$ and summing Equation 3.19 over the 3 directions yields an expression for δq_p^2:

$$\frac{\partial}{\partial t}\alpha_l\rho_l\delta q_p^2 + \frac{\partial}{\partial x_k}\alpha_l\rho_l\delta q_p^2 = -2\alpha_l\rho_l\delta q_p^2\left(\frac{\partial \breve{u}_{p,i}}{\partial x_i} + \frac{1}{\breve{\tau}_p}\right) \tag{3.20}$$

Including HIVD, the one dimensional non-conservative transport equations for the gas phase quantities and the dispersed phase mesoscopic mass weighted averaged quantities, denoted here by $\breve{\cdot}$, in a

laminar compressible gas flow become:

$$\frac{D_g \rho_g}{Dt} = -\rho_g \frac{\partial u_g}{\partial x} \tag{3.21}$$

$$\frac{D_g Y_{F,g}}{Dt} = 0 \tag{3.22}$$

$$\frac{D_g u_g}{Dt} = -\frac{1}{\rho_g}\frac{\partial p}{\partial x} + \frac{\alpha_l \rho_l}{\rho_g}\frac{\breve{u}_p - u_g}{\breve{\tau}_p} \tag{3.23}$$

$$\frac{D_g p}{Dt} = -\gamma_g p \frac{\partial u_g}{\partial x} \tag{3.24}$$

$$\frac{D_p \alpha_l}{Dt} = -\alpha_l \frac{\partial \breve{u}_p}{\partial x} \tag{3.25}$$

$$\frac{D_p \breve{u}_p}{Dt} = -\frac{2}{\alpha_l}\frac{\partial \alpha_l \delta q_p^2}{\partial x} - \frac{\breve{u}_p - u_g}{\breve{\tau}_p} \tag{3.26}$$

$$\frac{D_p \delta q_p^2}{Dt} = -2\delta q_p^2 \left(\frac{\partial \breve{u}_p}{\partial x} + \frac{1}{\breve{\tau}_p}\right) \tag{3.27}$$

$$\frac{D_p T_p}{Dt} = 0 \tag{3.28}$$

$$\frac{D_p n_p}{Dt} = -n_p \frac{\partial \breve{u}_p}{\partial x} \tag{3.29}$$

where $\frac{D_g \cdot}{Dt} = \frac{\partial \cdot}{\partial t} + u_g, \frac{\partial \cdot}{\partial x}$ and $\frac{D_P \cdot}{Dt} = \frac{\partial \cdot}{\partial t} + \breve{u}_p \frac{\partial \cdot}{\partial x}$ are respectively the gas and the particle Lagrangian derivatives.

The mass weighted averaged particle relaxation time $\breve{\tau}_p$ appearing in the previous set of equations is modeled with Equation (3.2) adapted to take into account the net effect of the instantaneous relative particle velocity at the mesoscopic scale [215].

The system of Equations (3.21)-(3.29) is similar to Equations (3.11)-(3.17). Here, the RUE adds the transport Equation (3.27) and an additional term on the right hand side of the dispersed phase momentum balance Equation (3.26), describing how RUE alters the dynamics of droplets at the mesoscopic scale in a gaseous laminar flow. Its influence on the particle velocity and number density waves is analyzed in Chapter 5.

Chapter 4

Acoustic response of a perfectly monodisperse spray in a uniform laminar gas flow

Un fait brutal s'imposa peu à peu à moi: je n'arrivais pas à dépasser la sixième balle. J'ai essayé, pourtant, Dieu sait que j'ai essayé. Il m'arrivait à cette époque de jongler sept, huit heures par jour. Je sentais confusément que l'enjeu était important, capital même, que je jouais là toute ma vie, tout mon rêve, toute ma nature profonde [...] Mais j'avais beau faire, la septième balle se dérobait toujours à mes efforts. Le chef-d'œuvre demeurait inaccessible, éternellement latent, éternellement pressenti, mais toujours hors de portée. Ce fut seulement aux abords de ma quarantième année, après avoir longuement erré parmi les chefs-d'œuvre, que peu à peu la vérité se fit en moi, et que je compris que la dernière balle n'existait pas.

– Romain Gary, *La promesse de l'aube, 1960*

Euler-Euler equations are linearized and attempt is made to solve the problem. The case where the fuel droplets are injected at the same velocity as the gas is considered first. The more difficult problem with an initial particle velocity different from the gas velocity is considered next. The expressions derived for the particle velocity and number density waves confirm the observations of particle clustering documented in the literature. Dimensionless quantities including the Stokes and Mach number introduced. They provide a theoretical framework to understand the formation and the propagation of number density waves in flow field. The validity of these expressions is then assessed with numerical flow simulations.

Overview

4.1. Introduction

The objective is to develop an analytical homework to study the interactions between an acoustic field and a monodispere non-evaporating 1D spray. The Eulerian-Lagrangian or the Eulerian-Eulerian framework may be used for the description of the two-phase flow dynamics. In the Eulerian-Lagrangian description, a set of equations describes only the temporal evolution of each single particle in a given carrier flow. This description raises several difficulties. The first issue is that it is necessary to solve also the trajectory equation for each particle to access the spatial evolution of these particles. Expressions for the velocities and the trajectories of the particles in a standing wave have been derived in several studies [115, 186, 189, 190, 193, 202, 223], but these expressions are complex, due in particular to the expression of the particle position. They need numerical integration. The second issue with the Eulerian-Lagrangian formalism is that the evolution of two-phase flow properties like the number density or volume fraction are not accessible without prior computation or interpolation from the particle position and properties. For instance, Kulkarni et al. [148] recently derived an analytical expression for velocity and number density fluctuations from Lagrangian description when the initial particle velocity is equal to the mean gas velocity. However, to obtain their expressions along the computational domain, the expression of the particle position need to be derived first according to the injection time and the lifetime of the particle. Moreover, validation are made with very low values for the gas and particle velocities, around 1 m/s, which are not representative of typical flow velocities in systems powered by spray flames.

The problem is revisited here with the objective to derive an analytical expression of an acoustic wave interacting with a non-evaporating and mono-disperse spray in 1D configuration using an Eulerian-Eulerian framework. There is to our knowledge no analytical expressions derived with this framework yet. The balance equations constituting the 1D Eulerian-Eulerian flow model are presented first. They are then linearized to get a low-order model for the response of the spray submitted to an acoustic perturbation. Fully analytical expressions of the particle velocity and number density perturbations are firstly given when the initial particle velocity is equal to the mean gas velocity. They are then derived when the initial particle velocity differs from the mean gas velocity. Influence of the parameters and limits of the model are finally investigated.

4.2. Theoretical Framework

4.2.1. Governing equations

For a perfectly monodisperse and isothermal spray, the one-dimensional Euler-Euler equations governing the particles dynamics can be summarized as:

$$\frac{\partial u_p}{\partial t} + u_p \frac{\partial u_p}{\partial x} = -\frac{u_p - u_g}{\tau_p} \tag{4.1}$$

$$\frac{\partial n_p}{\partial t} + u_p \frac{\partial n_p}{\partial x} = -n_p \frac{\partial u_p}{\partial x_i} \tag{4.2}$$

The liquid volume fraction α_l being directly proportional to the number density of particles n_p in sprays with a monodisperse diameter distribution, there is no need of a balance equation for $\alpha_l = n_p m_p/\rho_l$.

For linear acoustic perturbations, any acoustic variable x can be decomposed as the sum of temporal mean component, $\overline{x}$, and a fluctuating component x' which is much smaller than to the mean component [130] : $u'_g \ll \overline{u}_g$, $u'_p \ll \overline{u}_p$, $n'_p \ll \overline{n}_p$. In the following analysis, one only considers the mean particle relaxation time $\overline{\tau}_p$ and neglect fluctuations τ'_p. This approximation will be shown to be valid by comparing the analytical results with a constant relaxation times with numerical flow simulations

conducted with the exact expression of the relaxation time.

Hence, for a non-reacting, non-evaporating and mono-dispersed two-phase flow, the linearized forms of Equations (4.1) and (4.2) reduce to:

– for the mean particle velocity $\overline{u}_p(x)$:

$$\overline{\tau}_p \overline{u}_p \frac{\partial \overline{u}_p}{\partial x} + \overline{u}_p = \overline{u}_g \tag{4.3}$$

– for the particle velocity fluctuation $u'_p(x,t)$:

$$\overline{\tau}_p \left(\frac{\partial u'_p}{\partial t} + u'_p \frac{\partial \overline{u}_p}{\partial x} + \overline{u}_p \frac{\partial u'_p}{\partial x} \right) + u'_p = u'_g \tag{4.4}$$

– for the mean particle density $\overline{n}_p(x)$:

$$\overline{u}_p \frac{\partial \overline{n}_p}{\partial x} + \overline{n}_p \frac{\partial \overline{u}_p}{\partial x} = 0 \tag{4.5}$$

– for the particle number density fluctuation $n'_p(x,t)$:

$$\frac{\partial n'_p}{\partial t} + \overline{u}_p \frac{\partial n'_p}{\partial x} + n'_p \frac{\partial \overline{u}_p}{\partial x} = -u'_p \frac{\partial \overline{n}_p}{\partial x} - \overline{n}_p \frac{\partial u'_p}{\partial x} \tag{4.6}$$

The set of equations (4.3)-(4.6) is solved for gas velocity fluctuation $u'_g = U_g \cos(k_a^+ x - \omega t)$, where U_g is the amplitude of the velocity excitation, ω is the angular frequency, $k_a^+ = \omega/(\overline{u}_g + c)$ is the acoustic wave number of sound waves propagating in the direction $+x$, and c is the speed of sound.

To solve equations (4.4) and (4.6), a Fourier transform is applied. This yields a new set of equations for the complex amplitudes $\hat{u}_p$ and $\hat{n}_p$ of the respective Fourier transforms $\tilde{u}_p = \hat{u}_p(x) e^{-\mathrm{i}\omega t}$ and $\tilde{n}_p = \hat{n}_p(x) e^{-\mathrm{i}\omega t}$ for the input $\tilde{u}_g = \hat{u}_g e^{-\mathrm{i}\omega t} = U_g e^{\mathrm{i}k_a^+ x} e^{-\mathrm{i}\omega t}$. This leads to

– an equation for the complex amplitude of the particle velocity fluctuation $\hat{u}_p$:

$$\frac{\partial \hat{u}_p}{\partial x} + \hat{u}_p \left(\frac{1}{\overline{\tau}_p \overline{u}_p} - \mathrm{i}\frac{\omega}{\overline{u}_p} + \frac{\frac{\partial \overline{u}_p}{\partial x}}{\overline{u}_p} \right) = \frac{\hat{u}_g}{\overline{\tau}_p \overline{u}_p} \tag{4.7}$$

– and an equation for the complex amplitude of the particle number density fluctuation $\hat{n}_p$:

$$\frac{\partial \hat{n}_p}{\partial x} + \hat{n}_p \left(\frac{\frac{\partial \overline{u}_p}{\partial x}}{\overline{u}_p} - \mathrm{i}\frac{\omega}{\overline{u}_p} \right) = -\frac{\hat{u}_p}{\overline{u}_p} \frac{\partial \overline{n}_p}{\partial x} - \frac{\overline{n}_p}{\overline{u}_p} \frac{\partial \hat{u}_p}{\partial x} \tag{4.8}$$

To solve Equations (4.7) and (4.8), it is necessary to solve first the equations for the mean components (4.3) and (4.5). When the particle injection velocity $\overline{u}_p(0)$ differs from the mean gas velocity $\overline{u}_g$, a transient regime appears where the mean particle velocity $\overline{u}_p$ tends to the particle mean gas velocity $\overline{u}_g$. This transition triggers another transient regime for the mean particle number density $\overline{n}_p$. These transient regimes lead to more difficulties to solve Equations (4.7) and (4.8). Hence, the study is conducted first when there is not transient regime for the mean components, $\overline{u}_p(0) = \overline{u}_g$. The results in this regime will help to solve the problem for a transient regime $\overline{u}_p(0) \neq \overline{u}_g$.

4.2.2. Numerical validation

The expressions for u'_p and n'_p will be compared with numerical results from 1D Eulerian-Eulerian simulations, conducted on the computational domain shown in Figure 3.3. It has a length L =0.80 m discretized by 2000 identical elements of length $\Delta x = 0.4$ mm. The numerical model relies on a finite difference method with second-order centered schemes and a fourth-order Runge-Kutta scheme for the temporal resolution. At the inlet of the computational domain, the air velocity is modulated by imposing $u_g(t) = \overline{u}_g + U_g \cos(2\pi f t)$. In the case considered, the gas flow velocity is fixed to $\overline{u}_g = 40$ m/s which gives a Mach number $M = \overline{u}_g/c \approx 0.12$. The excitation parameters are the relative amplitude $U_g/\overline{u}_g = 1\%$ and the frequency $f = 250$ Hz. Air is at ambient pressure $p = 1$ bar and ambient temperature $T_g = 293$ K. Non-evaporating n-heptane droplets with a density $\rho_l = 688$ kg.m^{-3} are injected at a mass flow rate $\dot{m}_F = 0.15$ g/s, with a temperature $T_p = T_g$ with a monodisperse spray at a point located at the inlet of the computational domain. Simulations are carried out for sprays with the particle diameters $d_p = 10$, 25 and 50 μm to analyze the cases where the particles are respectively very, moderately and little responsive to the acoustic field as exemplified in Figure 3.2.

4.3. Analytical solution without initial velocity mismatch ($\overline{u}_p(0) = \overline{u}_g$)

Full details of the derivations executed in this section are given in appendix A. When $\overline{u}_p(0) = \overline{u}_g$, the transport equations for the mean components (4.3) and (4.5) give trivial solutions $\overline{u}_p = \overline{u}_g$ and $\overline{n}_p = n_p(0)$. Assuming that the particle relaxation time is defined by Equation (3.2) with $\overline{Re}_p \approx \rho_l |\overline{u}_p - \overline{u}_g| d_p/\mu_g$, a direct resolution of Equation (4.7) yields:

$$\hat{u}_p = \hat{U}_p \left(e^{\mathrm{i}k_a^+ x} - e^{-\frac{x}{\bar{l}_p}} e^{\mathrm{i}\frac{\omega}{\overline{u}_g} x} \right) \tag{4.9}$$

where

$$\hat{U}_p = \frac{U_g}{1 - \mathrm{i}\frac{St}{1+M}} \tag{4.10}$$

and $\bar{l}_p = \overline{\tau}_p \overline{u}_p$ is the mean particle relaxation length.

Example of the evolution of the relative particle velocity fluctuations $u'_p/\overline{u}_p$ for $d_p = 10, 25$ and 50 μm are given in Figure 4.1. Equation (4.9) indicates that $\hat{u}_p$ is the sum of two distinct waves. The first wave is a propagating acoustic wave with the wave speed k_a^+, caused by the particle velocity following the oscillating gas velocity. As the particle diameter increases, the final amplitudes of the particle velocity oscillation decreases. Their amplitudes correspond to those computed for the isolated droplet in Chapter 3 and presented in Figure 3.2. The second component is an evanescent convective wave with a decay rate of $1/\bar{l}_p$ and a wave speed $\omega/\overline{u}_g$. This vanishing wave can be attributed to the transient response as the particle goes from a constant velocity, when it is is injected, to an oscillating velocity, when the particle follows the gas movement. The distance over which this transition takes place is the so-called particle relaxation zone (PRZ) highlighted in [193]. The transient wave amplitude drops to less than 3% of its initial value downstream $3\bar{l}_p$. As the particle diameter increases, $\bar{l}_p$ increases as well as the evanescent convective wave last longer and its effect is more perceptible.

The acoustic propagating wave and the evanescent wave share the same complex amplitude $\hat{U}_p$. The following expressions give the final amplitude of the oscillations and its argument the final phase lag

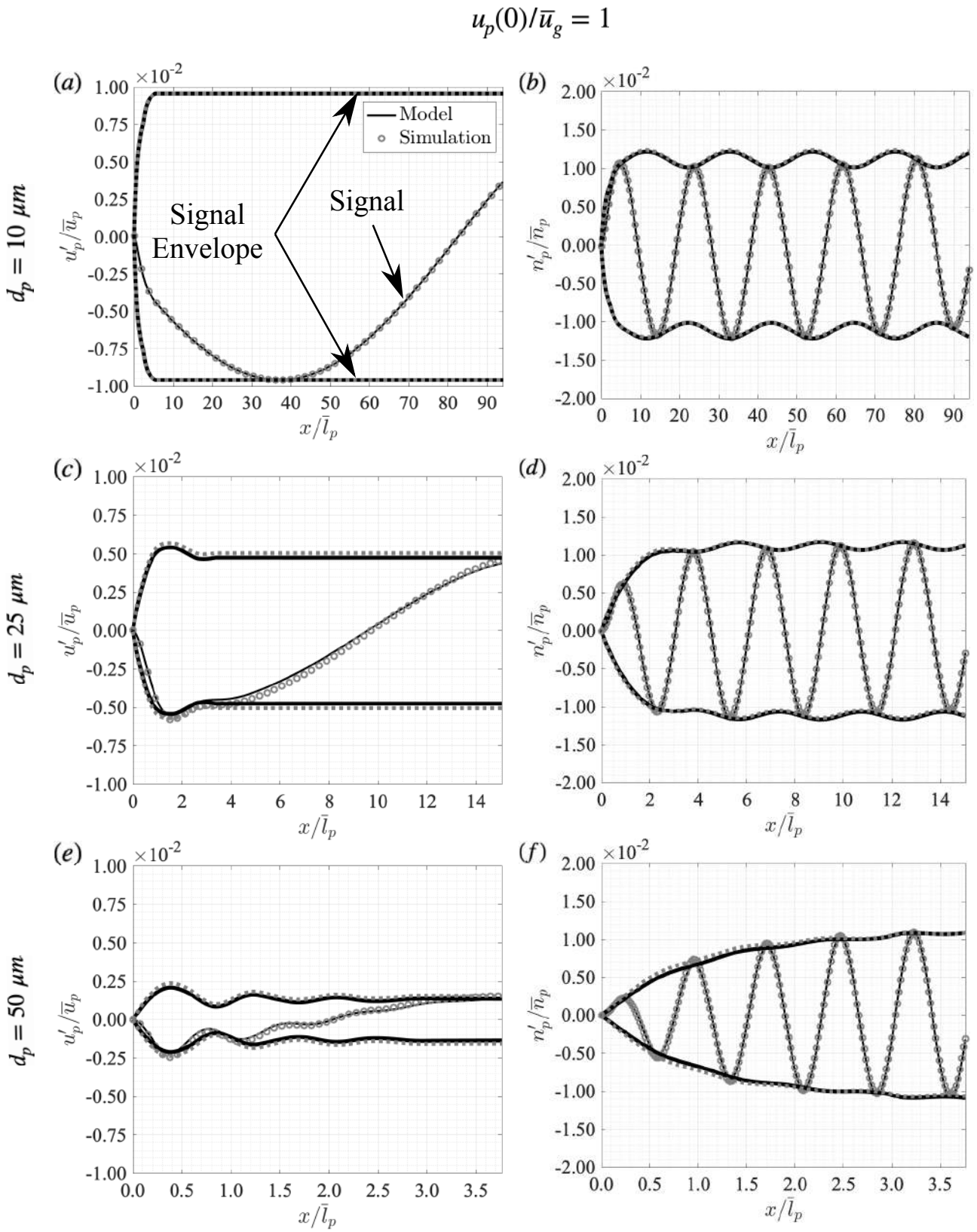

Figure 4.1. – Instantaneous of the evolution of the relative particle velocity fluctuation $u'_p/\overline{u}_p$ (left) and the relative particle number density fluctuation $n'_p/\overline{n}_p$ (right) for d_p =10 μm (a,b), 25 μm (c,d) and 50 μm (e,f) with $u_p(0) = \overline{u}_g = 40$ m/s, $U_g = 0.4$ m/s, $f = 250$ Hz and $\dot{m}_F = 0.15$ g/s obtained with the model (black) and the simulation (grey). Thin lines and round symbols represent the instantaneous fluctuation while thick solid and dotted lines represent the envelopes of their oscillations. Each abscissa covers the whole computational length $L = 0.8$ m which is normalized by the mean particle relaxation length $\bar{l}_p$.

between u_p and u_g oscillations:

$$\frac{|\tilde{u}_p|}{|\tilde{u}_g|} = \left[1 + \left(\frac{St}{1+M}\right)^2\right]^{-1/2} \tag{4.11}$$

$$\arg(\tilde{u}_p) - \arg(\tilde{u}_g) = \arctan\left[\frac{St}{1+M}\right] \tag{4.12}$$

As it can be seen in (4.11) and (4.12), the amplitude and the phase response of the particle velocity oscillations to the gas velocity oscillations are directly piloted by St but also by M. When $M \ll 1$, the amplitude ratio and the phase lag given in equations (4.11) and (4.12) are roughly the ones obtained in equations (3.3) and (3.4) with the Single Droplet Model which explained why the amplitude of the acoustic waves are really close to the ones predicted in figure 3.2. The Single Droplet Model is able to reproduce the acoustic wave u'_p but does not succeed to capture the transient convective wave: it is due to the Eulerian-Lagrangian description which does not consider the convection of a material field while the Eulerian-Eulerian description does.

The amplitude and the phase predicted by the theoretical expression are slightly below than those obtained in simulation: these differences are due to that we assume that $\bar{l}_p$ is constant, while in reality, it oscillates along the domain due to the difference between instantaneous particle velocity differs from the gas one. Hence, the values of $\overline{\tau}_p$ and then $\bar{l}_p$ are smaller along the domain than the one retained in the analytical resolution, decreasing, as we can see in 4.11 and 4.12, the amplitude and the phase response of the particle velocity oscillations.

Sill assuming that $\bar{l}_p$ is constant, a direct resolution of the equation 4.8 gives

$$\hat{n}_p = -\overline{n}_p \left[(1+M)\frac{U_g}{\overline{u}_g}\left(1 - e^{-\frac{x}{\bar{l}_p}}\right) e^{\mathrm{i}\frac{\omega}{\overline{u}_g}x} - M\frac{\hat{u}_p}{\overline{u}_g}\right] \tag{4.13}$$

Examples of the evolution of the particle number density fluctuations $n'_p/\overline{n}_p$ are given for $d_p = 10, 25$ and 50 μm in Figure 4.1. Equation (4.13) reveals that the number density wave n'_p is also the sum of two contributions. The formation of the number density wave n'_p is explained as follows. As highlighted in [193], Equation 4.2 can be reformulated as:

$$\frac{1}{n_p}\frac{Dn_p}{Dt} = -\frac{\partial u_p}{\partial x} \tag{4.14}$$

where $\dfrac{D\cdot}{Dt}$ is the Lagrangian derivative.

Equation 4.14 indicates that the relative fluctuation of n_p along the trajectory of the particles is caused by the divergence of the Eulerian particle velocity field u_p. Hence, the particle clustering phenomena is explained as illustrated in Figure 4.2. At instant $t = t_0$, one considers a set of particles represented by black dots equally spaced along an x-axis a with the Eulerian particle velocity u_p field drawn by a full line. Every particle has a different velocity, represented with a red arrow, depending on their position relatively to the particle velocity wave. Their position at the instant $t = t_0 + \Delta t$ is now investigated for two different situations. At the instant $t = t_0$, if $\partial u_p/\partial x < 0$ along the whole x-axis as illustrated in Figure 4.2.a, the particle at the location x is faster than the particle located further on the x-axis. Then, the distance between the particles decreases at the instant $t = t_0 + \Delta t$: a cluster of particles is created around the position where $\partial u_p/\partial x$ is the minimum. On the contrary, if $\partial u_p/\partial x > 0$ along the whole x-axis at the instant $t = t_0$ as illustrated in Figure 4.2.b, a particle at the location

x is slower than the particle located further on the x-axis. So, the distance between the particles increases at the instant $t = t_0 + \Delta t$: a sparse zone of particles is created occurs around the position where $\partial u_p/\partial x$ is the maximum. The particle velocity fluctuation u'_p is the sum of two distinct waves, which leads to the particle number density wave n'_p originating two simultaneous particle clustering, as shown in Equation 4.14.

The first contribution is a growing propagating convective wave with a growing rate of $1/\bar{l}_p$ and a wave speed $\omega/\overline{u}_g$. The convective particle clustering (CPC) is created in the particle relaxation zone (PRZ) by the convective wave of u'_p. In this region, where a particle goes from a constant velocity regime to the oscillating velocity regime, the convective wave of n'_p is growing as the convective wave of u'_p is vanishing. Its amplitude reaches more than 97% of its final value downstream $3\bar{l}_p$. Once outside the PRZ, its amplitude does not grow anymore due to the disappearance of the u'_p convective wave. According to Equation 4.9, the divergence of the convective wave of u'_p has an amplitude roughly equal to $(U_g/l_p)e^{-x/\bar{l}_p}$. Hence, the convective wave of n'_p does not depend on the acoustic coupling between the particle velocity and the flow perturbation. As also shown in [193], Equation (4.13) confirms that the amplitude of CPC is mainly related to the gas velocity fluctuation $u'_g/\overline{u}_g$ but Equation (4.13) shows here that it depends also on M.

The second contribution stems from the modulation of the particle velocity by the acoustic wave. This contribution originates from the acoustic wave of the particle velocity disturbances $\hat{u}_p/\overline{u}_p$ and is proportional to M. The influence of the acoustic particle clustering (APC) on the number density wave results into a modulation of the envelope of the convective wave. Having $\lambda_c = \overline{u}_g/f \ll \lambda_a = (\overline{u}_g + c)/f$, a convective oscillation is shifted towards positive or negative values depending on the phase of the acoustic wave at its location. However, this shift is relatively small compared to the amplitude of the convective oscillations and is all the more reduced as d_p is large, being almost insignificant when $d_p = 50\ \mu m$. The complex amplitudes of these two kind of clustering are given as

$$\hat{N}_A = \overline{n}_p M \frac{\hat{U}_p}{\overline{u}_g} \tag{4.15}$$

$$\hat{N}_C = -\overline{n}_p \left(1 + M\right) \frac{U_g}{\overline{u}_g} \tag{4.16}$$

$$\frac{|\hat{N}_A|}{|\hat{N}_C|} = \frac{M}{1+M} \left[1 + St^2\right]^{-1/2} \tag{4.17}$$

where $\hat{N}_A$ and $\hat{N}_C$ are the complex amplitudes of APC and CPC respectively.

Equation (4.17) shows that CPC is more important than APC. This is due to the higher velocity divergence of the convective wave of u'_p in the PRZ than the velocity divergence of the acoustic wave of u'_p. The CPC wave amplitude does not depend on St. The APC wave amplitude decreases when St increases while its phase lag with the gas velocity wave increases. The amplitudes of the APC and CPC waves are related to M. Although a small difference exists between the model and the simulation for $u'_p/\overline{u}_p$, the amplitude and the phase of $n'_p/\overline{n}_p$ predicted by the theoretical expression match very closely those obtained in simulation for the case $u_p(0) = \overline{u}_g$ as shown in Figure 4.1.

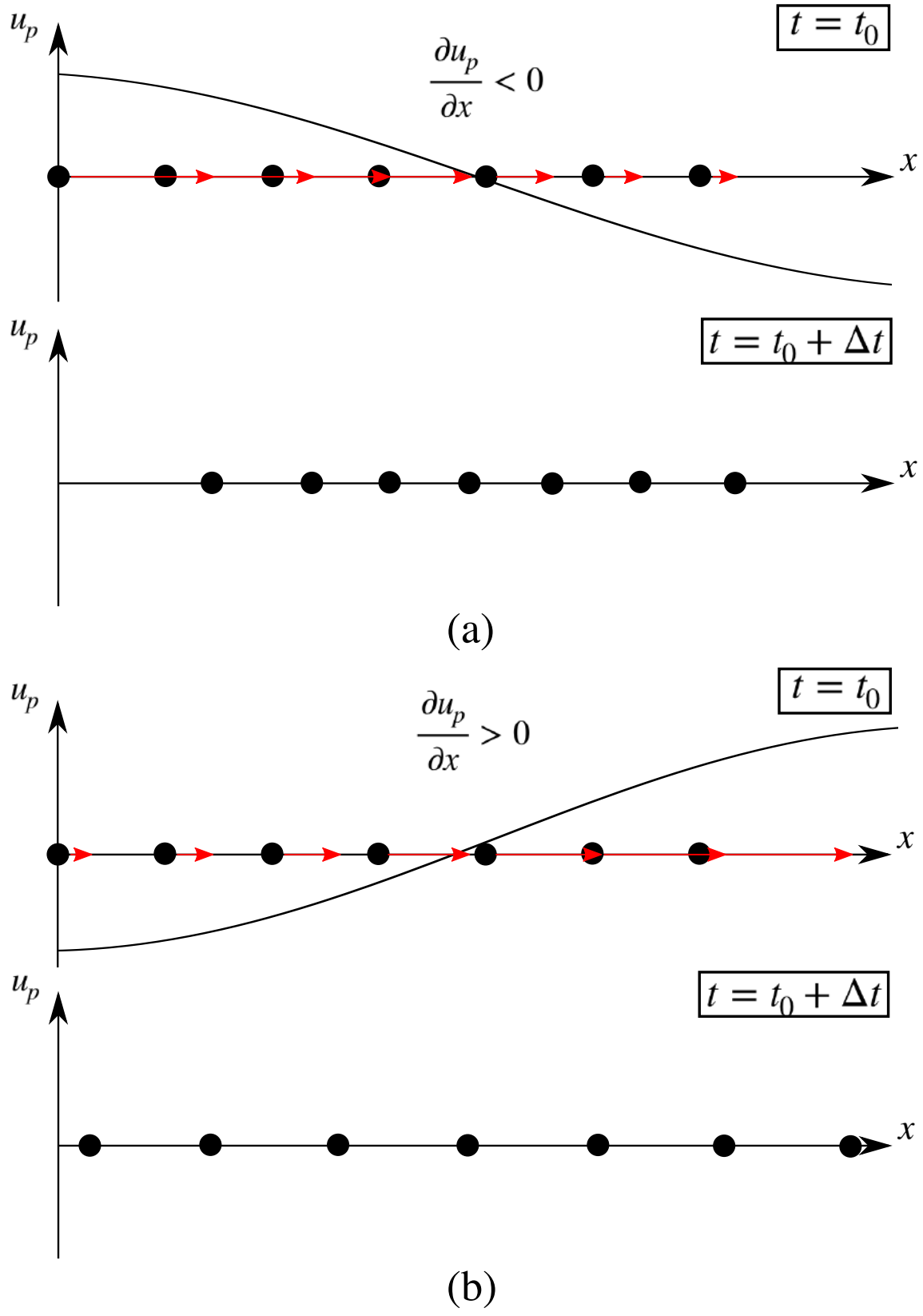

Figure 4.2. – Illustration of the particle clustering phenomena in the case where (a) $\partial u_p/\partial x < 0$ and (b) $\partial u_p/\partial x > 0$ over the x-axis. Particles are represented with black dots. The top pictures of each case correspond to the the instant $t = t_0$ where particles are equally spaced along x. Their respective velocity are indicated by red arrows. The Eulerian particle velocity u_p is represented with a full line. Their resulting position after a time step Δt on the bottom pictures of each case.

4.4. Analytical solution with initial velocity mismatch ($\overline{u}_p(0) \neq \overline{u}_g$)

Full details of the derivations of this section are given in appendix B. When $\overline{u}_p(0) \neq \overline{u}_g$, it is now mandatory to solve Equations (4.3) and (4.5) to get the evolution of the transient regimes where $\overline{u}_p$ and $\overline{n}_p$ reach their final values. Assuming that the exponential growth and decay are only determined by the initial mean relaxation length $\overline{l}_p(0) = \overline{\tau}_p(0)\overline{u}_p(0)$, one obtains:

$$\overline{u}_p = \overline{u}_g + (\overline{u}_p(0) - \overline{u}_g)e^{-\frac{x}{\overline{l}_p(0)}} \tag{4.18}$$

$$\overline{n}_p = n_p(0)\frac{\overline{u}_p(0)}{\overline{u}_p} \tag{4.19}$$

Evolution of $\overline{u}_p$ is given in Figure 4.3 for $d_p = 10, 25$ and 50 μm and for $\overline{u}_p(0)/\overline{u}_g = 0.75$ and 1.25. Having an exponential growing rate or decaying rate in $1/\overline{l}_p(0)$, they reach 97 % of their final value downstream $3\overline{l}_p(0)$, over a much shorter distance than when there is no initial velocity difference between the particle and the gas velocities. As d_p increases, the particle velocity takes longer to reach the gas velocity. It can be noted that the steady state is reached farther in the case $u_p(0)/\overline{u}_g > 1$ than in the case $u_p(0)/\overline{u}_g < 1$, highlighting the nonlinear nature of Equation (4.3). Submitted to the same drag during its life time as depicted in Equation (3.1), the particle travels more distance when $u_p(0)/\overline{u}_g > 1$ than when $u_p(0)/\overline{u}_g < 1$ due to their higher initial injection velocity. Hence, even if particles with the same diameter d_p share the same initial relaxation time $\overline{\tau}_p(0)$ in both cases, their mean relaxation length $\overline{l}_p$ differs. The approximation $\overline{l}_p = \overline{l}_p(0)$ gives a reasonable good transcription of this phenomenon in the analytical evolution of $\overline{u}_p$ and $\overline{n}_p$. Yet, one can observe that the growth and decay of the perturbations are well captured at the beginning of the PRZ but they are then overestimated when assuming that they are exponential with a constant decaying rate of $1/\overline{l}_p(0)$. These observations also apply for $\overline{n}_p$.

Analytical resolution of the Equations (4.7) and (4.8) is now difficult without numerical integration. However, it is possible to obtain approximate solutions by assuming that the form of the expressions for $\hat{u}_p$ and $\hat{n}_p$ when $\overline{u}_p(0) \neq \overline{u}_g$ are the same as those obtained when $\overline{u}_p(0) = \overline{u}_g$. Also, the complex amplitudes of the acoustic waves are supposed to vary spatially much slowly than their phase like in the WKB approximation [69]. The expressions for $\hat{u}_p$ and $\hat{n}_p$ become:

$$\hat{u}_p = \hat{U}_p(e^{\mathrm{i}k_a^+ x} - \frac{\hat{U}_p(0)}{\hat{U}_p}\left(\frac{\overline{u}_p(0)}{\overline{u}_p}\right)^{(1-\mathrm{i}Sr(0))} e^{-\frac{x}{\overline{l}_p(0)}} e^{\mathrm{i}\frac{\omega}{\overline{u}_g}x}) \tag{4.20}$$

$$\begin{aligned}\hat{n}_p = -\overline{n}_p\Bigg[&\left(1 - \frac{1}{\left(1 - \frac{\overline{u}_p/c}{1+M}\right) + \mathrm{i}\frac{1}{St}\left(1 - \frac{\overline{u}_g}{\overline{u}_p}\right)}\right)\frac{\hat{u}_p}{\overline{u}_p} \\ &+ \frac{\hat{U}_p(0)}{\overline{u}_p}\left(\frac{\overline{u}_p(0)}{\overline{u}_p}\right)^{\left(1-\mathrm{i}Sr(0)\right)}\left(\frac{\left(\frac{\overline{u}_p}{\overline{u}_p(0)}\right)^2 - e^{-\frac{x}{\overline{l}_p(0)}}}{\left(1 - \frac{\overline{u}_p/c}{1+M}\right) + \mathrm{i}\frac{1}{St}\left(1 - \frac{\overline{u}_g}{\overline{u}_p}\right)} - \frac{\mathrm{i}}{2}St(0)\left(1 + \frac{\overline{u}_p}{\overline{u}_p(0)}\right)\left(1 - e^{-\frac{x}{\overline{l}_p(0)}}\right)\right)e^{\mathrm{i}\frac{\omega}{\overline{u}_g}x}\Bigg]\end{aligned} \tag{4.21}$$

where

$$\hat{U}_p = \frac{\overline{u}_p}{\overline{u}_g}\frac{U_g}{1 - \mathrm{i}(1 - \frac{\overline{u}_p/c}{1+M})Sr} \tag{4.22}$$

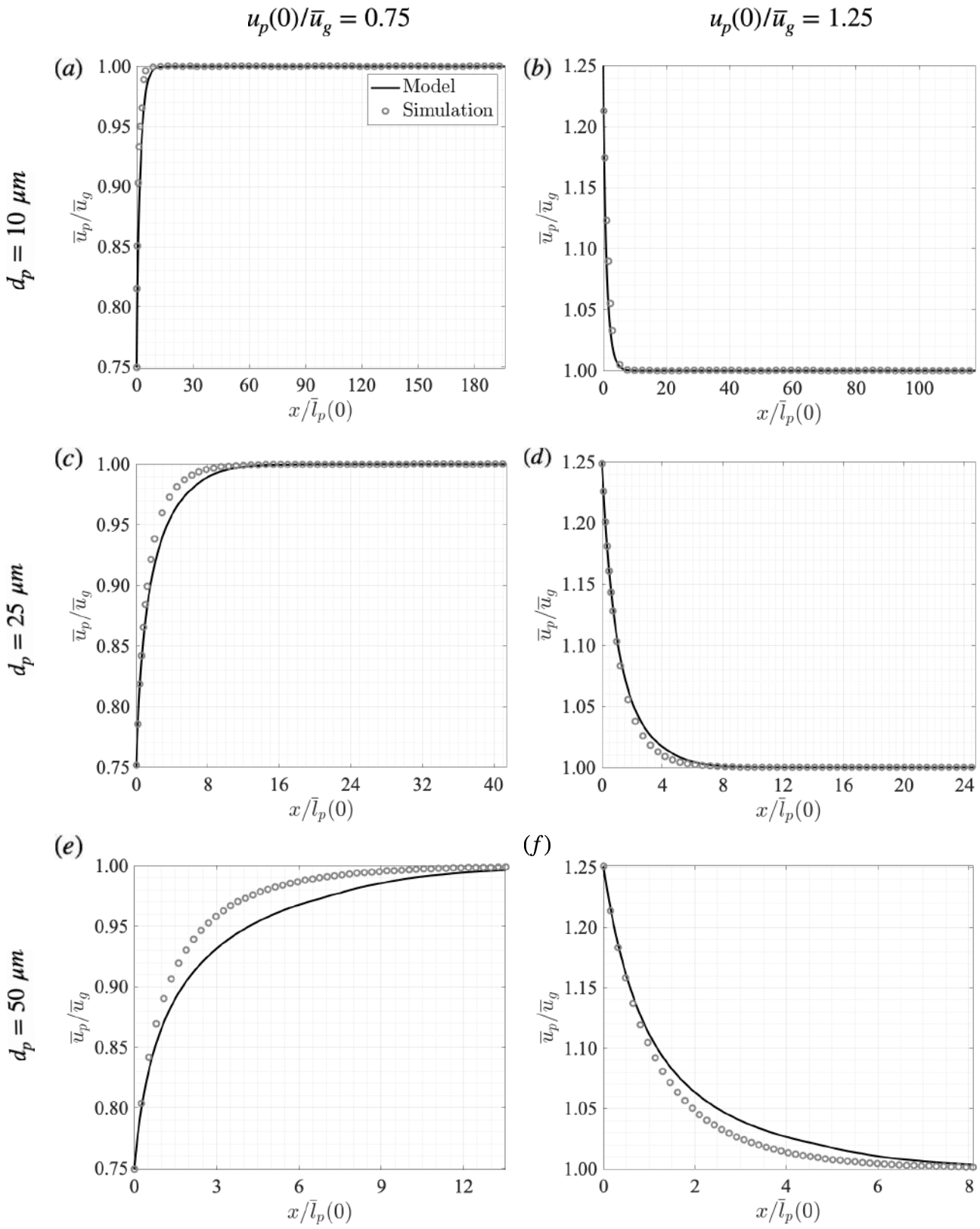

Figure 4.3. – Evolution of the mean particle velocity $\overline{u}_p$ for $u_p(0)/\overline{u}_g = 0.75$ (left) and $u_p(0)/\overline{u}_g = 1.25$ (right), d_p =10 μm (a,b), 25 μm (c,d) and 50 μm (e,f) with $\dot{m}_F = 0.15$ g/s obtained analytically (black line) and numerically (grey round symbols). The x-abscissa covers the whole computational length $L = 0.8$ m and is normalized by the initial mean particle relaxation length $\bar{l}_p(0)$.

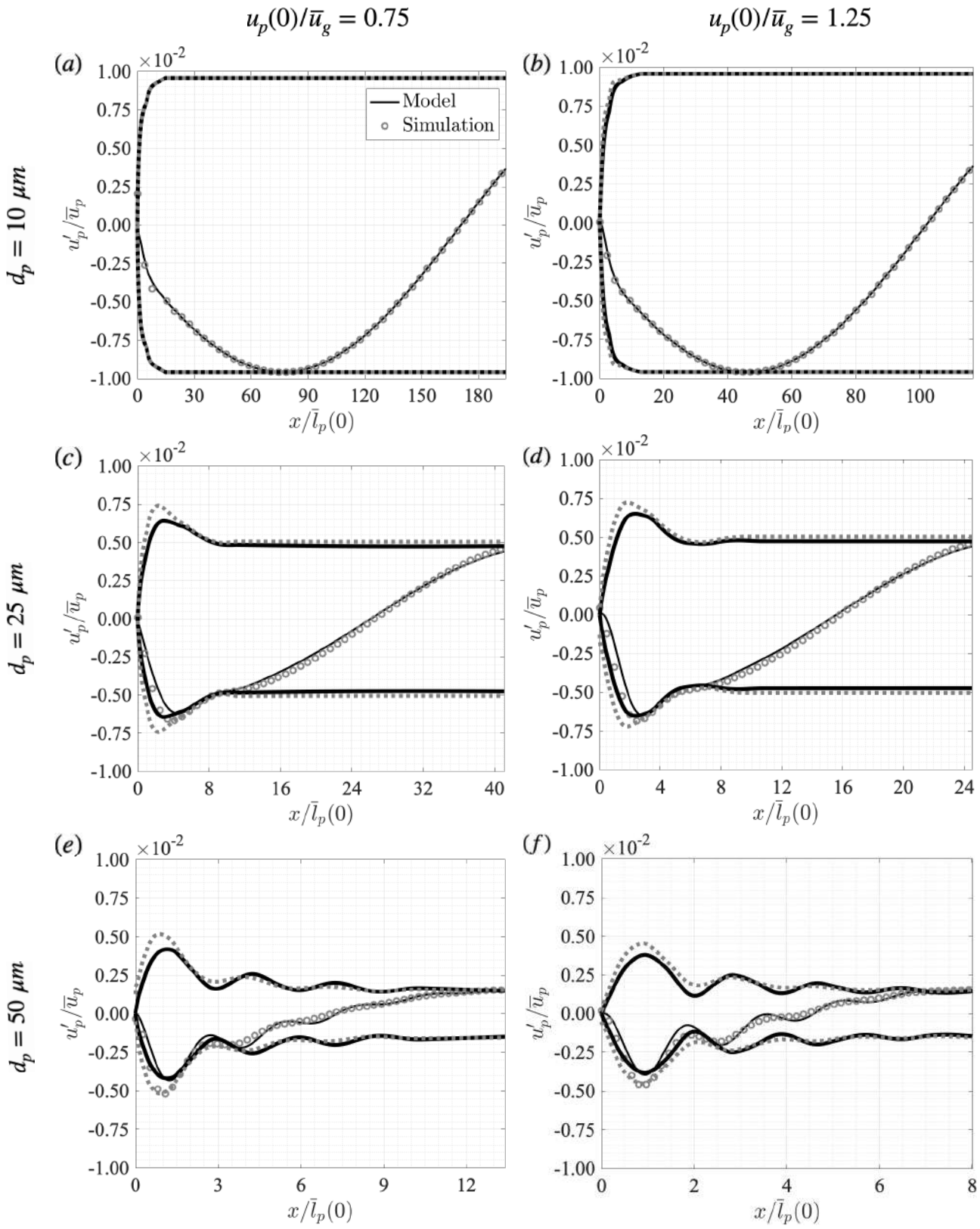

Figure 4.4. – Evolution of relative particle velocity fluctuation $u'_p/\overline{u}_p$ for (left) $u_p(0) = 30$ m/s and (right) $u_p(0) = 50$ m/s and for d_p =10 μm (a,b), 25 μm (c,d) and 50 μm (e,f) with $\overline{u}_g = 40$ m/s, $U_g = 0.4$ m/s, $f = 250$ Hz and $\dot{m}_F = 0.15$ g/s obtained with the analyticalmodel (black) and simulation (grey). Thin lines and round symbols represent the instantaneous fluctuation. Thick solid and dotted lines represent the envelopes of these oscillations. The x-abscissa covers the whole computational length $L = 0.8$ m and is normalized by the initial mean particle relaxation length $\bar{l}_p(0)$.

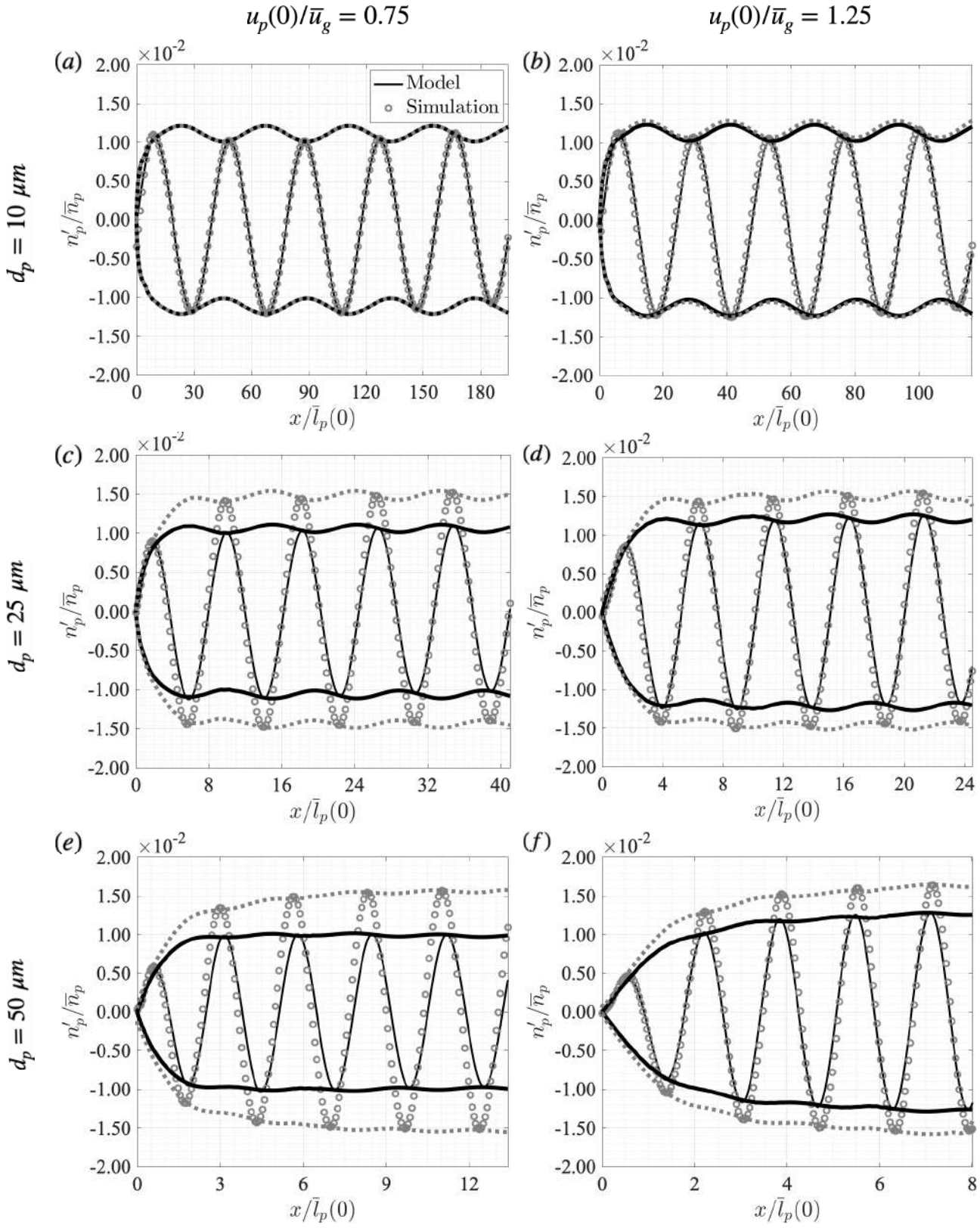

Figure 4.5. – Evolution of relative particle number density fluctuation $n'_p/\overline{n}_p$ for (left) $u_p(0) = 30$ m/s and (right) $u_p(0) = 50$ m/s and for d_p =10 μm (a,b), 25 μm (c,d) and 50 μm (e,f) with $\overline{u}_g = 40$ m/s, $U_g = 0.4$ m/s, $f = 250$ Hz and $\dot{m}_F = 0.15$ g/s obtained with the analytical model (black) and simulation (grey). Thin lines and round symbols represent the instantaneous fluctuation. Thick solid and dotted lines represent the envelopes of these oscillations. The x-abscissa covers the whole computational length $L = 0.8$ m and is normalized by the initial mean particle relaxation length $\bar{l}_p(0)$.

The evolutions of $u'_p/\overline{u}_p$ and $n'_p/\overline{n}_p$ are given in Figures (4.4) and (4.5) for $d_p = 10$, 25 and 50 μm and for $\overline{u}_p(0) = 30$ and 50 m/s. It can be noted that for $\overline{u}_p(0) = \overline{u}_g$, the expressions (4.20) and (4.21) become (4.9) and (4.13) respectively. As shown by Equations (4.20) and (4.21), $\hat{u}_p$ and $\hat{n}_p$ are still the sum of acoustic and convective waves as the ones observed in the case $\overline{u}_p(0) = \overline{u}_g$. Their evolution are similar to those observed in Figure 4.1. However, their complex amplitudes are modified by terms depending on the velocity ratios $\overline{u}_p(0)/\overline{u}_p$ and $\overline{u}_p/\overline{u}_g$ and on a Strouhal number $Sr = \omega\bar{l}_p/\overline{u}_g$, which is a Stokes number St multiplied by the velocity ratio $\overline{u}_p/\overline{u}_g$. The Strouhal number Sr represents the ratio of inertial forces due to the local increase and decrease of the velocity fluctuation u'_p to the inertial forces due to the global increase or decrease of $\overline{u}_p$ along the PRZ. It models the result of the interaction between the mean transient component and the oscillating transient.

When $\overline{u}_p(0) \neq \overline{u}_g$, the PRZ is now the location where two transitions take place: $\overline{u}_p$ is reaching $\overline{u}_g$ and u_p goes from an initial constant regime to an oscillatory regime. Piloted by local acceleration and deceleration due the relaxation process of the particle velocity in the PRZ, the modification of the amplitude of the convective wave compared to the case $\overline{u}_p(0) = \overline{u}_g$ is due to the difference of the initial particle velocity from the mean gas velocity, increasing the divergence of the particle velocity in the PRZ. As a result, the transient convective wave for $u'_p/\overline{u}_p$ and the convective waves $n'_p/\overline{n}_p$ feature higher amplitudes than in the case $\overline{u}_p(0) = \overline{u}_g$, in particular for the cases $d_p = 25$ μm and $d_p = 50$ μm.

When $x \to \infty$, the final wave complex amplitude of the different waves takes the asymptotic forms:

$$\hat{U}_p \xrightarrow{x\to\infty} \frac{U_g}{1 - \mathrm{i}\frac{St}{1+M}} \tag{4.23}$$

$$\hat{N}_A \xrightarrow{x\to\infty} -\overline{n}_p M \frac{U_p}{\overline{u}_g} \tag{4.24}$$

$$\hat{N}_C \xrightarrow{x\to\infty} -\overline{n}_p \frac{U_g}{\overline{u}_g} \left(\frac{\overline{u}_p(0)}{\overline{u}_g}\right)^{-\mathrm{i}Sr(0)} \frac{1 + M - \frac{\mathrm{i}}{2}Sr(0)\left(1 + \frac{\overline{u}_p(0)}{\overline{u}_g}\right)}{1 - \mathrm{i}(1 - \frac{\overline{u}_p(0)/c}{1+M})Sr(0)} \tag{4.25}$$

Compared to the case $\overline{u}_p(0) = \overline{u}_g$, the final complex amplitudes $\hat{U}_p$ and $\hat{N}_A$ for the acoustic waves of u'_p and n'_p differ only during the transient regime but their final expressions are still equal to Equations (4.10) and (4.15). Modifying the convective wave of u'_p in the PRZ, only the final CPC wave amplitude and phase are altered by the velocity ratio $\overline{u}_p(0)/\overline{u}_g$ and the initial Stokes number $St(0)$, and then differs from Equation (4.16).

Figures 4.4 and 4.5 show differences between theoretical and numerical results for $u'_p/\overline{u}_p$ and $n'_p/\overline{n}_p$. The amplitude of the convective waves is underestimated by the analytical model. These differences grow with the particle diameter d_p. For $d_p = 10$ μm, the amplitude predicted by the model match very closely those obtained in the numerical flow simulation. The phase of the different waves for $u'_p/\overline{u}_p$ and $n'_p/\overline{n}_p$ are well reproduced by the analytical model for all cases presented in Figures 4.4 and 4.5.

4.5. Model validation and limitations

The expressions of u'_p and n'_p depend on the Stokes number St and the initial velocity ratio $\overline{u}_p(0)/\overline{u}_g$. The amplitude and phase lag of the propagating waves obtained with the model are now compared with those obtained for the model for different particle diameter d_p and initial velocity ratio $\overline{u}_p(0)/\overline{u}_g$. The vanishing convective wave for u'_p is not considered here because its amplitude and phase lag are evolving along the domain, making it difficult to extract a reliable value. Only remaining waves at the end of the computational domain are considered in the analysis: the acoustic wave of u'_p, the

acoustic wave and the convective wave of n'_p. Their amplitude ratio (A_U, A_A, A_C) and phase lag ($\Delta\varphi_U$, $\Delta\varphi_A$, $\Delta\varphi_C$) between predictions and simulations are presented in Figure 4.6 for the particle velocity and the particle number density. The results are plotted as a function of the nominal Stokes number $St_0 = \omega\tau_{p,0}$ instead of the effective Stokes number $St = \omega\tau_p$, to only have two adimensional and independent parameters: St_0 and $\overline{u}_p(0)/\overline{u}_g$. For the acoustic wave in n'_p, results are only presented for $St \leq 0.6$. Above this value, the contribution to this wave to the global relative fluctuation $n'_p/\overline{n}_p$ is less than 2.5% and then, its wave amplitude is too small to extract reliable values.

For the case $\overline{u}_p(0) = \overline{u}_g$, the model reproduces very well the number density fluctuations n'_p while the particle velocity fluctuations u'_p match for low St_0 but differences between predictions and simulations appear for the acoustic wave amplitude at higher St_0. This is mainly due to the fact that the particle velocity differs from the gas velocity for high Stokes numbers, making the particle Reynolds number Re_p oscillating during the excitation cycle. In these conditions, $\bar{l}_p$ can not be considered constant. For the case $\overline{u}_p(0) \neq \overline{u}_g$, the final phase lag and amplitude for $u'_p/\overline{u}_p$ are not altered by $\overline{u}_p(0)/\overline{u}_g$, and then differences with the simulation remains the same as in the case $\overline{u}_p(0) = \overline{u}_g$. The same observation holds for the particle number density wave $n'_p/\overline{n}_p$.

Differences appear mainly for the convective wave of $n'_p/\overline{n}_p$ when $\overline{u}_p(0) \neq \overline{u}_g$. As mentioned before in Figure 4.5, a better prediction is achieved when $\overline{u}_p(0)/\overline{u}_g > 1$ than when $\overline{u}_p(0)/\overline{u}_g < 1$. The phase is relatively well reproduced, the differences do not exceed $\pi/4$ when $\overline{u}_p(0)/\overline{u}_g < 1$ (except for the limit case $\overline{u}_p(0)/\overline{u}_g = 0.10$) and $\pi/8$ when $\overline{u}_p(0)/\overline{u}_g > 1$. Its amplitude is generally underestimated by the model: the amplitude ratio A_C between the model and the simulation is about 0.60-0.75 when $\overline{u}_p(0)/\overline{u}_g < 1$ and about 0.8-0.9 when $\overline{u}_p(0)/\overline{u}_g > 1$. The phase lag calculated between predictions and simulations increases as St_0 and $|\overline{u}_p(0) - \overline{u}_g|$ increase. While the amplitude differs as all the more as St_0 increases (with a singularity for $\overline{u}_p(0)/\overline{u}_g = 0.10$), increasing $|\overline{u}_p(0) - \overline{u}_g|$ reduces the difference.

For a better understanding of these results, the amplitude modification $\mathscr{A}$ as well as the phase lag $\Delta\psi$ induced by $\overline{u}_p(0) \neq \overline{u}_g$ in the CPC are compared to the case $\overline{u}_p(0) = \overline{u}_g$. They are calculated as

$$\mathscr{A} = \frac{|\hat{N}_C\left(\overline{u}_p(0) \neq \overline{u}_g\right)|}{|\hat{N}_C\left(\overline{u}_p(0) = \overline{u}_g\right)|} \tag{4.26}$$

$$\Delta\psi = \arg\left[\frac{\hat{N}_C\left(\overline{u}_p(0) \neq \overline{u}_g\right)}{\hat{N}_C\left(\overline{u}_p(0) = \overline{u}_g\right)}\right] \tag{4.27}$$

for the model and the simulation are presented in Figure 4.7. $\Delta\psi$ is due to the lag accumulated by the particle during the transient to adjust to the gas flow mean velocity $\overline{u}_g$ and synchronize its motion with the acoustic wave speed $\omega/\overline{u}_g$. When $\overline{u}_p(0)/\overline{u}_g < 1$, the transient wave speed $\omega/\overline{u}_p$ is lower than the final wave speed $\omega/\overline{u}_g$ and $\Delta\psi > 0$. Conversely, when $\overline{u}_p(0)/\overline{u}_g > 1$, the transient wave speed $\omega/\overline{u}_p$ is higher than the final wave speed $\omega/\overline{u}_g$ and $\Delta\psi < 0$. The initial mean particle relaxation length $l_p(0) = \overline{\tau}_p(0)\overline{u}_p(0)$ decreases more when $\overline{u}_p(0)/\overline{u}_g(0)$ decreases than when $\overline{u}_p(0)/\overline{u}_g(0)$ increases. In this case the particle has more distance to accumulate phase lag when $\overline{u}_p(0)/\overline{u}_g(0) < 1$ than when $\overline{u}_p(0)/\overline{u}_g(0) > 1$. Moreover, $\Delta\psi$ increases with $St(0)$.

Even if the values of $\mathscr{A}$ predicted by the model are underestimated for the CPC, the model reproduces the trend for $\overline{u}_p(0)/\overline{u}_g(0) > 1$. The initial velocity difference amplifies the convective waves. This amplification grows with St_0 but saturates at a certain distance. However, the model depicts an attenuation for $\overline{u}_p(0)/\overline{u}_g(0) > 1$, while in reality, there is an amplification in both cases, except for the lower limit case $\overline{u}_p(0)/\overline{u}_g = 0.10$ where attenuation occurs when $St_0 < 0.4$.

Several elements can explain these differences. It is attempted here to linearly solve equations with strong non-linear terms like $\overline{\tau}_p$. For instance, when $\overline{u}_p$ tends to $\overline{u}_g$, $\overline{\tau}_p$ does not evolve in the same

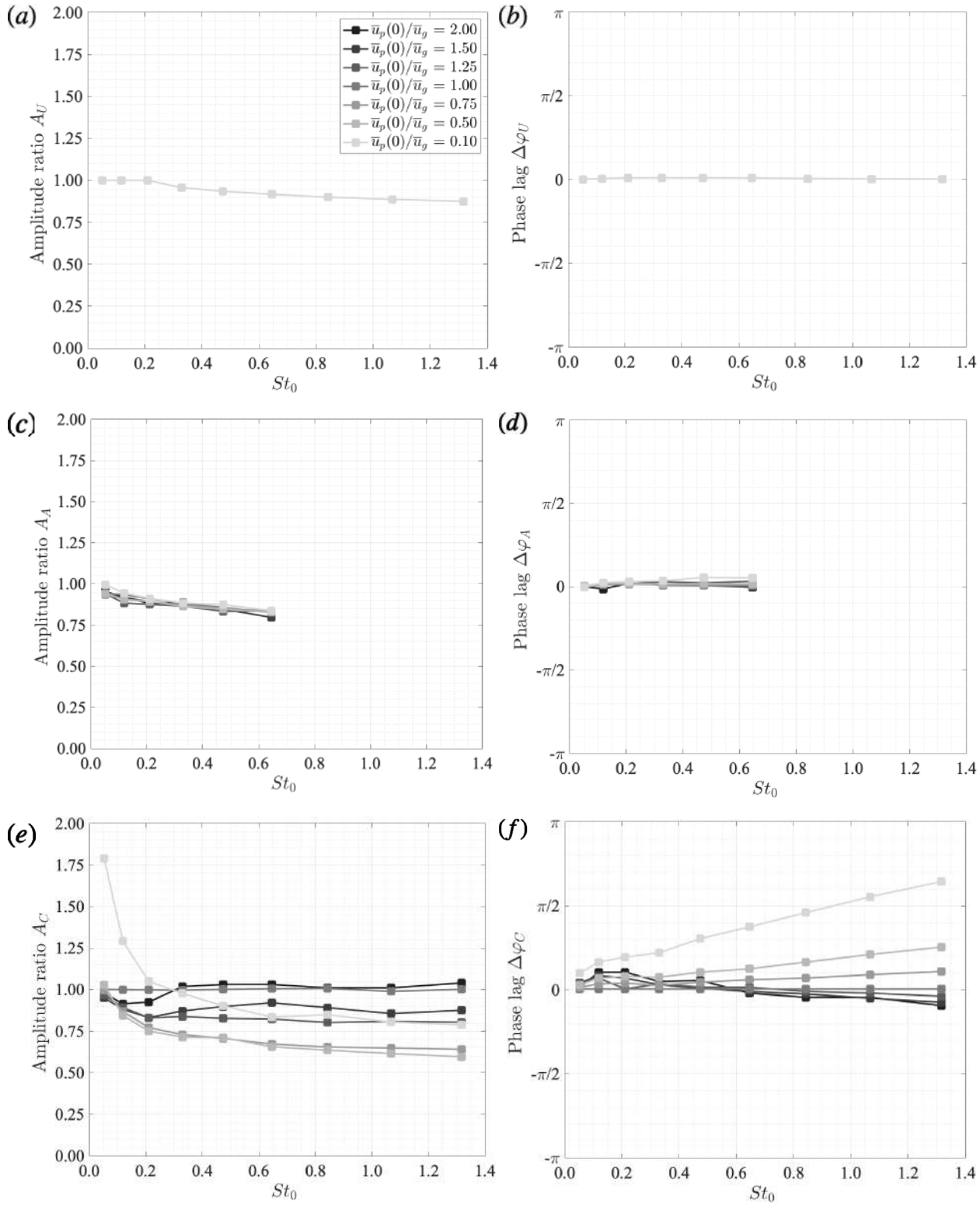

Figure 4.6. – Evolution of the model-to-simulation amplitude ratio A (left) and phase lag $\Delta\varphi$ (right) for the particle velocity acoustic wave $\hat{U}_p$ (a,b), the number density acoustic wave $\hat{N}_A$ (c,d) and the number density acoustic wave $\hat{N}_C$ (c,d) according to the nominal Stokes number St_0 for different injection velocity to gas velocity ratio

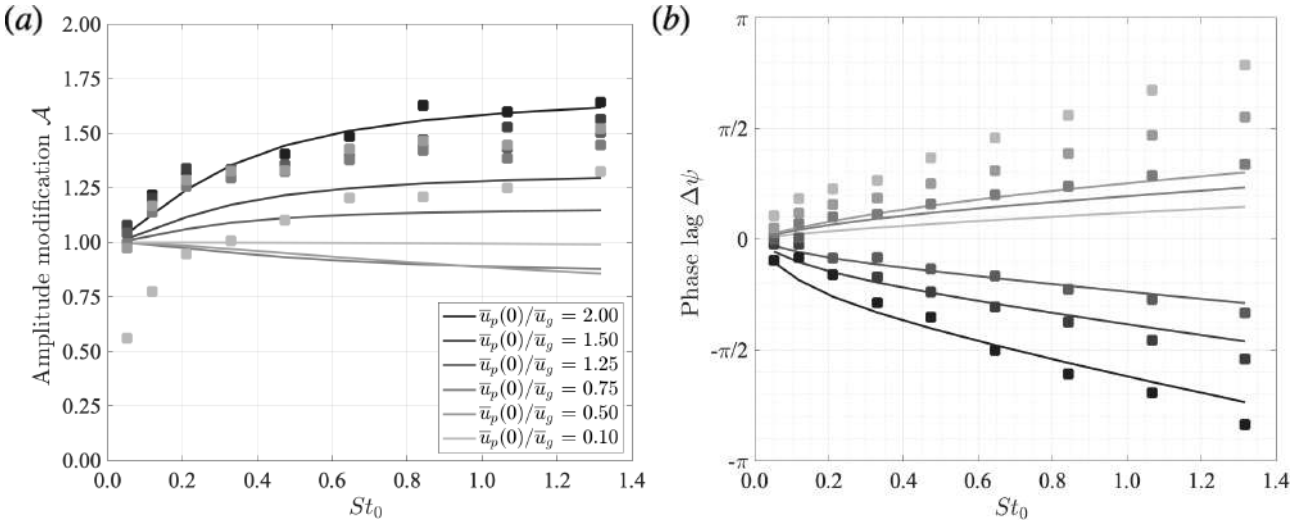

Figure 4.7. – Evolution of the amplitude modification $\mathscr{A}$ and the phase lag $\Delta\Psi$ induced by $\overline{u}_p(0) \neq \overline{u}_g$ for the CPC along the nominal Stokes number St_0 for different initial velocity ratios $\overline{u}_p(0)/\overline{u}_g$

manner when $\overline{u}_p/\overline{u}_g < 1$ as when $\overline{u}_p/\overline{u}_g > 1$. To achieve an analytical resolution when $\overline{u}_p(0) \neq \overline{u}_g$, an approximation of constant exponential growth/decay rate has been made for $\overline{u}_p$ and $\overline{n}_p$. Yet, this assumption underestimates the PRZ length as shown in Figure 4.3. The underestimation is more important when $\overline{u}_p(0)/\overline{u}_g < 1$ than when $\overline{u}_p(0)/\overline{u}_g > 1$. However, CPC is created in the PRZ by the convective wave of u'_p. An underestimation of its length let less distance for the clustering process to settle and to amplify. In our model, the growth and decay rate are captured only at the beginning of the PRZ. Then, the amplitude of CPC predicted by the model match better those obtained in the simulation for low St_0 because the transient is quickly evacuated. As a result, the error has less distance to be accumulated. Also, these errors are propagated during the analytical resolution because the integration relies on simplified expressions for $\overline{u}_p$ and $\overline{n}_p$ given respectively in Equations (4.18) and (4.19). They lead to the underestimation of the amplitude of the convective wave of u'_p which ultimately results in the underestimation of amplitude of the CPC.

Nonetheless, it should be emphasized that the resolution proposed here offers fully analytical expressions that yield excellent prediction for the case $\overline{u}_p(0) = \overline{u}_g$ and reproduces the main features of the spray response submitted to acoustic disturbances when $\overline{u}_p(0) \neq \overline{u}_g$. More specifically the phase lag response is well reproduced.

4.6. Conclusion

The response of a monodisperse liquid spray to acoustic disturbances has been examined. A Lagrangian description gives a simple model to study the acoustic response of a single particle velocity . It has shown that the harmonic response is governed by a first order low-pass filter and only depends on the Stokes number. the results obtained from the single droplet model have shown that the particle diameters play a significant role in determining the intensity of coupling between the particle motion and the acoustic field. An Euler-Euler description has been deployed to derive the linearized equations of a non-reacting, isothermal and monodisperse two-phase phase flow submitted to sound waves.

The set of equations has been first solved considering that the initial particle injection velocity is equal to mean gas velocity ($u_p(0) = \overline{u}_g$). The analytical expressions that have been derived enable to

explain the numerous results which have been observed in the literature, and but they also complete them. It has been shown that particle velocity fluctuations u'_p are the sum of an evanescent convective wave decaying over a Particle Relaxation Zone (PRZ), and a propagating acoustic wave. The final amplitude and phase of these waves depend on the Stokes number of the particles but also on the Mach Number of the gaseous flow. The expression for particle number density fluctuation n'_p confirms that two particle clustering dynamics are superposing: an Acoustic Particle Clustering (APC) with an amplitude proportional to u'_p, and the Convective Particle Clustering (CPC), growing along the PRZ with an amplitude proportional to the gas velocity fluctuation u'_g which does not depend on the acoustic coupling between the particle velocity and the flow perturbation. Also, the amplitude of CPC and APC waves are related to the Mach Number. The CPC is shown to be the major contribution of the whole number density fluctuation. The influence of the APC can be perceptible at low Stokes number. Hence, a spray can be composed of particles indifferent to acoustic perturbations but the whole population can still be fluctuating at the same order of magnitude as the gas velocity excitation u'_g.

When the initial particle injection velocity differs from the mean gas velocity ($u_p(0) \neq \overline{u}_g$), the PRZ becomes the location where the mean and the fluctuating components of u_p and n_p go both from a transient regime to a steady regime. The nature of the waves observed are the same as when $u_p(0) = \overline{u}_g$ but their amplitude and their phase are affected by the initial velocity difference between the particle velocity and gas velocity. The acoustic waves of u'_p and n'_p are temporarily changed during the PRZ, before recovering the same amplitude and phase than in the case $u_p(0) = \overline{u}_g$. On the contrary, the amplitude and the phase of the CPC are permanently changed depending on St and the initial particle velocity ratio $u_p(0)/\overline{u}_g$. The amplitude of CPC waves increases with $|u_p(0) - \overline{u}_g|$ and with St but this latter effect saturates at certain point. The phase linearly increases with $|u_p(0) - \overline{u}_g|$ for $u_p(0)/\overline{u}_g > 1$ and linearly decreases with $|u_p(0) - \overline{u}_g|$ for $u_p(0)/\overline{u}_g < 1$.

Comparison with simulations shows that the model well reproduces the acoustic response of the spray for $u_p(0) = \overline{u}_g$ and captures well the main features for $\overline{u}_p(0) \neq \overline{u}_g$, especially the phase response. Differences are detected for the amplitude of the CPC waves especially when St is high, $u_p(0)/\overline{u}_g < 1$ and $|u_p(0) - \overline{u}_g|$ is very important. These differences result from the underestimation of the PRZ length and the simplified expression for the mean particle velocity $\overline{u}_p$. Improvements on the resolution of the equation governing $\overline{u}_p$ could help to reduce these slight differences.

Chapter 5

Influence of the particle velocity dispersion on the acoustic spray response

Le sous-officier se tut ; Drogo le regardait épouvanté. Que restait-il de ce soldat au bout de vingt-deux ans passés au fort ? Tronk se souvenait-il encore qu'il existait quelque part dans le monde des millions d'hommes semblables à lui-même, qui ne portaient pas l'uniforme, et qui circulaient librement dans la ville, et qui pouvaient, la nuit, selon leur bon plaisir, aller au lit, au théâtre ou au cabaret ? Non, il suffisait de regarder Tronk pour comprendre qu'il ne se rappelait plus rien des autres hommes, que, pour lui, n'existaient plus que le fort et ses odieux règlements.

– Dino Buzzati, *Le désert des Tartares, 1940*

In this present chapter, this assumption is relaxed and a particle velocity distribution is considered. In the limit of a homogenous isotropic velocity dispersion (HIVD), the set of balance equations presented in Chapter 3 is transformed into its characteristic normal form. Doing so highlights how the particle velocity dispersion alters the way the information is transported in the disperse phase, and how it modifies the acoustic response of the spray. The case investigated is a uniform flow submitted to an acoustic wave in which a fuel spray is injected with an initial dispersion of particle velocities. The expressions derived with the HIVD model are validated against numerical results from a Lagrangian-Eulerian reference simulation. Next, simulations are performed to infer how the level of velocity dispersion alters the phase lag and the amplitude of particle number density waves observed in the simulations created by the acoustic forcing, for different Stokes numbers. Spatial spectrum analysis is conducted on the number density waves observed in the simulations to validate the analytical expressions of the velocity of the characteristic waves.

Overview

5.1. Introduction

Until now, the spray was considered in Chapter 4 to be perfectly monodisperse. In the control volume of observation, all droplets inside have the same size, velocity and temperature and an unique fuel is considered. However, in real sprays, droplets can have properties that differ from each other. Instead of using single values to describe the local properties of a spray, distribution functions named particle distribution functions (PDFs) are used. Example of these local PDFs measurements obtained with a phase doppler particle analyzer (PDPA) are presented in Figures 5.1. The influence of the dispersion diameter has been numerically investigated in [191]. Small droplets being more sensitive to the acoustic perturbation than large droplets, numerical simulations have shown that a phase lag appears between the corresponding convective clusters produced by the pulsating flow field.

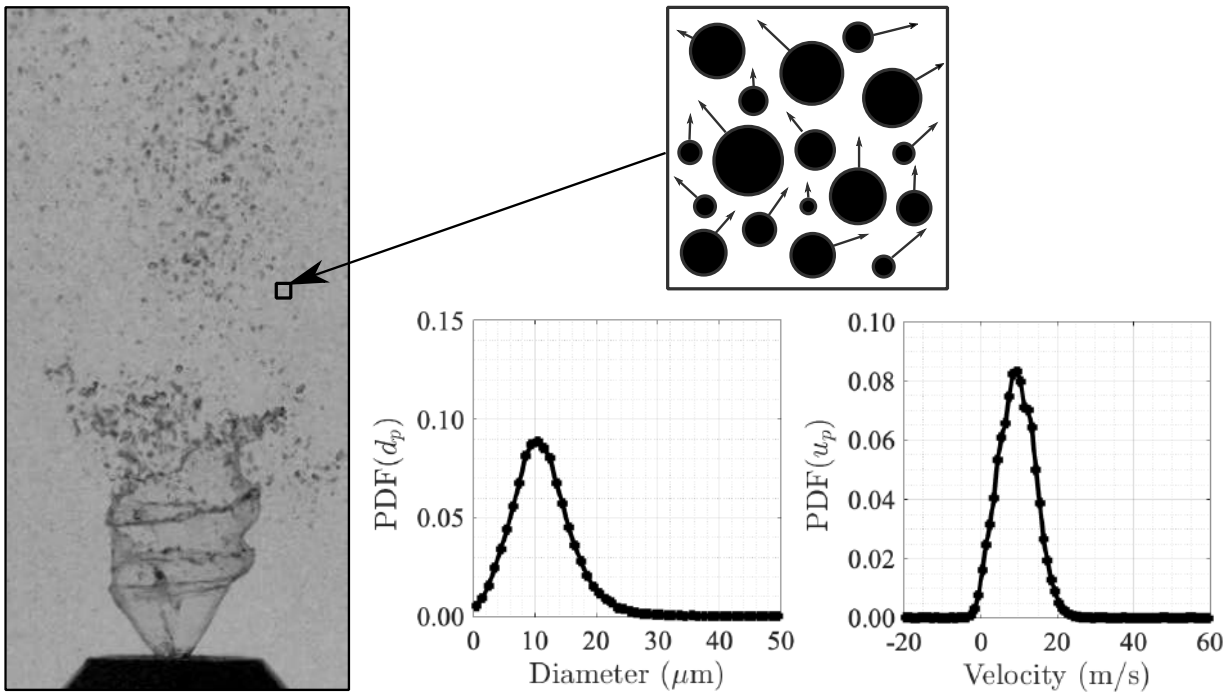

Figure 5.1. – (Left) Backlight image of the hollow-cone n-heptane spray produced by the TALISMAN injector captured by a fast camera (Right-Top) Illustration of the polydisperse distribution of the particles collected by the PDPA at a location of the n-heptane spray. (Bottom-right) Example of the particle distribution function (PDF) of the particle diameter d_p and the particle velocity u_p measurements obtained with a phase doppler particle analyzer (PDPA) on a n-heptane spray produced by this injector.

The influence of the velocity dispersion on the particle clusters has not been studied yet. This problem is investigated with a combined numerical and theoretical approach aiming at analyzing the impact of the initial dispersion of the droplet velocities around a mean value on the resulting spray response to acoustic excitation. The motivation is that in a turbulent spray, droplets are transported by the mean flow and any dispersion of the droplet velocity will in turn alter the phase lag and the amplitude of the spray response to acoustic excitation. The question addressed here is to evaluate this response for a spray featuring an initial dispersion of the droplet velocities with respect to a spray without initial dispersion in a laminar uniform gaseous flow.

The impact is evaluated for a monodisperse spray injected in a 1D laminar uniform gaseous flow with a certain initial level of dispersion for the droplet particles at the injector outlet when the flow is submitted to an harmonic acoustic excitation. In the following sections, the characteristic waves of the

hyperbolic system of equations are analyzed for a 1D Eulerian-Eulerian HIVD two-phase flow model to see how the particle velocity dispersion modifies the speed of these characteristic waves for the dispersed phase. Numerical results given by the Eulerian-Eulerian model are validated against Euler-Lagrange simulations for different levels of initial particle velocity dispersion at the injection location. Finally, numerical results from Eulerian-Eulerian model are examined to analyze the influence of particle velocity dispersion on the number particle density waves and validate theoretical results from the characteristic analysis.

5.2. Analysis of the characteristic waves in the HIVD spray model

The system of quations (3.21)-(3.29) presented in Section 3.2.3 governing the dynamics of a HIVD spray is considered in this section. It is worth looking into the previous system how information is conveyed. Considering only the projection of the previous set of equations along the main flow direction, the system can be cast in the following form:

$$\frac{\partial \mathbf{U}}{\partial t} + \mathbf{A}\frac{\partial \mathbf{U}}{\partial x} + \mathbf{C} = 0 \tag{5.1}$$

where the vector $\mathbf{U} = (\rho_g, Y_{F,g}, u_g, p, \alpha_l, \breve{u}_p, \delta q_p^2, T_p, n_p)^t$ stands for primitive variables. The vector $\mathbf{C}$ corresponds to source/coupling terms and is not detailed here. The eigenvalues λ_i of the matrix $\mathbf{A}$ being all real values and the eigenvectors being all linearly independent, the system is hyperbolic. It is then possible to find the so-called characteristic normal form of Equation (5.1), where each characteristic wave is associated to a characteristic speed λ_i. The eigenvalues λ_i of the 9×9 matrix $\mathbf{A}$ are:

$$\lambda_1 = u_g - c_g \tag{5.2}$$
$$\lambda_2 = u_g + c_g \tag{5.3}$$
$$\lambda_3 = \lambda_4 = u_g \tag{5.4}$$
$$\lambda_5 = \breve{u}_p - c_l \tag{5.5}$$
$$\lambda_6 = \breve{u}_p + c_l \tag{5.6}$$
$$\lambda_7 = \lambda_8 = \lambda_9 = \breve{u}_p \tag{5.7}$$

where $c_g^2 = \gamma_g p/\rho_g$ corresponds to the celerity of sound waves in the gaseous flow and c_l is linked to the RUE by $c_l^2 = 6\delta q_p^2$.

Like in a purely gaseous flow, λ_1 and λ_2 correspond to the wave speeds of a sound source advected by mean flow which is propagating upstream and downstream respectively. The eigenvalues $\lambda_3 = \lambda_4 = u_g$ indicate that entropy waves are convected by the mean flow [224, 225]. In the dispersed phase, information is essentially transmitted by the flow at the local flow velocity $\lambda_7 = \lambda_8 = \lambda_9 = \breve{u}_p$. The presence of such convective waves has been documented in [193]. But as described by Kaufmann [206], the RUE modifies the propagation of information in the dispersed phase by introducing two different wave velocities, λ_5 and λ_6, which differ from the velocity of liquid particles $\breve{u}_p$ by $\pm\, c_l$. In [206], the origin of c_l is attributed to the quasi-Brownian motion of the particles. Physically, this means that if at the mesoscopic level droplets feature some kinetic energy dispersion around their mean values, hence the information they carry propagates at different speeds.

Let $\mathbf{S_i}$ designate the left eigenvectors of the matrix $\mathbf{A}$, Equation 5.1 may be rewritten as:

$$\frac{\partial A_i}{\partial t} + \lambda_i \frac{\partial A_i}{\partial x} = -\mathbf{S_i C} \tag{5.8}$$

where the characteristic wave amplitude A_i is deduced by solving:

$$\mathrm{d}A_i = \mathbf{S_i}\mathrm{d}\mathbf{U} \tag{5.9}$$

along the characteristic lines $x + \lambda_i t = c$, where c is a constant. The variation of A_i is equal to the source/coupling $-\mathbf{S_i C}$ integrated along the path. If $-\mathbf{S_i C}$ vanishes, then A_i becomes a Riemann invariant, i.e. the wave amplitude remains unaltered along the characteristic line [121]. Consequently, any modification of the characteristic wave speeds by the RUE alters the evolution of the wave amplitudes propagating in the two phase flow.

To illustrate how deep the acoustic response of a gaseous flow with a dispersed phase is impacted by RUE, the Euler-Euler model is compared to an Euler-Lagrange simulation in which the dispersion of the particle velocities at the mesoscopic level is intrinsically taken into account in the Lagrangian model.

5.3. Numerical simulations

Lagrangian-Eulerian and Eulerian-Eulerian simulations are conducted on the same computational domain and for the same flow conditions as in Section 3.2.2. To introduce an initial particle velocity dispersion in Eulerian-Lagrangian simulations, droplets are injected with a velocity $u_p(0)$ following a continuous random uniform PDF on the interval $[\breve{u}_p(0)\,(1-a)\,, \breve{u}_p(0)\,(1+a)]$, where the control parameter is selected within $a \in [0,1]$ as illustrated in Figure 5.2. Hence, in Eulerian-Eulerian simulations, the equivalent initial RUE of the liquid phase injected at the inlet is $\delta q_p^2(0) = (a\breve{u}_p(0))^2/3$ and can be monitored by changing the value of the control parameter a.

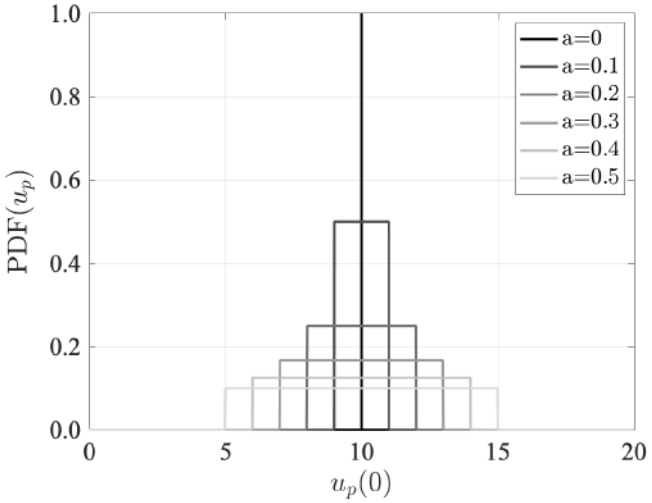

Figure 5.2. – Influence of the parameter a on the initial PDF used for the initial particle injection velocity $u_p(0)$ in the Euler-Lagrange simulation.

5.4. Analysis of the effect of velocity dispersion

One now looks into how the particle velocity dispersion of the liquid particles alters the previous results. Due to velocity dispersion in the liquid phase at the mesoscopic scale, the results obtained are noisy and require a filtering procedure. It is executed here by applying a 6^{th}-order Butterworth

bandpass filter on spatial series recorded at each instant. To avoid a filtering bias on the analysis of the results, the same filter is applied to results of both the Euler-Euler and Euler-Lagrange simulations.

Figure 5.3 compares the results obtained with Euler-Euler simulations and Euler-Lagrange simulations for different values of the parameter a, i.e. the initial value of RUE. Only one snapshot of the fluctuating pattern at some instant is shown in each plot for $a = 0$, 0.1, 0.2 and 0.3. Results from Euler-Euler simulations still match well the ones obtained from the Euler-Lagrange computation for $a = 0.1$. For higher values, differences between the two simulations appear.

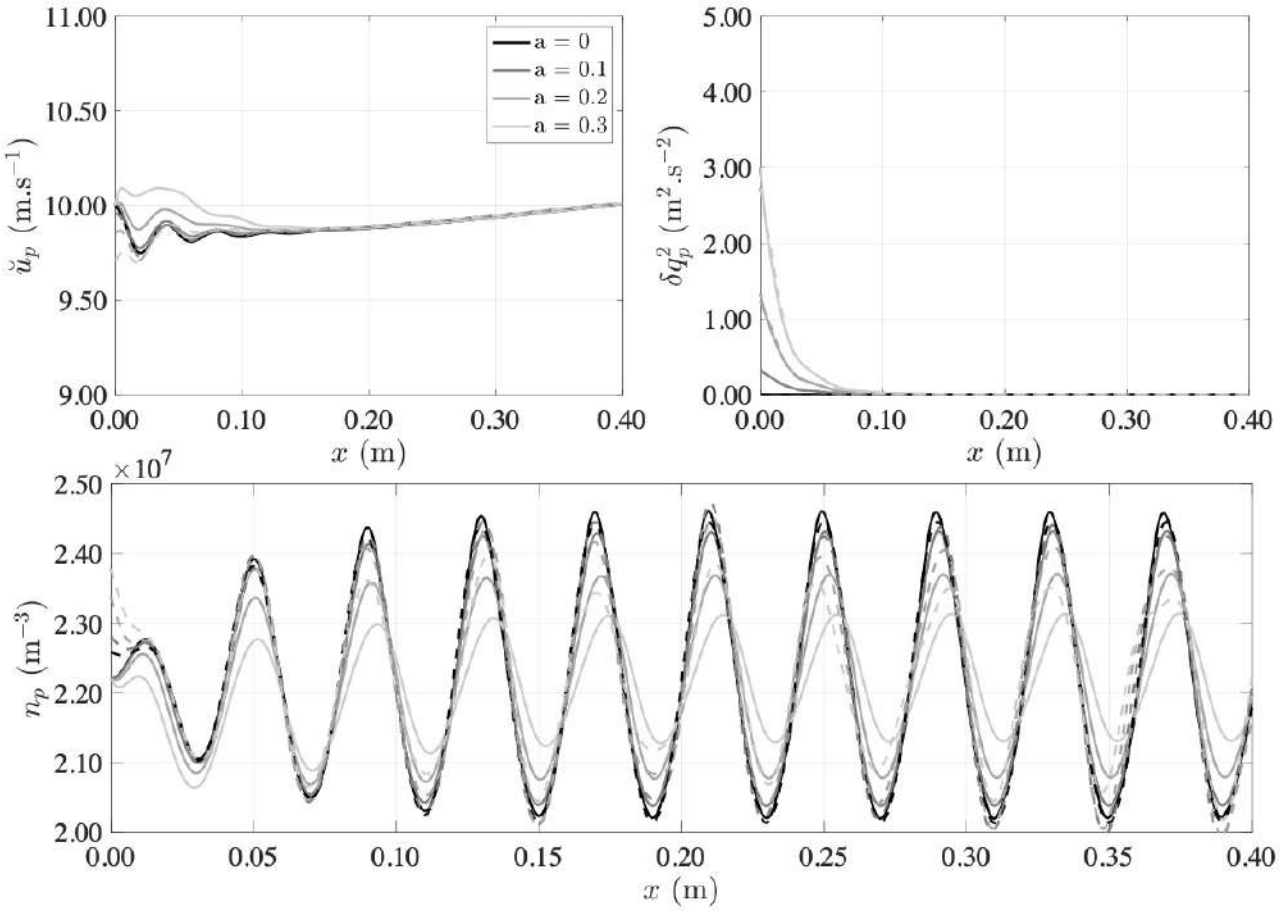

Figure 5.3. – Mass weighted averaged particle velocity $\breve{u}_p$ (top-left), RUE δq_p^2 (top-right) and particle number density n_p (bottom) evolution for $d_p = 50$ μm, $\breve{u}_p(0) = 10$ m/s, $\overline{u}_g = 10$ m/s, $u' = 1$ m/s and $f = 250$ Hz and different initial RUE $\delta q_p^2(0)$ piloted by the value of the control parameter a. Solid lines represent numerical results from Euler-Euler simulations and dashed lines represent Euler-Lagrange AVBP simulations.

The origin of these differences was found to be caused by the AVBP flow solver due to a small fluctuating component of the mean particle injection velocity when an initial dispersion velocity is introduced. This is why $\breve{u}_p(0)$ is oscillating around a mean value which is slightly below 10 m/s in the Euler-Lagrange model while in reality it should remained fixed to 10 m/s. This small deviation leads to higher amplitudes for the particle number density waves n_p compared to Euler-Euler model. Li et al. [193] have shown that the amplitude of the number density n_p waves is very sensitive to the initial relative velocity of the particle with respect to the gas flow velocity. This is why the phase and amplitude of the droplet number density wave are not uniform in Euler-Lagrange simulations compared to Euler-Euler simulations. This irregularity makes a quantitative comparison delicate

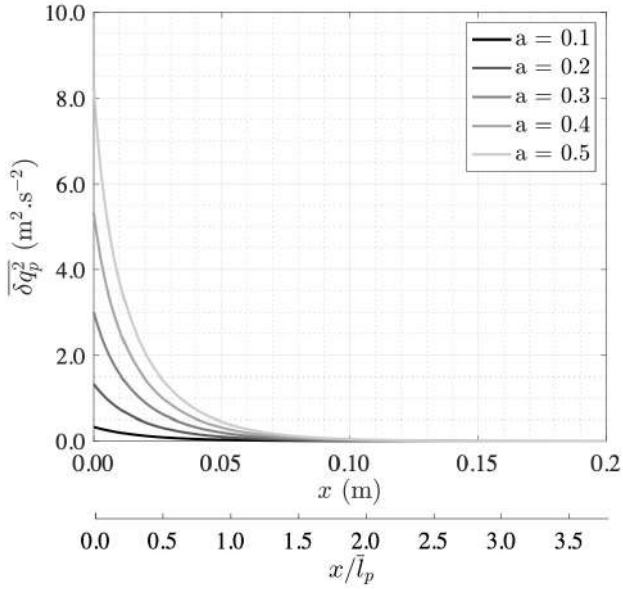

Figure 5.4. – Evolution of the time averaged RUE $\overline{\delta q_p^2}$ along the abscissa x and the abscissa normalized by the mean particle relaxation length $\bar{l}_p$ for $d_p = 50$ μm, $\breve{u}_p(0) = 10$ m/s, $\overline{u}_g = 10$ m/s, $u'_g = 1$ m/s and $f = 250$ Hz and different initial RUE $\delta q_p^2(0)$ piloted by the value of the control parameter a.

between number density waves n_p from the Euler-Lagrange and the Euler-Euler simulations when the RUE differs from 0, $a \neq 0$.

However, the shape of the velocity profiles $\breve{u}_p$ for the two simulations are consistent on the top left graph in Figure 5.3. Furthermore, increasing the RUE has qualitatively the same effect in both simulations. As the gas stream is laminar, the initial RUE decays with the distance to the spray injection as shown on the top right graph in Figure 5.3. The bottom plot shows how the initial RUE level, controlled by the value taken by the parameter a, leads to a modification of the amplitude and the phase of the droplet number density waves as they are convected downstream. The amplitude of these waves is attenuated and they are slightly shifted as a increases. These differences are further investigated in the following sections with the Euler-Euler model.

5.4.1. Amplitude reduction and phase lag

Figure 5.4 shows a zoomed region of the numerical domain where the evolution of the RUE δq_p^2 averaged over time is plotted for increasing values of the initial value of RUE $\delta q_p^2(0)$ by varying a from 0 to 0.5. Time average is carried out over 160 instants covering a duration correspond to 10 periods of the forcing frequency. As the gas stream is free of turbulence, the initial RUE conferred to the liquid particles decays with the distance to the injection point. The decay of the RUE spreads over the same length scale of about 110 mm for the different initial values of the RUE $\delta q_p^2(0)$. This distance to the injector outlet corresponds to a location where the phase lag and the amplitude of the oscillations observed in Figure 5.3 do not evolve anymore. Equation (3.27) indicates that this length scale is correlated to the mean particle relaxation length $\bar{l}_p = \overline{\breve{\tau}}_p \overline{\breve{u}}_p \approx 52.7$ mm, where $\overline{\breve{u}}_p = 10$ m/s is the time averaged particle velocity.

Results in Figure 5.4 plotted as a function of $x/\bar{l}_p$ confirm that the impact of RUE on the number particle density waves created by the acoustic forcing is significant until $3\bar{l}_p/2$. By matching the data,

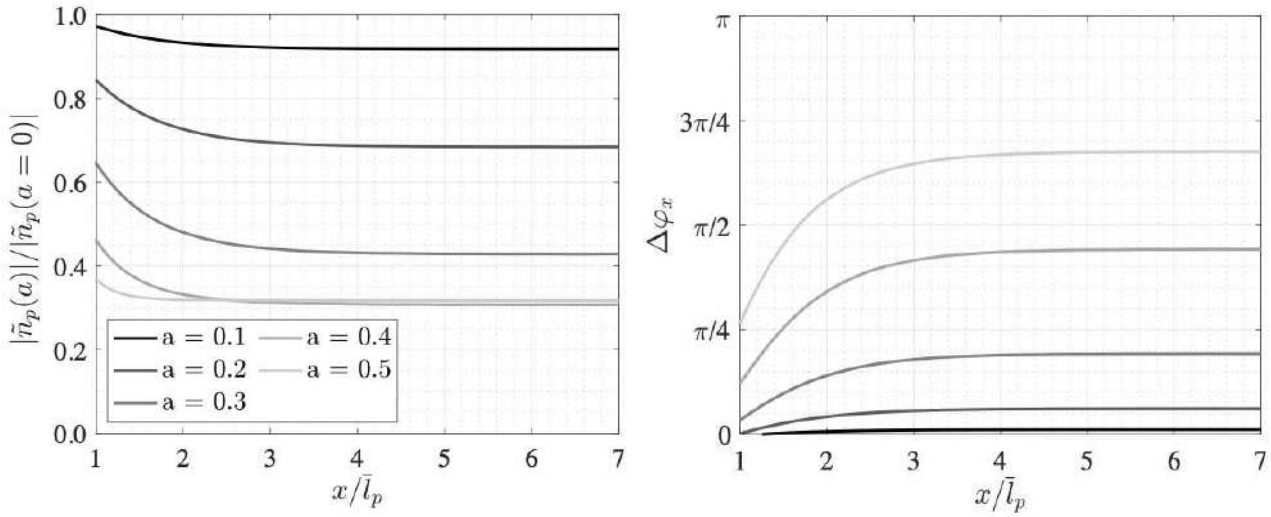

Figure 5.5. – Evolution of the amplitude ratio $|\tilde{n}_p(a)|/|\tilde{n}_p(a=0)|$ (top) and spatial phase lag $\Delta\varphi_x$ (bottom) along the normalized abscissa $x/\bar{l}_p$ for $\breve{u}_p(0) = 10$ m/s, $\overline{u}_g = 10$ m/s, $u'_g = 1$ m/s and $f = 250$ Hz and different initial RUE $\delta q_p^2(0)$ piloted by the value of the control parameter a.

it has been found that the RUE follows an exponential decay law:

$$\frac{\delta q_{p,x}^2}{\delta q_p^2(0)} = \exp\left(-\frac{x}{\bar{l}_p/2}\right) \tag{5.10}$$

This function is less than 3% its initial value downstream $x \geq 3l_p/2$. To confirm this observation, the amplitude ratio $|\tilde{n}_p(a)|/|\tilde{n}_p(a=0)|$ and the phase lag $\Delta\varphi_x$ along $x/\bar{l}_p$ are determined as follows:

$$\frac{|\tilde{n}_p(a)|}{|\tilde{n}_p(a=0)|} = \left(\frac{\mathrm{PSD}[n_p(a)](f)}{\mathrm{PSD}[n_p(a=0)](f)}\right)^{1/2} \tag{5.11}$$

$$\Delta\varphi_x = \arg\left(\mathrm{CPSD}[n_p(a), n_p(a=0)](f)\right) \tag{5.12}$$

where $\mathrm{PSD}[x](f)$ is the PSD of the time series $x(t)$ evaluated at the excitation frequency f, $\mathrm{CPSD}[x,y](f)$ is the CPSD of the time series $x(t)$ and $y(t)$ evaluated at the excitation frequency f and $n_p(a)$ is the particle number density for the parameter a.

Results are shown in Figure 5.5. The amplitude ratio $|\tilde{n}_p(a)|/|\tilde{n}_p(a=0)|$ and the spatial phase lag $\Delta\varphi_x$ between the droplet number density waves obtained for different initial RUE levels $\delta q_p^2(0)$ respectively decreases and increases from $x/\bar{l}_p = 1$ to $x/\bar{l}_p = 3$ until they reach a quasi-constant value with small oscillations at the wavelength $\lambda_c = \breve{\overline{u}}_p/f$ of the convected density waves. This corroborates the previous observations previously made on the RUE effects and the length scale over which the flow is modified by the RUE.

Hence, the impact of RUE on droplet number density waves increases when $\bar{l}_p$ is longer than the convective wavelength $\lambda_c = \overline{u}_p/f$. The ratio $\bar{l}_p/\lambda_c$ corresponds to the Stokes number $St = \omega\overline{\tau}_p = \bar{l}_p/\lambda_c$. Consequently, the Stokes number St gives an indication acoustic coupling between the particle velocity and the flow fluctuations, but also on the influence of RUE on the spray dynamics. If $St \gg 1$, the influence of RUE δq_p^2 on the convected droplet number density wave is significant, but the acoustic coupling remains weak. Conversely if $St \ll 1$, acoustic coupling between the gas and liquid streams

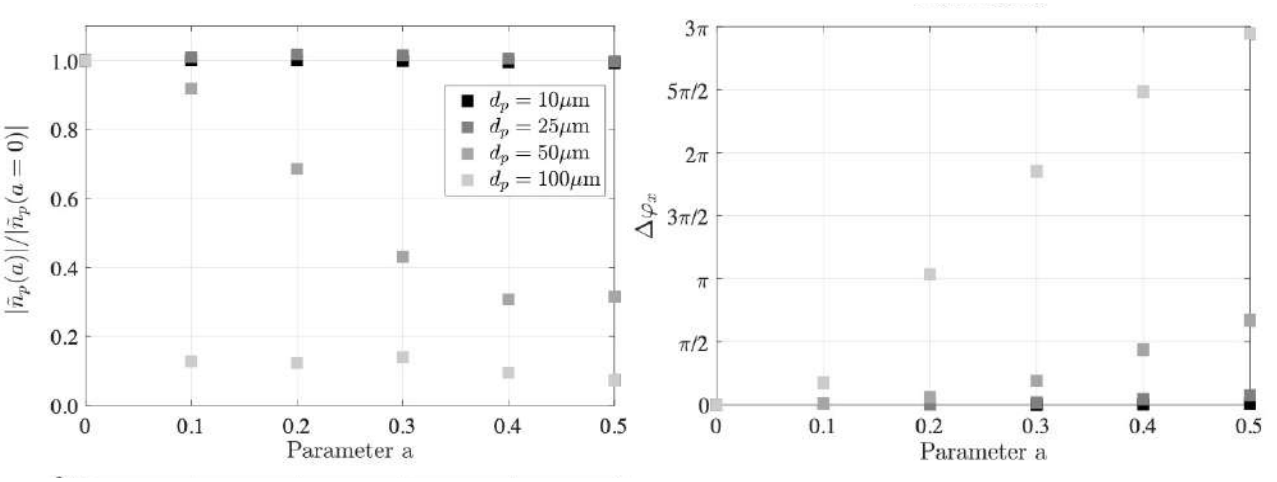

Figure 5.6. – Evolution of the amplitude ratio $|\tilde{n}_p(a)|/|\tilde{n}_p(a=0)|$ (top) and the spatial phase lag $\Delta\varphi_x$ (bottom) at the end of the domain according to the control parameter a for $\breve{u}_p(0) = 10$ m/s, $\overline{u}_g = 10$ m/s, $u'_g = 1$ m/s and $f = 250$ Hz for particle diameters $d_p = 10$, 25, 50, and 100 μm

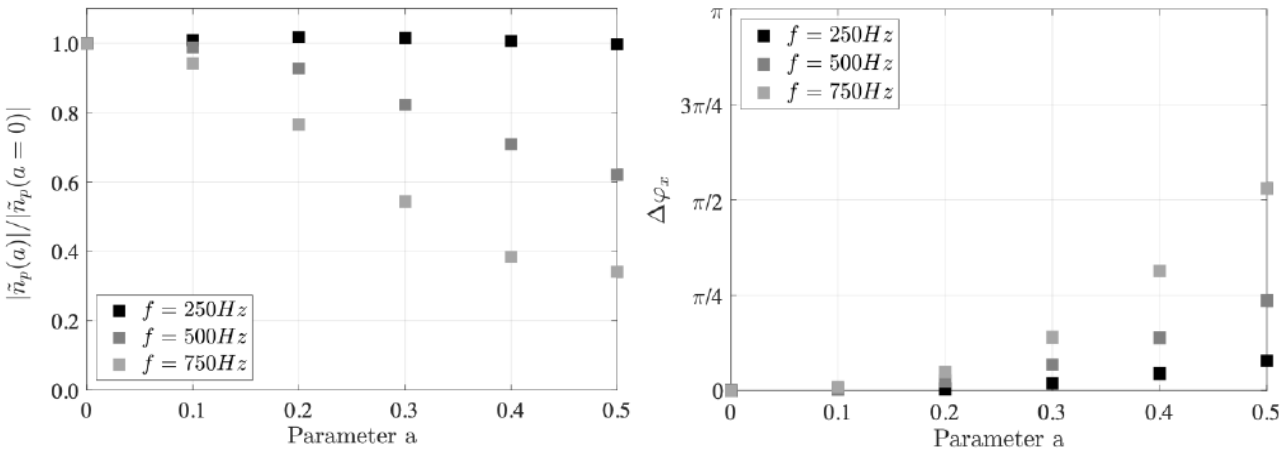

Figure 5.7. – Evolution of the amplitude ratio $|\tilde{n}_p(a)|/|\tilde{n}_p(a=0)|$ (top) and the spatial phase lag $\Delta\varphi_x$ (bottom) at the end of the domain according to the control parameter a for $\breve{u}_p(0) = 10$ m/s, $d_p = 25$ μm, $\overline{u}_g = 10$ m/s, $u'_g = 1$ m/s and for the excitation frequency $f = 250$, 500 and 750 Hz.

is strong, but the impact of RUE on the droplet number density waves that are created weakens.

The influence of the particle diameter d_p on the amplitude ratio $|\tilde{n}_p(a)|/|\tilde{n}_p(a=0)|$ and the spatial phase lag $\Delta\varphi_x$ from the droplet number density waves at the outlet of the computational domain are explored in Figure 5.6 for an excitation frequency $f = 250$ Hz. For $d_p = 10$ μm and $d_p = 25$ μm, the RUE barely changes the amplitude and the phase of the droplet number density waves. For $d_p = 50$ μm and $d_p = 100$ μm, a reduction of the amplitude and an increase of the phase shift of the density waves are observed when the initial RUE level increases. Saturation is also observed when $a = 0.4$ for $d_p = 50$ μm and when $a = 0.1$ for $d_p = 100$ μm.

The same analysis is repeated by examining the impact of the excitation frequency f for a fixed particle diameter $d_p = 25$ μm in Figure 5.7. For an excitation at $f = 250$ Hz, the RUE has a weak influence on the amplitude and the phase of the droplet number density waves. If the forcing frequency

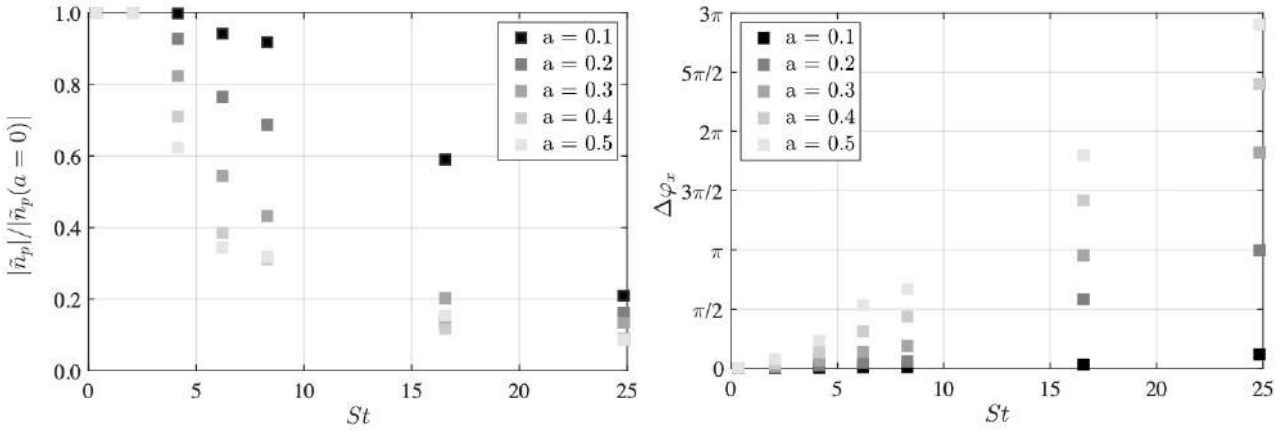

Figure 5.8. – Evolution of the amplitude ratio $|\tilde{n}_p(a)|/|\tilde{n}_p(a=0)|$ (top) and the spatial phase lag $\Delta\varphi_x$ (bottom) at the end of the domain as a function of the Stokes number St for $\breve{u}_p(0) = 10$ m/s, $\overline{u}_g = 10$ m/s, $u'_g = 1$ m/s and for different initial RUE levels $\delta q_p^2(0)$ governed by the value of the control parameter a. The (f,d_p) pair values associated to the Stokes number St simulated are presented in Tab. 5.1.

is increased to $f = 500$ Hz and $f = 750$ Hz, a strong reduction of the amplitude and an increasing phase shift of the density waves are noticeable with the value of the initial RUE $\delta q_p^2(0)$ level. Again, for high values of the RUE, saturation takes place for $a = 0.5$ at $f = 750$ Hz.

Table 5.1. – Cases simulated to draw Figure 5.8.

Excitation frequency f (Hz)	Particle diameter d_p (μm)	Stokes Number St
250	10	0.331
250	25	2.07
500	25	4.14
750	25	6.21
250	50	8.28
500	50	16.6
750	50	24.8

The trends observed in Figures 5.6 and 5.7 may be analyzed by examining the results in Figure 5.8 as a function of the Stokes number St that increases with the square of particle diameter d_p and the excitation frequency f. The (f,d_p) pair values associated to the Stokes number St are indicated in Table 5.1.

For $St < 5$, the RUE barely alters the number particle density waves because the mean particle relaxation length $\bar{l}_p$ is too small compared to the convective wavelength λ_c to modify the amplitude and the phase of these waves. For $5 < St < 25$, the RUE reduces the amplitude of the waves while it increases the phase shift. This alteration increases with St and a i.e the initial RUE $\delta q_p^2(0)$ level but the magnitude ratio saturates for $a = 0.4$.

Hence, for increasing Stokes numbers, the effect of the RUE expands even if the response of the particle velocity to the acoustic excitation from the surrounding gas remains weak. Conversely, effects of RUE are negligible for Stokes Number $St \leq 5$ when the particle velocity well responds to the acoustic excitation.

5.4.2. Spatial spectral analysis

The analysis of the characteristics of the hyperbolic system Equation (5.1) reveals that as soon as the RUE δq_p^2 differs from zero, two additional characteristic waves with velocities, $\breve{u}_p - c_l$ and $\breve{u}_p - c_l$, where $c_l^2 = 6\delta q_p^2$ appear. Since δq_p^2 decreases with the distance to the spray injection (see Figure 5.4), these wave velocities reach after a certain distance the convective velocity $\breve{u}_p$.

To verify the existence of such waves, a spray with large particle diameter $d_p = 100$ μm is submitted to an acoustic modulation at $f = 750$ Hz. The relaxation length is in this case $\bar{l}_p = 210$ mm and the convective wave number $k_c = \omega/\breve{u}_p = 471$ m^{-1}, corresponding to a large value of the Stokes number $St \approx 100$. A Short-Space Fourier Transform (SSFT) is performed on the numerical data for the number particle density $n_p(x, t_0)$ at each instant t_0 recorded in the simulation. Each series includes 1001 data over the numerical domain. The SSFT is made over windows of 200 points with a Hanning filter and with an overlap of 100 points between each window. The SSFT obtained at each instant t_0 is then averaged over the 160 computed instants from the simulation.

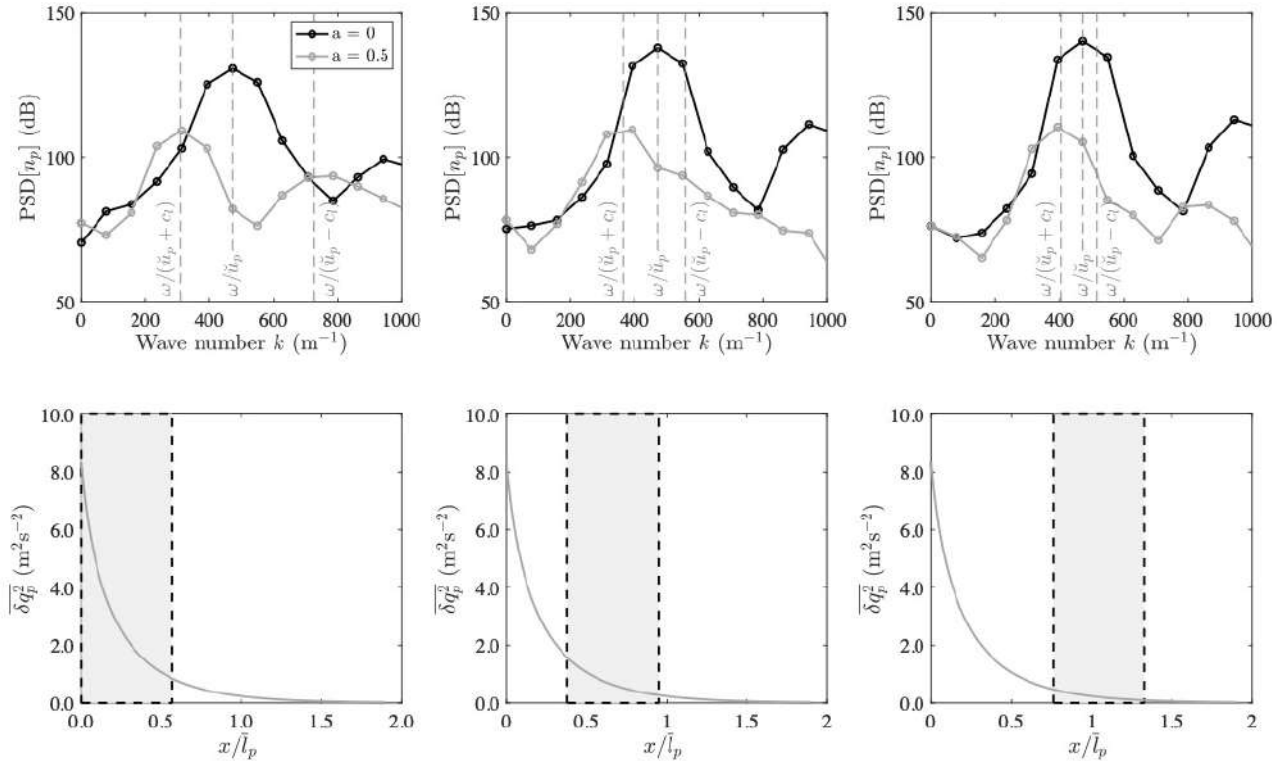

Figure 5.9. – Magnitude of the SSFT of the particle number density n_p signals (top) calculated for the data segment (grey zone) indicated on the evolution of the time averaged RUE $\overline{\delta q_p^2}$ (bottom) for $a = 0$ and $a = 0.5$. Dotted grey lines indicate the abscissa corresponding to the theoretical wave velocities (from left to right) $\breve{u}_p + c_l$, $\breve{u}_p$, $\breve{u}_p - c_l$, computed with values of RUE δq_p^2 evaluated at the middle of the data segments.

Results of this post-processing are shown in Figure 5.9 for two initial levels of RUE, $a = 0$ and $a = 0.5$. Without RUE, $a = 0$, only one peak emerges in the spectra shown in black on the top plots with a wave speed $\breve{u}_p$. When the initial RUE is set to $a = 0.5$, results depend on the selected window. On the left plots, close to the spray injection point, when the RUE is still high for $a = 0.5$, the characteristic wave with velocity $\breve{u}_p + c_l$ clearly emerges, followed by the one with velocity $\breve{u}_p - c_l$. It is more difficult to identify the characteristic wave featuring a velocity $\breve{u}_p$. One also clearly sees that the characteristic wave with velocity $\breve{u}_p$ in black for $a = 0$ has a much higher magnitude than the

waves in grey determined for $a = 0.5$.

In the middle plots, the interrogation window is sliding a bit further away from the spray nozzle. It is more difficult to make clear conclusion, but the waves identified in the left plots seem to merge. The right plots show results for a window located in a region where the RUE vanishes. The spectra in black and grey on the top plot are closer except that their magnitude differs. The characteristic waves tend toward the same velocity and merge giving a unique wave with velocity $\breve{u}_p$. The signal with $a = 0.5$ has a smaller magnitude than the one with $a = 0$. The reduction of the amplitude of the number density waves for $a = 0.5$ hence can be explained by a redistribution of energy among the three different characteristic waves. For $a = 0$, all the energy lies on the unique characteristic wave present in the system. Being dominant during this transient regiment, the characteristic wave with velocity $\breve{u}_p + c_l$ leads to a phase advance of the particle number density wave. This explains the sign and increase of the phase shift $\Delta\varphi_x$ observed in Figure 5.5.

5.5. Conclusion

While an analysis of the response of an isolated fuel particle submitted to acoustic forcing showed that it only depends on a Stokes number $St = \omega\tau_p$, simulations of the dynamics of a spray revealed a more complex dynamics.

Two different types of simulations were carried out by considering an Euler-Lagrange description and an Euler-Euler description of the two phase flow dynamics. The same observations were made in both simulations. The Euler-Euler description has then been used to interpret the results in an attempt to model the observed features.

The Euler-Euler description includes the dynamic effect of the velocity dispersion of the droplet particles by considering a transport equation for their uncorrelated kinetic energy δq_p^2 named RUE. Determination of the characteristic waves of the hyperbolic system of equations of the Euler-Euler model revealed that the RUE leads to a split of the way information is transmitted by the dispersed phase, adding, to the preexisting wave speed $\breve{u}_p$, two different wave speeds, $\breve{u}_p - c_l$ and $\breve{u}_p + c_l$, for the characteristics propagating in the domain.

In absence of RUE, it was shown that acoustic disturbances lead to velocity particle disturbances that are convected at the mean particle speed close to the spray injector outlet and are damped further away. Away from the spray injector, only acoustic disturbances of the spray particle velocity persist. The small perturbations of the spray velocity close to the spray injector lead however to strong disturbances of the droplet number particle density which grow with the distance to the spray injector before saturating. These disturbances are convected at the mean particle speed.

The way the initial RUE level modifies this dynamics has then been documented. RUE reduces the amplitude of the droplet number density waves while it advances their phase over length scale equal to $3\bar{l}_p$, where $\bar{l}_p = \overline{\tau}_p\breve{\overline{u}}_p$ is the mean particle relaxation length. The impact of RUE increases with the excitation frequency f_a and particle diameter d_p. It has been shown that the impact of RUE can be analyzed by considering the Stokes number St. The impact of RUE on the spray dynamics increases with St, while the impact of acoustic reduces at large St.

A spatial spectral analysis of the number particle density n_p signals confirmed the existence of the different wave velocities due to the presence of RUE δq_p^2. The reduction of the magnitude of the oscillation of the number density waves n_p can be attributed to an energy transfer over different characteristic waves when the RUE level increases. All the energy is conveyed at the mean particle

velocity in absence of RUE. The predominance of the characteristic wave with velocity $\breve{u}_p + c_l$ over the region with significant RUE explains the phase advance observed in the droplet number density wave signals.

In this analysis the gas stream was considered laminar, one dimensional and uniform. Further interactions need to be considered for fuel sprays in a turbulent flow field to fully interpret their response to acoustic excitation. This is left for further studies.

Chapter 6

Experimental and numerical investigations of the hollow-cone spray response to acoustic perturbations

La reddition sans condition de la méthode scientifique nous a rendus incapables de lire le mythe [...] Rabaissé au rang de trouvaille magique, ou simplement d'expression d'une certaine ignorance, il est combattu au nom de l'éclat pur de la vérité, qui a clignoté pour la première fois au cours de la mutation des Lumières. Mais seules les civilisations capables de reconnaître la production du mythe, en le faisant tourner autour du travail d'interprétation de la science, peuvent lire correctement leur propre destin.

– Alessandro Barrico, *Ce que nous cherchons, 2021*

Hollow-spray cone is widely used for the fuel pilot injection in many aerojet engines. Representing the spray injection in a numerical flow simulation is one of the most difficult task. The most advanced models consider a distribution of droplets and velocities at the injector location in numerical flow simulations. While this approach gives satisfactory results for steady injection, these models have not been evaluated when the spray is submitted to acoustic disturbances. In this chapter, the response of a hollow cone spray to acoustic disturbances is investigated numerically and experimentally. The validity of the FIM-UR model developed by CERFACS is examined by comparing Euler-Lagrange simulation with PDPA measurements. It is shown that the FIM-UR model enables to accurately reproduce the spray flow interaction in the steady flows but large differences appear for the pulsated flow. The structure of the spray, and specifically the response of the injection angle are compared with the experiments

Overview

6.1. Introduction

Accurate prediction of thermoacoustic instabilities during the design phase of an aerojet engines becomes critical for aeronautical gas turbines operating at lean conditions with low NOx emissions [27, 47]. While analytical and low-order models aim at analyzing a stability analysis of the combustor at very reduced cosst, they often require parameters which have to be obtained experimentally or numerically [49, 50, 64, 130, 131]. In addition to determine the stability of an engine at an operating point, Large Eddy Simulations (LES) constitute a powerful tool providing valuable information about the physics underlying the combustion instabilities which is often difficult to infer from experiments [52, 226]. LES have shown to be able to successfully compute swirled spray flames in gas turbines [29, 198, 227–229] and even to reproduce self-excited oscillations [114, 200, 230].

When studying the interaction between the acoustic field and spray flames, supplementary complexities arise due to the multi-phase nature of the flow investigated. It has been shown that external acoustic forcing can alter the dispersed flow dynamics by modifying the atomization process [111], the droplet evaporation rate [93, 116, 182] but also the transport of the dispersed phase in the gas flow resulting in the apparition of droplet number density waves with convected droplet clusters [101, 102, 110, 183, 184, 187, 188, 192, 193]. Modification of the spray dynamics by acoustic disturbances has been identified as being one of the main mechanisms leading to the triggering of thermo-acoustic instabilities in combustion chambers powered by liquid sprays [90, 101, 104, 112, 185, 200, 231, 232].

Hence, modelling the liquid phase dynamics is the crux of the matter when performing numerical simulations of a spray flame in an aeronautical combustion chamber. The governing equations depend on the large scale model description that is selected, namely: Eulerian-Lagrangian approach [233], Eulerian-Eulerian volumetric [209, 210] or mesoscopic formulation [215, 216, 221]. Furthermore, this effort of modelling swirling spray flames collides with an important number of complex and diverse phenomena occurring simultaneously at the droplet scale: atomization, droplet turbulence, internal recirculation, evaporation, combustion, particle-particle interactions, ... Many of these interactions can be neglected or described with simplified models when dealing with diluted flows and small spherical droplets [234, 235].

Still, modelling the spray atomization at the fuel injection remains one of the greatest challenges when performing spray flame simulations. Giving the initial diameter and velocity droplet distributions of the injected fuel, atomization has to be properly characterized in order to expect catching the interactions between the acoustic field and the spray, and hence the flame dynamics. Nonetheless, direct simulation of the atomization requires large computational resources [236–239]. Hence, in the dense regime, primary and secondary atomization physics modelling are often skipped in LES and traded to a simplified phenomenological model giving directly the resulting spray distribution characteristics in the dilute regime. In an aeronautical chamber, fuel is injected with a hollow cone spray pattern through an air blast and pressure-swirl (simplex) atomizer. Sanjose et al. [31] proposed a methodology, referred as FIM-UR (Fuel Injection Method by Upstream Reconstruction) to reconstruct the initial particle velocity profile injected by a simplex atomizer from its geometrical characteristics and the particle diameter distribution at the nozzle. Recently, the primary and secondary atomization from an air-blast atomizer were also modeled [240, 241].

The FIM-UR model has proved to be an efficient and versatile tool to compute swirling spray flames with good agreement with the experimental data for non-reacting and reacting sprays [31, 198, 200, 242, 243]. However, FIM-UR was designed for steady operation and has never been validated when the flow is acoustically excited. Yet, liquid differential pressure injection strongly affects the spray injection through the atomization process [97, 103, 110, 111] and the spray cone [22]. A periodic change of the air pressure at the nozzle outlet during the acoustic cycle leads to a periodic change of

the spray cone [110]. Lo Schiavo et al. [114] show that the value of the cone angle does not affect the flame anchoring point in stable regimes but, if it is poorly chosen in unstable regimes, the self-excited oscillations observed in experiments cannot be reproduced due to the proportion of fuel impinging on the injector lips being that is not well estimated. Furthermore, Su et al. [244] observed important variations of particle velocities and Sauter mean diameters during the acoustic forcing cycle of an aero-engine fuel injector.

The present study aims at evaluating the performance of the steady injection FIM-UR model to reproduce the velocity and diameter response from a hollow-cone spray injection to an acoustic excitation. Section 6.2 presents the experimental rig and the experimental protocol to perform phase-averaged velocity and diameter profiles. Section 6.3 describes the LES methodology for the two-phase simulations in steady and pulsed regimes. The FIM-UR model and the initialization of the spray in the computional domain are presented. Comparison between the experimental and numerical results are presented in Section 6.4 for the steady regime and for the pulsed regime in Section 6.5. The spray structure and the radial profiles of the axial velocities of the gaseous and disperse phases and the diameters of the liquid droplets are compared. Finally, differences observed between experiments and LES are discussed.

6.2. Experimental Setup

Measurements and simulations are performed on the swirled spray burner TALISMAN test-rig for the configuration $\mathscr{C}_{20}$ presented in Section 2.2.2 and reproduced in Figure 6.1. As detailed in Section 2.3.3.1, PDPA measurements are performed in the combustion chamber in order to obtain radial profiles of the gas and fuel particle velocities and radial profiles of the fuel particle diameters for the operating point $P = 7$ kW and $\Phi = 0.70$. To study the acoustic response of the spray to acoustic disturbances, acoustic forcing is generated upstream the combustion chamber with a loudspeaker connected to the bottom of the plenum through a convergent as presented in Section 2.3.2.2. In this study, the air velocity fluctuation frequency and relative amplitude are set to $f = 200$ Hz and $u'_{z,3}/\overline{u}_{z,3} = 0.20$ at the combustion chamber backplane.

The synchronization process for the phase-averaging in pulsed flow is shown in Figure 6.2. PDPA measurements are triggered by the TTL signal v_{TTL} and recorded over 10s. The loudspeaker voltage signal v_{SP} and v_{TTL} are recorded over a longer duration, 15 s here. Hence, it is possible to determine the actual phase φ of the axial velocity fluctuation $u'_{z,3}$ corresponding to each Doppler burst measured by the PDPA. To do so, the phase lag $\Delta\varphi_{SP}$ is measured between the loudspeaker voltage v_{SP} and the axial velocity fluctuations $u'_{z,2}/\overline{u}_{z,2}$ at the section S_2 recorded by HW2. As shown in Figure 6.2, $\Delta\varphi_{SP} = -3\pi/2$ at $f = 200$ Hz and does not depend on the voltage V_{SP} applied to the loudspeaker. Assuming that v_{SP} and $u'_{z,3}$ can be written as

$$v_{SP} = V_{SP}\sin(2\pi f t + \varphi_0) \tag{6.1}$$

$$u'_{z,3} = |u'_{z,3}|\sin(\varphi(t)) \tag{6.2}$$

where φ_0 is the initial phase of v_{SP} at which PDPA measurements begin, φ is then determined as:

$$\varphi(t) = 2\pi f t + \varphi_0 - \Delta\varphi_{SP}(f) - \angle\mathscr{U}(f) \tag{6.3}$$

where $\angle\mathscr{U}$ is the phase lag between $u'_{z,3}$ and $u'_{z,2}$ which roughly equal to $\pi/10$ at $f = 200$ Hz. Further information about the measurement of $\mathscr{U}$ can be found in Section 7.4.1.

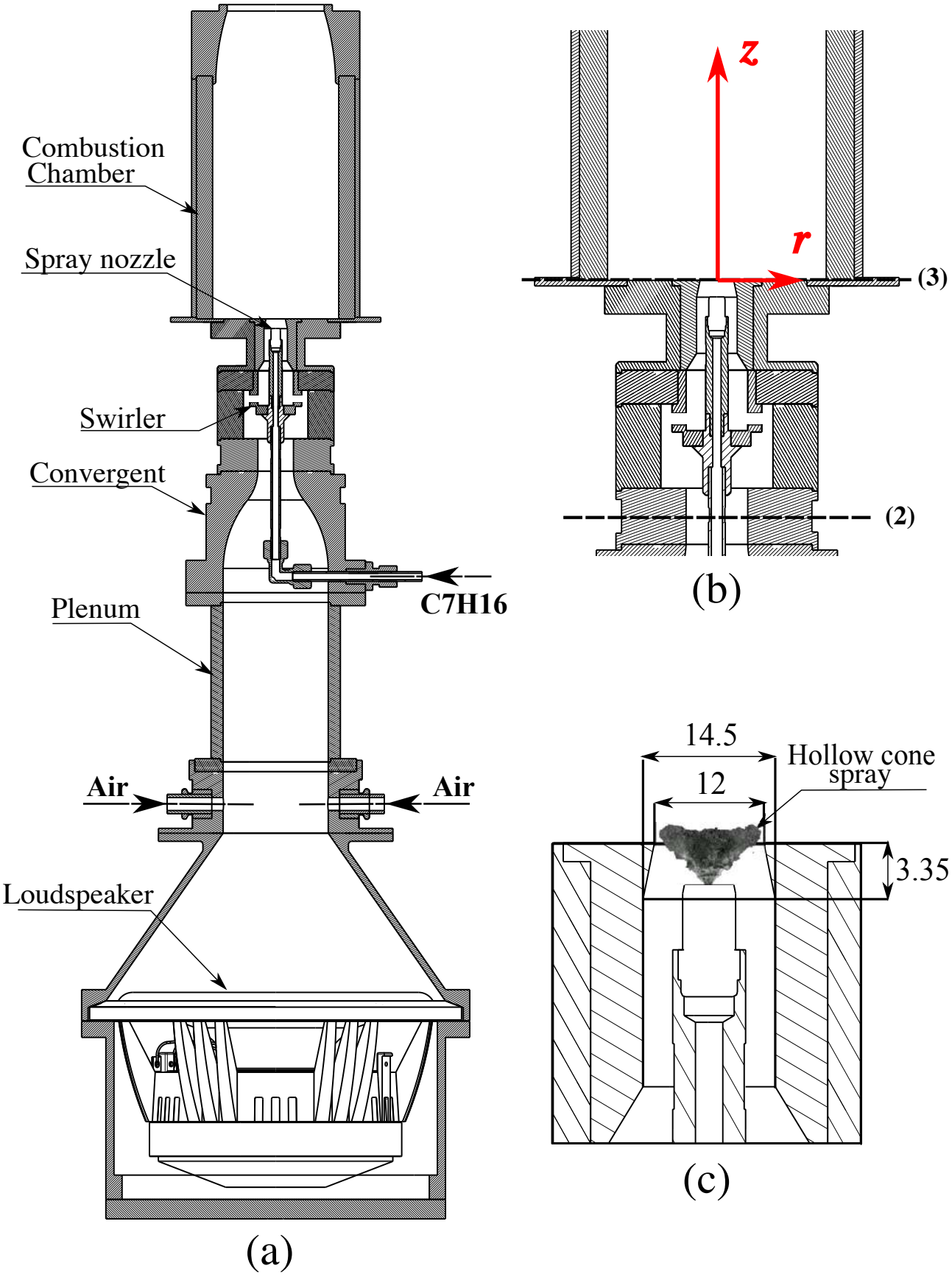

Figure 6.1. – (a) Sketch of TALISMAN experimental setup. (b) Zoom on the TALISMAN injector. Axis and sections used in the study are indicated. (c) Zoom on the spray injection zone. Dimensions are in mm.

When performing PDPA measurements, the data acquisition rate is not controlled by the user but dictated by how many particles cross the probed volume and with a validated Doppler burst. Hence, it is very unlikely to have an instant acquired by the PDPA where $\varphi(t) = \varphi_{PA}(k) = 2\pi k/N$ with $k \in [0, N-1]$. The phases φ_{PA} correspond to the phases of the flow excitation $u'_{z,3}$ over which phase average of the PDPA measurements is performed. Furthermore, to have a statistical convergence of the quantity measured, it is better to have a significant number of particles recorded by the PDPA. To overcome these two problems, PDPA data are retained over a phase windows $[\varphi_{PA}-\delta\varphi_{PA}, \varphi_{PA}+\delta\varphi_{PA}]$, where the width of the phase windows is set in these experiments to $\delta\varphi_{PA} = 5^o$. The choice of $\delta\varphi_{PA}$ slightly alters the measurement only for $\delta\varphi_{PA} \geq \pi/8$ for $N = 8$. More details about the influence of $\delta\varphi_{PA}$ on the phase-averaged results are presented in Appendix C.

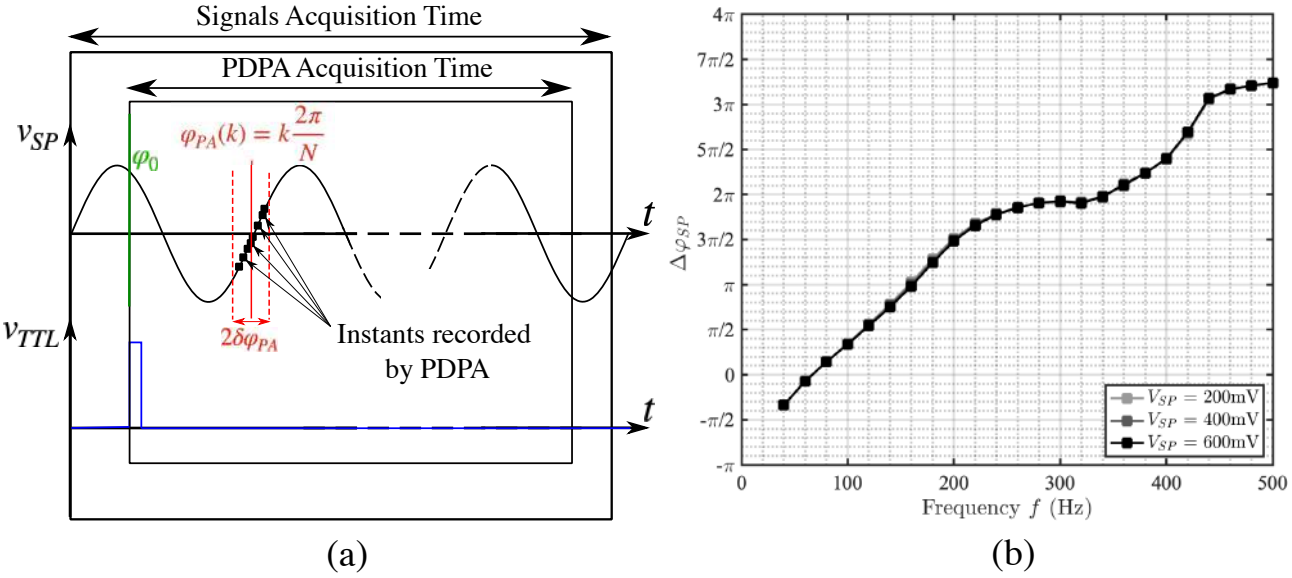

Figure 6.2. – (a) Illustration of the data synchronization procedure (b) Phase lag $\Delta\varphi_{SP}$ between the loudspeaker voltage V_{SP} and the axial velocity fluctuation $u'_{z,2}/\overline{u}_{z,2}$ at section S_2 ($e^{-i\omega t}$ convention).

Planar Mie scattering imaging is also carried out on the spray for the steady and pulsed regimes as described in Section 2.3.3.2. These images give insightful information about the spray structure inside the combustion chamber. Considering light scattering being constant over the range of particle studied, the light intensity I scattered by a group of particles in the volume observed by a pixel of the camera is proportional to the sum of the square particle diameter d_p^2 [169]. The volume of observation being the same for each pixel, it can be concluded that I is roughly proportional to the product $n_p d_{20}^2$ where n_p is the particle number density and d_{20}^2 the mean square diameter in the observed volume.

6.3. Numerical Setup

6.3.1. Initialization of the FIM-UR model

The numerical methodology and the computational domain used for this study were presented in Section 2.4. The input parameters of the FIM-UR model for the hollow-cone spray are set as follows: the fuel mass flow rate $\dot{m}_F$ is set to 0.157 g.s^{-1}, leading to a thermal power $P = 7$ kW assuming complete combustion. The nozzle manufacturer indicates that the diameter of the hole of the injector $R_0 = 100$ μm and the injector produces a spray with a half angle $\theta_s = 30^o$. However, as indicated in Figure 2.19, FIM-UR requires a particle diameter distribution $f_N(d_p)$ giving the fraction of particles

with the particle diameter d_p. To measure this distribution, burner parts occulting the optical access to the tip of the injector are removed. PDA measurements are performed on the spray in quiescent air (i.e $\dot{m}_F = 0$ kg.s^{-1}) as close as possible to the atomizer nozzle, here $z = -1.35$ mm. The axis (r, z) are indicated in Figure 6.1. Experimental results are given in Figure 6.3. They are used to feed the FIM-UR model.

Velocity and diameter profiles measured in Figure 6.3a confirm the hollow-cone structure of the spray with an inner recirculation zone between $r = -1$ mm and $r = 1$ mm. A slight asymmetry in the radial profiles can be noticed, probably caused by the thread of the injection tube or the atomizer nozzle being not perfectly straight mounted with respect to an horizontal probe. Figure 6.3 shows that the particle diameter distributions $f_{\mathrm{N}}(d_p)$ measured at different radius r are all single-peaked distributions but the peak location as well as its width and peak value differ along r. Hence, a Rosin-Rammler (RR) distribution is fitted to reproduce the distribution $f_{\mathrm{N}}(d_p)$ recorded with the PDA system [22, 245, 246]:

$$F_{\mathrm{RR}}(d_p) = 1 - \exp\left[-\left(\frac{d_p}{X}\right)^q\right] \tag{6.4}$$

$$f_{\mathrm{RR}}(d_p) = \frac{q}{X}\left(\frac{d_p}{X}\right)^{q-1} \exp\left[-\left(\frac{d_p}{X}\right)^q\right] \tag{6.5}$$

where $F_{\mathrm{RR}}(d_p)$ and $f_{\mathrm{RR}}(d_p)$ are the cumulative distribution and probability density functions respectively. The characteristic particle size X (μm) and the spread parameter q are both determined by minimizing the difference $|f_{\mathrm{N}}(d_p) - f_{\mathrm{RR}}(d_p)|$ with the method of least squares. Figure 6.3 shows that the RR distribution fits well the experimental distribution $f_{\mathrm{N}}(d_p)$ measured at the different radial positions r. The profiles of (X, q) estimated for each point measured in Figure 6.3a are given in Figure 6.3c. The parameter q remains constant along the injection radius, while X has a profile like d_{10}. Hence, the distribution law retained for $f_N(d_p)$ for the numerical spray injection is a RR distribution where the parameters (X, q) are chosen as the radial-averaged values of the profiles shown in Figure 6.3c. The resulting distribution $f_N(d_p)$ given in the FIMUR model is pictured in Figure 6.3d with $q = 2.76$ and $X = 15.4$ μm. Similar values for the parameters are obtained when fitting the RR law over all the PDPA measurements recorded over each real distance r at $z = -1.35$ mm.

6.3.2. Methodology for phase-averaging Euler-Lagrange results

When performing phase-averaging on numerical results from an Euler-Lagrange simulation, one faces the same difficulty as for the PDPA measurements mentioned in Section 6.2. In order to obtain the Eulerian field of the two-phase flow properties, it is necessary to interpolate the properties of the particles inside a cell to its nodes. However, two problems appear with this methodology. First, if there are few particles inside the surroundings cells of a node, the value obtained at this node is not statistically converged. Second, if there is no particle inside the surroundings cells of a node, an arbitrary value has to be attributed to the node but also a flag in order to discard this value from averaging. Hence, the average of the particle property y_p at the node location $\mathbf{x}$ and the instant t can be obtained with the following formula:

$$\overline{y}_p(\mathbf{x}, t) = \begin{cases} \displaystyle\sum_{t_i}^{t} \frac{y_p(\mathbf{x}, t_i)\chi(\mathbf{x}, t_i)}{\sum_{t_i}^{t} \chi(\mathbf{x}, t_i)} & \text{if } \displaystyle\sum_{t_i}^{t} \chi(\mathbf{x}, t_i) \neq 0 \\ \textbf{flag} & \text{else} \end{cases} \tag{6.6}$$

with

$$\chi(\mathbf{x}, t) = \begin{cases} 1 & \text{if } n_p(\mathbf{x}, t) \neq 0 \\ 0 & \text{else} \end{cases} \tag{6.7}$$

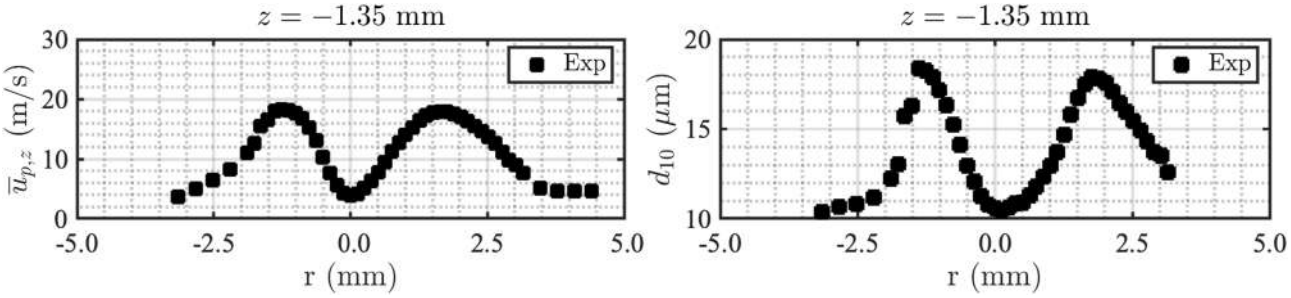

(a) Radial profiles of the (left) mean axial particle velocity $u_{p,z}$ and (right) mean diameter d_{10} recorded by PDPA carried out on the spray alone without gaseous flow at $z = -1.35$ mm.

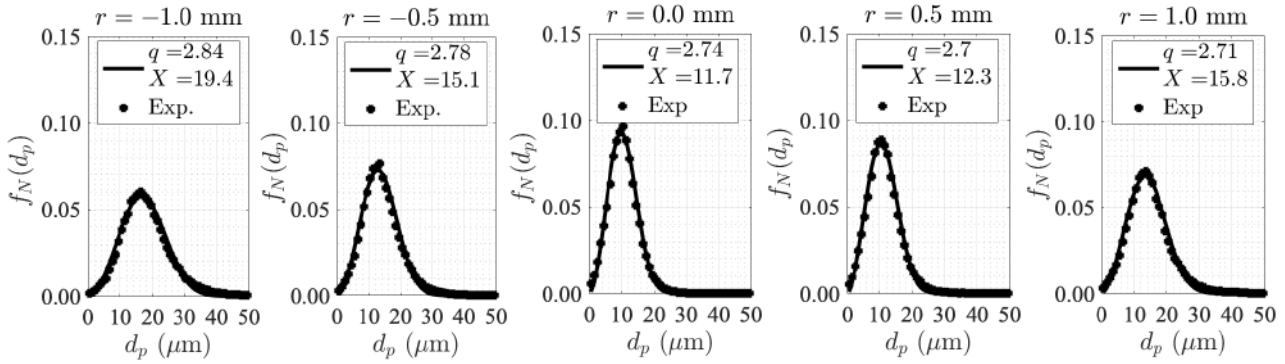

(b) Particle diameter distribution $f_{\mathrm{N}}(d_p)$ recorded for various radii r at $z = -1.35$ mm. Rosin-Rammler (RR) distributions are fitted on each of the experimental distributions with thin lines. The q and X parameters of the RR distributions are indicated on each graph.

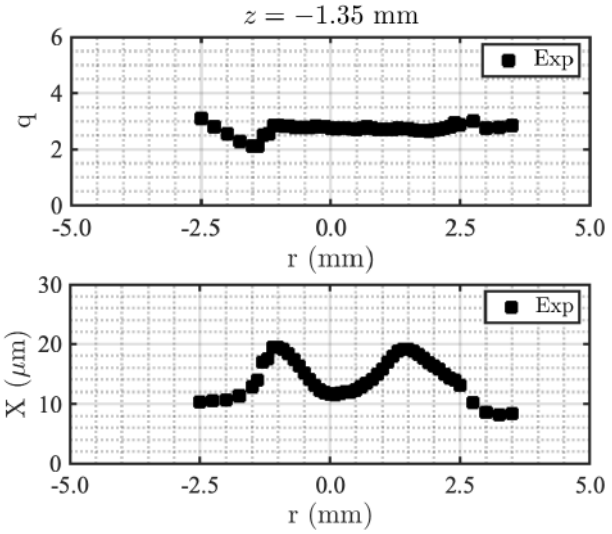

(c) Radial profiles of the q and X parameters of the RR distribution fitted to the experimental distributions at $z = -1.35$ mm

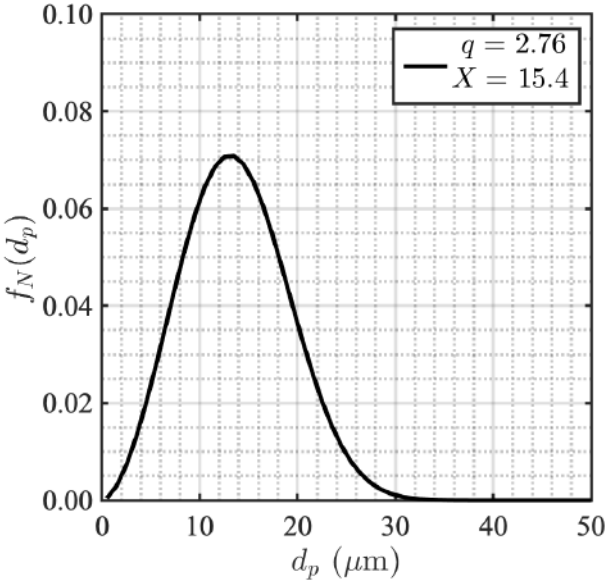

(d) Particle diameter distribution $f_{\mathrm{N}}(d_p)$ used as input for the FIM-UR model.

Figure 6.3. – (a)-(c) Experimental measurements of the spray characteristics without air flow at $z = -1.35$ mm used to fit the input distribution $f_{\mathrm{N}}(d_p)$ of the FIM-UR model shown in (d).

where t_i are the instants used for averaging and $\chi(\mathbf{x}, t)$ is the indicator function of the particle presence in the cells neighbouring the node at the location x.

In steady regime, it is possible to average over enough instantaneous solutions for a reasonable computational time in order to obtain field of $\overline{y}_p$ that is statistically converged. Nonetheless, for phase-averaging profiles in pulsed regimes, this computational time can be relatively high. It is here not possible to apply the same procedure as for the PDPA measurements, i.e., instead of saving an instantaneous solution at fixed phase φ_{PA} of the excitation, one saves the solution averaged on a phase windows $[\varphi_{PA} - \delta\varphi_{PA}, \varphi_{PA} + \delta\varphi_{PA}]$ to accelerate the convergence. This method is hardly conceivable because it would still require to save a large number of instantaneous solutions that leads to gigantic disk storage and large computational time dedicated to saving instead of computing solutions. Hence, another method is used here to accelerate the convergence of the particle properties. When the velocity and diameter profiles are axisymmetric, an alternative is to average along the azimuth angle the instantaneous solution saved at given phase φ_{PA} of the excitation. This latter method is performed in Section 6.5.

6.4. Results in steady regime

The velocity profiles measured with LDA are compared to numerical simulations obtained in steady regime. For each measurement volume, LDA data are recorded over approximately 10 s for a total number of oil particles counted $N_P = 50000$ while numerical simulations are averaged over 320 ms, corresponding to roughly 8 flow-through times. No differences were found when the solutions of the numerical simulations are angle-averaged or not. Angle averaged profiles are then shown in this section.

6.4.1. Gaseous phase

PDPA measurements are first realized on the gas flow without fuel spray. Radial mean and root-mean square axial velocity profiles of the gas flow, respectively $\overline{u}_z$ and $\overline{u}_z^{RMS}$, are shown in Figure 6.4 at three different heights: $z = 4$ mm, $z = 6$ mm and $z = 8$ mm. The velocity $\overline{u}_z$ and $\overline{u}_z^{RMS}$ profiles obtained numerically fit very closely those recorded experimentally, with only very slight differences in the inner shear layers (e.g. $|r| = 5$ mm). Hence, the geometry and the strength of the different recirculation zones of the swirling flow are well captured by LES as well as the turbulence velocity fluctuations. Mesh refinement does not improve the agreement between the LDA measurements and the LES results in steady regime. Nonetheless, while the pressure drop measured in experiments is about $\Delta P = 1920 \pm 25$ Pa, the pressure loss across the swirler predicted by LES for the COARSE and the FINE meshes are respectively $\Delta P = 2235$ Pa and $\Delta P = 2180$ Pa. A supplementary refinement would be then necessary to match closer to the experiments [247]. Linked to the injector impedance, the injection pressure loss modifies the dynamic response of a burner [248, 249] and then would have an influence on the results in the pulsed regime as shown later in the Section 6.5.

6.4.2. Fuel Spray

The fuel spray is now injected in the air flow in steady regime. At $z = 4$ mm, $z = 6$ mm and $z = 8$ mm, the mean axial velocity $\overline{u}_{p,z}$ and the root-mean square axial velocity $\overline{u}_{p,z}^{RMS}$ radial profiles of the liquid phase, are shown in Figure 6.5. Due to the thread mentioned in Section 2.4.2, experimental profiles show a small asymmetry in the radial profiles at $z = 4$ mm. Since the fuel particle velocity relaxes to the gas velocity, the asymmetry disappears further downstream with a particle velocity profile quasi-identical to the gas velocity profile at $z = 8$ mm. Agreement between the mean axial

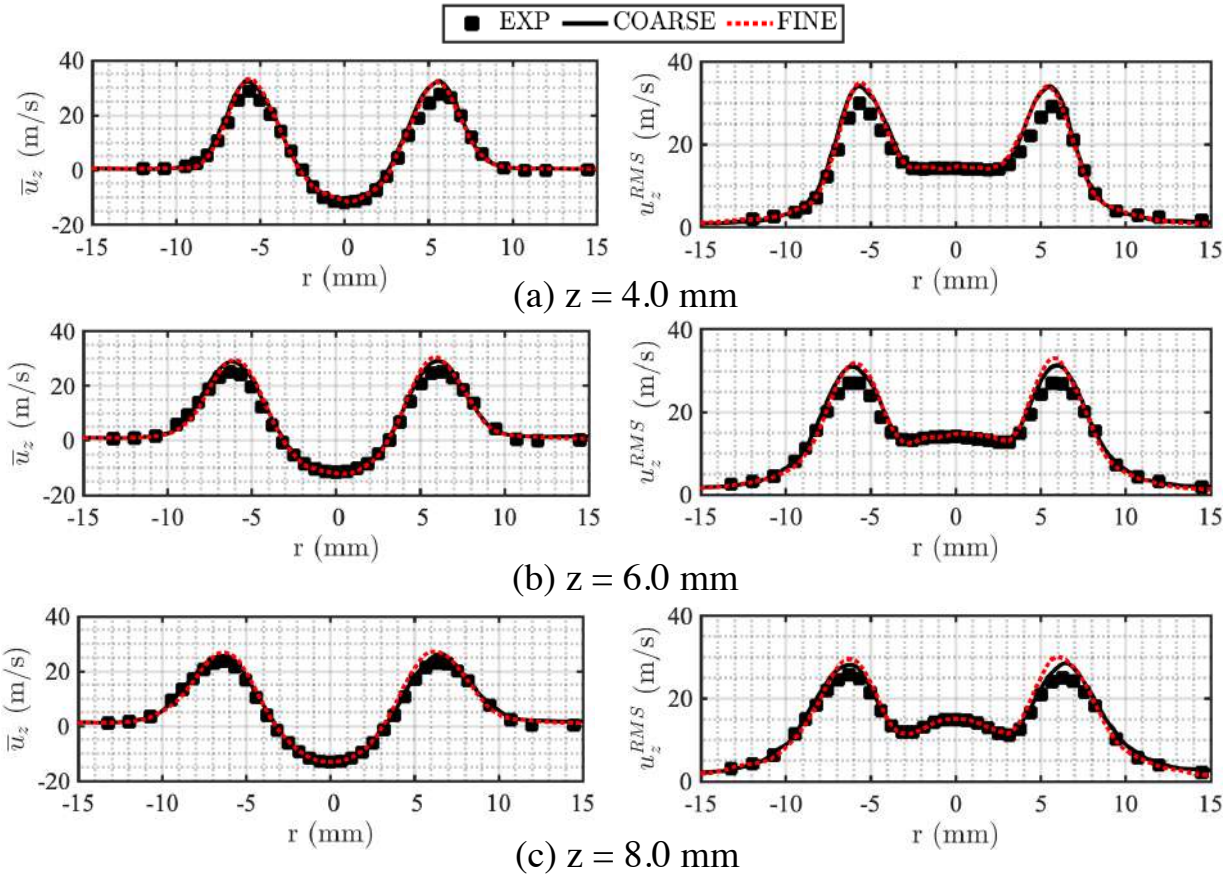

Figure 6.4. – Radial profiles of (left) the mean axial gas velocity $\overline{u}_z$ and (right) root-mean square axial gas velocity $\overline{u}_z^{RMS}$ at $z = 4$ mm, $z = 6$ mm and $z = 8$ mm. Experimental results are plotted with black filled squares.Simulations performed with the COARSE and FINE meshes are respectively plotted with continuous black lines and dotted red lines.

particle velocity $\overline{u}_{p,z}$ measured and obtained numerically is still very good, with small differences in the inner shear layers as for the gaseous phase. These comparisons indicate that the spray structure is well captured by LES. Finally, agreement on the root-mean square axial velocity $\overline{u}_{p,z}^{RMS}$ profiles shows that the particle velocity dispersion is also well reproduced by LES. Results are not improved with the FINER mesh.

The mean diameter d_{10} and the Sauter mean diameter d_{32} radial profiles of the liquid phase are shown in Figure 6.6. For a group of N_p particles, the Sauter mean diameter d_{32} is computed as:

$$d_{32} = \frac{\sum_{i=1}^{N_p} d_{p,i}^3}{\sum_{i=1}^{N_p} d_{p,i}^2} \tag{6.8}$$

The Sauter mean diameter of a polydisperse spray is defined as the diameter that a monodisperse group of droplets should have to possess the same total interfacial area as the polydisperse group of droplets being studied [250]. While differences for the d_{10} profiles between experiments and numerical simulations remain in the experimental margin error (< 2 μm), the numerical d_{32} values predicted are about half than the values recorded in the experiments. This feature indicates that the proportion of

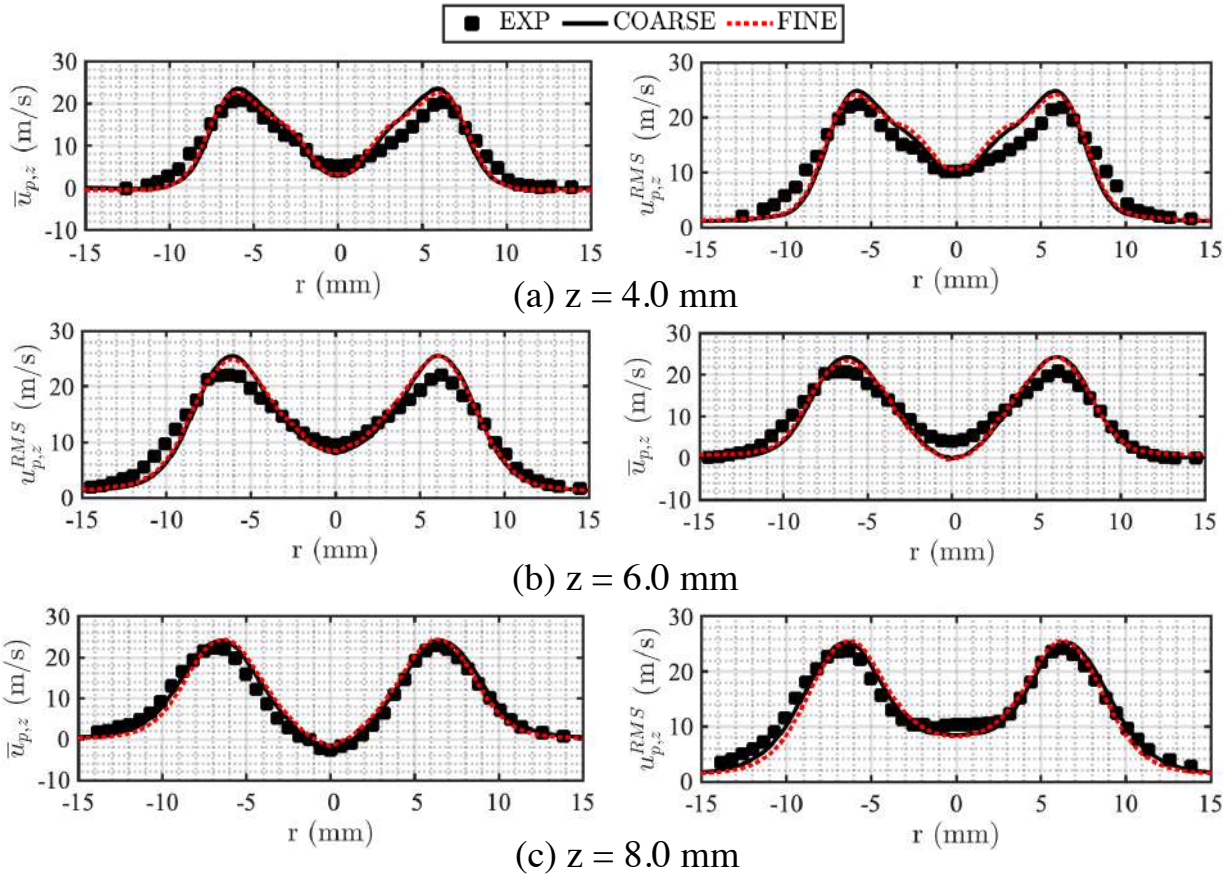

Figure 6.5. – Radial profiles of (left) the mean axial particle velocity $\overline{u}_{p,z}$ and (right) root-mean square axial particle velocity $\overline{u}_{p,z}^{RMS}$ at $z = 4$ mm, $z = 6$ mm and $z = 8$ mm. Experimental results are plotted with black filled squares. Simulations performed with the COARSE and FINE meshes are respectively plotted with continuous black lines and dotted red lines.

the largest particles injected is underestimated in the simulation but it does not affect strongly the mean particle diameter d_{10} which is well reproduced. This is due to the initialization of the FIMUR model described in Section 6.3.1. The initialization of the initial particle diameter distribution $f_N(d_p)$ for FIM-UR relies on averaging the parameters (X,q) of the RR distributions fitted to the experimental distributions measured on the spray without airflow at $z = -1.35$. As seen in Figure 6.3c, the parameter X varies from 10 μm in the recirculation zones to 20 μm in the jet shear layers. However, in Rosin-Rammler distribution, d_{10} and d_{32} are linked to q and X by the following relations :

$$d_{10} = X\left[\Gamma\left(1+\frac{1}{q}\right)\right] \tag{6.9}$$

$$d_{32} = X\left[\frac{\Gamma\left(1+\frac{3}{q}\right)}{\Gamma\left(1+\frac{2}{q}\right)}\right] \tag{6.10}$$

where Γ is the gamma function. Hence, with here $q = 2.74$, a shift on X of δX will induce a shift of $\delta d_{10} = 0.89\delta X$ on d_{10} and a even higher shift of $\delta d_{32} = 1.14\delta X$ on d_{32} for the particle diameter distribution at the injection. Thus, the choice of X of the initial particle diameter distribution $f_N(d_p)$ for FIM-UR has more consequences on the d_{32} profiles than the d_{10} profiles obtained downstream the injection. Furthermore, the real particle distribution of a hollow-cone spray is not necessary a RR

distribution. For instance, Treleaven et al. [241] observed that using a RR distribution as the injection distribution does not enable to capture the small number of large particles injected. They use instead a modified RR distribution where the peak location is the same as the RR distribution but spread over larger particles. Hence, this procedure would roughly keep the d_{10} values and increase the d_{32} values. Nonetheless, the study investigates cold non-reactive flow with negligible heat and mass transfer, the profiles of d_{10} and d_{32} obtained are satisfying to pursue the study with the injection parameters.

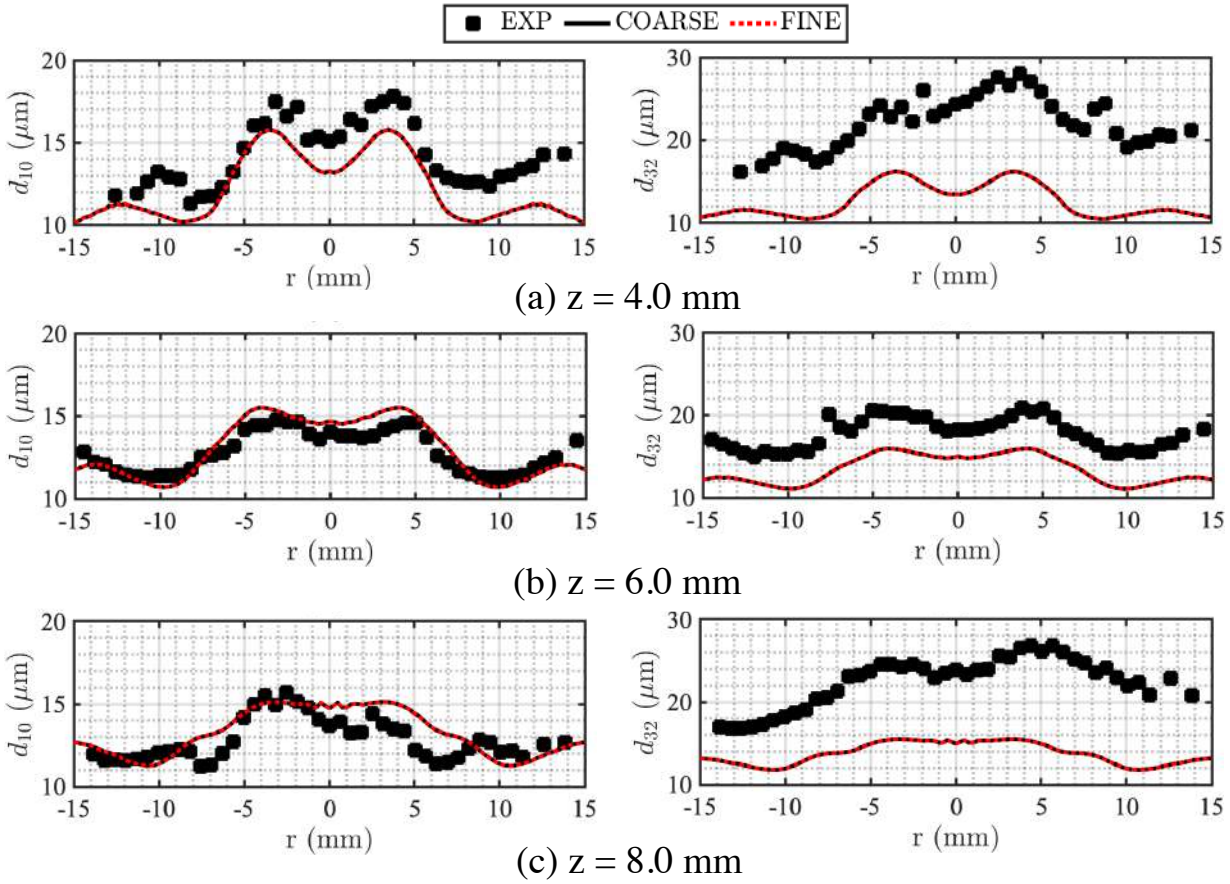

Figure 6.6. – Radial profiles of (left) the mean diameter d_{10} and (right) Sauter mean diameter d_{32} at $z = 4$ mm, $z = 6$ mm and $z = 8$ mm. Experimental results are plotted with black filled squares. Simulations performed with the COARSE and FINE meshes are respectively plotted with continuous black lines and dotted red lines.

Finally, the structure of the spray computed by LES is examined by comparing the normalized profile of the number density $[n_p d_{20}^2]_{norm}$ with the normalized profile of the light intensity I_{norm} obtained from Mie light scattering imaging in Figure 6.7. The contour of the spray is drawn with the Otsu method for both images [251]. The brightest zones with $I_{norm} > 0.5$ correspond to the hollow cone of the injected spray. Having small diameters, the particles act like fluid tracers. They are mainly present in the jets of the swirling air flow which are the curved branches expanding from $z = 5$ to 25 mm in Figure 6.7. The higher contrast found on the Mie images can be attributed to multiple factors. LES captures well the structure of the spray, but it underestimates the proportion of large particles which contributes significantly to the scattered light. Also, Mie imaging recorded by the camera is equivalent to the projection of 3D $[n_p d_{20}^2]_{norm}$ field onto a 2D structured grid composed by the pixels of the camera. On the other hand, the $[n_p d_{20}^2]_{norm}$ fields from the LES are interpolated from an unstructured mesh to a plane. Hence, the Mie images and the cut view of $[n_p d_{20}^2]_{norm}$ from LES are the results of the projections of quantities on two different grids. Finally, considering that

the light intensity I received by the camera is equivalent to $[n_p d_{20}^2]_{norm}$ is a rough approximation.

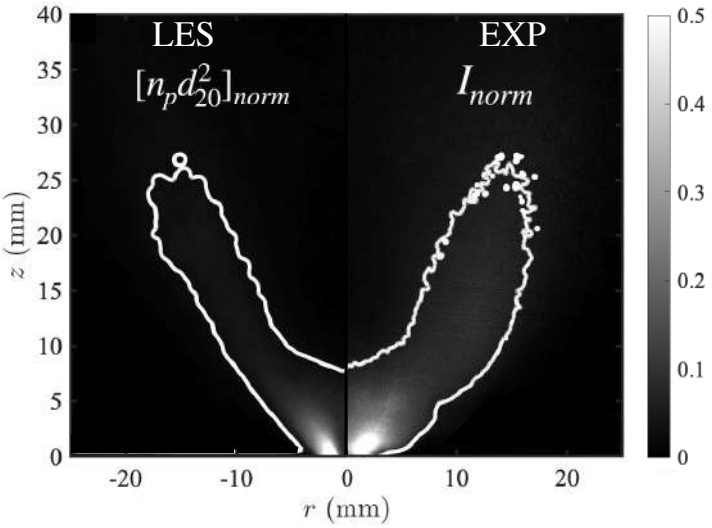

Figure 6.7. – Comparison between (left) the normalized product $[n_p d_{20}^2]_{norm}$ obtained with LES and (right) the normalized intensity signal I_{norm} recorded experimentally with planar Mie imaging. Contour plots are plotted for each field with Otsu's method [251].

6.5. Results in pulsed regime

The air flow is now pulsed with the loudspeaker at an harmonic excitation $f = 200$ Hz and a forcing level set to $u'_{z,3}/\overline{u}_{z,3} = 0.20$. Simulations are performed and phase-averaged over 60 acoustic cycles (300 ms). When the phase-averaged numerical results are angle-averaged, the resulting velocity profiles are less noisy. Hence, the angle-averaged results are presented in this section.

6.5.1. Gaseous phase

PDPA measurements are realized on the pulsated gas flow without fuel spray. Phase-averaged axial u_z velocity profiles and the differences $u'_z = u_z - \overline{u}_z$ of the gas flow are shown at three different heights: $z = 4$ mm, $z = 6$ mm and $z = 8$ mm in Figure 6.8, Figure 6.9 and Figure 6.10 respectively. The mean velocity profiles were shown to be axisymmetrical in the previous section. Half of the velocity profiles u_z and u'_z are plotted on the same chart. The evolution of the structure of the swirling flow is well captured by LES over the acoustic period, matching the position of the local extrema reached by u'_z with those measured experimentally. However, a phase lag about $\pi/10$ is computed between the experimental and numerical results for $z = 4$ mm for the COARSE mesh, while there is none for the FINE mesh. The positive extrema at $\varphi = 3\pi/4$ in the jet shear layers computed by LES match with experiments, but the negative extrema are still overestimated at $\varphi = 7\pi/4$ for $z = 4$ mm. These differences progressively reduce along z, where u'_z are well reproduced for $z = 6$ mm and $z = 8$ mm with a phase lag reduced to $\pi/12$. Better capturing the flow local structures and the impedance of the air injection, the mesh refinement performed in the FINE mesh improves the results for u'_z compared to the COARSE mesh. Hence, it can be expected that further mesh refinement will correct these differences. However, for both mesh, experimental and numerical results show overall very good agreement, the differences observed for u'_z not affecting strongly the total velocity u_z.

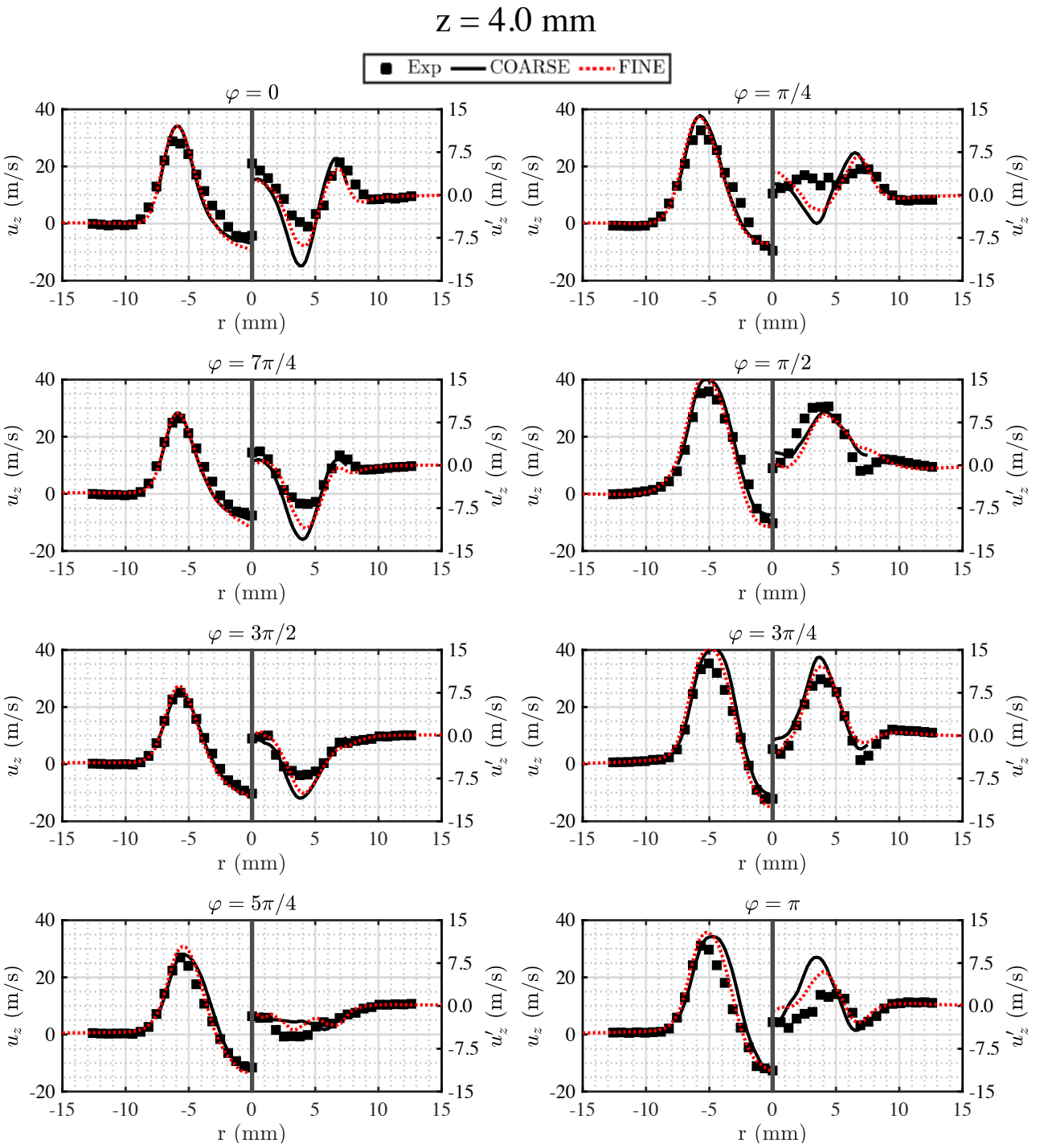

Figure 6.8. – Phase-averaged profiles of the (left-axis) axial gas velocity u_z and (right-axis) its fluctuation u'_z with respect to the unforced velocity field at $z = 4$ mm. Experimental results are plotted with black filled squares. Simulations performed with the COARSE and FINE meshes are respectively plotted with continuous black lines and dotted red lines. The common reference is the phase φ of the acoustic velocity excitation at the combustion chamber backplane computed with Equation 6.3.

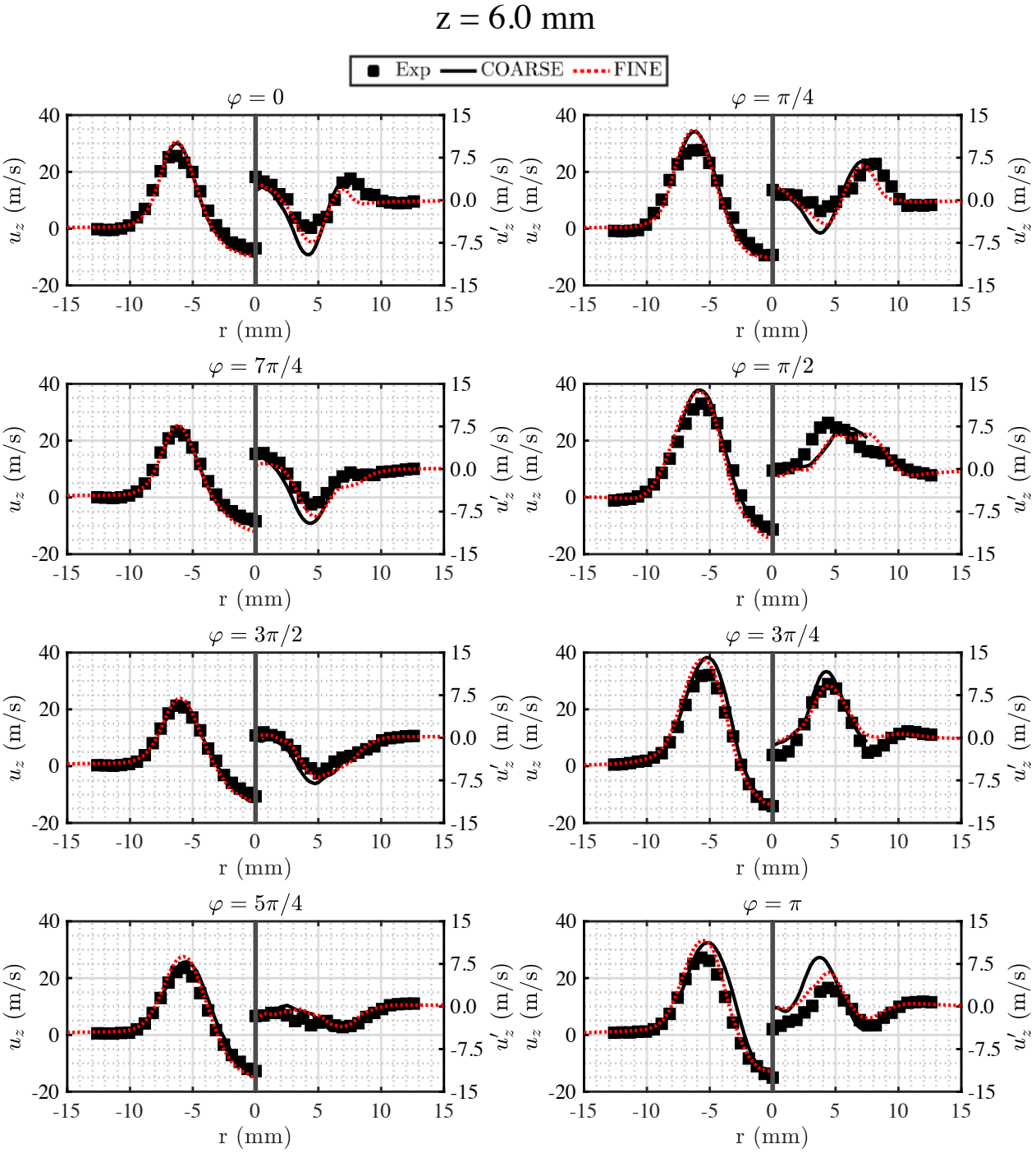

Figure 6.9. – Phase-averaged profiles of the (left-axis) axial gas velocity u_z and (right-axis) its fluctuation u'_z with respect to the unforced velocity field at $z = 6$ mm. Experimental results are plotted with black filled squares. Simulations performed with the COARSE and FINE meshes are respectively plotted with continuous black lines and dotted red lines. The common reference is the phase φ of the acoustic velocity excitation at the combustion chamber backplane computed with Equation 6.3.

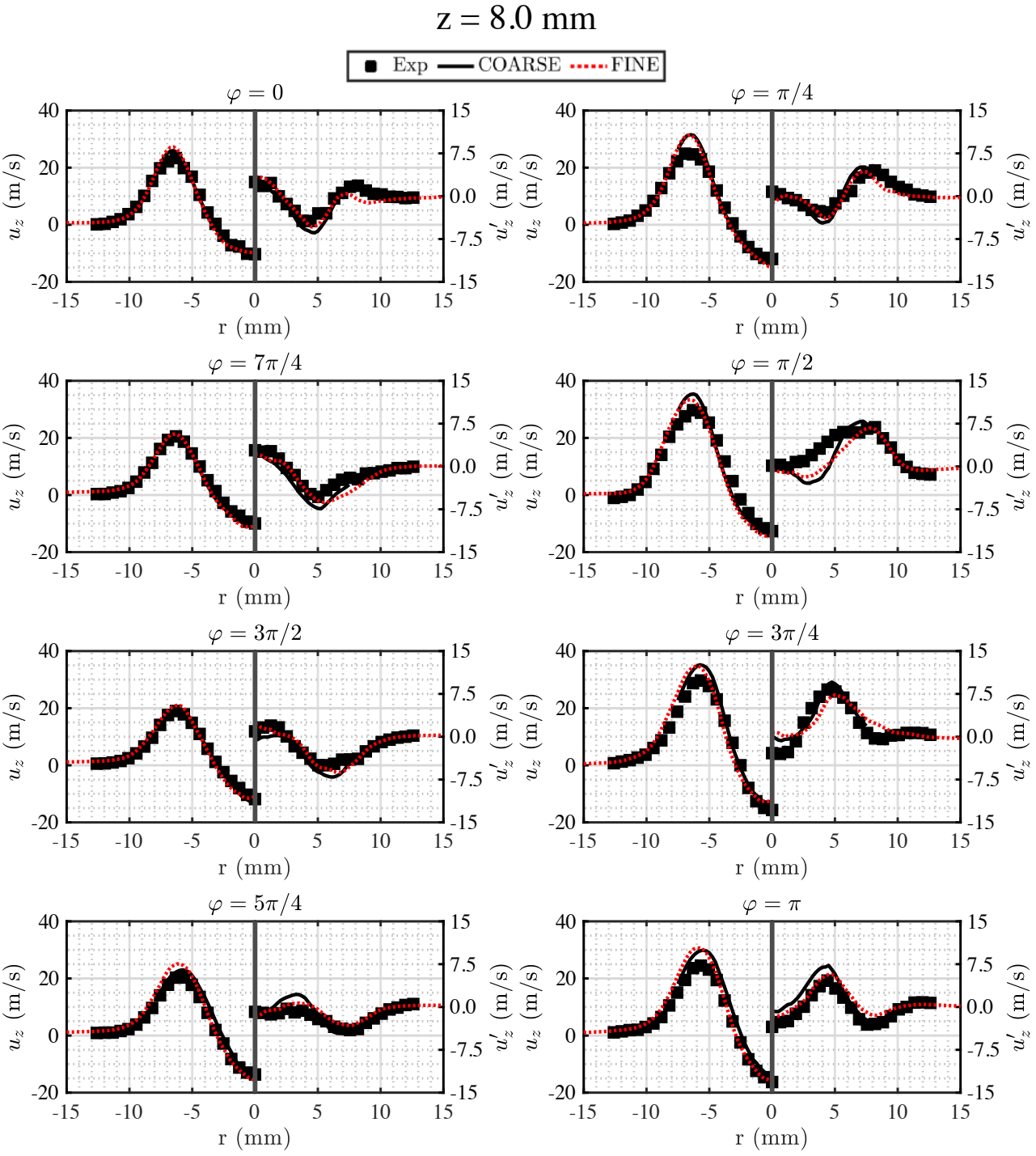

Figure 6.10. – Phase-averaged profiles of the (left-axis) axial gas velocity u_z and (right-axis) its fluctuation u'_z with respect to the unforced velocity field at $z = 8$ mm. Experimental results are plotted with black filled squares. Simulations performed with the COARSE and FINE meshes are respectively plotted with continuous black lines and dotted red lines. The common reference is the phase φ of the acoustic velocity excitation at the combustion chamber backplane computed with Equation 6.3.

6.5.2. Fuel Spray

The liquid fuel is now injected in the pulsed flow. Phase-averaged axial velocity profiles $u_{p,z}$ along r of the fuel particles are shown at three different heights: $z = 4$ mm, $z = 6$ mm and $z = 8$ mm in Figure 6.11, Figure 6.12 and Figure 6.13 respectively. Phase averaged diameter profiles are not shown because they are roughly constant along the entire acoustic cycle. Results are shown only for $|r| < 7$ mm. The regions of the flow in the combustion chamber where $|r| > 7$ mm correspond to the outer recirculation zones of the swirling flow, where a very few particles are present. Hence, in numerical simulations, the statistical convergence of the particle properties is not achieved in these zones. Even considering the differences observed for the gaseous flow, numerical simulations overestimate the spray velocity recorded in experiments. In particular, the positive extrema of the particle velocity fluctuations u'_p are overestimated for all z at $\varphi = 3\pi/4$ while the gaseous velocity fluctuations u' were correctly predicted by LES for the gaseous flow. On the contrary, the negative extrema of u'_p at $\varphi = 7\pi/4$ are rather well captured by LES. Furthermore, LES overestimates the width of the swirling spray jets and fails to capture their location, indicated by the peak of the velocity curve and predicted at smaller radius than those obtained experimentally. Although the FINE mesh better captures the pulsed flow, only a slight improvement is obtained compared to the COARSE mesh. It indicates that differences between LES and experiments on the particle velocity profiles would still remain even with a perfect resolution of the gas flow, and so they are caused by the model of the spray injection and.or dynamics. It is discussed in the next section.

The phase-averaged Mie scattering images are compared to the $[n_p d_{20}^2]_{norm}$ fields from LES and are presented in Figure 6.14. The periodic behaviour of the spray structure at the combustion chamber scale is captured by LES. For $\pi < \varphi < 2\pi$, $u'_z < 0$ at $z = 0$: the injected particles are slowed and accumulated at the backplane, delaying their arrival in the jet shear layers of the swirling air flow. In Figure 6.14, it results into the thickening of the base of the spray and the reduction of the branches, reaching a minimum height of $z = 20$ mm at $\varphi = 7\pi/4$. Then for $0 < \varphi < \pi$, u'_z becomes positive: the cluster of particles accumulated at its base is convected along the jets of the swirling flow. In Figure 6.14, it results into stretching branches reaching the maximum height of $z = 30$ mm at $\varphi = \pi$. For $3\pi/4 < \varphi < 3\pi/2$, it can be seen that the angle of the spray computed by LES is narrower than the angle observed experimentally.

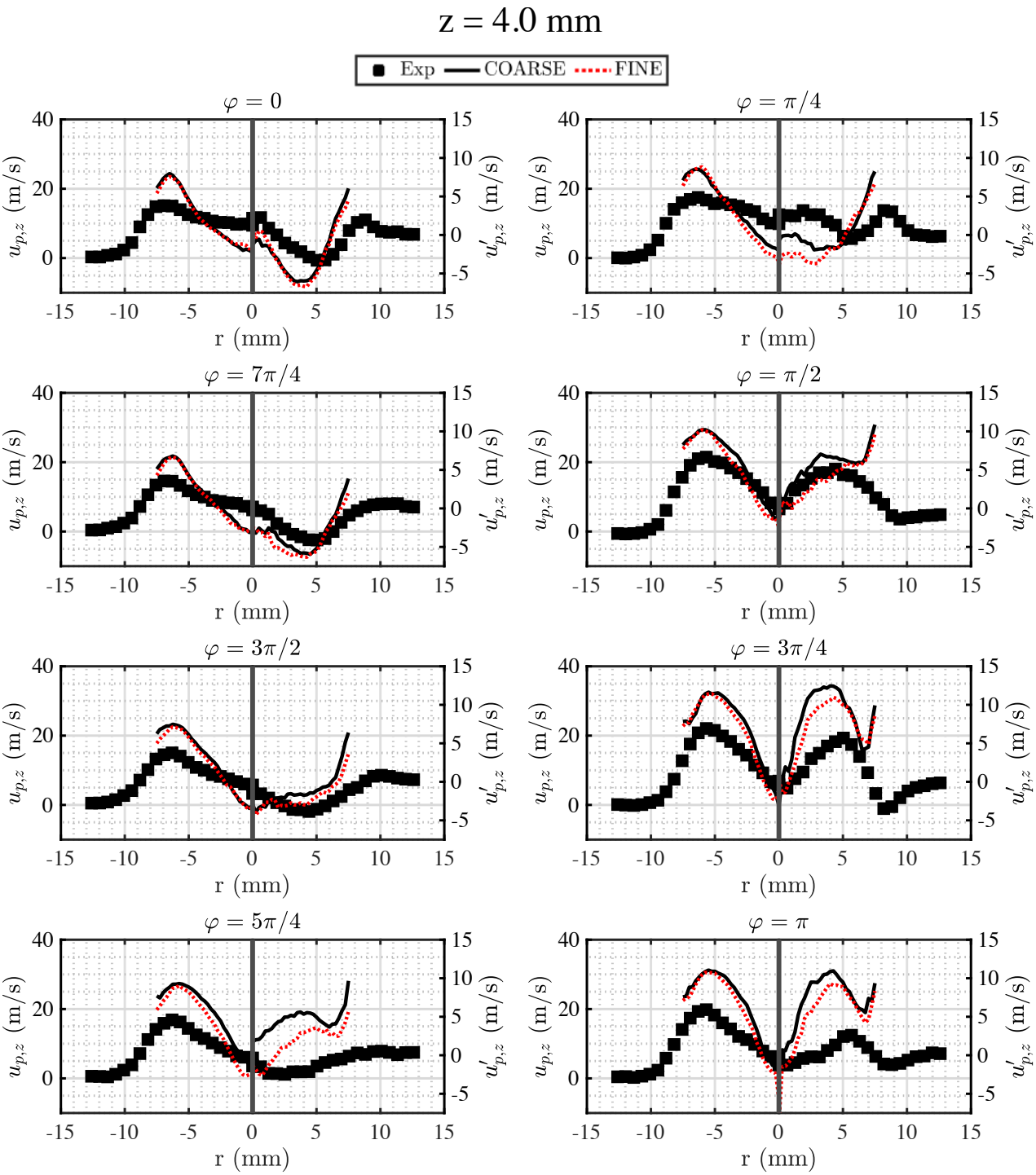

Figure 6.11. – Phase-averaged profiles of the (left-axis) axial particle velocity $u_{p,z}$ and (right-axis) its fluctuation $u'_{p,z}$ with respect to the unforced velocity field at $z = 4$ mm. Experimental results are plotted with black filled squares. Simulations performed with the COARSE and FINE meshes are respectively plotted with continuous black lines and dotted red lines. The common reference is the phase φ of the acoustic velocity excitation at the combustion chamber backplane computed with Equation 6.3.

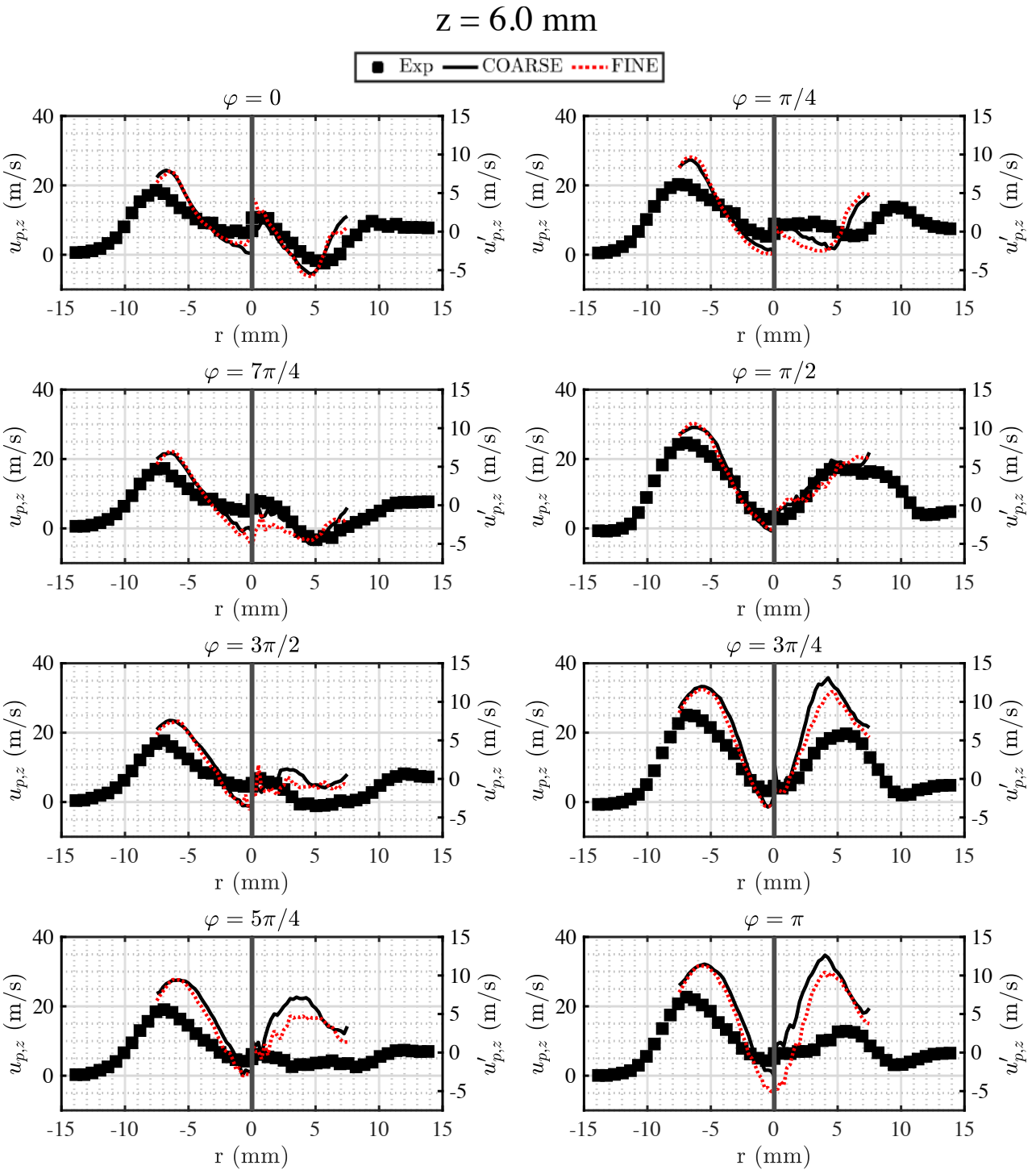

Figure 6.12. – Phase-averaged profiles of the (left-axis) axial particle velocity $u_{p,z}$ and (right-axis) its fluctuation $u'_{p,z}$ with respect to the unforced velocity field at $z = 6$ mm. Experimental results are plotted with black filled squares. Simulations performed with the COARSE and FINE meshes are respectively plotted with continuous black lines and dotted red lines. The common reference is the phase φ of the acoustic velocity excitation at the combustion chamber backplane computed with Equation 6.3.

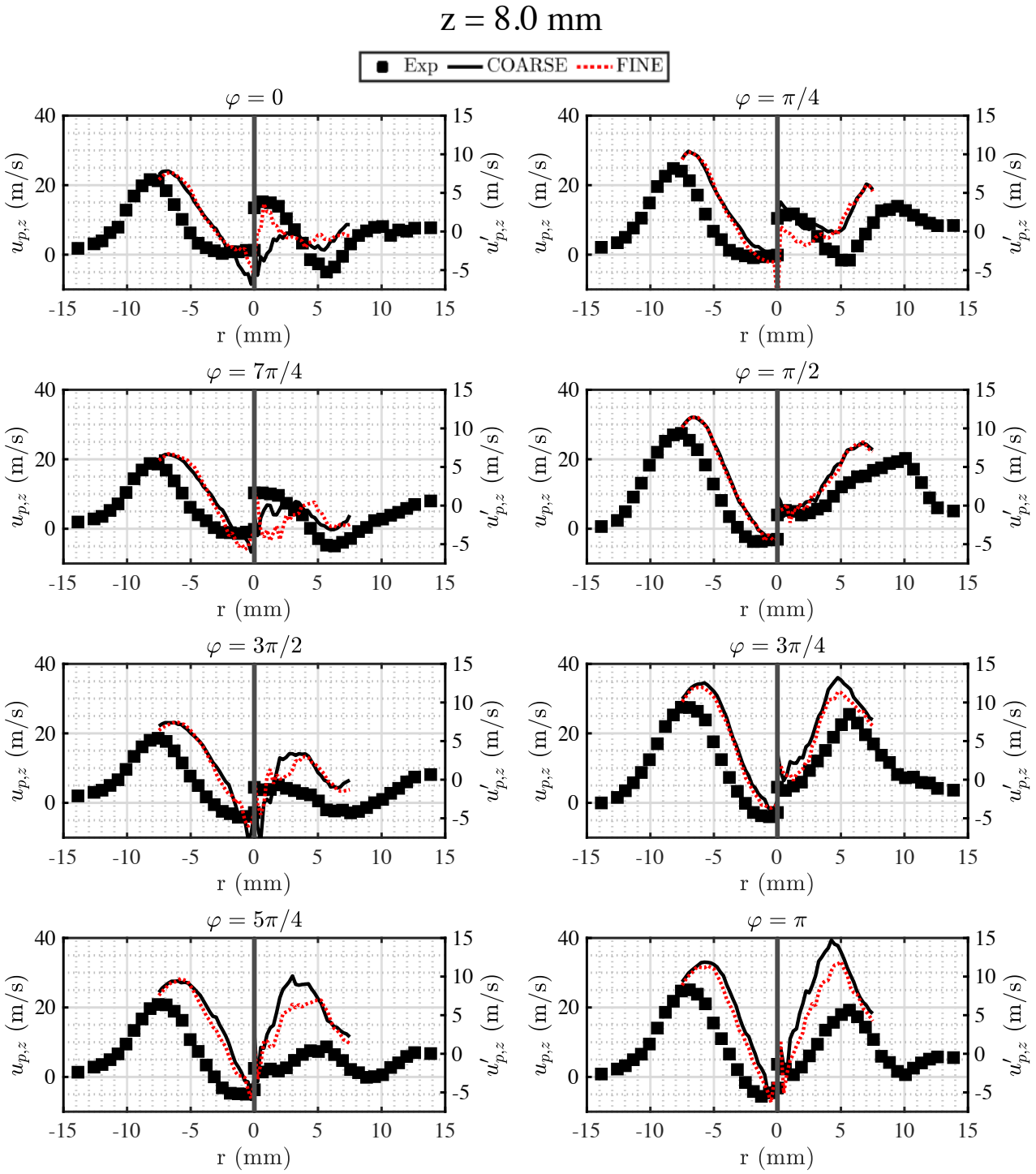

Figure 6.13. – Phase-averaged profiles of the (left-axis) axial particle velocity $u_{p,z}$ and (right-axis) its fluctuation $u'_{p,z}$ with respect to the unforced velocity field at $z = 8$ mm. Experimental results are plotted with black filled squares. Simulations performed with the COARSE and FINE meshes are respectively plotted with continuous black lines and dotted red lines. The common reference is the phase φ of the acoustic velocity excitation at the combustion chamber backplane computed with Equation 6.3.

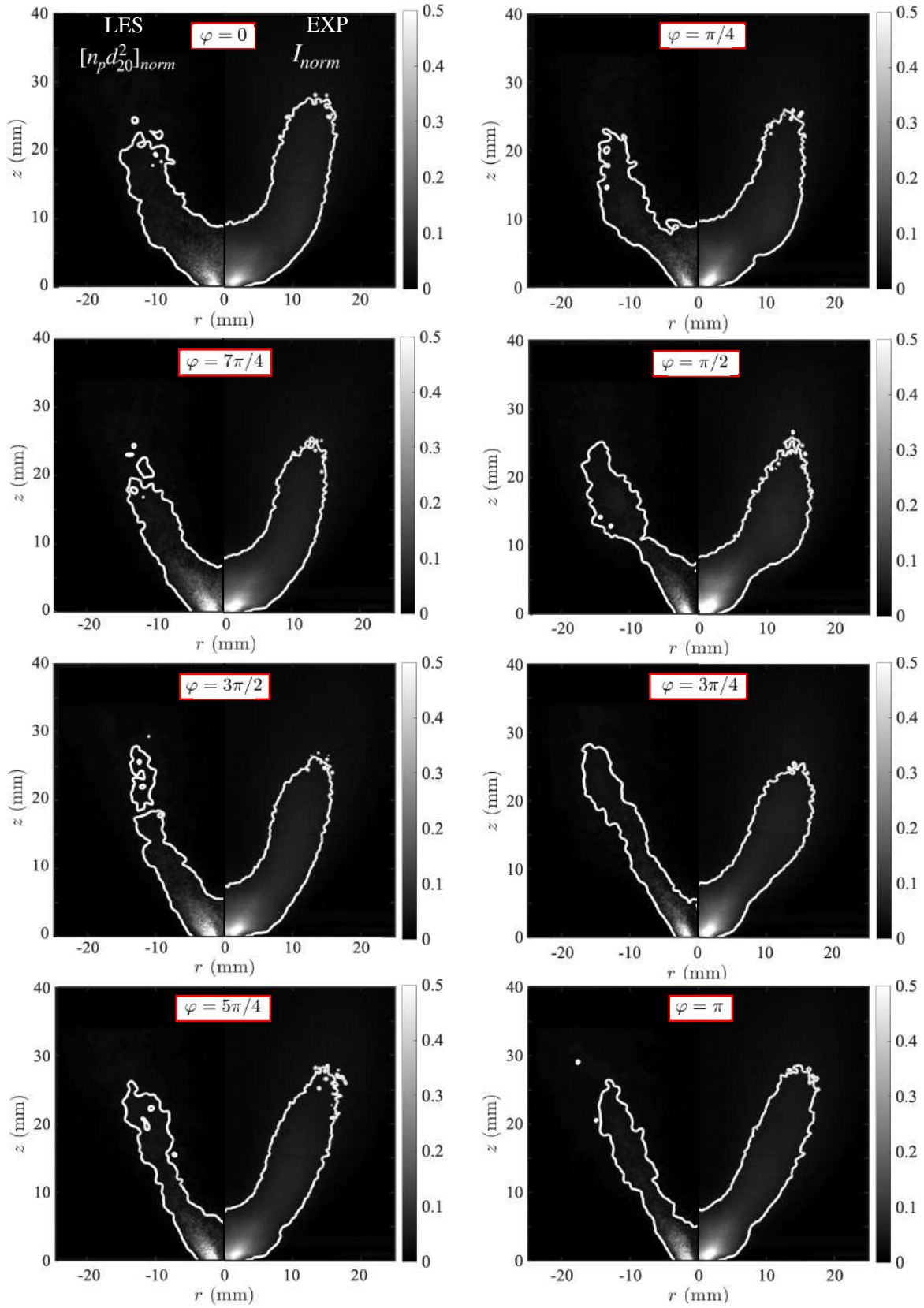

Figure 6.14. – Phase-averaged of (left-axis) the normalized intensity signal I_{norm} recorded experimentally with planar Mie imaging and (right-axis) the normalized product $[n_p d_{20}^2]_{norm}$ fields obtained with LES. Contour plots are plotted for each field with Otsu's method [251]. The common reference for the phase for the phase φ is the phase of the acoustic velocity excitation at the combustion chamber backplane computed in Equation 6.3.

6.6. Discussions

Differences between numerical and experimental results in pulsed flow are discussed in this section. The solver AVBP considering only the steady drag force for the motion equation of the particles, it is firstly questioned if other forces linked to the acceleration are at the origin of these discrepancies, such as the Basset force. In the conditions explored, it has already been shown in Chapter 3 that the model used in AVBP to reproduce the drag acting on the droplets well describe their dynamics and interactions for diluted sprays as for those studied in this work.

In this case, it can be deduced that the main origin of the difference for the droplet velocity field originates from the FIM-UR injection model. While it reproduces correctly the main spray behaviour as detailed in Section 6.4, FIM-UR does not feature the dynamic behavior to reproduce the modification of the injection when submitted to acoustic fluctuations. In particular, FIM-UR provides a constant injection angle, a steady particle velocity and a steady diameter distribution profile. Nonetheless, when a hollow-cone spray is submitted to acoustic disturbances, Figure 6.15 shows that liquid mushroom-shaped rings are periodically formed at the base of the hollow-cone which are convected along the injection axis and then atomized in droplets. Hence, at a given height, the radius of the injection cone over which particles are injected varies along the acoustic period, alternating between large and small angles of injections θ_a. Furthermore, when the hollow-cone spray is injected in a swirling flow, the acoustic disturbances also create local fluctuations of the swirl number at the spray location, which also disturb the injection angle. Particles injected in the smallest angle tend to be transported in the inner recirculation of the swirling flow while those at the largest angle tend to be in the jet shear layers. Finally, one may also suspect that the particle velocity and diameter profiles injected also spatially and temporally fluctuate in space and time. Hence, these elements indicate that the acoustic response of the hollow-cone spray injection cannot be neglected and has to be modelled.

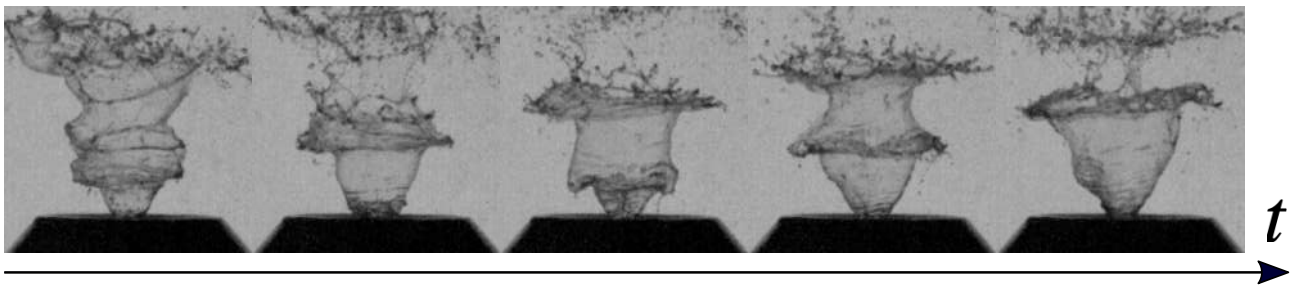

Figure 6.15. – High-speed images of the TALISMAN hollow-cone spray when it is submitted to an acoustic excitation at $f = 200$ Hz and $u'_{z,2}/\overline{u}_{z,2} = 0.20$ without airflow performed at 230,000 fps by a PHANTOM TMX7510 camera.

6.7. Conclusion

The capacity of the FIM-UR model to reproduce the spray particle velocity dynamics caused by acoustic excitation has been evaluated. Numerical and experimental results for the steady regime have shown to be in good agreement for the gaseous and particle velocity and the particle mean diameter profiles. Only the Sauter mean diameter profiles could not be matched due to the particle diameter distribution initialization of FIM-UR. The model requires to infer a single particle diameter distribution for the fuel injected at point from several experimental particle diameter distributions. These differences do not have importance for non-reacting cold flows. Comparison between Mie scattering images and $[n_p d_{20}^2]$ LES fields shows that the global structure of the spray inside the combustion chamber is well captured by the LES.

For the pulsed regime, rigorous experimental and numerical protocols were elaborated to synchronize experimental and numerical data for the spray dynamics and get comparable quantities. For an excitation frequency $f = 200$ Hz and a relative fluctuation amplitude $u'_{z,3}/\overline{u}_{z,3} = 0.20$ seen by the spray, numerical phase-averaged velocity profiles have been successfully validated against measurements for the gaseous phase. A small phase lag mismatch and slight differences for the amplitude of the gas velocity fluctuations persist between LES and experiments, but they are damped along the injection axis. They are caused by a mismatch of the pressure drop across the swirler influencing the acoustic response of the burner. They can be reduced using an increased mesh resolution in the small air injection channels. Nonetheless, the relative coarse mesh captures well enough the gas velocity fluctuations. The FIM-UR model having not a dynamic behaviour, numerical velocity profiles are greatly overestimated for the liquid phase. Moreover, the structure of the swirling liquid flow is not properly captured, the inner zone being narrower than in experiments. In reality, acoustic disturbances induce variations of the angle of injection cone but also spatial and temporal fluctuations of the particle diameter and velocity distributions.

Hence, in order to capture the particle velocity fluctuations in the combustion chamber, it is mandatory to model the dynamic response of a hollow cone spray injection to acoustic disturbances. Further experiments on the acoustic response of spray are necessary to obtain such a model. For the case of the swirling flow, it requires to measure the angle of injection and the particle diameter and velocity distribution change for various swirl numbers. Moreover, the fluctuations of the angle of injection in a laminar flow have to be recorded when submitted to acoustic disturbances for different frequencies and amplitudes of fluctuations. These data acquired would be the first steps to elaborate the dynamic behaviour of a hollow cone injection.

Part II.

Investigation of combustion instabilities in a swirl-stabilized spray burner

Chapter 7

Dynamic analysis of a swirl-stabilized spray flame

Je me lève en sursaut : si seulement je pouvais m'arrêter de penser, ça irait déjà mieux. Les pensées, c'est ce qu'il y a de plus fade. Plus fade encore que de la chair. Ça s'étire à n'en plus finir et ça laisse un drôle de goût. Et puis il y a les mots, au-dedans des pensées, les mots inachevés, les ébauches de phrase qui reviennent tout le temps: "Il faut que je fini... J'ex... Mort... M. de Roll est mort... Je ne suis pas... J'ex..." Ça va, ça va... et ça ne finit jamais. [...] Les pensées naissent par-derrière moi comme un vertige, je les sens naître derrière ma tête... si je cède, elles vont venir là devant, entre mes yeux - et je cède toujours, la pensée grossit, grossit et la voilà, l'immense, qui me remplit tout entier et renouvelle mon existence.

– Jean-Paul Sartre, *La Nausée, 1938*

A stability analysis of the TALISMAN burner with respect to thermoacoustic issues is carried out. First, transient self-sustained oscillations are examined for a burner configuration and their sensitivity to the temperature of the recirculation zones is highlighted. Then, the acoustic modes of the burner are characterized experimentally and compared to predictions of simulations conducted with low-order model. The velocity fluctuations inside the air injection unit and at the burner outlet are determined. Acoustic transfer matrices from a low-order model of the acoustic response of the air injection are fitted against experimental results for a large range of frequencies and different levels of fluctuation. They are then used to measure the Flame Transfer Functions between the OH^* light signal of the spray flame and the velocity fluctuations at the air channel outlet. A model is then used to infer the heat release rate disturbances from the OH^* signal. Finally, the thermoacoustic instabilities observed in setup are compared to predictions that combine a Helmholtz solver with the flame response.

Overview

7.1. Introduction

Thermoacoustic instabilities (TAI) can lead to high amplitude pressure and flow oscillations that can seriously damage gas turbines in many different ways: flame blow-off or flashback, vibrations that wear out the mechanical parts or disturb the acquisition and control systems, thermal flux overload over combustor walls or over turbine blades [49–52].

Reduced-order models provide useful predictions of TAI within a short time range with limited computational resources [64, 123, 130, 131, 252]. While modelling efforts were mostly dedicated to premixed flames and led to successful predictions in power generation systems [51, 52, 60, 253], low-order modelling of the system dynamics with spray flames remains difficult [149–154, 254, 255] and requires further investigations due to complexities of the two-phase flow dynamics, turbulence and flame interactions taking place in spray flames. To enable these predictions, the flame transfer function or Flame Describing Function (FDF) needs first to be determined [128, 256]. But experimental data for the FDF of spray-flames remain relatively scarce compared to premixed systems.

In spray flames, perturbations both in the air and fuel lines have to be considered. The response to fuel modulations in the supply line has been studied in [257, 258] for a lean direct injection spray flame configuration. Results for the flame response were found to scale linearly with the fuel modulation level, but they also exhibited a strong dependence to the air preheat temperature and to the air mass flow rate. An important effort for FDF measurements has been conducted at EM2C laboratory [149–155], in which cases only acoustic perturbations in the air stream are considered. For operation at globally lean conditions, FDFs measured for a steam assisted fuel atomizer in [150] were found to be very similar to those obtained for lean premixed flames, but both the FDF gain and phase lag were found to be highly sensitive to the perturbation level. At low frequency, the gain was found to tend to 0.5 for a non-sooty flame and to 1 for a sooty flame, instead of the theoretical limit $G = 0$ predicted by theory for a stiff fuel injection system [259]. Innocenti et al. [260] deduced the FDF from a spray flame in a lean direct injection system using lumped acoustic transfer matrices as detailed in [261]. In this combined numerical and experimental analysis, the gain of the experimental FDF shows important differences with the gain of the numerical FDF, especially at low-frequencies where the numerical gain tends towards 0 while the experimental gain tends towards values higher than unity. This limit does again not comply with theory [259]. Finally, [155] used both transfer matrix and optical method to determine the FDF from a RQL combustor. They obtained with both methods similar results for the FDF, but the low-frequency limits are still inconsistent with the theoretical limits of a non-premixed flame with a fuel stiff injector ($G = 0$). Baillot et al. [107] conducted FDF measurements of a swirling n-heptane spray flame located in the basin of a pressure antinode of a transverse acoustic wave for a linearly-arranged multiple-injection system of three swirling spray flames. They used normalized pressure fluctuations as input of the FDF, which can be linked to velocity fluctuations. Forcing the flame only at the frequency of azimuthal standing instabilities, they characterized the evolution of the FDF when varying the amplitude of the pressure fluctuations. They observed that the gain was decreasing non-linearly when the pressure amplitude increases, while the phase remains fairly unaltered. It results from the relative fluctuations of the CH^* signal I' emitted by the flame which linearly increases at low pressure amplitude, and then saturates at a maximum value and decreases for higher amplitudes. In the case of dodecane spray flame, Patat el al. [108] observed that gain of the FDF was shifted to lower values but kept the same evolution when varying the pressure amplitude as in n-heptane flame. However, the phase of the FDF remains unaltered. Patat el al. [109] extended the investigation for a swirling spray flame located at the maximum surface acoustic flux, where they obtain a similar FDF with a somewhat different phase response compared when the flame is located at a pressure antinode.

It is also worth mentioning that in the experiments conducted in [149–155], fluctuations of the heat

release rate $\dot{Q}'$ in the spray flames investigated burning at globally lean conditions are considered to be proportional to fluctuations of the OH^* signal I' emitted by the flame to determine the FDF. Baillot et al. [107] reported similar flame dynamics when using OH^* or CH^* emission for the high-speed visualization of the flame. The authors have attributed this equivalence to the absence of soot released by the swirling spray flames for the equivalence ratios considered. Recent experiments and simulations [262, 263] however indicate that the relationship applied to link these two fluctuations can lead to substantial differences for the FTF, and more specifically at low-frequencies. This conclusion is also corroborated by the recent experiments from [264] in which the flame transfer functions deduced from optical and acoustic techniques show substantial differences for technically premixed flames.

In this chapter, a stability analysis of the TALISMAN setup is carried out with a low-order model of the acoustic response of the combustor combined with measured FDF. Predictions are compared to measurements made during self-sustained combustions oscillations Section 7.2 describes the thermoacoustic instability that is observed for a given operating point. Then, in Section 7.3, the acoustic behaviour of the burner is reproduced with an acoustic network model with the low order instability simulator named OSCILOS developed by Imperial College London [117]. The acoustic modes of the burner are determined and are compared to measurements. Then, a low-order model of the flame is developed in Section 7.4. The acoustic transfer matrices modelling the air injection response to acoustic perturbations are computed and retrofitted against experimental measurements. They are used to infer the velocity fluctuations at the burner outlet in order to fulfil the compactness assumption necessary for the FDF approximation. Then, from measurements at globally lean conditions in steady regimes, an empirical scaling law between the light I from OH^* radical emission, the heat release rate $\dot{Q}$ and the equivalence ratio Φ is determined. This expression is used with a quasi-steady approximation to infer a relationship between the disturbances I', $\dot{Q}'$ and Φ'. Finally, FDF between heat release rate and velocity disturbances is reconstructed based on a model of the air-fuel injection response. Finally, in Section 7.5, the acoustic network model for the combustor and FDF models are coupled to predict thermoacoustic instabilities. Predictions are compared to experiments.

7.2. Self-sustained combustion oscillations

Self-excited oscillations have been observed over a large set of operating points for the configuration $\mathscr{C}_{21}$ described in Section 2.2.2, They appear when a long steel tube is added on the top on the square combustion chamber of the configuration $\mathscr{C}_{20}$, reproducing the turbine nozzle of an engine. These self-sustained oscillations change slowly with time even at limit cycle. They appear at the ignition and disappear as the temperature of the combustion chamber increases. So, to better study these instabilities, the backplane of the combustor chamber is water cooled with a copper tube wrapped around its cylindrical base. The behaviour of these self-excited oscillations, the diagnostics of the online monitoring set described in Section 2.3.1. Figure 7.1 depicts how the power spectra of the signal voltage recorded by the photomultiplier **PM**, the microphone **M2** and the hot-wire **HW** with time after ignition of the flame at $P = 7$ kW and $\Phi = 0.70$. Figure 7.2 shows the temporal evolution of the temperature T_{RZ} of the outer recirculation zone recorded by a thermocouple, the instability frequency, the relative fluctuations recorded by the different sensors and their phase lag $\Delta\varphi$ with the fluctuations recorded by **M1**.

While the thermocouple T_{RZ} does not give an accurate value of the temperature due to radiation losses, it gives a qualitative information about its evolution, in particular the transient regime after the combustor is ignited. The temperature of the recirculation zone reaches 95% of its final value after approximatively 10 minutes and 99% after 15 minutes. The frequency of the instability f_{TAI} also changes over time between 200 Hz and 245-250 Hz, reaching 95% of its final value after 10 minutes

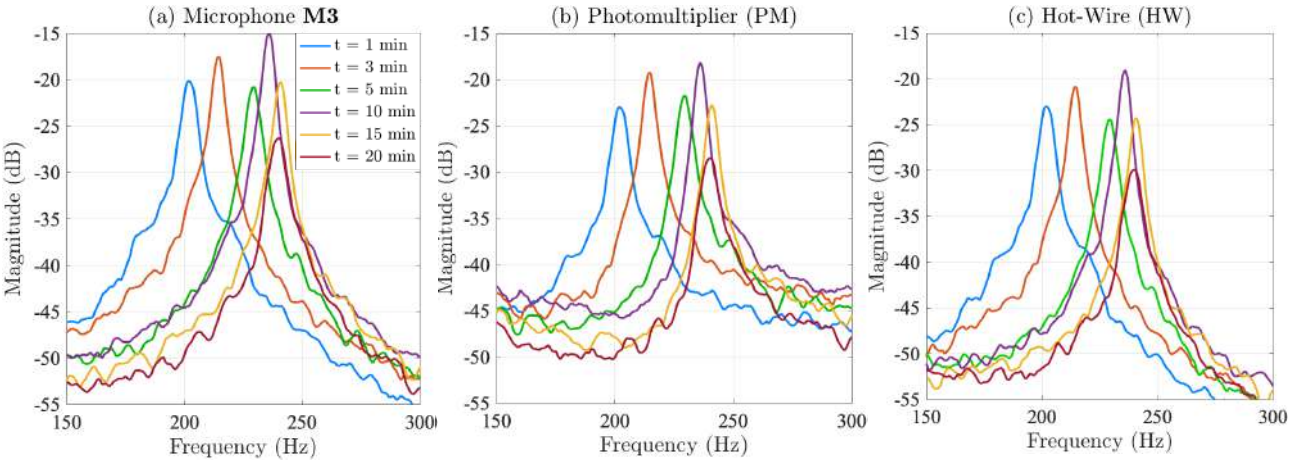

Figure 7.1. – Temporal evolution of the power spectra of the signal voltage recorded by (a) the microphone **M3**, (b) the photomultiplier (**PM**) and (c) the hot-wire (**HW**). The quantity t indicates the time from the flame ignition

and 99% after 15 minutes, confirming the link between the instability and the temperature of the recirculation zone. Being related to T_{RZ}, the phase shift $\Delta\varphi$ of the signals $I'/\overline{I}$ and $p'_3/\overline{p}_3$ with respect to the plenum microphone **M1** evolves only during the first 5 minutes where T_{RZ} and f_{TAI} grow linearly, and remain then constant. The phase lag between $I'/\overline{I}$ and $p'_3/\overline{p}_3$ being lower than $\pi/2$, it fulfils with the Rayleigh criterion. The signals $p'_2/\overline{p}_2$ and $u'/\overline{u}$ have a constant phase lag with **M1**. The fluctuation level $x'/\overline{x}$ of the signal x is computed using the relationship between the one-side power spectral density S_{xx} and the amplitude of the Fourier transform $|\hat{x}|$ [265]:

$$|\hat{x}(f)| = \sqrt{\frac{S_{xx}(f)\Delta f \mathrm{ENBW}}{2}} \tag{7.1}$$

where Δf is the frequency resolution and ENBW is the Equivalent Noise Bandwidth due to the FFT windowing. Assuming that the fluctuations are purely harmonic at the excitation frequency f_{TA} with the amplitude x', one has:

$$x' = \sqrt{2S_{xx}(f)\Delta f \mathrm{ENBW}} \tag{7.2}$$

The fluctuations recorded depend on the temperature T_{RZ} reached inside: all fluctuations follow the same trend reaching a maximum after 2 minutes,with relatively constant values between 2 minutes and 10 minutes before gradually decreasing from 10 to 20 minutes. The pressure fluctuations recorded by **M1** and **M3** are relatively small compared to the other fluctuations. When repeating successively the experiments, it has been observed that the deterioration of the seal during operation reduces these fluctuation levels, without changing their evolution. These changes do not alter T_{RZ}, f_{TAI} and $\Delta\varphi$. However, when looking at their amplitude ratio relatively to $|p'_1/\overline{p}_1|$, we can observe that they are also related as $\Delta\varphi$ to T_{RZ}, evolving mainly during the first 5 minutes and remaining roughly constant after.

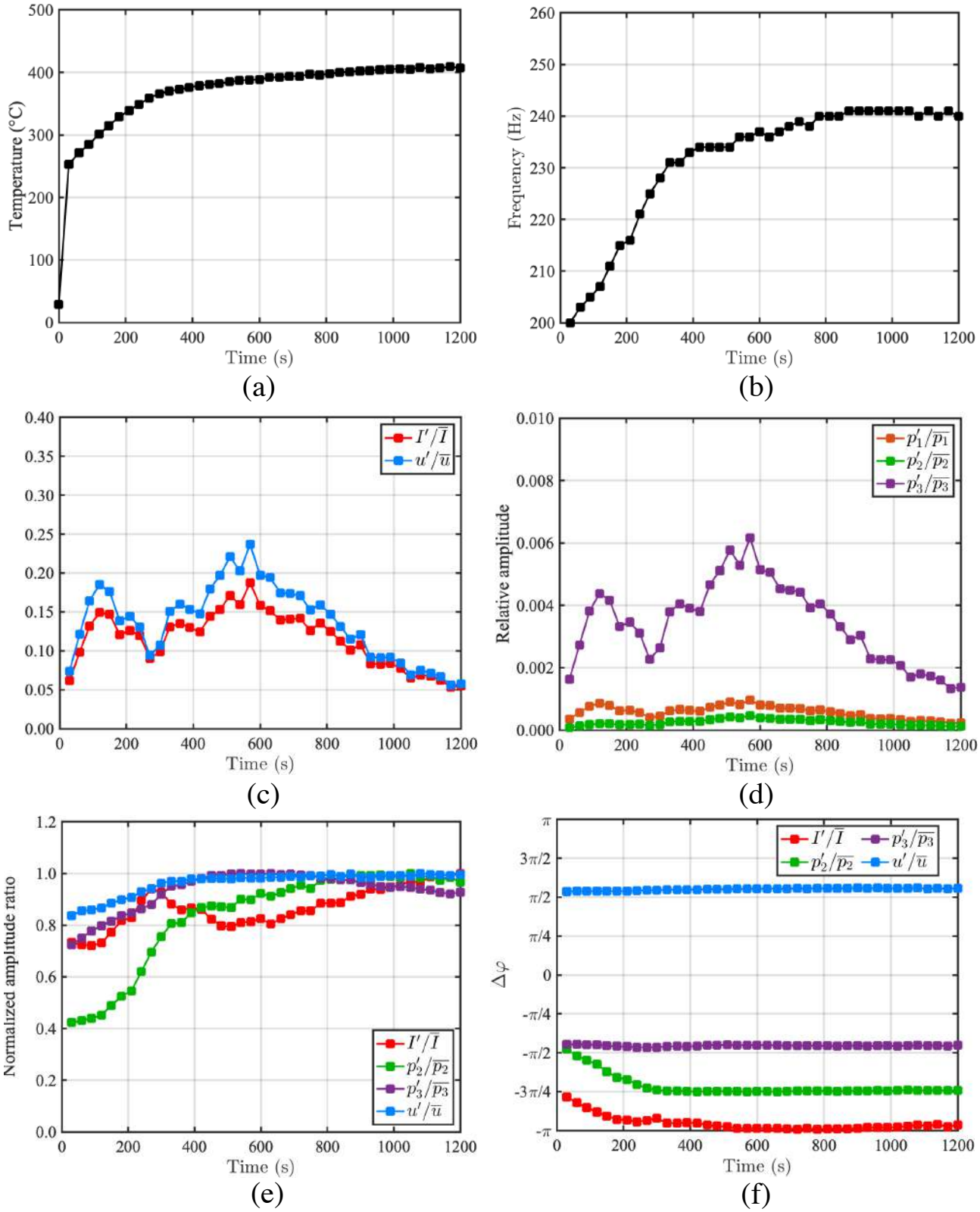

Figure 7.2. – Temporal evolution of (a) the temperature of the recirculation zone T_{RZ}, (b) the instability frequency f_{TAI}, (c-d) the fluctuation levels of $I'/\overline{I}$, $u'/\overline{u}$, $p'_1/\overline{p}_1$, $p'_2/\overline{p}_2$ and $p'_3/\overline{p}_3$ recorded respectively by **PM**, **HW**, **M1**, **M2** and **M3**, and the amplitude ratio normalized by its maximum and (f) the phase lag $\Delta\varphi$ of these fluctuations relatively to $p'_1/\overline{p}_1$ ($e^{-i\omega t}$ convention). The signal $p'_3/\overline{p}_3$ is corrected with the transfer function of the waveguide. "Time" zero indicates ignition

7.3. Low-order acoustic network model

A low-order acoustic network model of the burner has to determined. Assuming that the geometry of the burner can be represented as a succession of connected cylindrical tubes, this model is generated with OSCILOS [117]. Here, the convergent section is discretized as a succession of sections with infinitesimal length, but it can be simplified using an effective length which accounts for the inertia of the mass of gas inside [266]. The inlet is set as a closed condition with a reflection coefficient $\tilde{R} = 1$. The outlet condition is set with an unflanged Levine-Schwinger open condition [267]. Hence, the longitudinal acoustic modes of this model are determined with OSCILOS.

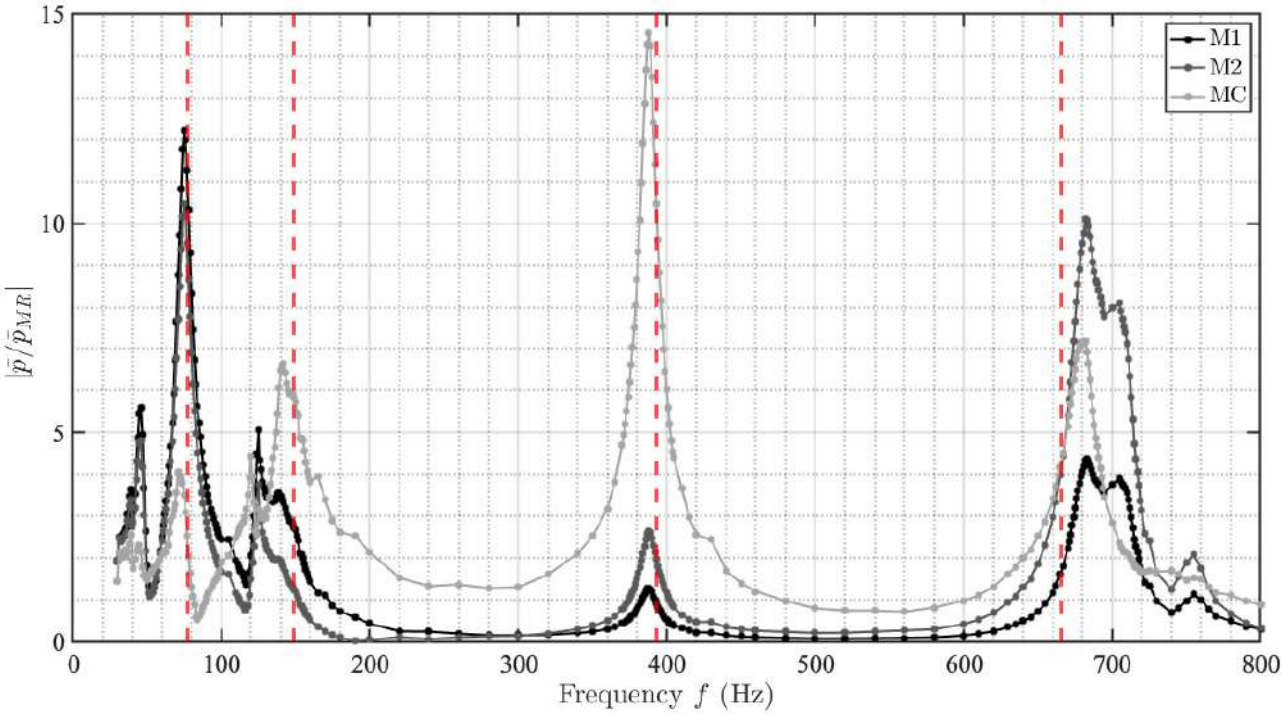

Figure 7.3. – Pressure fluctuations recorded by microphones **M1**, **M2** and **MC** normalized by the pressure generated at the outlet of the burner and recorded by **MR** without flow (Full lines - square dots). Dotted lines correspond to the frequencies of the modes computed by OSCILOS

Results are validated against experimental measurements performed without flow with the diagnostics set presented in Section 2.3.2.2. Figure 7.3 shows the amplitude response of the pressure fluctuations recorded by the microphones **M1**, **M2** and **MC** to those generated at the outlet of the burner and recorded by **MR**. The frequencies of the peaks correspond to the acoustic modes of the burner and are well reproduced by the low-acoustic order model computed by OSCILOS at 75 Hz, 141 Hz, 388 Hz and 683 Hz, with differences inferior to 5% . The shapes of the first three modes are computed and presented in Figure 7.4 by investigating $\mathrm{Re}[\tilde{p}/\tilde{p}_{M1}]$ along the burner, giving both the gain and the phase lag from the pressure measured at the bottom of the burner. They correspond respectively to the 1/4 mode of the whole burner and the 1/4 and 3/4 modes of the full combustion chamber. They are validated against experimental measurements.

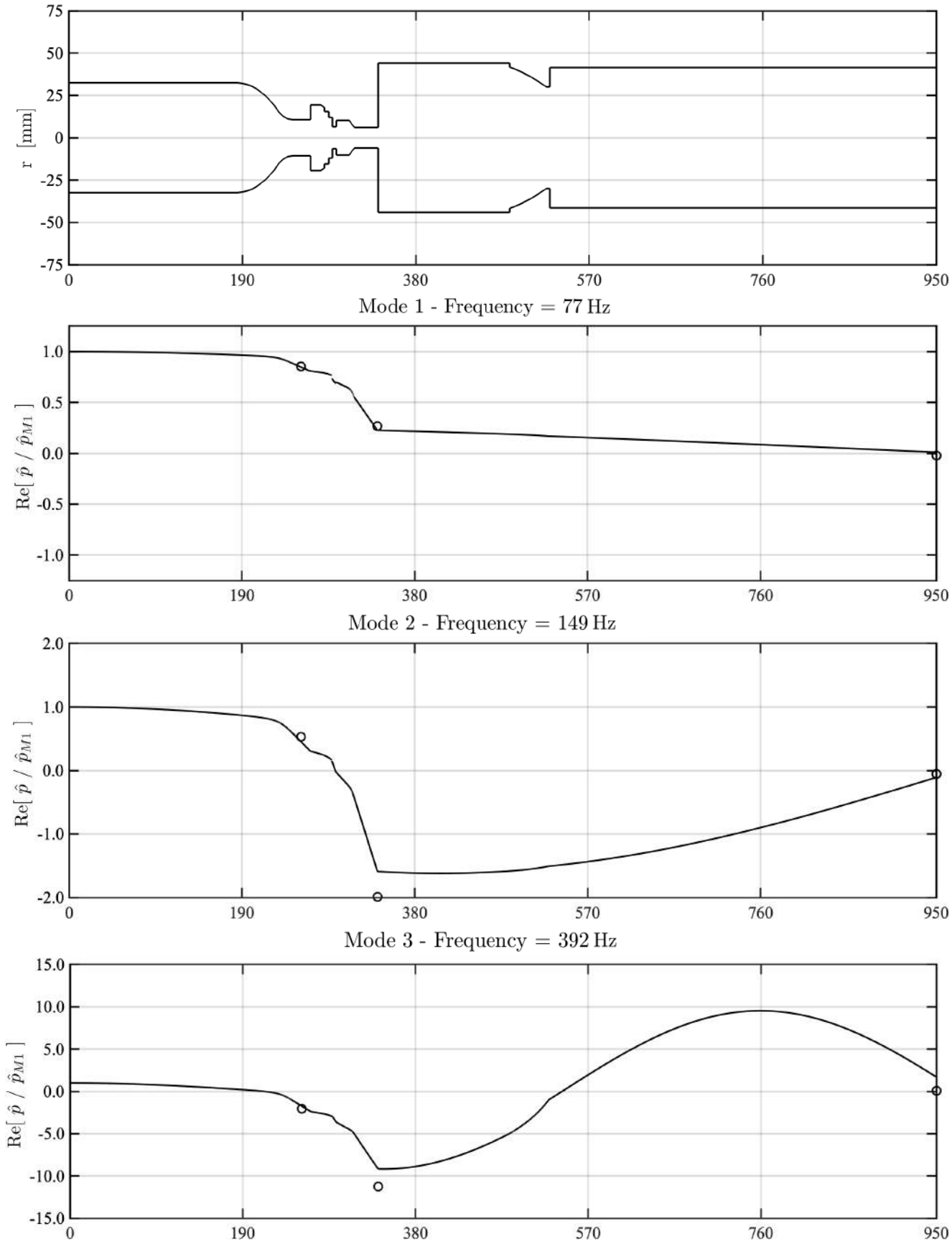

Figure 7.4. – Mode shape of the first three acoustic modes computed by OSCILOS (full lines). Circles represent measurements performed by **M2**, **MC** and **MR**

7.4. Low-order model of the flame response to acoustic disturbances

7.4.1. Preliminary analysis

The way the transfer matrix linking the velocity fluctuations u'_3 at the air injection outlet to the pressure p'_2 and velocity u'_2 fluctuations recorded below the swirler in a uniform flow is described in this section. The acoustic model of the air injector unit is given in Figure 7.5. It considers only the propagation of waves along a combination of straight ducts and compact area changes and discard effects of the mean flow. The acoustic fluctuations between sections S_2 and S_3 are linked by the burner matrix transfer $\tilde{\mathscr{T}}$:

$$\tilde{u}_3 = K\left[\tilde{\mathscr{T}}(2,1)\tilde{p}_2 + \tilde{\mathscr{T}}(2,2)\tilde{u}_2\right] \tag{7.3}$$

where the coefficients $\tilde{\mathscr{T}}(2,1)$ and $\tilde{\mathscr{T}}(2,2)$ of the burner transfer matrix are plotted in Figure 7.6 as a function of frequency. The constant coefficient K models acoustic losses. This model is linear meaning that it does not take into account the level of acoustic fluctuations.

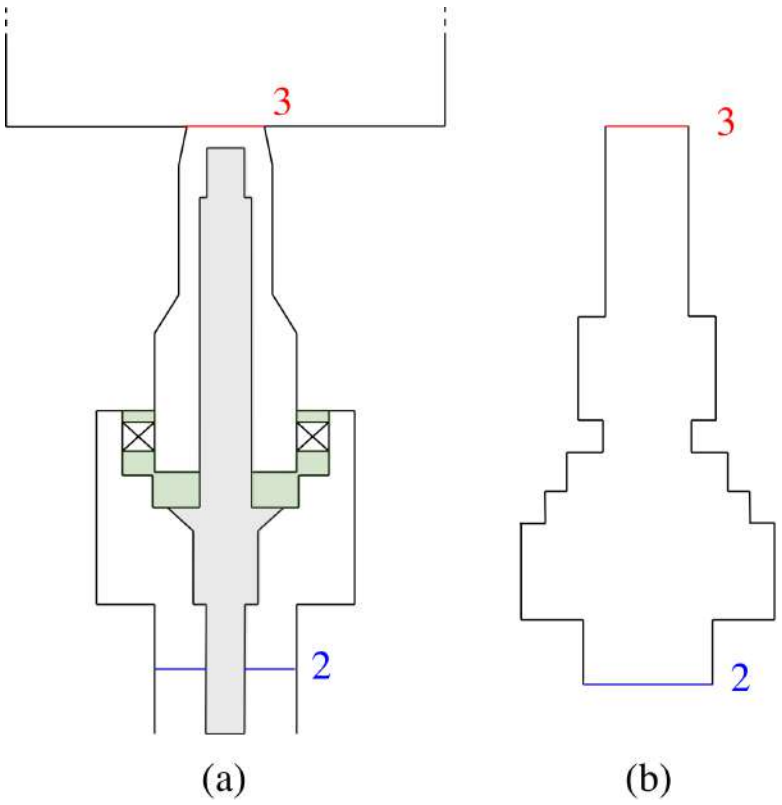

Figure 7.5. – (a) Schematic with dimensions of the air injection unit and (b) its equivalent acoustic model. Red lines represent sections where acoustic measurements are performed.

To validate the acoustic model and determine the value of K, measurements are carried out with the experimental setup presented in Figure 2.12(a). One first determines the transfer function $\mathscr{U}$:

$$\mathscr{U} = \frac{\tilde{u}_3/\overline{u}_3}{\tilde{u}_2/\overline{u}_2} \tag{7.4}$$

where the relative velocity fluctuations $\tilde{u}_2/\overline{u}_2$ and $\tilde{u}_3/\overline{u}_3$ are recorded respectively by HW2 and HW3 shown in Figure 2.12(a) and the bulk velocities in sections S_2 and S_3 are related by:

$$\overline{u}_3 = \frac{R_2^2}{R_3^2}\overline{u}_2 \tag{7.5}$$

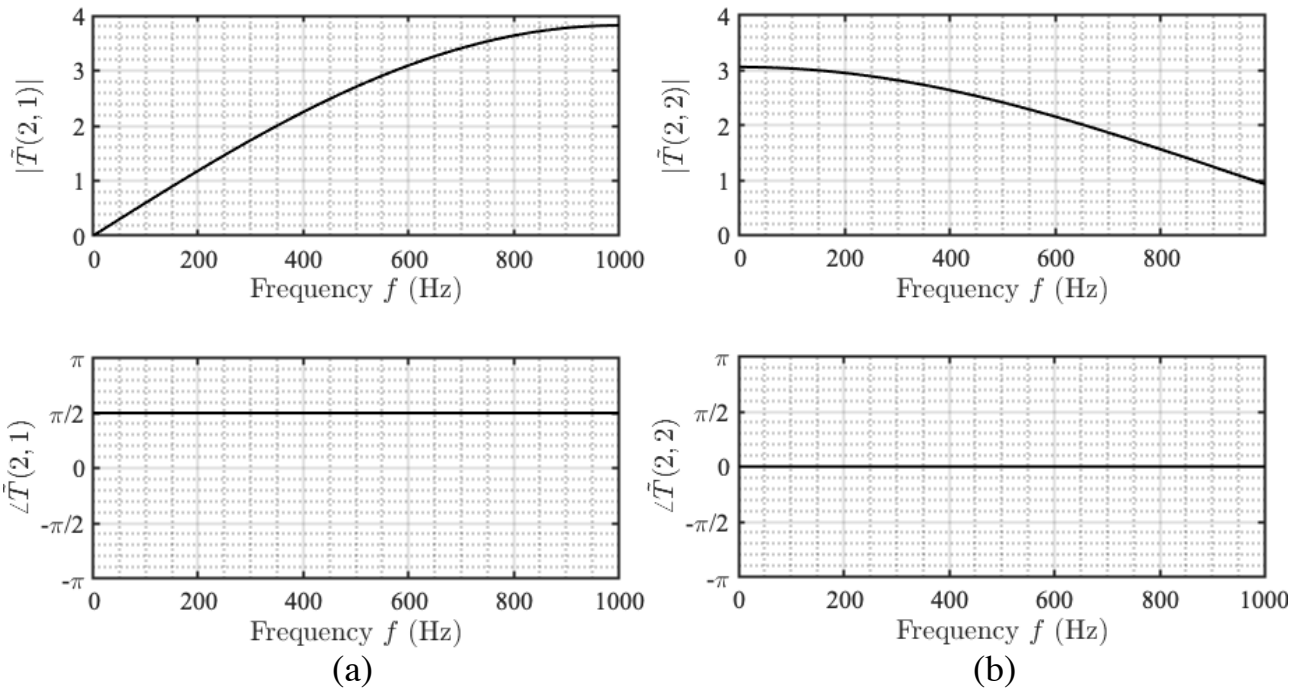

Figure 7.6. – (Up) Gain and (bottom) phase of the paramaters (a) $\tilde{\mathcal{T}}(2,1)$ and (b) $\tilde{\mathcal{T}}(2,2)$ of the global acoustic matrix transfer.

In this expression, R_2 and R_3 designate the radius of the local cross section. Using Equations (7.3)-(7.5), the transfer function $\mathscr{U}$ can also be reconstructed from the modeled burner transfer matrix $\tilde{\mathscr{T}}$:

$$\mathscr{U} = K\frac{\overline{u}_3}{\overline{u}_2}\left[\tilde{\mathscr{T}}(2,1)\frac{\tilde{p}_2}{\tilde{u}_2} + \tilde{\mathscr{T}}(2,2)\right] \tag{7.6}$$

The transfer function $\mathscr{U}$ has been determined for different forcing levels $|u'_3/\overline{u}_3|$ at the combustion chamber inlet. The amplitude voltage used to excite the loudspeaker had to be adjusted to reach the desired fluctuation level $|u'_3/\overline{u}_3|$ for each forcing frequency as shown in Figure 7.7(a-b). Several hundred measurements were necessary to get a precise value of the voltage amplitude V_{sp} that excites the loudspeaker. All transfer functions presented in this study are computed by determining the statistical power and cross-power spectral densities with a Welch periodogram method using the relationships detailed in Appendix A.

The gain and phase lag of the measured transfer function $\mathscr{U}$ in Figure 7.7(c-d) indeed slightly depends on the amplitude of $u'_3/\overline{u}_3$, indicating that the burner response is slightly nonlinear [268**?**]. Differences remain however small except at a few forcing frequencies, as for example near 350 Hz and the burner response will be considered linear in the rest of this study. The value of the coefficient K appearing in Equation (7.3) is then determined by matching the reconstructed transfer function $\mathscr{U}$ with the one measured. There is a very good agreement between the measured transfer function and the reconstructed one for $K = 0.8$ in Figure 7.7(c-d).

More complex models (see for examples [269, 270]) can be used for the burner transfer matrix, but the predictions were considered sufficiently close to measurements for the purpose of this study. These experiments validate the burner transfer matrix model $\tilde{\mathscr{T}}$ which is used in the following to reconstruct velocity disturbances at the burner outlet $\tilde{u}_3$ from acoustic measurements made below the swirler by assuming that $\tilde{\mathscr{T}}$ is not altered by the combustion process.

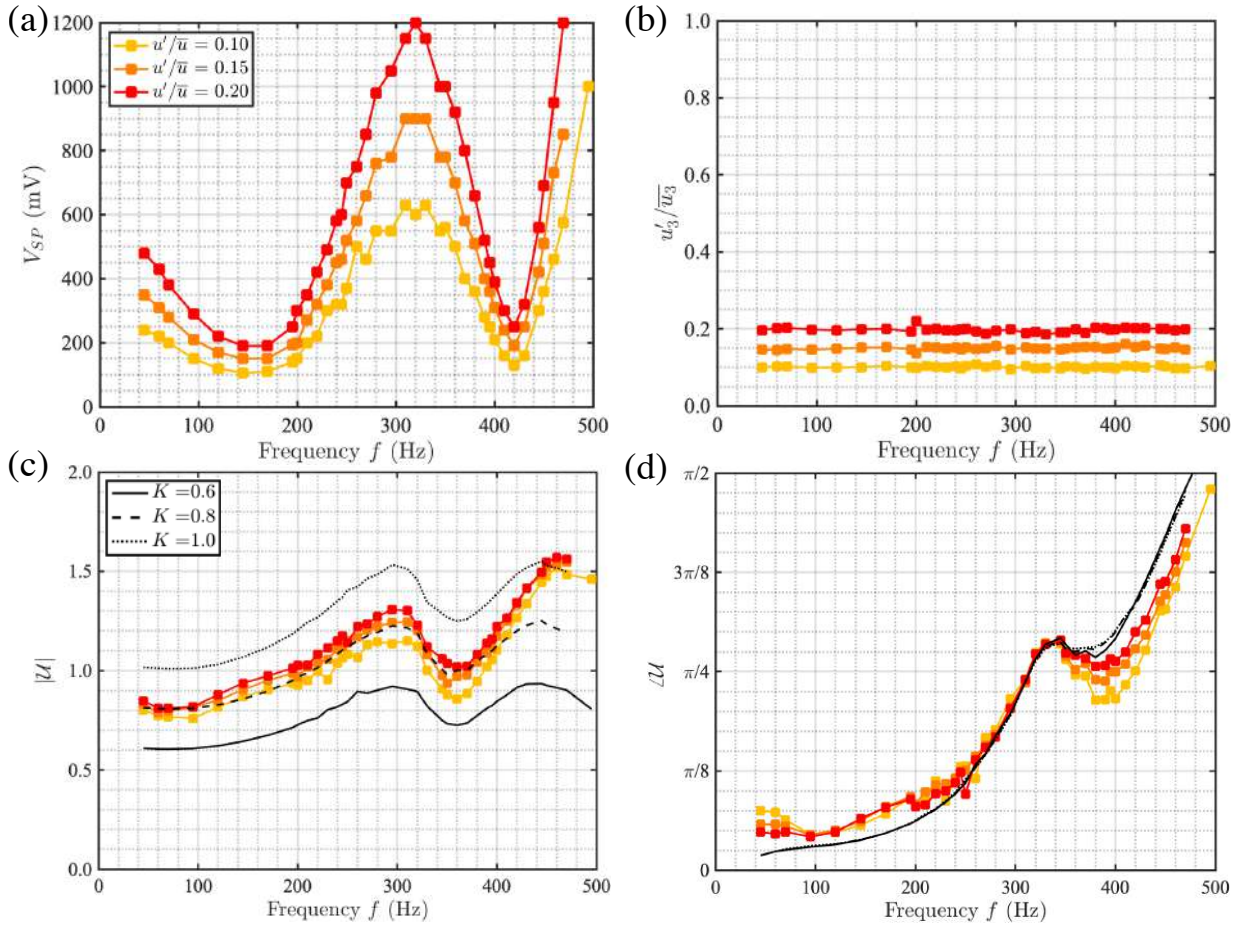

Figure 7.7. – (a) Amplitude V_{sp} of the voltage supplied to the loudspeaker to obtain a velocity fluctuations level $|u'_3/\overline{u}_3|$ at the combustion chamber inlet and (b) effective amplitude $|u'_3/\overline{u}_3|$ recorded by HW3 using V_{sp}. (c) Gain and (d) phase of the transfer function $\mathscr{U}$ for different excitation levels $|u'_3/\overline{u}_3|$ recorded by HW3 ($e^{-\mathrm{i}\omega t}$ convention). All results are presented as a function of the forcing frequency.

7.4.2. Relationship between OH* intensity and heat release rate

For non-premixed injection units as spray injectors, fluctuations of the heat release rate can result from inlet velocity fluctuations $\tilde{u}/\overline{u}$ and equivalence ratio fluctuations $\tilde{\Phi}/\overline{\Phi}$ [132, 133]. Hence, heat release rate fluctuations can be expressed as:

$$\frac{\tilde{\dot{Q}}}{\overline{\dot{Q}}} = F_u(\omega)\frac{\tilde{u}}{\overline{u}} + F_\Phi(\omega)\frac{\tilde{\Phi}}{\overline{\Phi}} \tag{7.7}$$

where Φ is the equivalence ratio at the burner outlet based on indications of the mass flow rates of fuel and air, F_u and F_Φ are the gas velocity and equivalence ratio transfer functions respectively. However, in many fuel/air injection systems, $\tilde{\Phi}/\overline{\Phi}$ can be related to air flowrate disturbances $\tilde{u}/\overline{u}$ only. Hence, it is possible to define a Flame Transfer Function of a Flame Describing Function (FDF) $\mathscr{F}$ using only the input $\tilde{u}/\overline{u}$ but which does not separate the perturbations on $\tilde{\dot{Q}}/\overline{\dot{Q}}$ caused by $\tilde{\Phi}/\overline{\Phi}$ from those caused by $\tilde{u}/\overline{u}$. The FDF $\mathscr{F}$ is determined here using the following relationship:

$$\mathscr{F}(\omega, |\tilde{u}|) = \frac{\tilde{\dot{Q}}/\overline{\dot{Q}}}{\tilde{u}/\overline{u}} = Ge^{\mathrm{i}\varphi_F} \tag{7.8}$$

with

$$\mathscr{F} = F_u + F_\Phi H \tag{7.9}$$

where G and φ_F are respectively the gain and the phase lag of the FDF $\mathscr{F}$, and H is the transfer function linking $\tilde{\Phi}/\overline{\Phi}$ and $\tilde{u}/\overline{u}$ at the burner outlet. The relative heat release fluctuations $\tilde{\dot{Q}}/\overline{\dot{Q}}$ cannot be measured directly. In fully premixed flames, $\tilde{\dot{Q}}/\overline{\dot{Q}}$ is proportional the relative fluctuations of light intensity $\tilde{I}/\overline{I}$ of OH^* radicals produced by the flame and measured by a photomultiplier. In partially premixed flames, acoustic disturbances can also lead to local fluctuations $\tilde{\Phi}/\overline{\Phi}$ of the equivalence ratio. For a stiff fuel injector, in which case the mass fuel rate $\dot{m}_F$ is not modified by the acoustic disturbances in the air channel, fluctuations of the light intensity I occur without a change of the global heat release rate $\dot{Q}$. Hence, $\tilde{I}/\overline{I}$ and $\tilde{\dot{Q}}/\overline{\dot{Q}}$ are not equivalent any more. To determine the relationship between these two fluctuations, the intensity I is measured, firstly, at constant power $\dot{Q} = 7$ kW for different equivalence ratios Φ. In a second set of experiments, the same measurements are repeated at constant equivalence ratio $\Phi = 0.70$ for different powers $\dot{Q}$. Data are presented in Figure 7.8 and the following empirical law is used to fit them:

$$I = k\left(\dot{Q} - \dot{Q}_0\right)(\Phi - \Phi_0)^\beta \tag{7.10}$$

where here $k = 4.30 \times 10^{-4}$ V.W^{-1}, $\beta = 0.20$, $\dot{Q}_0 = 2.3$ kW and $\Phi_0 = 0.43$.

Due to the two additional parameters $\dot{Q}_0$ and Φ_0, the empirical relationships between the OH^* signal and the heat release rate found in this study differ from the one observed in lean partially premixed flames where $I = k\dot{Q}\Phi^\beta$ [271–273]. At fixed $\dot{Q}$, the intensity I decreases when Φ increases with a concave evolution ($\beta < 1$) instead of a convex evolution as often observed for lean partially premixed systems ($\beta > 1$). In the setup from [149], I was found to remain constant over $0.68 < \Phi < 1.14$. In the setup studied by Vignat [63], the light intensity I was found to be constant over $0.9 < \Phi < 1.1$, but it decreased for $0.7 < \Phi < 0.9$. Nonetheless, in [63], the influence of Φ is neglected in the nonlinear relationship between I and $\dot{Q}$. This is why $\tilde{I}/\overline{I}$ was considered as equivalent to $\tilde{\dot{Q}}/\overline{\dot{Q}}$ for FDF measurements conducted in many studies [150, 152, 153, 274]. However, in the present case, Figure 7.8 shows that for $0.50 < \Phi < 0.80$ the influence of Φ on Icannot be neglected . This behaviour is confirmed when investigating a larger range of operating points as shown in Appendix E, for $0.50 < \Phi < 0.80$. As a consequence, equivalence ratio perturbations $\tilde{\Phi}/\overline{\Phi}$ at the burner outlet need to be taken into account to characterizethe relationship between $\tilde{\dot{Q}}/\overline{\dot{Q}}$ and $\tilde{I}/\overline{I}$.

In this work, heat release rate disturbances $\tilde{Q}$ are deduced from OH^* intensity fluctuations $\tilde{I}$ using the following quasi-steady state approximation for small perturbations:

$$\frac{\tilde{\dot{Q}}}{\overline{\dot{Q}}} = \left(\frac{\tilde{I}}{\overline{I}} - \beta\frac{\tilde{\Phi}}{\overline{\Phi}}\frac{\overline{\Phi}}{\overline{\Phi} - \Phi_0}\right)\frac{\overline{\dot{Q}} - \dot{Q}_0}{\overline{\dot{Q}}} \tag{7.11}$$

with $\overline{\dot{Q}} = 7$ kW and $\overline{\Phi} = 0.70$.

Equation 7.11 is used to determine the FDF from measurements of light intensity fluctuations $\tilde{I}/\overline{I}$ for two models of the response of the fuel injection line. The first one is to neglect the influence of $\tilde{\Phi}/\overline{\Phi}$ on $\tilde{\dot{Q}}/\overline{\dot{Q}}$ as in a fully premixed flame. This regime is obtained by assuming that the liquid fuel injected is quickly evaporated at the fuel nozzle and then homogeneously mixed with air before the combustion reaction. In this case, there is no equivalence ratio fluctuations:

$$\tilde{\Phi}/\overline{\Phi} = 0 \tag{7.12}$$

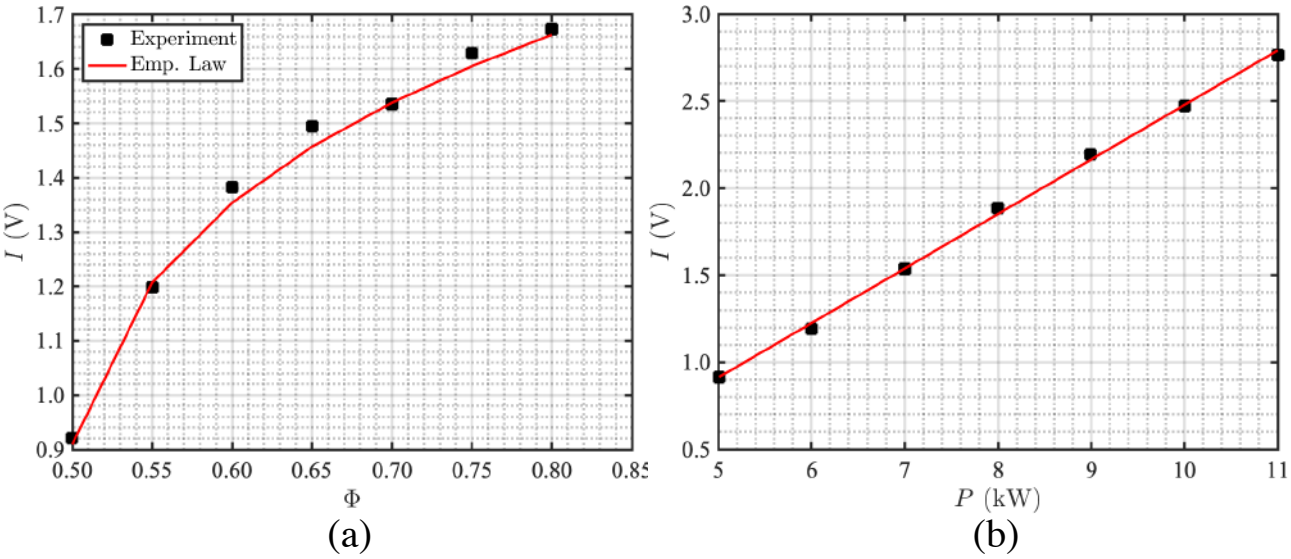

Figure 7.8. – OH^* light intensity recorded by the PM (a) for a fixed thermal power $\dot{Q} = 7$ kW at different equivalence ratios Φ, and (b) for a fixed equivalence ratio $\Phi = 0.7$ at different thermal powers $\dot{Q}$

The second asymptotic case takes into account that the pressure inside the fuel line is several bars with respect to air atmospheric pressure. One may consider that the fuel mass flow rate is not altered by the acoustic disturbances and droplets do not evaporate before reaching the flame. It corresponds to the case of a stiff fuel injector with low volatility liquid fuel injected at low Mach number, where equivalence ratio disturbances are fully determined by the perturbations in the air supply:

$$\tilde{\Phi}/\overline{\Phi} = -\tilde{u}/\overline{u} \tag{7.13}$$

Finally, the interaction between the spray and acoustics need to be considered. The analysis is limited to the modulation of the particle density n_p and the particle velocity u_p. The previous notation u for the gas flow velocity becomes then u_g. Still neglecting the pre-vaporisation, one considers the case of a spray which is perfectly monodisperse with $d_p = d_{10} \approx 15$ μm (see Chapter 6). At low Mach number, equivalence ratio fluctuations are given by:

$$\frac{\tilde{\Phi}}{\overline{\Phi}} = \frac{\tilde{u}_p}{\overline{u_p}} + \frac{\tilde{n}_p}{\overline{n}_p} - \frac{\tilde{u}_g}{\overline{u_g}} \tag{7.14}$$

For instance, if the particles are injected with the same velocity as the mean gas flow (i.e $u_p(0) = \overline{u}_g$), this expression becomes (see Chapter 4):

$$\frac{\tilde{\Phi}}{\overline{\Phi}} = \left[\frac{iSt}{1 - iSt} \left(1 - e^{-\frac{l_f}{\bar{l}_p}} e^{i(k_c - k_a) l_f} \right) - e^{\mathrm{i}(k_c - k_a) l_f} \right] \frac{\tilde{u}_g}{\overline{u_g}} \tag{7.15}$$

Equation (7.15) indicates that equivalence ratio fluctuations $\tilde{\Phi}/\overline{\Phi}$ at the flame location depend on the distance l_f between the spray nozzle and the flame, a mean particle relaxation length $\bar{l}_p$, a convective wavenumber $k_c = \omega/\overline{u}_g$ and the Stokes number St of the particles. Similar but more complex expressions can be derived for $u_p(0) \neq \overline{u}_g$, with an additional dependence to the initial particle-to-gas velocity ratio $u_p(0)/\overline{u}_g$.

7.4.3. Flame Describing Function Measurements

Taking as input the acoustic velocity fluctuations at the air burner outlet $\tilde{u}_3/\overline{u}_3$, Figure 7.9 shows the FDFs $\mathscr{F}$ determined at $\dot{Q} = 7$ kW and $\Phi = 0.70$ for the different models of heat release rate: the premixed case (squares, Equations (7.11) and (7.12)), the fuel stiff case (disks, Equations (7.11) and (7.13)) and the disturbed spray case (triangles, Equations (7.11) and (7.15)).

The impact of the forcing level is briefly described first. In all cases, the FDF gain G only weakly depends on the amplitude $u_3'/\overline{u}_3$ for forcing frequencies below 75 Hz. The gain then slightly decreases when the modulation level $|u_3'/\overline{u}_3|$ increases from 0.10 to 0.20. The phase lag φ_F is relatively insensitive to the perturbation level.

The gain G and phase lag φ_F of the FDFs in Figure 7.9 strongly depend on the selected model for heat release rate perturbations, i.e. they depend on the hypothesis made for the equivalence ratio fluctuations $\tilde{\Phi}/\overline{\Phi}$ appearing in the expression for $\tilde{\dot{Q}}/\overline{\dot{Q}}$.

One considers first the '*premixed case*' when $\tilde{\Phi}/\overline{\Phi}$ are neglected (squares in Figure 7.9), i.e. the OH^* light intensity is directly used to estimate the heat release rate. In this case, the FDF gain G decreases between 15 Hz and 75 Hz and then exhibits a constant plateau until 400 Hz where $0.6 < G < 1$, before again decreasing. Similar plateaux for G were already reported at intermediate frequencies for FDFs based on the OH^* intensity that were measured in different swirl combustors (see e.g. [152, 154, 262]). The phase lag φ_F of the '*premixed case*'evolves roughly linearly with the frequency between $-\pi$ and $3\pi/2$ with a time lag $\tau_F = 2.6$ ms. Examining now the low frequency limit of the FDF for this premixed model, the gain G goes towards 0.75 and the phase lag goes to $-\pi$ as the frequency goes to zero. These values are not consistent with theory for premixed flames, the theoretical low-frequency limits being $G = 0$ and $\varphi_F = 0$ [259]. Furthermore, Mie scattering images recorded from a vertical laser sheet intersecting the spray during combustion shown in Figure 7.10 indicate that a large fraction of the fuel spray is not evaporated when reaching the flame in the TALISMAN setup for these operating conditions.

Results are now examined for the '*stiff fuel injection*' model that combines Equation (7.11) for heat release rate disturbances and Equation (7.13) for equivalence ratio disturbances. The FDF from an isothermal stiff fuel injector is plotted in Figure 7.9 as dashed lines with circle symbols. The gain G exhibits now humps, with values increasing from 0.3 to 1.5 between 15 Hz and 120 Hz. The FDF gain then decreases to 0.3 until 380 Hz before increasing again. These humps possibly hint destabilizing mechanisms and were often reported for FDFs in swirl combustors (see e.g. [82, 149, 150]). Even though the burner configurations are different, the shape of the FDF measured in the TALISMAN setup is also close to the one obtained in the numerical simulations from [260]. The phase lag φ_F determined with the stiff fuel model has roughly the same slope as for the premixed flame model. However, when the frequency goes to zero, φ_F tends with the stiff fuel injection model towards a value slightly below $-\pi/2$. The FDF gain now also features a slope which brings values of the gain towards zero at zero frequency. This value is in agreement with theoretical prediction derived in the low frequency limit for the response of flames with a stiff fuel injector [259]. Further justifications for the cases of spray flame will be provided in the discussion section.

One now examines results obtained for the '*disturbed fuel injection model*' that combines Equation (7.11) and Equation (7.15) to determine the resulting heat release rate disturbances from light intensity fluctuations. In Chapter 6, it was shown that the hollow-cone spray injection was altered by the acoustic forcing for $f = 200$ Hz and $u_g'/\overline{u}_g = 0.20$ in cold flow conditions with oscillations of the spray angle, the particle number density n_p and velocity u_p fields. When pulsating now the flame in the same conditions, Mie scattering images pictured in Figure 7.11 show that the spray is still disturbed in reactive conditions like in the cold conditions. In this case, the hollow-cone fuel spray

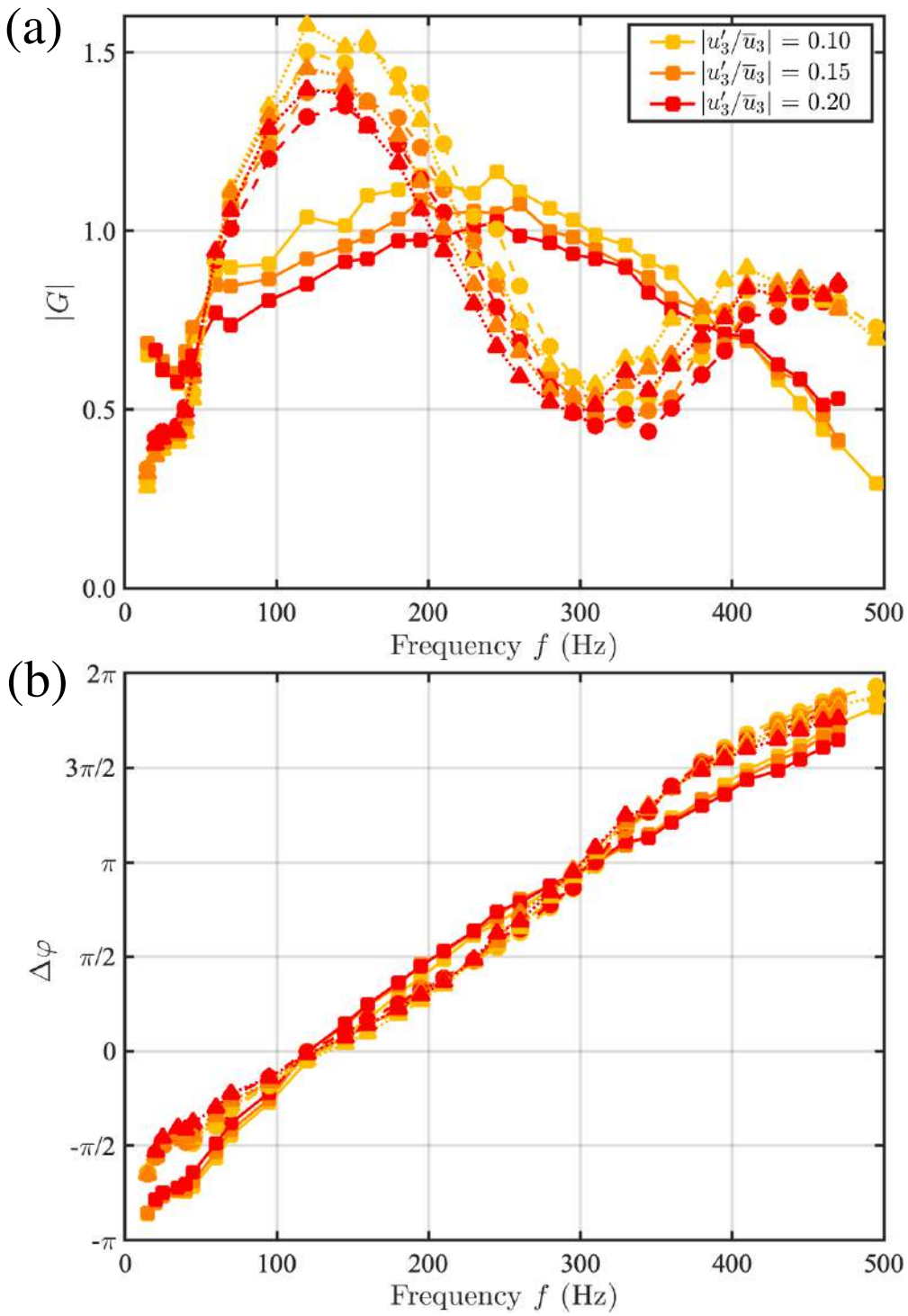

Figure 7.9. – (a) Gain G and (b) phase lag φ_F ($e^{-\mathrm{i}\omega t}$ convention) of the FDF $\mathscr{F}$ for different excitation levels $|u_3'/\overline{u}_3|$ reconstructed with the acoustic transfer matrix $\mathscr{T}$. The FDFs are computed for different relations between $\tilde{\dot{Q}}/\overline{\dot{Q}}$ and $\tilde{I}/\overline{I}$. Full line-square symbols: perfectly premixed flame model Equation (7.12). Dashed line-circle symbols: stiff fuel injection model Equation (7.13). Dotted line-triangle symbols: disturbed fuel injection model Equation (7.15). $\overline{\dot{Q}} = 7$ kW and $\Phi = 0.70$.

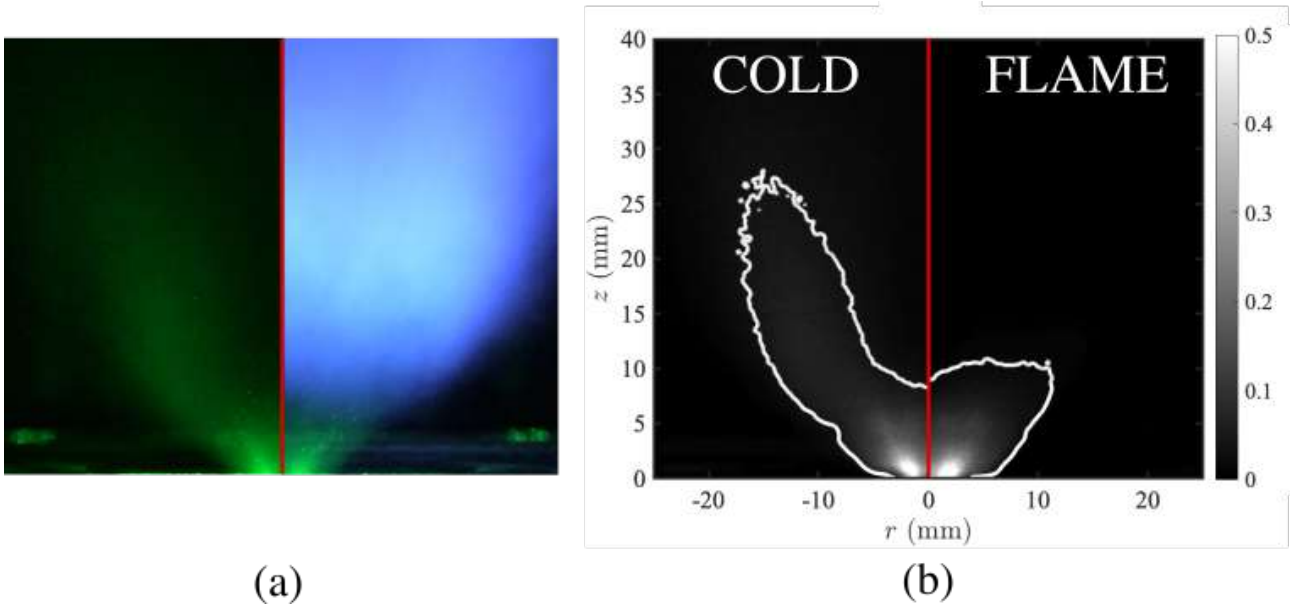

Figure 7.10. – (a) Snapshot of the spray with laser tomography (b) Normalized intensity signal I_{norm} recorded without (left) and with (right) flame obtained by planar Mie imaging in the steady case. The intensity signal I_{norm} is normalized with the maximum value of the intensity. Contours are plotted with Otsu's method [251].

is altered by the acoustic forcing with oscillations of the spray angle, of the particle number density n_p and of the particle velocity u_p fields. This is modeled by Equation (7.14) with $l_f = 13.35$ mm which has been deduced from the Mie scattering images shown in Figure 7.10. The results plotted in Figure 7.9 as dotted lines with triangles are close to those found for the stiff fuel injector response. Deviations with respect to the FDF for stiff fuel injector response (dashed lines, square symbols) lead to a slight increase of the FDF gain G at low frequencies, a reduction of the width of the first hump and a reduction of the peak of the second hump. The FDF phase lag φ_F is barely altered by this correction with respect to the stiff fuel injector response.

7.4.4. Discussions

Reconstruction of $\tilde{\dot{Q}}/\overline{\dot{Q}}$ from light intensity fluctuations with the different models for equivalence ratio disturbances $\tilde{\Phi}/\overline{\Phi}$ have been made with a quasi-steady approximation in Equation (7.11), which is only valid at very low frequencies. At higher frequencies, the flame cannot be considered compact and an improved description of the fuel transport processes including evaporation, convection, diffusion and its mixing with air is needed. Also, the transport model for droplets in Equation (7.15) does not include evaporation which in general cannot be neglected along the droplets path in a combustion process. Nonetheless, despite these limitations, it has been shown that the way the fuel injector response is modeled deeply impacts the low-frequency behavior of the FDF reconstruction from OH^* light intensity fluctuations. In this section, attempt is made to lay the theoretical foundation for determining the appropriate fuel injector response model for spray flames submitted to acoustic disturbances in the air stream in the limit of zero frequency. The objective is to extend the framework of [259] to the case of spray flames.

Only the case of dilute sprays is considered with a large pressure drop through the fuel injector, in which case the fuel mass flowrate is unaltered by the acoustic disturbances in the air stream. The impact of acoustic forcing on primary atomization is also neglected in the following. In this case,

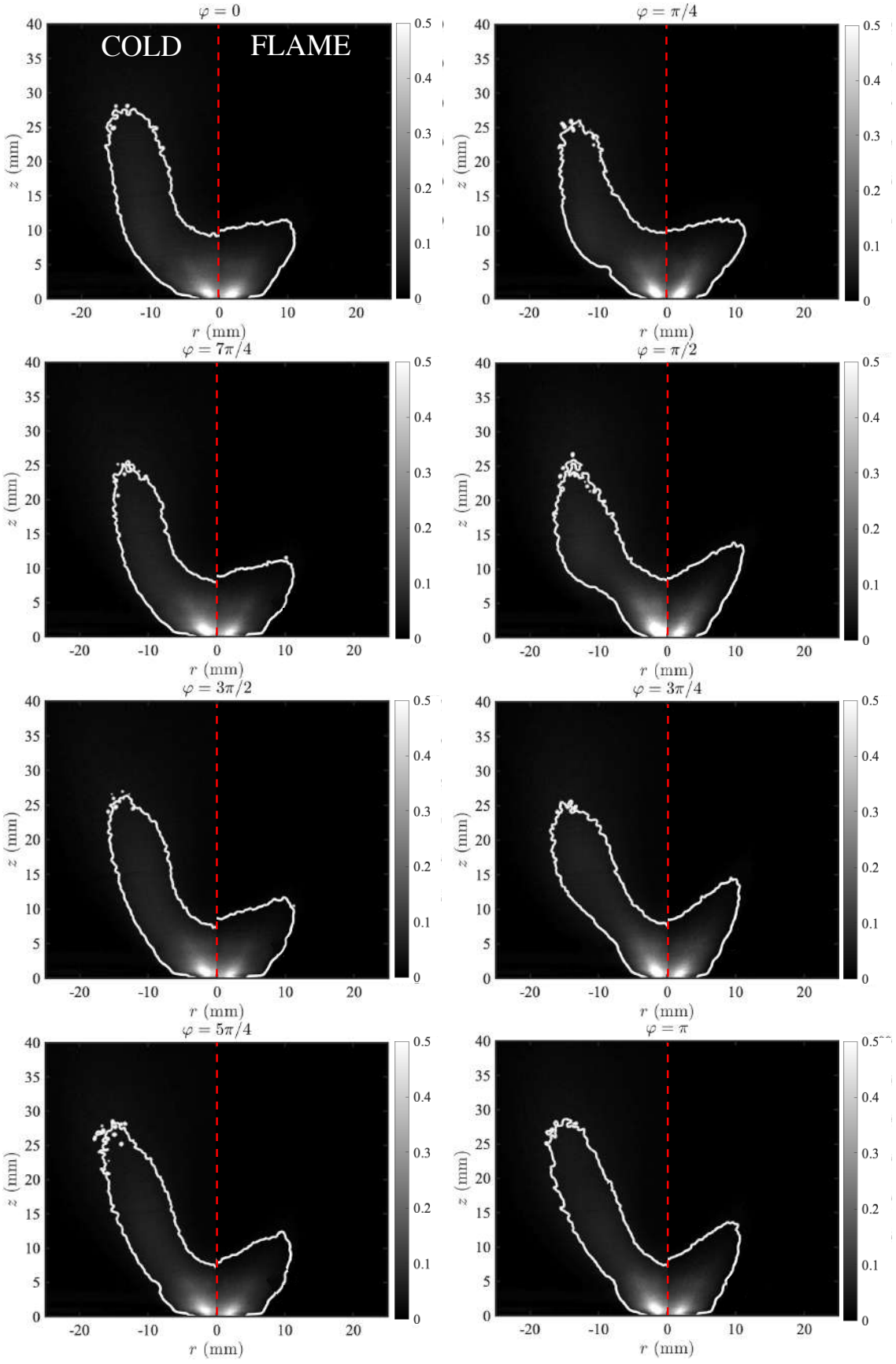

Figure 7.11. – Phase-averaged of the normalized intensity signal I_{norm} measured (a) without and (b) with flame obtained with planar Mie imaging. The intensity signal I_{norm} is normalized with the maximum value of the intensity over all phases. Contours are plotted with Otsu's method [251].

fuel droplets are submitted to a drag force due to the imbalance between the fuel droplet velocity and air velocity and one may define a mean relaxation time $\overline{\tau}_p$ of the injected particles towards the gas velocity or alternatively a mean relaxation particle length $\bar{l}_p = \overline{\tau}_p(0)u_p(0)$, where the subscript 0 denotes the condition at fuel injection. When the particle relaxation length is large compared to the distance between the fuel injector outlet and the flame, i.e. for $l_f/\bar{l}_p \ll 1$, perturbations related to the transport of droplets can be discarded. Also, particle velocity disturbances $\tilde{u}_p$ and in particular droplet number density fluctuations $\tilde{n}_p$ being mainly advected by the mean gas flow disturbances, they will not influence the transport of fuel droplets over the distance l_f if this distance remains small with respect to the wavelength $\lambda_g = \overline{u}_g/f$ of disturbances convected by the gaseous stream, i.e. when $l_f \ll \lambda_c$.

As a consequence, if $l_f/\bar{l}_p \ll 1$ or $l_f/\lambda_g \ll 1$, the liquid fuel injection response to acoustic perturbations in the gaseous stream can be considered with the standard definition of a '*stiff fuel injection*'. In all other cases, acoustic-spray interactions have to be included in the air-fuel injection model. In the case explored in Figure 7.9, $l_f/\bar{l}_p \approx 1.5$ and $l_f/\lambda_g \approx 0.25$, explaining why differences for $\mathscr{F}$ between the '*stiff fuel injection*' and the '*disturbed fuel injection model*' were small in the frequency range explored below 500 Hz.

Considering now evaporating droplets, a characteristic length $\bar{l}_{ev}$ of the evaporation process can be defined analogously using $l_{ev} = \tau_{ev}u_p(0)$, with the characteristic evaporation time τ_{ev} that can be estimated with the D^2-law for example. Hence, when $l_f/l_{ev} \ll 1$, the spray can be considered as isothermal. Otherwise, heating and evaporation of the droplets have to be included in the air-fuel injection model. As a conclusion, the expression retained to determine equivalence ratio perturbations $\tilde{\Phi}/\overline{\Phi}$ at low frequencies has to be selected according to the values of $l_f/\bar{l}_p$ and l_f/l_{ev}.

The reason why the low-frequency limit of φ_F for an isothermal spray flame should be $-\pi/2$ is now clarified. At very low-frequencies, the spray flame can be considered compact and modelled by a flame sheet. For spray flames operating at globally lean conditions, heat release perturbations resulting from a monodisperse fuel spray are given in this case by:

$$\frac{\tilde{\dot{Q}}}{\overline{\dot{Q}}} = \frac{\tilde{u}_p}{\overline{u_p}} + \frac{\tilde{n}_p}{\overline{n}_p} \tag{7.16}$$

Expressions for the perturbations $\tilde{u}_p/\overline{u}_p$ and $\tilde{n}_p/\overline{n}_p$ can be derived. Only the case with $u_p(0) = \overline{u}_g$ is developed here. However, it can be shown that the more general case $u_p(0) \neq \overline{u}_g$ leads to the same results for the low-frequency limits. The outcome of this derivation leads for $u_p(0) = \overline{u}_g$ to the following analytical expression for the FDF $\mathscr{F}$ of an isothermal monodisperse spray impinging a planar flame:

$$\mathscr{F} = (1 - \exp(\mathrm{i}k_c l_f)) - \left(1 - \frac{1}{1 - \mathrm{i}St}\right)\left(1 - \exp(-l_f/\bar{l}_p)\exp(\mathrm{i}(k_c l_f)\right) \tag{7.17}$$

The low-frequency limit of the gain $G = 0$ is immediate. To obtain the low-frequency limit of phase lag φ_F, a series expansion to the leading order of Equation (7.17) yields when $\omega \to 0$:

$$\mathscr{F}(\omega \to 0) \approx -\mathrm{i}\left[\left(1 - \exp(-l_f/\bar{l}_p)\right) St + k_c l_f\right] \tag{7.18}$$

This expression confirms that the low-frequency limit of the phase lag φ_F is $-\pi/2$ for the spray flames considered with the '*disturbed fuel injection model*'. These limit values are also valid for the

'*stiff fuel injection*' as shown by performing a series expansion to the leading order of Equation (7.18) when l_f/l_p or l_f/λ_c go towards zero. One obtains in these cases:

$$\mathscr{F}(\omega \to 0, l_f/\bar{l}_p \text{ or } l_f/\lambda_c \to 0) \approx -\mathrm{i}k_c l_f \tag{7.19}$$

Therefore, being consistent with the low-frequency limits of spray flames with a stiff fuel injector, the FDF deduced with Equations (7.11) and (7.15) slightly improve the results for $\mathscr{F}$ at low frequencies. The deviation from the theoretical limits $\lim_{\omega\to 0} G = 0$ and $\lim_{\omega\to 0} \varphi_F = -\pi/2$ observed in Figure 7.9 might result from partial evaporation of the droplets and mixing of the evaporated fuel with air that takes place along the fuel path from the nozzle tip to the reaction front.

7.5. Prediction of the thermoacoustic instability

In order to know the excited mode among the different acoustic modes determined in Section 7.3, computations are first performed with OSCILOS using a steady heat source at the combustion chamber inlet i.e a passive flame model. In OSCILOS, the gas temperature upstream the combustion chamber is set to 293.15 K , while the temperature of the burnt gas T_b in the combustion chamber is determined from measurements recorded at 3 different locations: in the outer recirculation zone, at the base and at the end of the steel tube. They are measured using a pair of thermocouples R with bead ends of different diameters (0.68 mm and 1.55 mm) in order to correct the radiation error [275]. The recorded temperatures are respectively about 1385 K, 1314 K and 1016 K. Pondering these values by the length of the square chamber and the steel tube, the hot gases have an average temperature about 1200 K.

OSCILOS simulations are performed for 3 different T_b corresponding to the minimum, average and maximum temperature recorded in the combustion chamber, respectively 1016 K, 1200 K and 1385 K. As shown in Figure 7.12, the solver predicts a single acoustic mode between 0 and 500 Hz corresponding to the Mode 2 of the cold case which is the quarter wave of the combustion chamber. Thus, it shows that the limit cycles of the instability occur around the second acoustic mode of the system. When varying the temperature of the hot gases from 1016 K to 1385 K, the mode relative amplitude $|\tilde{p}/\tilde{p}_{M1}|$ and the mode frequency increase respectively from 5 to 6.3 and from 247 Hz to 283 Hz Hence, the discrepancy between the computed and the measured mode is the result of the original difference obtained in cold situations and the incertitude on the hot gas temperature. Due to the considerable length of the whole combustion chamber (614 mm), the hot gas temperature can vary from 1016 K at the inlet of the combustion chamber to 1385 K at its outlet. Furthermore, the unsteady flame response can shift the instability frequency of the acoustic mode.

Finally, OSCILOS simulations are performed with a unsteady heat source, using the FDFs measured in Section 7.4 with $T_b = 1200$ K. The results are shown in Figure 7.13 and are compared to experimental measurements recorded during self-excited oscillations as presented in Section 7.2. For each FDF considered, the excited frequency predicted is roughly the same as the one predicted for the steady heat source. The structure of the mode computed upstream the combustion chamber does not change with the FDF and corroborates the experimental measurements. However, the amplitude of the quarter-wave mode computed increases when using the corrected FDFs and gets closer to the amplitude measured, reducing the difference from 26% to 9%.

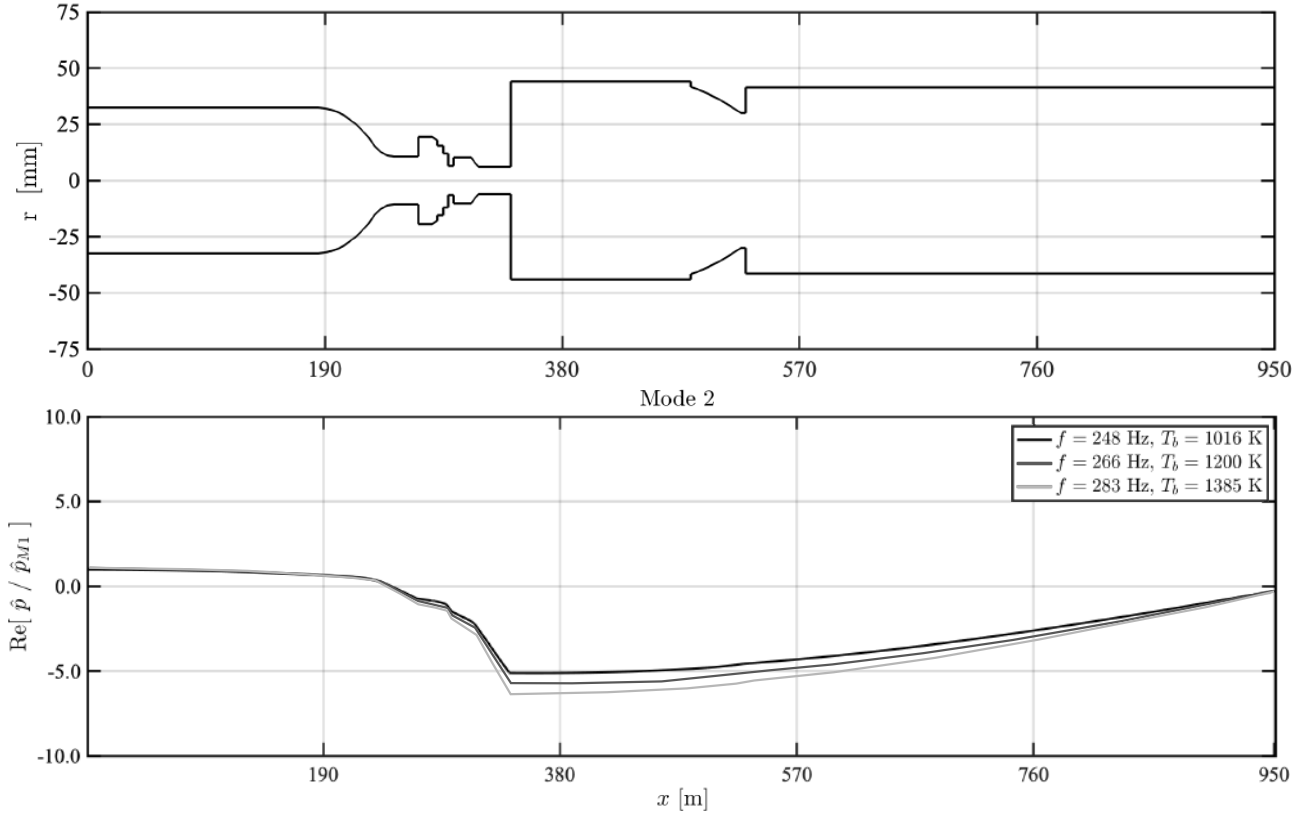

Figure 7.12. – Acoustic geometry of the burner and shape of the second acoustic mode computed by OSCILOS gave by $\mathrm{Re}[\tilde{p}/\tilde{p}_{M1}]$ for $T_b = 1016\ K$, $T_b = 1200\ K$ and $T_b = 1385\ K$ considering a steady heat source.

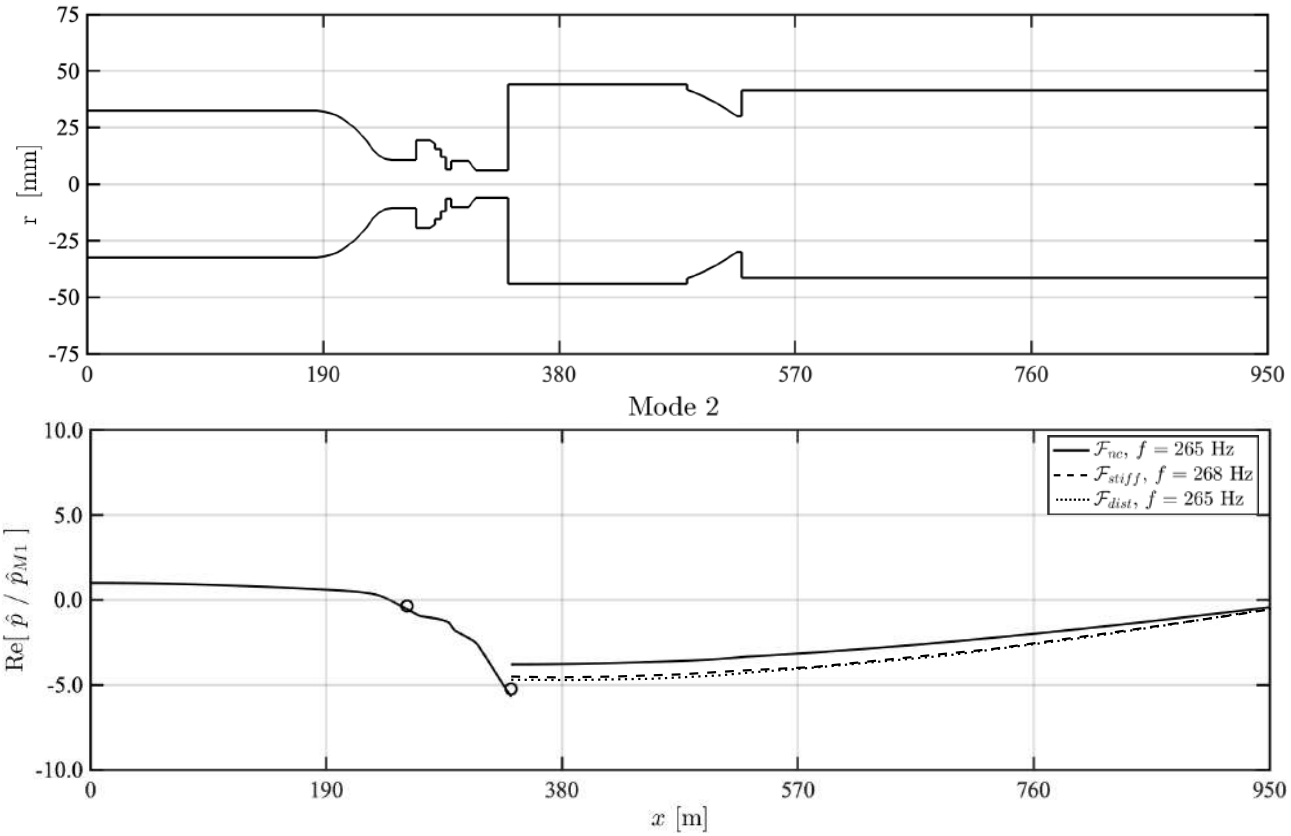

Figure 7.13. – Acoustic geometry of the burner and shape of the second acoustic mode computed by OSCILOS gave by $\mathrm{Re}[\tilde{p}/\tilde{p}_{M1}]$ with T_b = 1200 K and unsing a unsteady heat source. The acoustic response of the heat source are given through the FDF non corrected (full line), and the FDF corrected assuming a stiff injection (dashed lines) and a disturbed injection (dotted lines) presented in Section 7.4. Circles represent the measurements performed by **M2** and **M3**

7.6. Conclusion

A dynamic analysis of the TALISMAN burner has been performed. For a given configuration, self-sustained oscillations occur in the burner. They were shown to be very sensitive to the temperature of the burnt gases. While the frequency and the phase lag between the recorded signals are stabilized once the burner has reached its steady thermal state, the amplitude of the oscillations changes over the period of observation before decreasing monotonously after a certain point.

Low-order model of the whole burner has been built and simulated under OSCILOS. The acoustic behaviour of the burner in cold conditions was successfully reproduced, obtaining the same acoustic modes as in experiments. A low-order model of the spray flame was also provided using FDFs. On the one hand, they are based on the gas velocity fluctuations at the flame location. Thus, in order to reconstruct them from upstream measurements, acoustic transfer matrices were analytically derived and tuned according to experimental measurements. On the other hand, FDFs required measurements of the heat release rate of the flame which are commonly performed through the measurements OH^* signal emitted by the flame.

The relation between OH^* light intensity fluctuations I' emitted by a flame and fluctuations of its heat release rate $\dot{Q}$ has been investigated for a swirled spray flame operating at globally lean conditions. In particular, the proportionality of these signals has been questioned. It has been shown that in the TALISMAN setup the fuel spray is not instantaneously prevaporized and premixed with the air at the burner outlet, indicating that equivalence ratio fluctuations contribute also to fluctuations of the heat release rate.

Therefore, the relation between heat release rate fluctuations and OH^* intensity disturbances needs to be corrected by considering the impact of the resulting equivalence ratio fluctuations. In this study, they have been inferred with a quasi-steady state model based on an empirical scaling law determined for steady injection conditions. Results for the FDF have then been presented by considering different models for the response of the fuel injector.

FDF determined as if the reactants would have been perfectly premixed have been compared to the FDFs deduced for a stiff fuel injector response and for a disturbed spray injection model. The last model considers a disturbed non-evaporating monodisperse spray, where the transport of the droplets from the fuel injection to the flame is modulated by the pulsated air flow.

It has been shown that the reconstructed FDFs feature substantial differences for their gain and their phase lag at low-frequencies depending on the selected model for the fuel injector response. Over the frequency domain investigated, the FDF with the premixed flame model features a roughly constant gain while the FDFs deduced with the stiff fuel and disturbed fuel injection models have a bell shape. Due to the small distance between the spray nozzle and the flame, only slight differences on the FDF gain were found between the two latter FDF models for frequencies lower than 500 Hz.

It has been shown that (i) the low-frequency limits of the FDF obtained with the well premixed model do not comply with theoretical limits of a perfectly premixed flame, while (ii) the FDF deduced with the stiff fuel injector model and disturbed fuel injector model yield low frequency limits of the gain G and phase lag φ_F that are consistent with theoretical predictions for the cases considered: $G = 0$ for the gain and $\varphi_F = -\pi/2$ for the phase lag at zero frequency.

Finally, theoretical expressions have been derived for the low frequency limit of the FDF of spray flames featuring a large pressure drop at the fuel injector outlet. These expressions show that the zero limits of the FDF gain and phase lag depend on the distance travelled by the fuel droplets l_f from their injection location to the flame, the mean particle relaxation length $\bar{l}_p$ of the droplet velocities to

the gas stream velocity, the wavelength λ_g of disturbances advected by the gaseous flow and a particle evaporation length l_{ev}. In the experimental conditions explored, when $l_f/\bar{l}_p \ll 1$ and $\bar{l}_p/\lambda_g \ll 1$, they reduce to $G = 0$ and $\varphi_F = -\pi/2$ as for a perfectly stiff fuel injector.

When finally coupling the low-order acoustic model with the FDF on OSCILOS, the corrected FDFs are better able to reproduce the amplitude of the quarter-mode in the combustion chamber. Further investigations are still required to know the limits of the corrections.

Chapter 8

A thermoacoustic instability precursor based on the acoustic flux at the combustion chamber inlet

Évidemment Alcide évoluait dans le sublime à son aise et pour ainsi dire familièrement,-il tutoyait les anges, ce garçon, et il n'avait l'air de rien. Il avait offert sans presque s'en douter à une petite fille vaguement parente des années de torture, l'annihilement de sa pauvre vie dans cette monotonie torride, sans conditions, sans marchandage, sans intérêt que celui de son bon cœur. Il offrait à cette petite fille lointaine assez de tendresse pour refaire un monde entier et cela ne se voyait pas. Il s'endormit d'un coup, à la lueur de la bougie. Je finis par me relever pour bien regarder ses traits à la lumière. Il dormait comme tout le monde. Il avait l'air bien ordinaire

– Louis-Ferdinand Céline, *Voyage au bout de la nuit, 1932*

When TAI can potentially happen in a combustion chamber, they have to be detected before serious damage to the system can be done to the system. Restricted until now to the monitoring of the pressure fluctuations in the combustion chamber, the arsenal of the possible tools used to detect upcoming TAI has to be widened. In the present chapter, this topic has been investigated using the swirl-stabilized spray burner TALISMAN. A new precursor of TAI has been found based on the acoustic flux recorded at the inlet of the air injection. To compute it, a global acoustic energy balance is applied on the whole combustion chamber. Its performances are evaluated and compared to other indicators commonly used for online monitoring. Furthermore, the method is applied to a different burner with complex stability charts to know its capacity of generalization. Finally, it is discussed the possibility of developing and validating a new post-processing method base on Deep-Learning for the detection of impending TAI.

Overview

8.1. Chapter Introduction

Gas turbines are prone to thermo-acoustic instabilities (TAI) that need to be prevented during operation [51, 52]. An online monitoring of the combustion state is useful to watch for potential occurrence of dynamic combustion issues [276–278]. Hence, the detection of a specific signature in the turbulent reacting flow inside the gas turbine prior to impending TAI is an active field of investigation.

Lieuwen [279] used an uncoupled set of linear, second-order oscillator model to describe the thermo-acoustic oscillations that occur prior to large instabilities. He estimated the combustor damping coefficient and observed its evolution when varying the flow velocity to quantify the proximity to an instability. Yi and Gutkmark [280] applied the same low-order model but used a frequency analysis to compute the damping rate, and found similar trends as in Lieuwen [279]. Nonetheless, these methods require a mathematical model of the TAI and a linear description of the system dynamics prior to instability was assumed. These conditions are difficult to meet in practice. Combustors exhibit in general a nonlinear dynamics with intermittent pressure oscillations and noise-induced transitions to instabilities and large synchronized bursts followed by stochastic sequences with reduced root mean square (RMS) fluctuations levels [281]. Moreover, the estimation of acoustic damping is harsh when the frequency spectrum shows several resonant peaks.

To cope with the different limitations of the linear approach, nonlinear and complex dynamic system tools have also been developed over the last decade. Much of the work has been undertaken at Madras Indian Institute of Technology. New precursors have been introduced to characterize the transition from a chaotic state with multiple length and time scales that characterize combustion noise to intermittent bursts and finally a limit cycle with large pressure oscillations with a predominant time and length scale [282–285]. For instance, a multi-fractal analysis allowed to characterize this transition by a drop of the Hurst exponent H^2 (or H) close to 0, indicating a very strong correlated signal typical of quasi-periodic signals and a loss of multi-fractality nature [286]. A wide set of precursors to detect the onset of TAI has been been reviewed by Sujith and Unni [287]. These precursors are very difficult to link to a direct physical representation of flame dynamics or to quantities commonly used in combustion to describe the stability of a flame. Furthermore, precursors derived from nonlinear dynamic tools generally rely on the detection of intermittent bursts during the transition from stable to unstable states. However, this phase with strong intermittency does not occur in all combustors for impending TAI, which makes these precursors more difficult to use in these cases.

In this study, a swirl spray combustor featuring TAI at some operating conditions is considered. The signals recorded by different sensors are examined and used to determine a stability chart with safe, warning and critical regions with respect to TAI. Based on a global acoustic energy balance over the combustion chamber, the acoustic flux entering the combustion chamber is reconstructed from acoustic pressure and velocity measurements. This acoustic flux is then envisaged as a precursor of TAI and its performance is compared to standard precursors.

8.2. Experimental setup and stability chart

The thermo-acoustic state of the combustor is investigated at globally lean operating conditions, with $0.65 < \phi < 0.80$ and for a thermal power range 5 kW$< P <$ 10 kW. In these experiments, ϕ designates the global equivalence ratio deduced from the fuel and air mass-flow rate indications. Experiments are conducted at constant ϕ, varying P from 5 to 10 kW by increasing simultaneously the air mass-flow rate $\dot{m}_{air}$ and the fuel mass-flow rate $\dot{m}_f$. For each operating condition (P, ϕ) considered, once the indications from $\dot{m}_{air}$, $\dot{m}_F$ and T_{RZ} are stabilized, the signals from the PM, HW and M1 to M3 are recorded at sampling frequency $f_s = 16384$ Hz over 10 s. The same procedure is

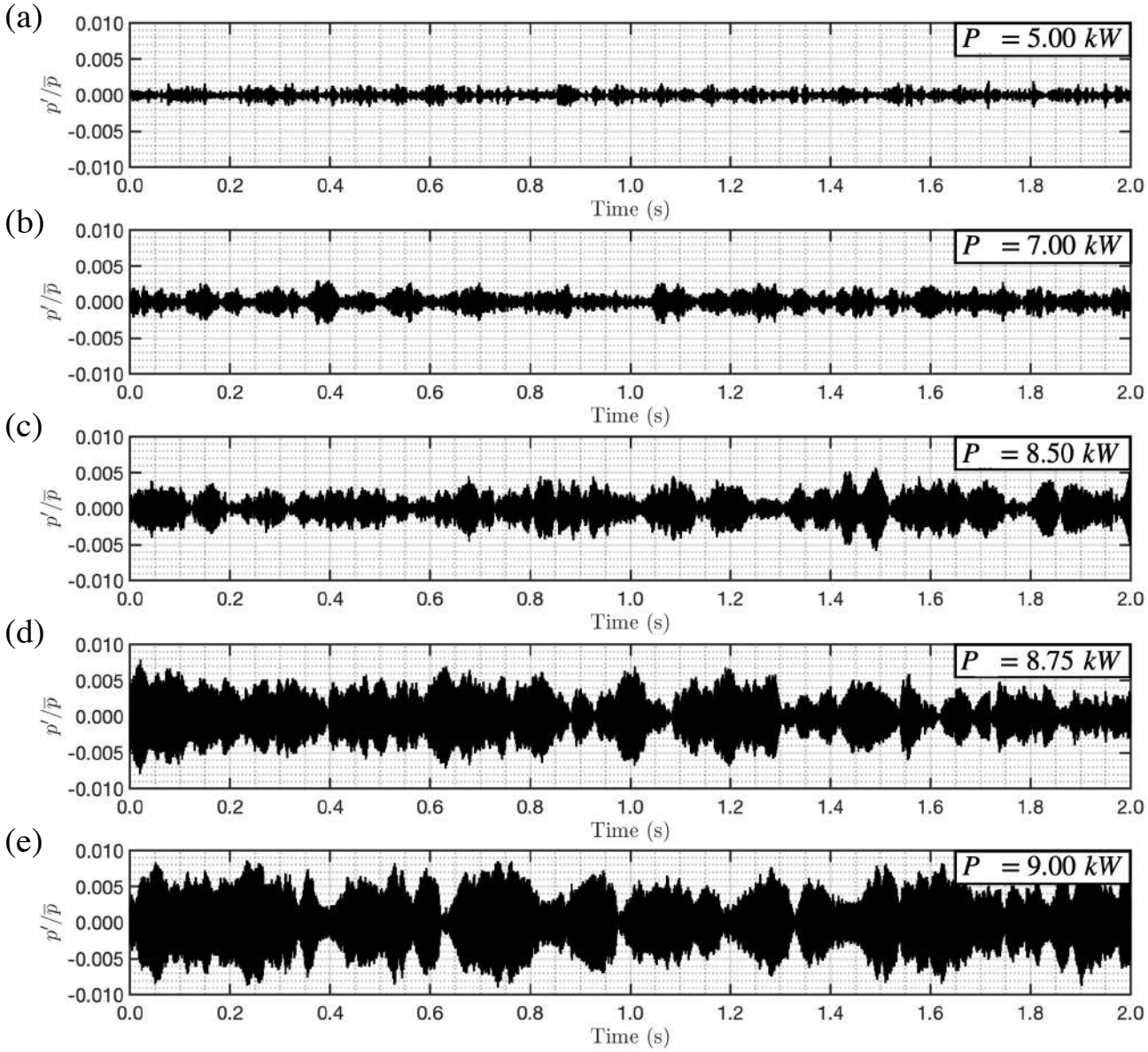

Figure 8.1. – Acoustic pressure time traces $p'/\bar{p}$ recorded by M3 at $\phi = 0.75$ for different thermal powers P indicated at the top-right of each plot.

repeated for each operating condition investigated.

Figure 8.1 shows the evolution of the acoustic pressure fluctuations $p'/\bar{p}$ detected by M3 when the power P increases from 5 to 9 kW and the equivalence ratio $\phi = 0.75$. Signals are made dimensionless by the mean chamber pressure $\bar{p}$. At $P = 5$ kW, the acoustic activity remains low with small bursts reaching an average amplitude around 0.08% of the mean pressure $\bar{p}$ and lasting between 20 to 100 ms with an average duration of 40 ms. When the power increases to $P = 7$ kW, the amplitude of the fluctuations p' almost doubles reaching now in average 0.14% of the mean pressure. The signal features also more bursts with amplitudes covering a wider range from 0.10% to 0.25% of the mean pressure. The average duration of the pressure bursts also increases to 45 ms. When the power is further increased to $P = 8.5$ kW, bursts now last between 20 to 160 ms with an average duration of 50 ms and their amplitude spreads between 0.15% and 0.50% with an average amplitude of 0.28% of the mean pressure. A small increase from $P = 8.5$ kW to $P = 8.75$ kW results in substantial changes of

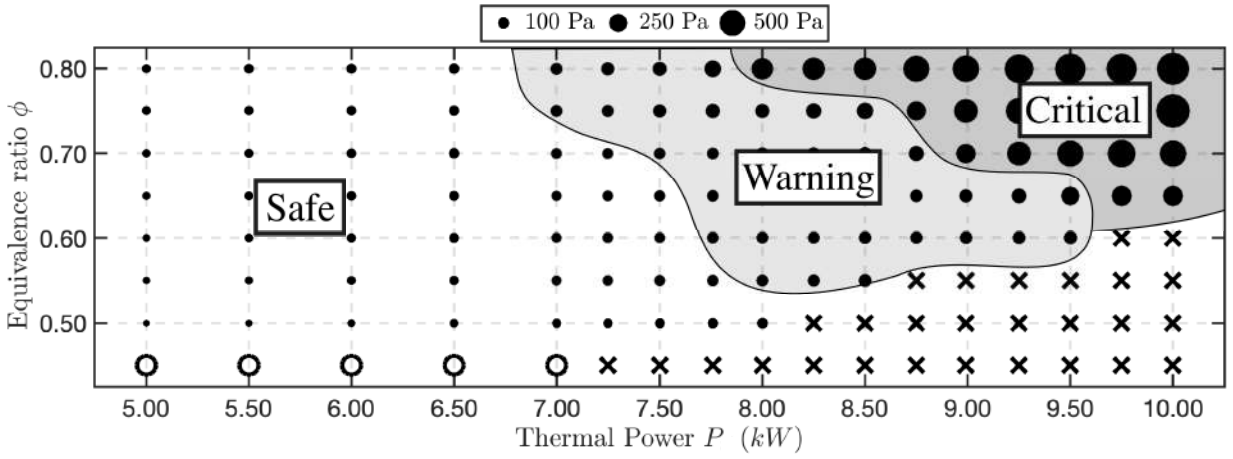

Figure 8.2. – Stability chart of the TALISMAN burner. The diameters of the filled disks are proportional to the RMS pressure fluctuation level p_{RMS} measured by M3.

the acoustic pressure signature. The signal features longer periods of several hundreds of milliseconds with large oscillations levels. The bursts are longer with amplitudes spanning from 0.25% to 1.00% and an average amplitude of 0.50% of the mean pressure. They last up to 200 ms with an average duration of 58 ms. At $P = 9$ kW, the pressure signal shows almost no time intervals with reduced acoustic fluctuations over the 10 s record. The bursts feature in this case high amplitudes varying from 0.50% to 1.00% with an average amplitude of 0.70% of the mean pressure and mean duration of 67 ms. Similar observations are made for all other signals recorded by the different probes (M1, M2, HW and PM) mounted on the burner.

These data are used to classify the thermo-acoustic state of the test rig into three main zones shown in Figure 8.2: safe, warning and critical. The potential mechanical wear-out and damages caused by TAI to the system are directly linked to the amplitude of pressure oscillations in the system. Therefore, the operating points are here categorized according their root-mean-square (RMS) value of the pressure fluctuation p_{RMS} measured by M3 inside the combustion chamber. The boundary between the safe and the warning zones is defined in the following as $p_{RMS} \approx 100$ Pa reached for example at $(P, \phi) = (7.00, 0.75)$. The limit between the warning and the critical zones is reached for $p_{RMS} \approx 250$ Pa. At $\phi = 0.75$, this limit is reached for $P = 8.75$ kW. The choices for the thresholds levels delimiting these boundaries are made arbitrary. The number of zones and the criteria used to delineate these zones depends on safety and operating requirements which are unique to each setup. For instance, the criteria can be frequency dependent and/or based on the peak amplitude from the Fast Fourier Transform of the pressure signal [51]. Here, the selected delimitation provides a simple and comprehensive baseline for the evaluation of the precursors investigated in this work. They are also representative of what is usually done in the industry.

For instance, the operating point $(P, \phi) = (5.00, 0.75)$ is considered here to be in the safe zone in Figure 8.2 without significant acoustic activity (Figure 8.1a). The operating conditions $(P, \phi) = (7.00, 0.75)$ and $(P, \phi) = (8.50, 0.75)$ are considered to be in the warning zone in Figure 8.2 with the presence of numerous bursts in their signals (Figure 8.1b-c). Finally, the conditions $(P, \phi) = (8.75, 0.75)$ and $(P, \phi) = (9.00, 0.75)$ belong to the critical zone showing large bursts and almost no time interval with low acoustic activity (Figure 8.1d-e). One may note also that the system never reaches a well defined limit cycle that would be characterized by oscillations at a single frequency with a large amplitude. This system exhibits instead galloping limit cycles during which the oscillation level and the oscillation frequency are well defined over short time intervals but change rapidly and randomly over longer time scales [288].

The same experiments were repeated for other operating conditions by varying the global equivalence ratio ϕ to produce the stability chart shown in Figure 8.2. The crosses correspond to operating points which were not reachable because the air flow rate required exceeds what the device could deliver. The other symbols correspond to operating conditions that were explored. The diameter of the disk is proportional to the value of p_{RMS} measured by M3. Empty circles are operating points where lean blow-off occurs. The white zone corresponds to the safe operating regime, free of any TAI. The light grey zone delineates the warning zone, defined by 100 Pa $< p_{RMS} <$ 250 Pa, with impeding pressure bursts due to thermo-acoustic coupling. The dark grey region delineates the critical zone with large amplitude TAI defined by $p_{RMS} >$ 250 Pa. Figure 8.2 shows that this region lies on the right upper-corner of the operational domain at high power when stoechiometry is approached. At these operating conditions large self-sustained oscillations develop and the power spectra recorded by the different probes feature a large peak with a main frequency ranging between 500 Hz and 530 Hz.

8.3. Acoustic Energy Balance

The acoustic energy balance is now revisited to introduce an indicator of impeding TAI based on energetic considerations. Neglecting damping mechanisms and considering harmonic flow disturbances of period T, the period and spatial averaged balance equation for the acoustic energy over a combustion chamber with a volume V and boundary area A yields (see for example [130]):

$$\frac{d\mathcal{E}}{d\tau} = \mathcal{R} - \mathcal{D} \tag{8.1}$$

where $\mathcal{E}$, $\mathcal{D}$ and $\mathcal{R}$ designate respectively the acoustic energy inside the combustor, the acoustic flux leaving the combustor and the thermo-acoustic power all determined at frequency $f = 1/T$:

$$\mathcal{E} = \int_V \left(\frac{1}{4\bar{\rho}c^2} \tilde{p}\tilde{p}^* + \frac{1}{4}\bar{\rho}\tilde{\boldsymbol{u}} \cdot \tilde{\boldsymbol{u}}^* \right) \mathrm{d}V \tag{8.2}$$

$$\mathcal{D} = \int_A \frac{1}{2} \mathrm{Re}\left(\tilde{p}\tilde{\boldsymbol{u}}^* \cdot \boldsymbol{n}\right) \mathrm{d}A \quad \text{and} \quad \mathcal{R} = \int_V \frac{(\gamma - 1)}{2\gamma\bar{p}} \mathrm{Re}\left(\tilde{p}\tilde{q}^*\right) \mathrm{d}V \tag{8.3}$$

where γ is the ratio of heat capacities, $\overline{p}$, $\overline{\rho}$ and c denote respectively the pressure, density and sound speed of the unperturbed flow and $\boldsymbol{n}$ is the local normal vector to the surface A. In these expressions, $\tilde{x}$ denotes the complex amplitude of the fluctuating quantity x' where $x' = \mathrm{Re}\left[\tilde{x}\mathrm{e}^{-\mathrm{i}\omega t}\right]$ with $\omega = 2\pi/T$ the angular frequency. The quantities $\mathcal{E}$, $\mathcal{D}$ and $\mathcal{R}$ are time averages considering that the period T of the acoustic oscillations is much smaller than the time scale τ over which they vary [130].

Equations (8.1) to (8.3) are only valid for pure harmonic oscillations at the frequency $f = 1/T$ of the thermo-acoustic instability. In many thermo-acoustic systems characterized by a unique oscillation frequency, this framework is enough to assess the system stability and infer the acoustic fluxes [**?** **?**]. In the present case, the amplitude and the frequency of the thermo-acoustic bursts vary substantially, particularly during the transition from the safe to the warning zone and the TAI frequency is more difficult to isolate. This is why the acoustic energy budget needs to be reconsidered to take this feature into account.

In practice, the acoustic pressure and acoustic velocity and the resulting heat release rate disturbances can be considered as stationary ergodic random signals when the system lies in the stable (safe zone) or intermittent (warning zone) combustion regimes [282, 283, 285, 286, 289]. Therefore, a direct use of the Fourier transform of these signals over the record duration t_{ac} does not yield a statistically meaningful information. However, estimates of the Power Spectral Density (PSD) S_{xx}

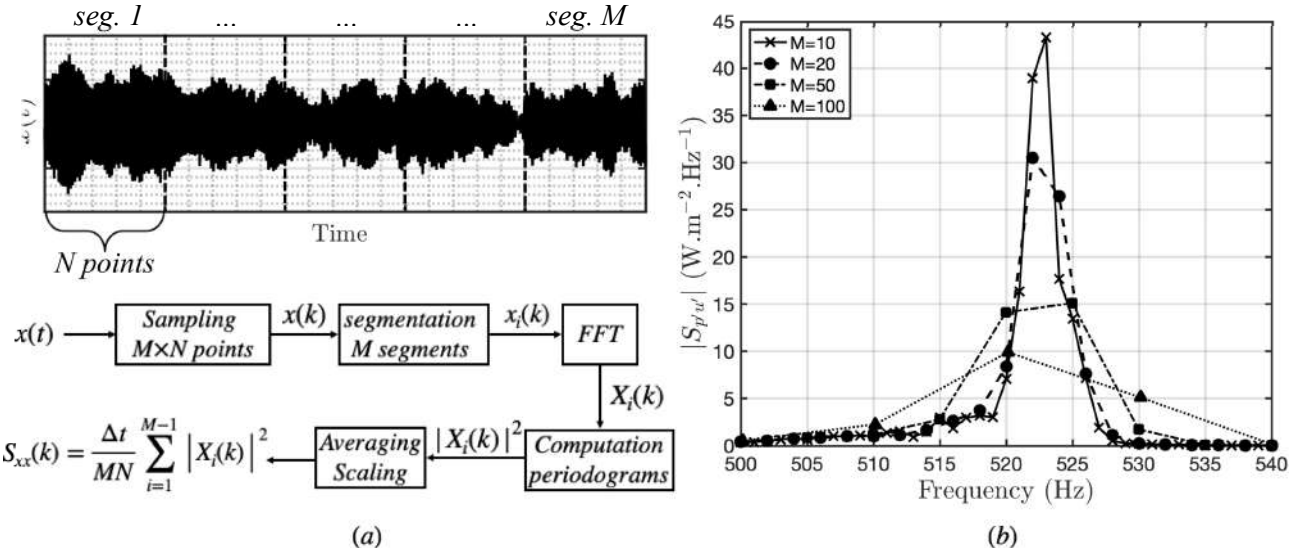

Figure 8.3. – (a) Illustration of the periodogram algorithm used to estimate the PSD S_{xx}. (b) Influence of the number of segments M on the CPSD $S_{p'u'}$ at $P = 8.75$ kW and $\phi = 0.75$, where p' is the pressure fluctuation measured by M2 and u' the velocity fluctuation measured by HW.

and Cross Power Spectral Density (CPSD) S_{xy} of these signals can be determined with the method of averaged periodograms [208]. Applying these operators to Equations (8.1) to (8.3) and integrating the resulting expressions over frequency yields the following modified version of the acoustic energy balance:

$$\frac{d\mathscr{E}}{d\tau} = \mathscr{R} - \mathscr{D} \tag{8.4}$$

with:

$$\mathscr{E} = \int_V \int_f \left(\frac{1}{4\overline{\rho}c^2} S_{p'p'}(f) + \frac{1}{4}\overline{\rho} S_{u'u'}(f) \right) \mathrm{d}V \mathrm{d}f \tag{8.5}$$

$$\mathscr{D} = \int_A \int_f \frac{1}{2} Re\left(S_{p'u'}(f)\right) \mathrm{d}A \mathrm{d}f \quad \text{and} \quad \mathscr{R} = \int_V \int_f \frac{\gamma - 1}{2\gamma \overline{p}} S_{p'\dot{q}'}(f) \mathrm{d}V \mathrm{d}f \tag{8.6}$$

The quantities $\mathscr{E}$, $\mathscr{D}$ and $\mathscr{R}$ correspond now to averages of the acoustic energy inside the combustor volume V, the acoustic flux leaving the combustor and the thermo-acoustic power integrated over all the frequency spectrum to infer the actual acoustic power over all frequencies. The time scale τ in Equation (8.4) needs to be large compared to the lowest frequency f_1 over which Equations (8.5) and (8.6) are integrated for $f_1 \leq f \leq f_2$.

This spectral integration has two main advantages. First, it enables to deal with thermo-acoustic systems featuring multiple peak frequencies without requiring to identify these frequencies in the spectrum. Secondly, it overcomes the segmentation dependence related to the computation of estimates of the PSD and CPSD for noisy signals with Welch's averaged periodogram method as illustrated in Figure 8.3a. The signal $x(t)$ sampled at frequency f_s over the time interval $[0,t_{ac}]$ is cut into M segments, each including the same number N of data. These segments may also be overlapped and/or windowed to increase the final signal to noise ratio. Then, the Discrete Fourier transform (DFT) $X_i(k)$ and the associated periodogram $|X_i(k)|^2 = X_i(k)X_i(k)^*$ are computed for each segment, where i is the segment number and k the index corresponding to the discrete frequency f_k. The series $|X_i(k)|^2$ are then averaged over the M segments to obtain an estimate of the PSD S_{xx}. The same method is

used to estimate the CPSD S_{xy} of signals x and y by also computing the DFT of the y signal and $X_i(k)Y_i^*(k)$ instead of $|X_i(k)|^2$. Hence, increasing the number M of segments allows to obtain a better statistical averaged information. However, it also decreases the frequency resolution, but the method preserves the power, i.e. the area below the peak in Figure 8.3b. Consequently, the integration over the frequency domain removes the segmentation dependency and allows to recover the power from the signal.

In the present study, the acoustic flux $\mathscr{D}_{in}$ given by Equation (8.6) crossing the annular channel in the air stream is selected as a candidate indicator for precursors of thermo-acoustic instabilities. It is computed using p' and u' measured by M2 and HW, assuming a flat velocity profile over the cross section area of the channel where it is measured. Welch's method is applied to deduce $\mathscr{D}_{in}$ from these pressure and velocity measurements. In a gas turbine, the measurement of u' with a hot-wire probe is not always possible but this signal can be reconstructed using only microphones with the multiple microphone method for example [290**?** , 291]. The acoustic flux $\mathscr{D}_{in}$ relates to the fundamental combustion dynamics occurring inside the chamber without need of optical diagnostics and will be shown to feature several advantages with respect to other indicators.

8.4. Guidelines for a TAI precursor

We follow the guidelines proposed by [292] for blowout to define the key performance metrics for a TAI precursor indicator I:

1. The indicator I has to evolve monotonically when the stability margin is reduced.
2. The value I_{cr} of the indicator when entering the critical regime has to be as much as possible greater than the value I_w when entering the warning zone, i.e. $I_{cr}/I_w \gg 1$ in order to discriminate clearly the proximity to TAI.
3. When choosing a TAI precursor, the functional dependence I to the varying operational parameter is the crux of the matter because it defines the safety margin retained for the system. The way they are determined is described below. Examples of functional dependencies are illustrated in Figure 8.4 for power functions. For a linear evolution (curve 1), I evolves monotonically with P, but its gradient remains constant even if the system is very close to the instability. This function does not yield any supplementary information about the proximity to the critical regime. It is better to have a convex curve with a positive gradient that increases when approaching the instability.
4. The point where the curve undergoes an important inflection should not appear too soon when the system is still safe like curve 2 in Figure 8.4, but not too late when the system is almost in the critical regime like curve 5. Curves 3 and 4 comply with this requirement.
5. The computation time for I, comprising the duration for signal acquisition and its post-processing, has to be short enough for the operator to intervene if needed.
6. The indicator I has to be robust with respect to noise levels, signal processing parameters change (e.g. t_{ac} and M) and burner design modifications.

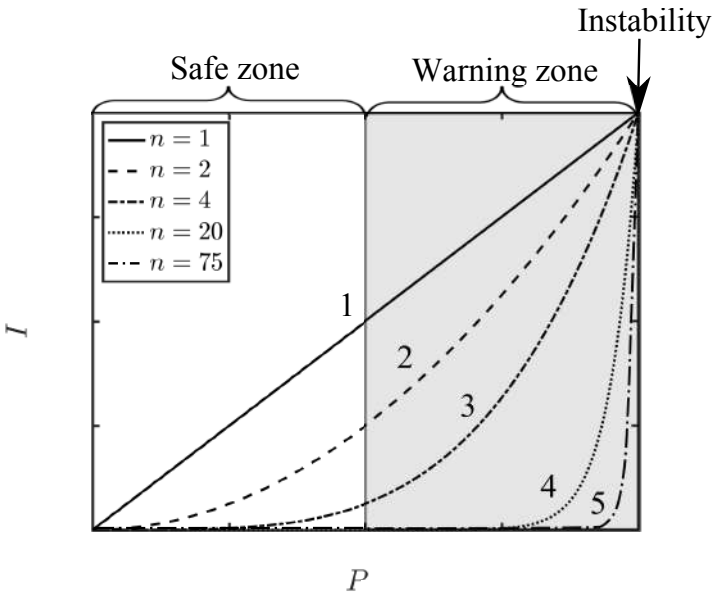

Figure 8.4. – Evolution of the TAI indicator I with the parameter P affecting the flame thermoacoustic stability. In these experiments P corresponds to the thermal power. I is here modeled as a power function x^n for increasing values of n. Adapted from [292].

8.5. Comparison of TAI precursor performances

The performance of the selected indicator $\mathscr{D}_{in}$ is compared to other indicators of impeding TAI with respect to the requirements listed in the previous section. Due to its simplicity, the RMS value of acoustic pressure inside the combustion chamber is the precursor examined in most studies [279, 280, 286, 289, 293–295]. The p_{RMS} level measured by M3 is thus used as a reference TAI indicator in this study. The peak amplitude from the PSD recorded by M3 is also considered as in **(author?)** [286]. Finally, the phase lag $\Delta\varphi$ between the OH* signal and the acoustic pressure inside the combustion chamber is also considered. The acoustic pressure inside the chamber is deduced from the signal recorded by M3 and the waveguide transfer function. The phase lag $\Delta\varphi$ corresponds to the Rayleigh criterion assuming the OH* light and heat release rate fluctuations are in phase [149]. This latter indicator makes use of two sensors as for the acoustic flux $\mathscr{D}_{in}$. The Rayleigh criterion constitutes the standard way to identify TAI [54, 296].

Figure 8.5 shows the evolution of these precursors when approaching TAI by increasing the power P at fixed global equivalence ratio ϕ. Indicators p_{RMS}, p_{PSD} and $\mathscr{D}_{in}$ all increase monotonically when approaching the TAI (requirement 1), except $\Delta\varphi$. The Rayleigh criterion $\Delta\varphi < \pi/2$ is always satisfied for all cases explored and it is difficult to distinguish the warning and critical zones. The indicators $\mathscr{D}_{in}$ and p_{PSD} feature a larger ratio I_{cr}/I_w respectively about 10 and 15 than p_{RMS} in which case I_{cr}/I_w is roughly about 2. The indicator $\Delta\varphi$ is thus excluded from the analysis in the following.

The performance of indicators p_{RMS}, p_{PSD} and $\mathscr{D}_{in}$ is further analyzed. To ease comparisons, quantities are rescaled. In the following, the power P is made dimensionless as $P_{rs} = (P - P_{sf}) / (P_{cr} - P_{sf})$. In this expression, P_{sf} corresponds to the power from the safest operating point and P_{cr} is the critical power above which the system enters the critical regime. The rescaled indicator I_{rs} is defined the same way $I_{rs} = (I - I_{sf}) / (I_{cr} - I_{sf})$, where I_{sf} and I_{cr} are the indicator values corresponding to P_{sf} and P_{cr} respectively. Figure 8.4 shows a domain split in safe and warning zones of equal length, i.e for a thermal power P_w at the beginning of the warning regime equal to $P_w = (P_{sf} + P_{cr})/2$. In order to compare results for indicators p_{RMS}, p_{PSD} and $\mathscr{D}_{in}$ on a similar plot as in Figure 8.4, the power

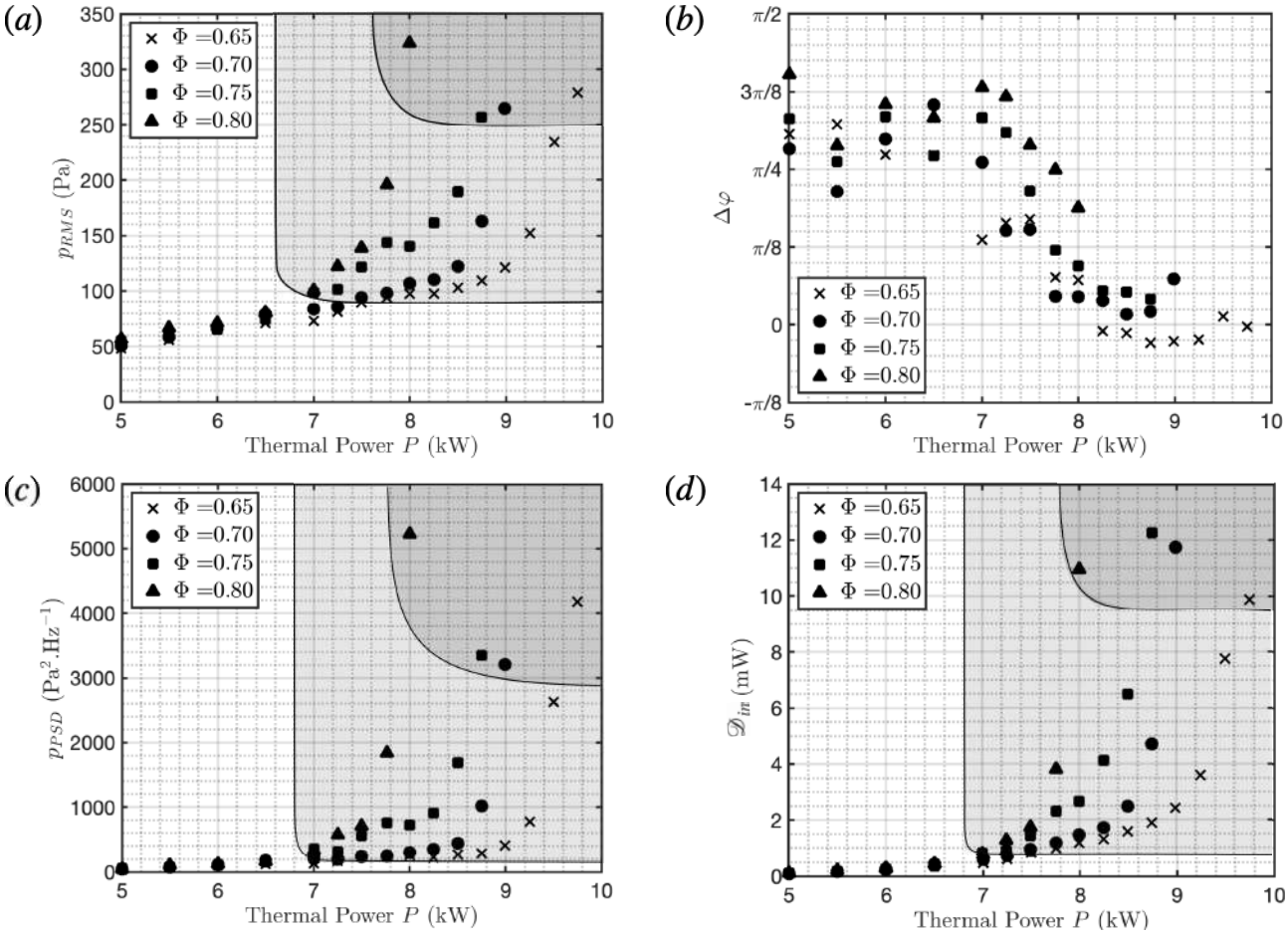

Figure 8.5. – Evolution of indicator (a) p_{RMS}, (b) $\Delta\varphi$, (c) p_{PSD} and (d) $\mathscr{D}_{in}$ when approaching TAI by increasing the power P at fixed equivalence ratio ϕ for $M = 100$ and $t_{ac} = 10$ s. The warning zone (light grey) and the critical zone (dark grey) from Figure 8.2 are reproduced on each plot when it is possible.

Table 8.1. – Values of the power P and the TAI indicators p_{RMS}, PSD, $\mathscr{D}_{in}$ at the safe (sf), warning (w) and critical (cr) thresholds used to draw the normalized plots in Figure 8.6. P_{sf} is selected such as $P_w = (P_{sf} + P_{cr})/2$.

ϕ	P (kW)			p_{RMS} (Pa)			p_{PSD} (Pa^2.Hz $^{-1}$)			$\mathscr{D}_{in}$ (mW)		
	P_{sf}	P_w	P_{cr}	I_{sf}	I_w	I_{cr}	I_{sf}	I_w	I_{cr}	I_{sf}	I_w	I_{cr}
0.80	6.00	7.00	8.00	70.8	101	323	125	320	5220	0.293	0.766	11.0
0.75	5.00	7.00	8.75	55.1	98.8	257	55.6	352	3334	0.104	0.783	12.3
0.70	6.00	7.5	9.00	66.3	94.7	264	113	236	3207	0.251	0.923	11.7
0.65	5.50	7.75	9.75	56.1	94.8	279	67	256	4187	0.160	0.971	9.88

P_{sf} of the safest operating condition is chosen such that the power corresponding to the beginning of the warning zone is $P_w = (P_{sf} + P_{cr})/2$ for each set of experiments conducted at constant ϕ. As a consequence, for each precursor, the critical value I_{cr} of the TAI indicator also depends on the global equivalence ratio ϕ and a common threshold value for all ϕ cannot be defined. The values used to rescale the data are summarized in Table 8.1.

In order to assess requirements 3 and 4, Figure 8.6 shows the results for the rescaled indicators p_{RMS},

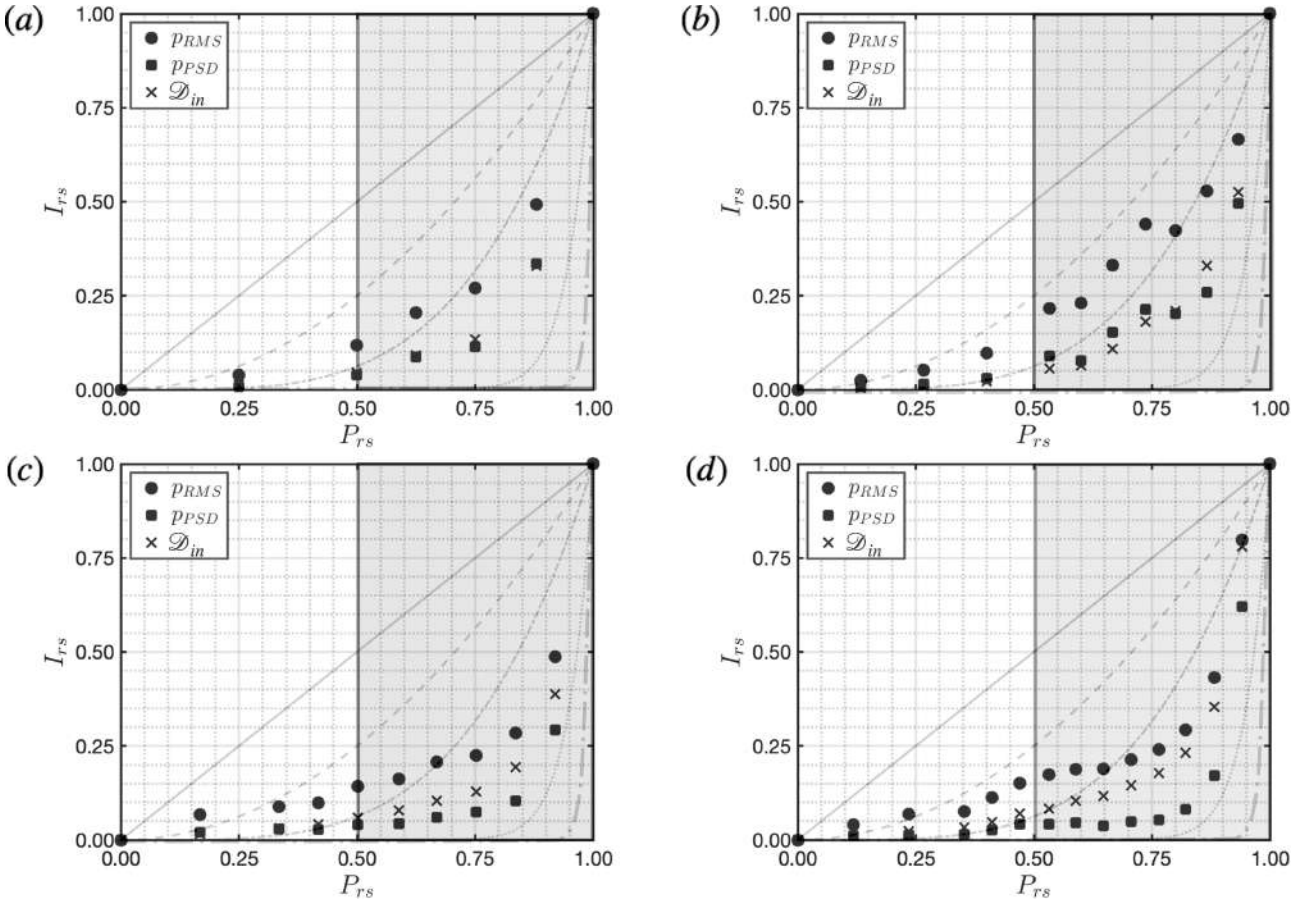

Figure 8.6. – Normalized evolution of p_{RMS}, p_{PSD} and $\mathscr{D}_{in}$ as a function of the dimensonless power P_{rs} for (a) $\phi = 0.80$ (b) $\phi = 0.75$ (c) $\phi = 0.70$ and (d) $\phi = 0.65$ for $M = 100$ and $t_{ac} = 10$ s. Values for the normalization are indicated in Table 8.1.

p_{PSD} and $\mathscr{D}_{in}$ as a function of P_{rs}. The same model power laws as in Figure 8.4 are superimposed on the background. For all indicators, the gradient dI/dP is globally positive, but p_{RMS} and p_{PSD} feature also a plateau or slightly decrease locally at $\phi = 0.65$ and $\phi = 0.70$, while $\mathscr{D}_{in}$ regularly increases for all conditions explored. Also, the shape of p_{RMS} and p_{PSD} signals depends on ϕ while $\mathscr{D}_{in}$ features always the same behavior with data lying between the curves 3 and 4 in Figure 8.6. In the safe zone, the indicator p_{RMS} has an evolution between the curves 2 and 3 while in the warning zone, it lies close to curve 3 except for $\phi = 0.70$. The indicator p_{PSD} better fits the desired evolution between curves 3 and 4 but it is rather close to curve 4 for $\phi = 0.65 - 0.70$.

Only standard mathematical operations are needed to estimate p_{RMS}, p_{PSD} and $\mathscr{D}_{in}$. Differences in computation time between these different indicators are negligible, meaning that requirement 5 is not decisive for these indicators. Tests of their performance with respect to requirement 6 are now considered when the signal sampling duration t_{ac} and the post-processing parameters are modified. Their evolution at $\phi = 0.75$ is shown in Figure 8.7 for different numbers of segments M and in Figure 8.8 when the sampling time duration t_{ac} is modified. Change of p_{RMS} with the numbers of segments M of the periodogram is not plotted because its computation is not altered by the segmentation.

Figure 8.3b shows that when the number of segments M increases, the value p_{PSD} drops and the power spectral density is distributed over a wider range of frequencies. The acoustic power $\mathscr{D}_{in}$ instead remains unaltered because it is integrated over all frequencies. A decrease of the sampling

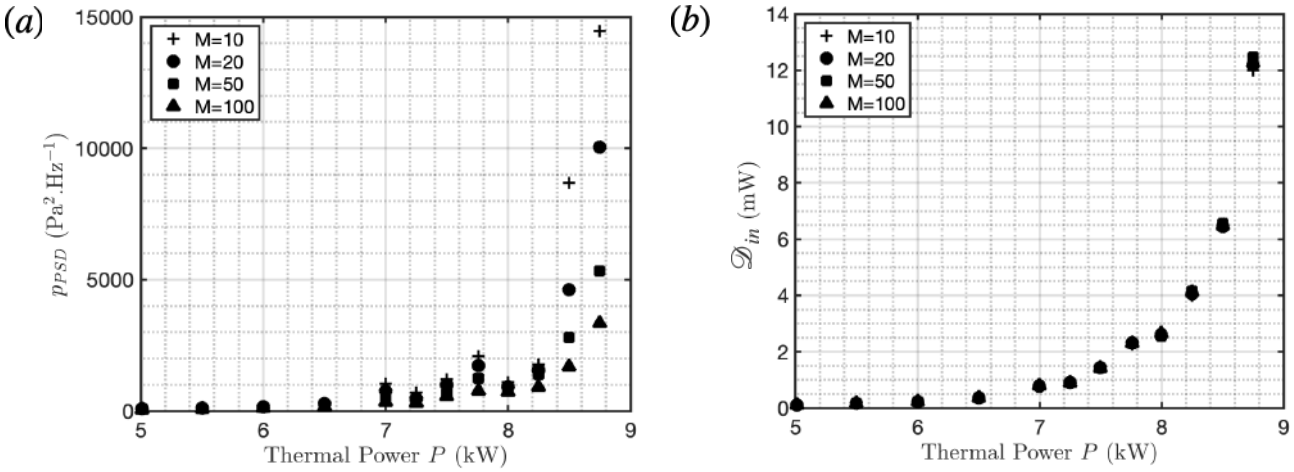

Figure 8.7. – Evolution of (a) p_{RMS} and (b) p_{PSD} when approaching TAI by increasing P at $\phi = 0.75$ with varying segmentations M of the signal recorded over $t_{ac} = 10$ s.

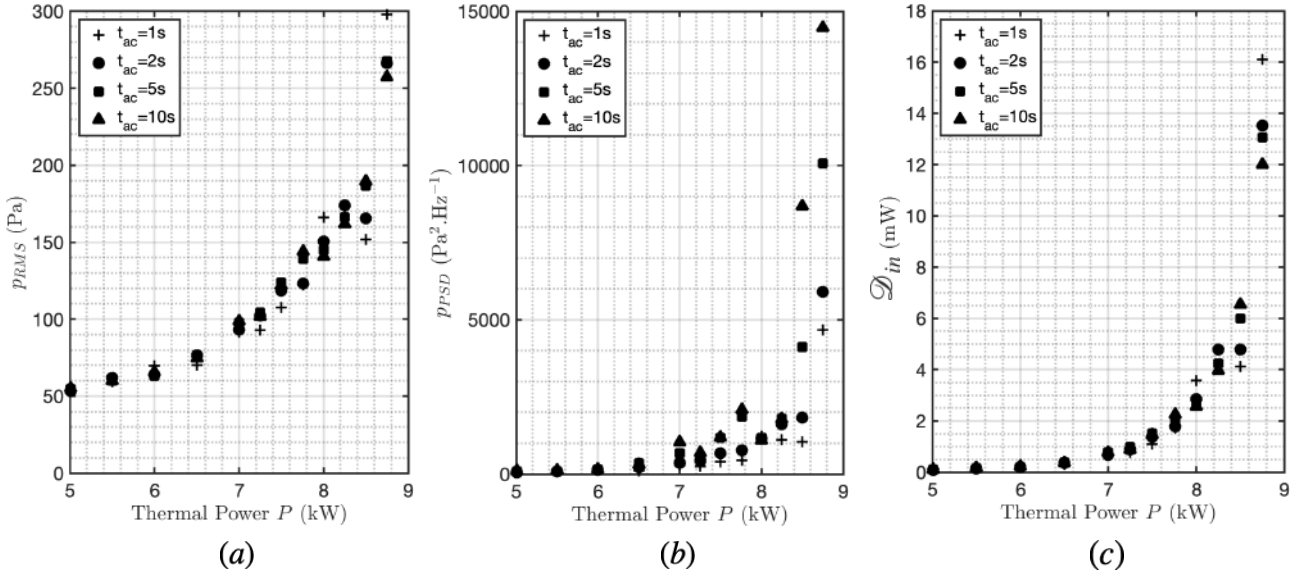

Figure 8.8. – Evolution of (a) p_{RMS}, (b) p_{PSD} and (c) $\mathscr{D}_{in}$ when approaching TAI by increasing P at $\phi = 0.75$ for different record durations t_{ac} and a signal segmentation of $M = 10$ windows.

time duration from $t_{ac} = 10$ s to 1 s also leads to a strong decrease of the values p_{PSD} while the two other indicators p_{RMS} and $\mathscr{D}_{in}$ are barely altered with changes less than 20% with respect to their values for $t_{ac} = 10$ s. Nonetheless, the shape of the evolution of p_{RMS} and $\mathscr{D}_{in}$ are relatively preserved. Hence, one can conclude that the indicators p_{RMS} and $\mathscr{D}_{in}$ are fairly unaltered to choices made for signal sampling and signal processing, which is not the case for the peak value p_{PSD} of the PSD.

8.6. Application to another burner configuration

The precursor $\mathscr{D}_{in}$ is now tested on the MIRADAS (Mitigation of Instabilities by Radially and/or Axially Directed Addition of Species) setup shown in Figure 8.9. It is extensively described in [162]. The main difference with the TALISMAN setup is the fuel injection system. Instead of injecting hollow cone fuel spray, H_2 or CH_4 can be injected separated from the air directly in the combustion chamber through a middle pilot tube, or both premixed with the air upstream the chamber. They

are respectively named PH*, PC* and MH*. For PH*, PC*, "∗" denotes the percentage of the total thermal power attributed to the pilot fuel while for MH* it indicates the the percentage of the total thermal power attributed to the hydrogen enrichment.

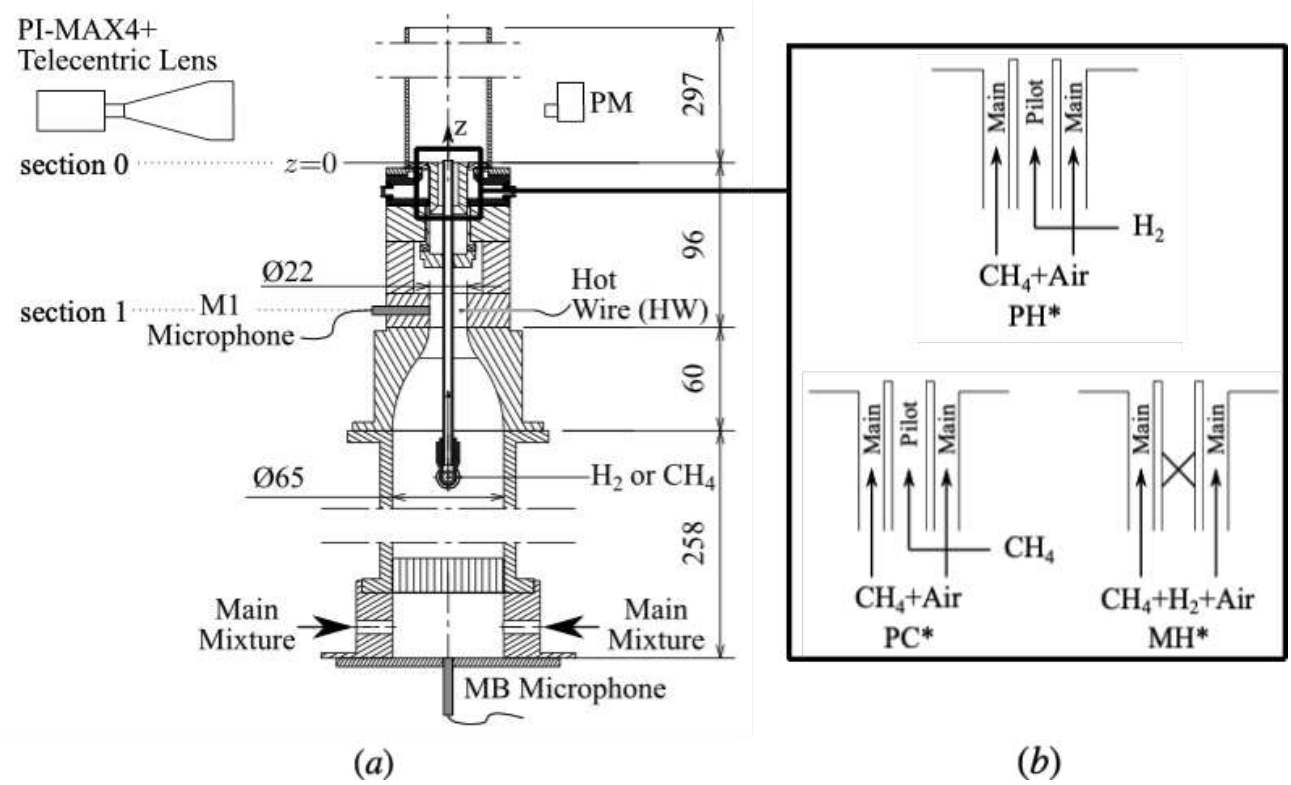

Figure 8.9. – (a) Sketch of the experimental setup MIRADAS and (b) illustration of the different possibilities of injection fuel strategy

The dynamic stability of the burner has been studied for different fuel injection strategy in [297]. Their corresponding operating maps are drawn in Figure 8.10, varying the global equivalence ratio ϕ and the bulk flow velocities recorded by HW, 14 $m.s^{-1} \leq U_{sw} \leq 40$ $m.s^{-1}$, corresponding to thermal powers in the range 2700 W $\leq P \leq$ 9300 W. These operating maps show a dynamic behavior more complex than the one obtained with the TALISMAN setup. Apart from the PH2, critical zones are not located at a specific zone of the operating map but are scattered over the whole map, where critical and safe points can coexist next each other without intermediate warning points between them. Also the intermediate zones are way less discretized as they were in Figure 8.2. Hence, these twisted operating maps offer more challenges for TAI prediction. Paths retained to test the conformity of the evolution of $\mathscr{D}_{in}$ when approaching TAI are pictured by arrows on Figure 8.10. The varying parameter here is U_{sw} at a fixed ϕ. The starting point of the paths are selected as being the most stable point at each ϕ when it's possible. When the starting point is surrounded by two critical points then the critical ending point is chosen in order to have the maximum number of operating points along the path and so to properly characterize the $\mathscr{D}_{in}$ evolution.

Figure 8.11 shows the $\mathscr{D}_{in}$ evolution for the different operating maps along these paths. Globally, it can be observed that $\mathscr{D}_{in}$ still features the same behavior as before with a convex and monotonic evolution and data lying between the curves 3 and 4. For PH1 and PC1, data evolution is not ideal with a less convex evolution between the curves 2 and 3. Nonetheless, for MH* injections at $\phi = 0.75$, the evolution $\mathscr{D}_{in}$ is closer to the curve 2. It is due to the fact that the starting point is already in the warning zone and not in the safe zone as it should be to properly compare it to the examples curves.

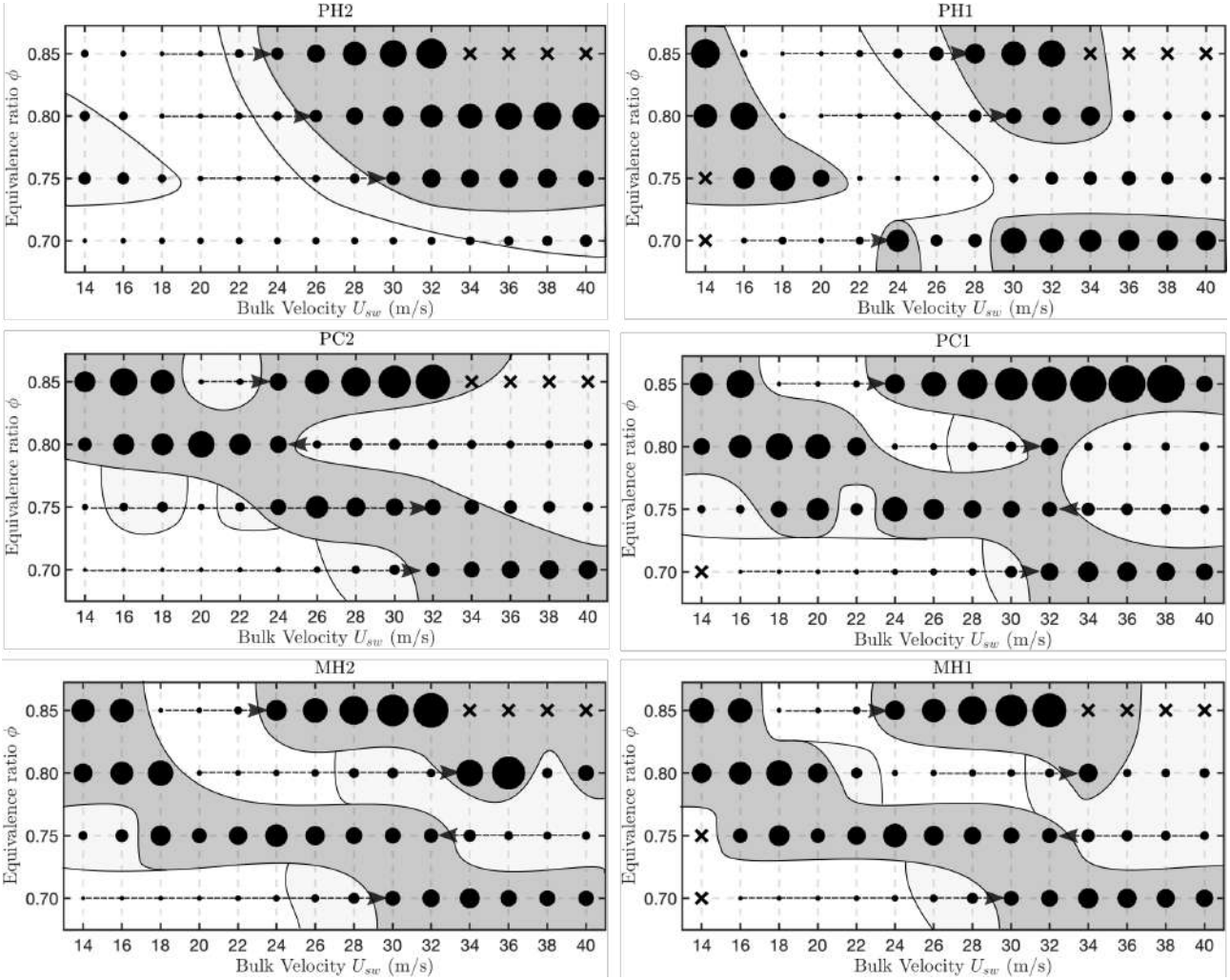

Figure 8.10. – Stability chart of the MIRADAS burner for different fuel injection strategy shown in Figure 8.9. The warning zone is indicated in light grey while the danger zone is represented in dark grey. The diameters of the filled disks are proportional to the rms pressure fluctuation level p_{rms} measured by M3. Arrows shows paths of parameter change to test the $\mathscr{D}_{in}$ evolution

Also, there is a beginning of increase for PC2 at $\phi = 0.75$ before decreasing to safe values due to the appearance of warning zone before another safe zone, which validates the fact that $\mathscr{D}_{in}$ is a good indicator for the dynamic regime. Finally, for some cases such as MH1 at $\phi \geq 0.8$, some intermediate points in the warning zones are lacking to capture the inflexion between the critical points and to prevent them. Still, one can conclude that $\mathscr{D}_{in}$ is robust to the burner configuration change.

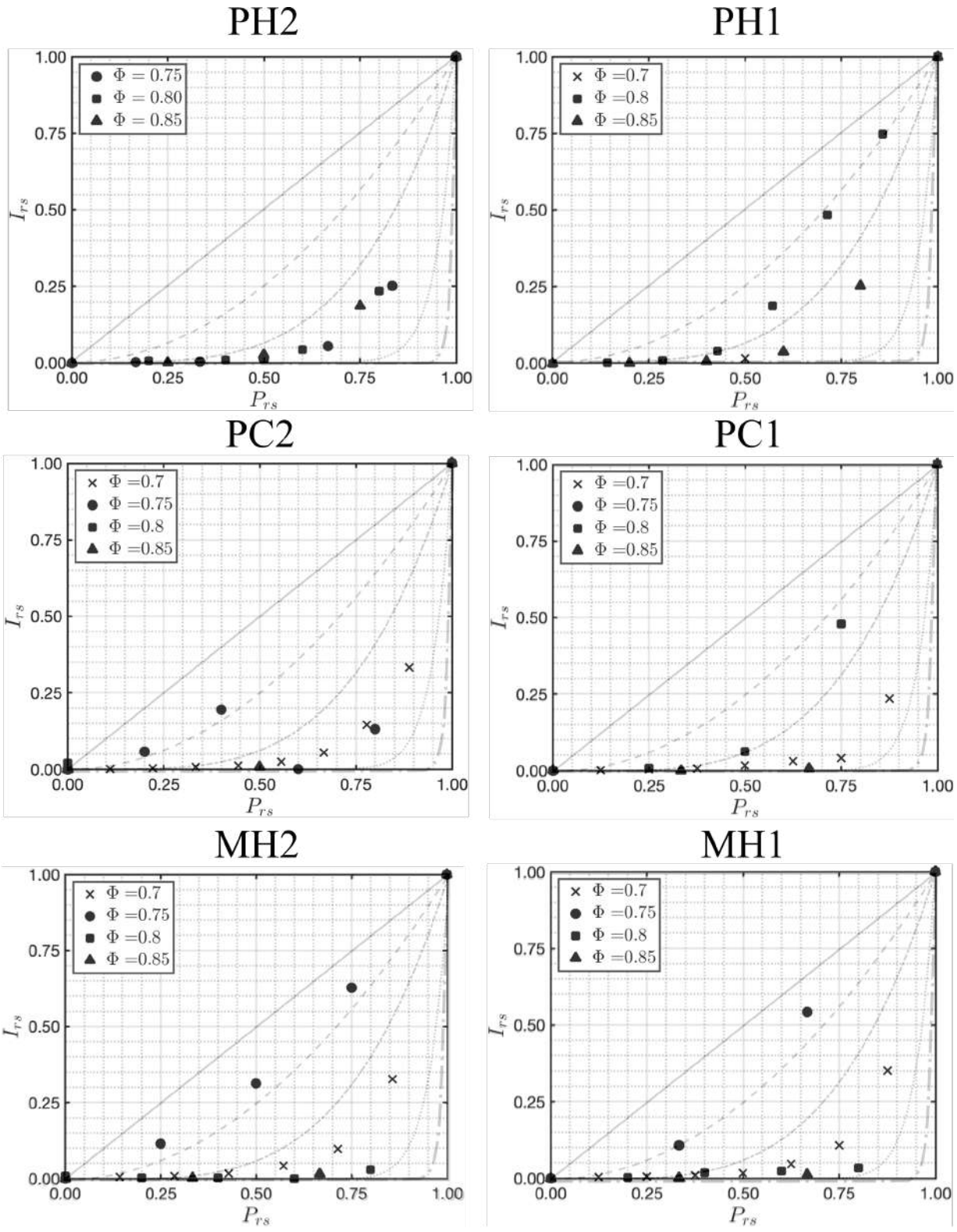

Figure 8.11. – Normalized evolution of $\mathscr{D}_{in}$ for different fuel injection strategy in MIRADAS along the paths shown in Figure 8.10 for $M = 100$ and $t_{ac} = 10$ s.

8.7. Discussions about Deep-Learning applications

While the evolution of an indicator combustion instabilities has been mostly used in the literature to prevent combustion instabilities as done in Section 8.6, this method encounters an intrinsic limitation. When changing the operation parameters by steps, it is necessary to encounter enough intermediate points before reaching the critical point, as it has been highlighted in the previous section. However, combustion instabilities do not always appear progressively with intermittent burst before reaching limit-cycle oscillations as observed in Figure 8.1. It can be seen in Figure 8.10 that TAI appear sometimes abruptly with a small parameter change from an operating point where the system is very stable. Moreover, when changing operating conditions, the operator will not always progress by enough successive and time spaced small steps to properly capture the evolution of the chosen indicator.

Hence, in this case, the detection of potential unstable neighbors operating points from signals only recorded at a single operation point is needed as complementary tool of indicator evolution analysis. The former technique would be used as a short-range detection while the latter technique as a long-range detection. Cellier et al. [298] proposed recently to apply Deep-Learning technique on the operating maps presented in Figure 8.10 for the short-range detection. The task of the neural network was to attribute a label to each of the 4 points surrounding a considered operating point indicating if it is stable or not. The neural network was able to have a validation rate around 90 % and to perform better than if the task was done by logistic regression. These results would indicate that some elements in the signal can inform on the parameter direction of the surrounding combustion instabilities but the question still holds due to the data starvation problem as mentioned by the authors. Hence, if this result is confirmed with further studies, it would show that some hidden patterns exist in these signals and then Deep-Learning would be an efficient tool to realize this task.

For Deep-Learning use, a very large and diverse data-set has to be available when training a neural network in order to be able to conclude on its performances. For instance, the image recognition dataset ImageNet gives access for free to 70 GB, 1000 classes, 1.4M labeled images. In [298], only 187 operating points were considered from the same burner with different fuel injection. Therefore, it is required, on the first hand, to perform a gigantic work of, data collection, and on the other hand, to share data with the combustion community. This work has just begun in 2022 with the BLASTNet project but it is mostly about numerical data [299]. Therefore, without these resources at disposition, at the scale of a PhD student in a laboratory, a Deep-Learning study the results of which would be difficult to interpret. For instance, while Cellier et al. [298] shows promising results, it is not concluding about the existence of hidden patterns in the recorded signals. Ideally, to pursue Deep Learning applications, it would be necessary to establish a preliminary proof of concept which would consist to distinguish different signatures characteristic of the direction of an instability. Else, this tremendous work of data collection and the construction of neural network can result into a dead-end.

To conclude, among the 20 operating maps obtained during this PhD, most of them were very similar to the one presented in Figure 8.2 despite geometrical change such as plenum length, injector recess, swirl rate, combustion chamber and length. Then, it was not possible to constitute singular operating maps such in Figure 8.10 and so to complete the MIRADAS data set for further studies using Deep-Learning. Furthermore, the warning zone being quite large without the problem of sudden TAI, the prevention based on the evolution of indicator such as $\mathscr{D}_{in}$ already fulfils well the prediction of TAI. The neural network for short range detection would be no use here: it would have detected the TAI only at a single parameter change while $\mathscr{D}_{in}$ evolution analysis would have prevented earlier. That is why Deep-Learning has been not applied in this PhD.

8.8. Conclusion

The acoustic flux $\mathscr{D}_{in}$ in the air channel at the combustion chamber inlet has been shown to comply with many of the features needed to infer impending TAI. It is deduced from the cross-power spectral densities between the acoustic pressure and local velocity measured by a hot wire set below the swirler unit in a spray burner. A specificity is that this acoustic power is integrated over all frequencies. This TAI indicator has been shown to be robust to modifications of the signal sampling duration and to the number of segments used to compute an average periodogram. When approaching TAI, $\mathscr{D}_{in}$ has a convex and monotonic evolution with a regular increase. When entering the warning zone defined as the region with irregular impeding thermo-acoustic bursts, its value increases over an order of magnitude, which allows a clear discrimination of the safety margin. Also, in the safe zone characterized by stochastic noise, $\mathscr{D}_{in}$ remains low, but has a strong inflexion when the burner enters the warning zone. This behaviour allows to reduce the safety margin while being enough conservative to prevent impending TAI. Hence, the acoustic flux $\mathscr{D}_{in}$ features many of the qualities needed for a precursor to detect impending TAI. Its performances have been tested for another combustor equipped with different fuel injection systems and showing complex stability charts where very stable operating points are neighbouring unstable points. The evolution $\mathscr{D}_{in}$ still succeeds to predict the approach of impending combustions instabilities but struggles when no a very few points are available between the stable and the unstable point. However this does not question the performance of $\mathscr{D}_{in}$ but rather the intrinsic limitation of using the evolution of an indicator as a method of prediction.

Hence, it shows the necessity of a short-range prediction of combustion instabilities, using only the characteristics of a single operating point to detect the unstable points around it. The application of using Deep-Learning for such purposes is then questioned. Even if it has shown satisfying results to perform such a task, it has not been demonstrated yet that such task was theoretically possible to perform and so these results have to be considered carefully. Without this analytical proof, it would require many data from different burners and implying different kinds of combustion instabilities to confirm these results. The configurations of TALISMAN showing similar stability charts where short-range prediction is less effective than using the evolution of indicator, it has not been performed in this thesis.

Further work is also necessary on the development on new probes to perform online monitoring as an alternative to the exclusive use of microphones. This has been investigating in the present thesis by the evaluating the performance of Rayleigh Criterion Probes developed by CBOne. The results are presented in Appendix F.

Conclusion and perspectives

Vers le soir, je regagnais une partie du parc plus ordonnée, arrangée en jardin, au bord de la route nationale. Au sortir du tumulte des parfums et du soleil, dans l'air maintenant rafraîchi par le soir, l'esprit s'y calmait, le corps détendu goûtait le silence intérieur qui naît de l'amour satisfait. Je m'étais assis sur un banc. Je regardais la campagne s'arrondir avec le jour. J'étais repu [...] J'avais au cœur une joie étrange, celle-là même qui naît d'une conscience tranquille. Il y a un sentiment que connaissent les acteurs lorsqu'ils ont conscience d'avoir bien rempli leur rôle, c'est-à-dire, au sens le plus précis, d'avoir fait coïncider leurs gestes et ceux du personnage idéal qu'ils incarnent, d'être entrés en quelque sorte dans un dessin fait à l'avance et qu'ils ont d'un coup fait vivre et battre avec leur propre cœur. C'était précisément cela que je ressentais: j'avais bien joué mon rôle. J'avais fait mon métier d'homme et d'avoir connu la joie tout un long jour ne me semblait pas une réussite exceptionnelle, mais l'accomplissement ému d'une condition qui, en certaines circonstances, nous fait un devoir d'être heureux. Nous retrouvons alors une solitude, mais cette fois dans la satisfaction.

– Albert Camus, *Noces, 1938*

Conclusions

This work has contributed to a better understanding of swirled flames powered by spray interacting with acoustic waves: in the first part, progress has been made on the description of interactions between the fuel injection and the acoustic field. In the second part, progress has been made the dynamic stability of a swirl-stabilized spray burner through low-order modelling and online monitoring. The main results of this work can be synthesized as follows:

- A new swirl-stabilized spray burner named TALISMAN has been designed and built at IMFT to analyze the interactions between spray flames and acoustic field on model of single sector of an annular combustion chamber. Fuel injection is realized with a hollow-cone spray of n-heptane. This burner have interchangeable parts to modify easily its geometry: injector recess, swirl number, combustion chamber length, ... This modularity is used to investigate the TALISMAN burner dynamics during self-sustained thermoacoustic instabilities and stable conditions with external acoustic forcing.
- Modeling spray flames presents additional complexities to the multiphase nature of the fuel used and have then supplementary ways to trigger CI than gaseous flames. The particle velocity fluctuations and particle clustering caused by the interactions between the acoustic field and the fuel injection studied as destabilizing mechanisms. Analytical models have been developed in Euler-Lagrange and Euler-Euler formalisms to determine the relations between the acoustic

disturbances and the particles disturbances for a monodisperse spray in a laminar flow.

- When studying the acoustic response of a single particle with Euler-Lagrange formalism to acoustic disturbances, the particle velocity response is governed by a first order low-pass filter where the frequency-cut is directly related to Stokes number. Hence, only small particles are sensitive to particle velocity perturbations. However, when investigating the particle number density response to acoustic perturbations with numerical flow simulations, important particle number density waves are created whatever the particle diameter is.
- Expressions for the particle velocity and number density fluctuations have been derived by linearizing the Euler-Euler equations of a perfectly monodisperse spray in a laminar flow field, confirming numerical and experimental results found in literature. Particle velocity fluctuations can be decomposed as the sum of a convective wave vanishing over a particle relaxation length and a propagating acoustic wave. The final amplitude and phase lag with the gas velocity fluctuations depend on the Stokes number and the Mach number. The particle number density expression corresponds to the superposition of two particle clustering phenomena: an Acoustic Particle Clustering (APC) directly proportional to the relative particle velocity fluctuations, and a Convective Particle Clustering (CPC) over the particle relaxation length and proportional to the relative gas velocity fluctuations, but independent of the acoustic coupling between the particle velocity and the flow perturbation. CPC is shown to be way more important than APC, where the influence of the latter can be only perceptible at low Stokes number. The difference between the particle injection velocity and the gas mean velocity does not change the nature of the waves constituting the fluctuations. However, it modifies permanently the amplitude and the phase of the CPC.
- While the distribution of the particle diameter at the injection is often considered in many fuel injection simulations, the dispersion of the particle velocity is often neglected or is arbitrary modelled without real justifications. Hence, the impact of the dispersion of the liquid particle velocity at the injector inlet in a turbulent spray was investigated. As gas turbulence, particle velocity dispersion can be modelled as homogeneous and isotropic and included in the set of balance equations describing the gaseous and disperse phases dynamics through an uncorrelated particle kinetic energy quantity. Put in his characteristic normal form, this system of equations shows, for the gaseous phase, that the characteristics match those of a purely gaseous flow with information conveyed by the mean flow and by acoustic waves. However, for the disperse phase, it is shown that the uncorrelated particle kinetic energy alters the way information is transported by the disperse phase. This in turn modifies the way acoustic modulations imposed to the gaseous flow and alters the response of the spray. A mesoscopic Eulerian-Eulerian description is first validated against numerical results from a Lagrangian-Eulerian reference simulation. Simulations performed with the Euler-Euler model show how particle velocity dispersion shifts the phase lag and alters the amplitude of particle number density waves created by the acoustic forcing for different fuel droplet diameters and air injection conditions. The damping and the phase shift of the number density waves increase with the Stokes number and the initial particle velocity dispersion at the injection. These numerical results are also corroborated by a theoretical analysis and shed light on the way acoustic waves alter the dynamics of a 1D fuel spray featuring an initial prescribed velocity dispersion at the particle injection location.
- The response of the hollow-cone spray to acoustic disturbances has been also investigated by a companion experimental and numerical study. In particular, the capacity of the numerical FIM-UR is evaluated. Modelling the injection of a hollow cone spray, has been evaluated regarding its reproduction of the particle velocity fluctuations caused by acoustic excitation. Results from numerical and experimental analysis at steady conditions were found to be in complete agreement when examining the velocity and mean diameter profiles for both the gaseous and liquid phases. The only noticeable difference was in the Sauter mean diameter profiles. It

is caused by the initialization of the FIM-UR particle diameter distribution. In particular, it is required to go from multiple particle diameter distributions measured at the injector's tip to a single particle diameter distribution used as an input of the FIM-UR model. Further numerical simulations would be necessary to iterate on the particle diameter distribution injected by FIM-UR which would capture accurately the Sauter mean diameter. However, since heat and mass were negligible, the differences on the Sauter mean diameter were neglected and thus not corrected. For the pulsed regime, small differences and phase lags exist for negative extrema fluctuations between LES and experimental results, but they are attenuated along the injection axis. The discrepancies are attributed to a mismatch in pressure drop across the swirler, which impacts the acoustic response of the burner. However, increasing the mesh resolution in the air injection area mitigate these differences. Despite this, the relatively coarse mesh is sufficient for capturing gas velocity fluctuations, saving computational time that a finer mesh would require for only marginally better results. The FIM-UR model does not have dynamic behavior. It leads to overestimated particle velocity profiles. Furthermore, the swirling liquid flow structure is not accurately represented, with the inner zone being narrower than in experiments. It has been shown that acoustic disturbances induce changes in the angle of the injection cone, as well as variations in particle diameter and velocity distributions along the injection radius.

- A dynamic stability analysis has been performed on the TALISMAN burner. Self-excited sustained oscillations around 240 Hz were observed and characterized. Acoustic modes and transfer matrices computed with a low-order acoustic model of the burner are successfully validated against experimental measurements. The Flame Describing Functions of spray flames have been determined using the OH^* signal recorded by the photomultiplier. In fully premixed systems, relative heat release rate fluctuations can directly be deduced from relative OH^* fluctuations. The FDF with the fully premixed model has roughly a constant gain over the frequency domain studied. However, it is shown that the low-frequency limit of the FDF deduced with the fully premixed model does not match that predicted by theory for a perfectly premixed flame. In spray flames, equivalence ratio disturbances need also to be considered as they affect the OH^* chemiluminescence. Experiments at steady state conditions are considered at different thermal powers and different equivalence ratios to deduce an empirical scaling law linking the OH^* intensity as a function of heat release rate and equivalence ratio. It is used to infer how the OH^* relative fluctuations and relative heat release rate disturbances are interrelated in the limit of quasi-static disturbances. Hence, different FDFs have been determined from the measurements depending on the correction applied. It has been shown that the corrections change deeply the shape of the FDF, especially its gain. The gain of the corrected FDFs exhibits now different humps. This correction gives a low frequency limits of the gain of 0 and a phase of $-\pi/2$. These values are consistent with those obtained with an analytical expression of the FDF of spray flame. Being only valid for low frequencies, further investigations are however required to extend the corrections to higher frequencies.

- The acoustic flux at the inlet of the combustion chamber has been finally used to indicate the proximity to impending CI in the TALISMAN setup. This acoustic power is integrated over all frequencies and is deduced from acoustic pressure and velocity measurements made upstream the combustion chamber. Results with this TAI precursor have been compared to those obtained by considering the root mean square value of the acoustic pressure inside the combustion chamber, the peak of the power spectral density of the combustion chamber acoustic pressure and the phase lag between the acoustic pressure inside the chamber and the OH^* chemiluminescence. It has been shown that the acoustic flux outperforms the other indicators in terms of order of magnitude change and shape evolution when approaching CI while being relatively insensitive to signal processing parameter modifications.

Perspectives

Extension to polydisperse and evaporative sprays

The analytical expressions of particle velocity and number density fluctuations that have been derived in this work are restricted to perfectly monodisperse 1D sprays. This simplified case has allowed to highlight the structure of the number density waves and to characterize them through some adimensional parameters. Polydisperse sprays can be modeled as an infinite ponderated sum of sprays with monodisperse diameter. Firstly, it will be then important to know the optimal diameters which will well reproduce the polydisperse spray behavior with the minimum of monodisperse sprays summed for a given distribution. It would give valuable information about how to perform Euler-Euler simulations with minimal diameter classes that reproduce the dynamics of polydisperse sprays. Secondly, it should be attempted to solve the Eulerian-Eulerian linearized equations for isothermal polydisperse sprays, assuming if necessary a particle diameter distribution. Hence, it is important to study the influence of diameter polydispersion on the response of a spray. Finally, the evaporation should be also included in the monodisperse case. However, many assumptions would have to be carefully made in order to obtain a meaningful resolution.

Incorporation of Homogeneous Isotropic Turbulence

The effects of the particle velocity dispersion have been investigated considering only a initial level of dispersion at the spray injection. Without any turbulence in the carrier flow, the particle velocity dispersion is then damped by the drag force over a distance relative of the order of the characteristic length. The effects of particle velocity dispersion were concerning particles with important Stokes number which are rarely seen in aeronautical injection. However, when the carrier flow is turbulent, it maintains the particle velocity dispersion to the gas velocity turbulence and then increases the effect on the number density waves. An analytical model has to be derived taken into account the gas turbulence. For instance, when assuming a homogeneous isotropic turbulence in the gas phase and neglecting the local variations of the gas velocity between particles of the dispersed phase (i.e $\langle u'_{g,i}\rangle_l = u'_{g,i}$), the transport equations of the uncorrelated particle kinetic energy are modified as follows:

$$\frac{D_p \delta q_p^2}{Dt} = -2\delta q_p^2 \frac{\partial \breve{u}_{p,i}}{\partial x_i} + \left(\frac{q_{gp} - 2\delta q_p^2}{\overline{\tau}_p} \right) \tag{8.7}$$

$$\frac{D_p q_{gp}}{Dt} = q_{gp} \left(G_{gp,ii} - \frac{\partial \breve{u}_{p,i}}{\partial x_i} - \frac{\partial \tilde{u}_{g,i}}{\partial x_i} - \frac{1}{\bar{\tau}_p} \right) + \frac{2q_g^2}{\overline{\tau}_p} \tag{8.8}$$

where here $q_{gp} = \langle u'_{g,i} u''_{p,i} \rangle_l$ and $q_g^2 = \frac{1}{2}\widetilde{u'_{g,i}u'_{g,i}}$ are respectively the fluid-particle velocity covariance and the kinetic turbulent energy [215, 300]. In Equation 8.8, G_{gp} denotes the second-order tensor function of one-point statistics of the fluid velocity field viewed by the particles consistent. Fed by q_g^2, it can be seen that q_{gp} is acting as a source term in the transport equation for δq_p^2, counter acting the decay. But this formalism is complex and has to be validated against Euler-Lagrange numerical results first.

Modelling the dynamic behavior of a hollow-cone spray

While the steady behavior of a hollow-cone spray injection is well reproduced by the FIM-UR model, its dynamic behavior still needs to be improved in order to avoid large discrepancies with the reality. To do so, it is important to gather experimental data on the response of hollow-cone sprays to acoustic disturbances. In particular, it has been found that the angle of injection as well as the particle velocity and diameter distributions are modified. A square transparent air-injection before the combustion chamber, it would allow to have an optical access to the spray injection and help to better characterize its dynamics. It would be then possible to perform high speed-camera imaging and PDPA in order to characterize the modification of the angle of injection as well as the particle velocity and diameter distributions during the acoustic forcing. In swirling flows, the angle of injection and changes in particle diameter and velocity distributions during the acoustic period can be attributed to local change of swirling number on one hand and on the local change of the axial velocity on the other hand. Thus, it would be interesting to measure the angle of injection and changes in particle diameter and velocity distributions at various swirl numbers. Additionally, measuring the fluctuations of these variables under acoustic disturbances in a laminar flow at different frequencies and levels of fluctuation would also be insightful.

Impact of the injector recess on the FDFs of a spray flame

It has been shown that the recess distance from the injector to the flame is decisive to determine if the transport of the injected fuel is insensitive to the acoustic disturbances and the injector can be considered as stiff. Hence, the FDFs will change with the injector recess distance, increasing the acoustic-spray interactions. Using the corrections for OH^* signal detailed in Chapter 7, it is important to see how the FDFs are modified when increasing the distance between the injector and flame distance. Further comparisons would be insightful when replacing the liquid fuel by a gaseous fuel.

Appendices

Appendix A

Detailed derivations of the expressions obtained in Section 4.3

A.1. Expression for the particle velocity fluctuation u'_p

When $u_p(0) = \overline{u}_g$, we have $\overline{u}_p = \overline{u}_g$. Hence, the equation (4.4) becomes

$$\frac{\partial \hat{u}_p}{\partial x} + \left(\frac{1}{\overline{\tau}_p \overline{u}_g} - i\frac{\omega}{\overline{u}_g} \right) \hat{u}_p = \frac{\hat{u}_g}{\overline{\tau}_p \overline{u}_g} \tag{A.1}$$

First, the solution of the homogeneous differential equation is:

$$\frac{\partial \hat{u}_p}{\partial x} + \left(\frac{1}{\overline{\tau}_p \overline{u}_g} - i\frac{\omega}{\overline{u}_g} \right) \hat{u}_p = 0 \tag{A.2}$$

In this expression, $\overline{u}_p$ and $\overline{\tau}_p$ being constant, the homogeneous solution is

$$\hat{u}_{p,H} = K_0 e^{-\frac{x}{\bar{l}_p}} e^{i\frac{\omega}{\overline{u}_g}x} \tag{A.3}$$

where $\bar{l}_p = \overline{\tau}_p \overline{u}_g$ is the mean particle relaxation length and K_0 is a constant that needs to be determined. Now a particular solution of Equation (A.1) has to be found. The method of variation of constant is applied here, looking for a solution of the following form :

$$\hat{u}_{p,p} = K(x) e^{-\frac{x}{\bar{l}_p}} e^{i\frac{\omega}{\overline{u}_g}x} \tag{A.4}$$

Re-injecting this solution in (A.1) in order to find $K(x)$, one may write successively

$$\frac{\partial K}{\partial x} = \frac{\hat{u}_g}{\bar{l}_p} e^{\frac{x}{\bar{l}_p}} e^{-i\frac{\omega}{\overline{u}_g}x} \tag{A.5}$$

$$\frac{\partial K}{\partial x} = \frac{U_g}{\bar{l}_p} e^{\frac{x}{\bar{l}_p}} e^{i\left(k_a^+ - \frac{\omega}{\overline{u}_g}x\right)} \tag{A.6}$$

One obtains by integration:

$$K(x) = \frac{U_g}{1 + i(k_a^+ - \frac{\omega}{\overline{u}_g})\bar{l}_p} e^{\frac{x}{\bar{l}_p}} e^{i(k_a^+ - \frac{\omega}{\overline{u}_g})x} \tag{A.7}$$

which can be reformulated using $M = \overline{u}_g/c$ and $St = \omega/\overline{\tau}_p$ as:

$$K(x) = \frac{U_g}{1 - i\frac{St}{1+M}} e^{i(k_a^+ - \frac{\omega}{\overline{u}_g})x} \tag{A.8}$$

One finally obtains:

$$\hat{u}_{p,p} = \frac{U_g}{1 - i\frac{St}{1+M}} e^{ik_a^+ x} \tag{A.9}$$

where $St = \omega\overline{\tau}_p$ is the Stokes number comparing the characteristic time of a particle to the characteristic time of the flow, here the period frequency. Having $\hat{u}_p = \hat{u}_{p,H} + \hat{u}_{p,p}$, K_0 is determined with the initial condition $\hat{u}_p(0) = 0$ and one finds:

$$K_0 = -\frac{U_g}{1 - i\frac{St}{1+M}} \tag{A.10}$$

Hence, we obtain the expressions given in §4.3 for u_p:

$$\hat{u}_p = U_p \left(e^{ik_a^+ x} - e^{-\frac{x}{\overline{l}_p}} e^{i\frac{\omega}{\overline{u}_g}x} \right) \tag{A.11}$$

where:

$$U_p = \frac{U_g}{1 - \mathrm{i}\frac{St}{1+M}} \tag{A.12}$$

A.2. Expression for the particle number density fluctuation n'_p

When $u_p(0) = \overline{u}_g$, $\overline{n}_p = \overline{n}_p(0)$, and so Equation (4.6) becomes:

$$\frac{\partial \hat{n}_p}{\partial x} - \mathrm{i}\frac{\omega}{\overline{u}_g}\hat{n}_p = -\frac{\overline{n}_p}{\overline{u}_g}\frac{\partial \hat{u}_p}{\partial x} \tag{A.13}$$

First, one looks for the solution of the homogeneous differential equation:

$$\frac{\partial \hat{n}_p}{\partial x} - \mathrm{i}\frac{\omega}{\overline{u}_g}\hat{n}_p = 0$$

$\overline{u}_p$ being constant, the homogeneous solution is:

$$\hat{n}_{p,H} = K_0 e^{i\frac{\omega}{\overline{u}_g}x}$$

Now a particular solution of the equation (A.13) has to be found. The method of variation of constant is again applied here, with:

$$\hat{n}_{p,p} = K(x) e^{i\frac{\omega}{\overline{u}_g}x} \tag{A.14}$$

Re-injecting this solution in (A.13), $K(x)$ is found to obey to:

$$\frac{\partial K}{\partial x} = -\overline{n}_p \frac{U_p^+}{\overline{u}_g} \left(i k_a^+ e^{i\left(k_a^+ - \frac{\omega}{\overline{u}_g}\right)} - \left(-\frac{1}{\overline{l}_p} + i\frac{\omega}{\overline{u}_g} \right) e^{-\frac{x}{\overline{l}_p}} \right) \tag{A.15}$$

Integrating this expression, one obtains:

$$K(x) = -\overline{n}_p \frac{U_p^+}{\overline{u}_g} \left(\frac{k_a^+}{k_a^+ - \frac{\omega}{\overline{u}_g}} e^{i\left(k_a^+ - \frac{\omega}{\overline{u}_g}\right)} - \left(1 - i\frac{\omega}{\overline{u}_g}\overline{l}_p \right) e^{-\frac{x}{\overline{l}_p}} \right) \tag{A.16}$$

which can be reformulated as

$$K(x) = \overline{n}_p \frac{U_p^+}{\overline{u}_g} \left[M e^{i\left(k_a^+ - \frac{\omega}{\overline{u}_g}\right)} + (1 - iSt)\, e^{-\frac{x}{\overline{l}_p}} \right] \tag{A.17}$$

One is now able to write $\hat{n}_{p,p}$ as:

$$\hat{n}_{p,p} = \overline{n}_p \frac{U_p^+}{\overline{u}_g} \left[M e^{i k_a^+ x} + (1 - iSt)\, e^{-\frac{x}{\overline{l}_p}} e^{i\frac{\omega}{\overline{u}_g}x} \right] \tag{A.18}$$

Having $\hat{n}_p = \hat{n}_{p,H} + \hat{n}_{p,p}$, the initial condition $\hat{n}_p(0) = 0$ allows to express K_0 as:

$$K_0 = -\overline{n}_p \frac{U_p^+}{\overline{u}_g} \left[1 + M - iSt \right] \tag{A.19}$$

$$K_0 = -\overline{n}_p \frac{U_g^+}{\overline{u}_g} \left(1 + M \right) \tag{A.20}$$

Combining (A.2), (A.18) and (A.20), $\hat{n}_p$ can be written as:

$$\hat{n}_p = -\overline{n}_p \left[\frac{U_g}{\overline{u}_g} \left(1 + M \right) e^{i\frac{\omega}{\overline{u}_g}x} - \frac{U_p}{\overline{u}_g} \left[M e^{i k_a^+ x} + (1 - iSt)\, e^{-\frac{x}{\overline{l}_p}} e^{i\frac{\omega}{\overline{u}_g}x} \right] \right] \tag{A.21}$$

As given in § 4.3, it is possible to reformulate this expression as:

$$\hat{n}_p = -\overline{n}_p \left[(1 + M) \frac{U_g}{\overline{u}_g} \left(1 - e^{-\frac{x}{\overline{l}_p}} \right) e^{\mathrm{i}\frac{\omega}{\overline{u}_g}x} - M\frac{\hat{u}_p}{\overline{u}_g} \right] \tag{A.22}$$

Appendix B

Detailed derivations of the expressions obtained in Section 4.4

When $\overline{u}_p(0) \neq \overline{u}_g$, it is now mandatory to solve the equations (4.3) and (4.5) to get the evolution the transient regimes where $\overline{u}_p$ and $\overline{n}_p$ reach their final value.

B.1. Expression for the particle velocity fluctuations u'_p

The equation for the mean particle velocity $\overline{u}_p$ (4.3) is given as follows :

$$\overline{\tau}_p \overline{u}_p \frac{\partial \overline{u}_p}{\partial x} + \overline{u}_p = \overline{u}_g \tag{B.1}$$

It is a non-linear differential equation where $\overline{\tau}_p$ and $\overline{u}_p$ are non constant. Assuming that the exponential growth or decay of $\overline{u}_p$ is defined by the initial mean relaxation length $\overline{l}_p(0) = \overline{\tau}_p(0)\overline{u}_p(0)$ and one gets:

$$\overline{u}_p = \overline{u}_g + (\overline{u}_p(0) - \overline{u}_g) e^{-\frac{x}{\overline{l}_p(0)}} \tag{B.2}$$

The expression for $\overline{u}_p$ is used to Equation (4.4) that can be written as follows:

$$\frac{\partial \hat{u}_p}{\partial x} + \hat{u}_p \left(\frac{1}{\overline{l}_p} - i\frac{\omega}{\overline{u}_p} + \frac{\frac{\partial \overline{u}_p}{\partial x}}{\overline{u}_p} \right) = \frac{\hat{u}_g}{\overline{l}_p} \tag{B.3}$$

A straightforward analytical resolution of the Equation (4.7) is now difficult without further approximation. The following hypothesis are made: (1) the general form of the expression for $\hat{u}_p$ when $\overline{u}_p(0) \neq \overline{u}_g$ is the same as the one obtained when $\overline{u}_p(0) = \overline{u}_g$ and (2) the complex amplitudes of the waves are spatially varying much slowly than their phase like in the WKB approximation [69].

Let $\hat{u}_p = A(x)e^{ik_a^+ x} + B(x)e^{i\theta_b(x)}$, where $A \in \mathbb{C}$ while $B, \theta_b \in \mathbb{R}$, and reinject this expression in (B.3):

$$\left[\frac{\partial A}{\partial x} + A \left(i(k_a^+ - \frac{\omega}{\overline{u}_p}) + \frac{1}{\overline{l}_p} + \frac{\frac{\partial \overline{u}_p}{\partial x}}{\overline{u}_p} \right) \right] e^{ik_a^+ x} + \left[\frac{\partial B}{\partial x} + B \left(i \left(\frac{\partial \theta_b}{\partial x} - \frac{\omega}{\overline{u}_p} \right) + \frac{1}{\overline{l}_p} + \frac{\frac{\partial \overline{u}_p}{\partial x}}{\overline{u}_p} \right) \right] e^{i\theta_b(x)} = \frac{U_g}{\overline{l}_p} e^{ik_a^+ x} \tag{B.4}$$

The equation for the complex amplitude A writes:

$$\frac{\partial A}{\partial x} + A\left(i(k_a^+ - \frac{\omega}{\overline{u}_p}) + \frac{1}{\bar{l}_p} + \frac{\frac{\partial \overline{u}_p}{\partial x}}{\overline{u}_p}\right) = \frac{U_g}{\bar{l}_p} \tag{B.5}$$

where the gradient $\dfrac{\partial A}{\partial x}$ compared to the other terms in the above equation. Also from Equation (4.3), one may write:

$$\frac{\frac{\partial \overline{u}_p}{\partial x}}{\overline{u}_p} = \frac{1}{\bar{l}_p}(\frac{\overline{u}_g}{\overline{u}_p} - 1) \tag{B.6}$$

Hence the following expression for A, named as U_p :

$$A = U_p = \frac{U_g}{\frac{\overline{u}_g}{\overline{u}_p} + i(k_a^+ - \frac{\omega}{\overline{u}_p})\bar{l}_p} \tag{B.7}$$

which can also be written as:

$$\hat{U}_p = \frac{\overline{u}_p}{\overline{u}_g}\frac{U_g}{1 - \mathrm{i}(1 - \frac{\overline{u}_p/c}{1+M})Sr} \tag{B.8}$$

where $Sr = \omega\bar{l}_p/\overline{u}_g = St\overline{u}_p/\overline{u}_g$

The second equation for B writes:

$$\frac{\partial B}{\partial x} + B\left[i\left(\frac{\partial \theta_b}{\partial x} - \frac{\omega}{\overline{u}_p}\right) + \frac{1}{\bar{l}_p} + \frac{\frac{\partial \overline{u}_p}{\partial x}}{\overline{u}_p}\right] = 0 \tag{B.9}$$

Here, since $B, \theta_b \in \mathbb{R}$, one can separate the above equations in two independent equation for B and θ_b:

$$\begin{cases} \dfrac{\partial B}{\partial x} + B\left(\dfrac{\frac{\partial \overline{u}_p}{\partial x}}{\overline{u}_p} + \dfrac{1}{\bar{l}_p}\right) = 0 \\ \dfrac{\partial \theta_b}{\partial x} = \dfrac{\omega}{\overline{u}_p} \end{cases} \tag{B.10}$$

Also from Equation (4.3), the following relationship comes:

$$\frac{1}{\bar{l}_p} = \frac{1}{\overline{\tau}_p\overline{u}_p} = -\frac{\frac{\partial \overline{u}_p}{\partial x}}{\overline{u}_p - \overline{u}_g} \tag{B.11}$$

So a straightforward resolution can be done for the amplitude B:

$$B = \mathscr{B}\frac{\overline{u}_p - \overline{u}_g}{\overline{u}_p} \tag{B.12}$$

where $\mathscr{B}$ is a real constant that has to be determined.

For the resolution of the equation of θ_b, we are unable to perform a analytical resolution without assuming the form of $\overline{u}_p$. Hence, the Equation (B.2) is used and one obtains:

$$\theta_b = \frac{\omega}{\overline{u}_g}x + \varphi_b(x) + \Theta_b \tag{B.13}$$

where Θ_b is a constant that needs to be determined and φ_b is the expression of the phase accumulated along the Particle Relaxation Zone (PRZ) given by:

$$\varphi_b(x) = \frac{\omega \bar{l}_p(0)}{\overline{u}_g} \ln(\overline{u}_p) = Sr(0)\ln(\overline{u}_p) \tag{B.14}$$

At this stage, the particle velocity fluctuations can be written as:

$$\hat{u}_p = U_p^+(0)e^{ik_a^+ x} + \mathscr{B}\left(\overline{u}_p - \overline{u}_g\right)\left(\frac{1}{\overline{u}_p}\right)^{(1-iSr(0))} e^{i\left(\frac{\omega}{\overline{u}_g}x + \Theta_b\right)} \tag{B.15}$$

To compute $\mathscr{B}$ and Θ_b, the initial condition $\hat{u}_p(0) = 0$ is used:

$$\hat{u}_p(0) = U_p^+(0) + \mathscr{B}\left(\overline{u}_p(0) - \overline{u}_g\right)\left(\frac{1}{\overline{u}_p(0)}\right)^{(1-iSr(0))} e^{i\Theta_b} = 0 \tag{B.16}$$

$$\mathscr{B}e^{i\Theta_b} = -U_p^+(0)\frac{\overline{u}_p(0)}{\overline{u}_p(0) - \overline{u}_g}\overline{u}_p(0)^{-iSr(0)} \tag{B.17}$$

Hence one gets:

$$\begin{cases} \mathscr{B} = -|U_p(0)|\dfrac{\overline{u}_p(0)}{\overline{u}_p(0) - \overline{u}_{g,0}} \\ \Theta_b = \arg(U_p(0)) - \varphi_b(0) = \arg(U_p(0)) - Sr(0)\ln(\overline{u}_p(0)) \end{cases} \tag{B.18}$$

The final expression for $\tilde{u}_p$ writes:

$$\hat{u}_p = U_p\left(e^{ik_a^+ x} - \frac{U_p(0)}{U_p}\frac{\overline{u}_p - \overline{u}_g}{\overline{u}_p(0) - \overline{u}_g}\left(\frac{\overline{u}_p(0)}{\overline{u}_p}\right)^{(1-iSr(0))} e^{i\frac{\omega}{\overline{u}_g}x}\right) \tag{B.19}$$

Taking the expression given in Equation (B.2) for $\overline{u}_p$, one gets:

$$\hat{u}_p = U_p\left(e^{ik_a^+ x} - \frac{U_p(0)}{U_p}\left(\frac{\overline{u}_p(0)}{\overline{u}_p}\right)^{(1-iSr0))} e^{-\frac{x}{\overline{l}_p(0)}} e^{i\frac{\omega}{\overline{u}_g}x}\right) \tag{B.20}$$

This expression yiels Equation (4.9) for $\overline{u}_p(0) = \overline{u}_g$.

B.2. Expression for the particle number density fluctuations n'_p

The equation for the mean particle number density $\overline{n}_p$ given in (4.5) can be rewritten as follows :

$$\frac{\partial \overline{n}_p}{\partial x} + \overline{n}_p \frac{\frac{\partial \overline{u}_p}{\partial x}}{\overline{u}_p} = 0 \tag{B.21}$$

It comes the following expression for $\overline{n}_p$:

$$\overline{n}_p = \overline{n}_p(0)\frac{\overline{u}_p(0)}{\overline{u}_p} \tag{B.22}$$

Using Equation (B.21), Equation (4.8) can be rewritten as follows:

$$\frac{\partial \hat{n}_p}{\partial x} + \hat{n}_p\left(\frac{\frac{\partial \overline{u}_p}{\partial x}}{\overline{u}_p} - i\frac{\omega}{\overline{u}_p}\right) = \frac{\overline{n}_p}{\overline{u}_p}\left(\hat{u}_p\frac{\frac{\partial \overline{u}_p}{\partial x}}{\overline{u}_p} - \frac{\partial \hat{u}_p}{\partial x}\right) \tag{B.23}$$

Assuming that the solution $\hat{n}_p$ has the form:

$$\hat{n}_p = \frac{\overline{n}_p}{\overline{u}_p}\left[K_1 e^{ik_a^+ x} + K_2 e^{i\theta_b}\right] \tag{B.24}$$

where θ_b is given Equation (B.13), and $K_1, K_2 \in \mathbb{C}$ are two complex amplitudes.

One first computes the expression of $\dfrac{\partial \hat{n}_p}{\partial x}$:

$$\frac{\partial \hat{n}_p}{\partial x} = \hat{n}_p\left(\frac{\frac{\partial \overline{n}_p}{\partial x}}{\overline{n}_p} - \frac{\frac{\partial \overline{u}_p}{\partial x}}{\overline{u}_p}\right) + \frac{\overline{n}_p}{\overline{u}_p}\left[\left(\frac{\partial K_1}{\partial x} + K_1 i k_a^+\right)e^{ik_a^+ x} + \left(\frac{\partial K_2}{\partial x} + iK_2\frac{\partial \theta_b}{\partial x}\right)e^{i\theta_b}\right] \tag{B.25}$$

This expression is written using Equation (B.21) and Equation (B.10) for θ_b:

$$\frac{\partial \hat{n}_p}{\partial x} = -2\hat{n}_p\left(\frac{\frac{\partial \overline{u}_p}{\partial x}}{\overline{u}_p}\right) + \frac{\overline{n}_p}{\overline{u}_p}\left[\left(\frac{\partial K_1}{\partial x} + K_1 i k_a^+\right)e^{ik_a^+ x} + \left(\frac{\partial K_2}{\partial x} + iK_2\frac{\omega}{\overline{u}_p}\right)e^{i\theta_b}\right] \tag{B.26}$$

For the left hand term of Equation (B.23), one may write:

$$\begin{aligned}\frac{\partial \hat{n}_p}{\partial x} + \hat{n}_p\left(\frac{\frac{\partial \overline{u}_p}{\partial x}}{\overline{u}_p} - i\frac{\omega}{\overline{u}_p}\right) = &- \hat{n}_p\left(\frac{\frac{\partial \overline{u}_p}{\partial x}}{\overline{u}_p} + i\frac{\omega}{\overline{u}_p}\right) \\ &+ \frac{\overline{n}_p}{\overline{u}_p}\left[\left(\frac{\partial K_1}{\partial x} + K_1 i k_a^+\right)e^{ik_a^+ x} + \left(\frac{\partial K_2}{\partial x} + iK_2\frac{\omega}{\overline{u}_p}\right)e^{i\theta_b}\right]\end{aligned} \tag{B.27}$$

$$\begin{aligned}\frac{\partial \hat{n}_p}{\partial x} + \hat{n}_p\left(\frac{\frac{\partial \overline{u}_p}{\partial x}}{\overline{u}_p} - i\frac{\omega}{\overline{u}_p}\right) = &\frac{\overline{n}_p}{\overline{u}_p}\left[\frac{\partial K_1}{\partial x} + K_1\left(i\left(k_a^+ - \frac{\omega}{\overline{u}_p}\right) - \frac{\frac{\partial \overline{u}_p}{\partial x}}{\overline{u}_p}\right)\right]e^{ik_a^+ x} \\ &+ \frac{\overline{n}_p}{\overline{u}_p}\left(\frac{\partial K_2}{\partial x} - K_2\frac{\frac{\partial \overline{u}_p}{\partial x}}{\overline{u}_p}\right)e^{i\theta_b}\end{aligned} \tag{B.28}$$

While, using the Equation (B.3) to rewrite $\dfrac{\partial \hat{u}_p}{\partial x}$, the right term of the Equation (B.23) yields:

$$\frac{\overline{n}_p}{\overline{u}_p}\left[\hat{u}_p\frac{\frac{\partial \overline{u}_p}{\partial x}}{\overline{u}_p} - \frac{\partial \hat{u}_p}{\partial x}\right] = \frac{\overline{n}_p}{\overline{u}_p}\left[\hat{u}_p\left(\frac{1}{\overline{l}_p} + 2\frac{\frac{\partial \overline{u}_p}{\partial x}}{\overline{u}_p} - i\frac{\omega}{\overline{u}_p}\right) - \frac{\hat{u}_g}{\overline{l}_p}\right] \tag{B.29}$$

Then Equation (B.23) becomes:

$$\left(\frac{\partial K_1}{\partial x} + K_1\left(i\left(k_a^+ - \frac{\omega}{\overline{u}_p}\right) - \frac{\frac{\partial \overline{u}_p}{\partial x}}{\overline{u}_p}\right)\right)e^{ik_a^+ x} + \left(\frac{\partial K_2}{\partial x} - K_2\frac{\frac{\partial \overline{u}_p}{\partial x}}{\overline{u}_p}\right)e^{i\theta_b}$$
$$= \left[U_p^+\left(\frac{1}{\bar{l}_p} + 2\frac{\frac{\partial \overline{u}_p}{\partial x}}{\overline{u}_p} - i\frac{\omega}{\overline{u}_p}\right) - \frac{U_g^+}{\bar{l}_p}\right]e^{ik_a^+ x} + B\left(\frac{1}{\bar{l}_p} + 2\frac{\frac{\partial \overline{u}_p}{\partial x}}{\overline{u}_p} - i\frac{\omega}{\overline{u}_p}\right)e^{i\theta_b} \quad \text{(B.30)}$$

B.2.1. Determination of K_1

Grouping the terms with the factor $e^{ik_a^+ x}$ in Equation (B.2) leaves an equation for K_1:

$$\frac{\partial K_1}{\partial x} + K_1\left(i\left(k_a^+ - \frac{\omega}{\overline{u}_p}\right) - \frac{\frac{\partial \overline{u}_p}{\partial x}}{\overline{u}_p}\right) = U_p^+\left(\frac{1}{\bar{l}_p} + 2\frac{\frac{\partial \overline{u}_p}{\partial x}}{\overline{u}_p} - i\frac{\omega}{\overline{u}_p}\right) - \frac{U_g^+}{\bar{l}_p} \quad \text{(B.31)}$$

Neglecting here the gradient $\dfrac{\partial A}{\partial x}$ compared to the other terms in the above equation and using Equation (B.6), one obtains:

$$K_1\left[i\left(k_a^+ - \frac{\omega}{\overline{u}_p}\right) + \left(1 - \frac{\overline{u}_g}{\overline{u}_p}\right)\frac{1}{\bar{l}_p}\right] = U_p\left(\frac{2}{\bar{l}_p}\frac{\overline{u}_g}{\overline{u}_p} - \frac{1}{\bar{l}_p} - i\frac{\omega}{\overline{u}_p}\right) - U_p\left(\frac{\overline{u}_g}{\overline{u}_p}\frac{1}{\bar{l}_p} + i(k_a^+ - \frac{\omega}{\overline{u}_p})\right) \quad \text{(B.32)}$$

which can be reformulated as:

$$K_1 = -k_1 U_p \quad \text{(B.33)}$$

where:

$$k_1 = 1 - \frac{1}{\left(1 - \frac{\overline{u}_p/\overline{u}_g}{1+M}\right) + i\frac{1}{St}\left(1 - \frac{\overline{u}_g}{\overline{u}_p}\right)} \quad \text{(B.34)}$$

B.2.2. Computation of K_2

Grouping the terms with the factor $e^{i\theta_b}$ in Equation (B.2) yields an equation for K_2:

$$\frac{\partial K_2}{\partial x} - K_2\frac{\frac{\partial \overline{u}_p}{\partial x}}{\overline{u}_p} = B\left(\frac{1}{\bar{l}_p} + 2\frac{\frac{\partial \overline{u}_p}{\partial x}}{\overline{u}_p} - i\frac{\omega}{\overline{u}_p}\right) \quad \text{(B.35)}$$

The solution of the homogeneous equation is:

$$K_{2,H} = K_0\overline{u}_p \quad \text{(B.36)}$$

Hence, one looks for a particular solution with the method of the constant variation with:

$$K_{2,p} = K(x)\overline{u}_p \quad \text{(B.37)}$$

One solves the equation for $K_R(x) = \mathrm{Re}\,[K(x)]$ first and $K_I(x) = \mathrm{Im}\,[K(x)]$ in a second time.

– **Resolution for $K_R(x) = \mathbf{Re}\,[K(x)]$:**

Only considering the real part of Equation B.35, the equation to solve is :

$$\frac{\partial K_R}{\partial x} = \frac{B}{\overline{u}_p}\left(\frac{1}{\bar{l}_p} + 2\frac{\frac{\partial \overline{u}_p}{\partial x}}{\overline{u}_p}\right) \tag{B.38}$$

Using the relationship (B.11) and the expression for B in Equation (B.12), one gets:

$$\frac{\partial K_R}{\partial x} = \mathscr{B}\frac{\partial \overline{u}_p}{\partial x}\frac{\overline{u}_p - \overline{u}_g}{\overline{u}_p^2}\left(2\frac{1}{\overline{u}_p} - \frac{1}{\overline{u}_p - \overline{u}_g}\right) \tag{B.39}$$

which can be rewritten replacing the variable x by $\overline{u}_p$ as

$$\frac{\partial K_R}{\partial \overline{u}_p} = \mathscr{B}\left(\frac{1}{\overline{u}_p^2} - 2\frac{\overline{u}_g}{\overline{u}_p^3}\right) \tag{B.40}$$

Integrating this equation gives:

$$K_R = \mathscr{B}\left(-\frac{1}{\overline{u}_p} + \frac{\overline{u}_g}{\overline{u}_p^2}\right) \tag{B.41}$$

which can be rewritten using Equation (B.12) as

$$K_R = -\frac{B}{\overline{u}_p} \tag{B.42}$$

– **Resolution for $K_I(x) = \mathbf{Im}\,[K(x)]$:**

Only considering the imaginary part of Equation (B.35), the equation to solve is:

$$\frac{\partial K_I}{\partial x} = -\mathscr{B}\frac{\overline{u}_p - \overline{u}_g}{\overline{u}_p}\frac{\omega}{\overline{u}_p^2} \tag{B.43}$$

Unable to determine an analytical resolution without assuming the form of $\overline{u}_p$, one uses the Equations (B.2) and (B.18) to write:

$$\frac{\partial K_I}{\partial x} \approx -|U_p(0)|\overline{u}_p(0)\omega\frac{e^{-\frac{x}{\bar{l}_p}}}{\overline{u}_p^3} \tag{B.44}$$

Integrating this equation gives:

$$K_I \approx -\frac{|U'_{p,+}(0)|}{2}\frac{\overline{u}_p(0)}{\overline{u}_p(0) - \overline{u}_g}\bar{l}_p(0)\omega\frac{1}{\overline{u}_p^2} \tag{B.45}$$

which can reformulated using (B.18) as:

$$K_I = -\frac{1}{2}\mathscr{B}\frac{\omega\bar{l}_p(0)}{\overline{u}_p} \tag{B.46}$$

This leads to an expression for K_2

$$K_2 = K_0\overline{u}_p - B - i\frac{1}{2}\mathscr{B}\frac{\omega\bar{l}_p(0)}{\overline{u}_p}$$

Using the initial condition $\hat{n}_p(x=0)=0$ to find K_0, one gets:

$$K_1(0) + K_2(0)e^{i\theta_b(0)} = 0 - U'_{p,+}(0)k_1(0) + \left(K_0\overline{u}_p(0) - B(0) - i\frac{1}{2}\mathscr{B}\frac{\omega\bar{l}_p(0)}{\overline{u}_p(0)}\right)e^{i\theta_b(0)} \tag{B.47}$$

which gives:

$$K_0 = \frac{1}{\overline{u}_p(0)}\left(-|U_p(0)|k_1(0) + B(0) + i\frac{1}{2}\mathscr{B}\omega\overline{\tau}_p(0)\right) \tag{B.48}$$

Hence, K_2 finally writes:

$$K_2 = -|U_p(0)|\left(1-k_1(0)\right)\frac{\overline{u}_p}{\overline{u}_p(0)} - B - i\frac{1}{2}\mathscr{B}\frac{\omega\bar{l}_p(0)}{\overline{u}_p}\left(1-\left(\frac{\overline{u}_p}{\overline{u}_p(0)}\right)^2\right) \tag{B.49}$$

which can be reformulated as:

$$\begin{aligned} K_2 = &-|U_p(0)|\left(1-k_1(0)\right)\frac{\overline{u}_p}{\overline{u}_p(0)} - B \\ &+ \frac{i}{2}|U_p(0)|\omega\overline{\tau}_p(0)\left(1+\frac{\overline{u}_p(0)}{\overline{u}_p}\right)\left(1-e^{-\frac{x}{\bar{l}_p(0)}}\right) \end{aligned} \tag{B.50}$$

Using the expression for K_2, k_1 instead of $k_1(0)$ because it gives a better formulation for $\hat{n}_p$ and the results fit closer to the numerical solution. After a few derivations, one obtains for $\hat{n}_p$:

$$\begin{aligned} \hat{n}_p = &-\overline{n}_p\Bigg[\left(1-\frac{1}{\left(1-\frac{\overline{u}_{p/c}}{1+M}\right)+\mathrm{i}\frac{1}{St}\left(1-\frac{\overline{u}_g}{\overline{u}_p}\right)}\right)\frac{\hat{u}_p}{\overline{u}_p} \\ &+\frac{\hat{U}_p(0)}{\overline{u}_p}\left(\frac{\overline{u}_p(0)}{\overline{u}_p}\right)^{\left(1-\mathrm{i}Sr(0)\right)}\left(\frac{\left(\frac{\overline{u}_p}{\overline{u}_p(0)}\right)^2 - e^{-\frac{x}{\bar{l}_p(0)}}}{\left(1-\frac{\overline{u}_{p/c}}{1+M}\right)+\mathrm{i}\frac{1}{St}\left(1-\frac{\overline{u}_g}{\overline{u}_p}\right)}\right. \\ &\left.-\frac{\mathrm{i}}{2}St(0)\left(1+\frac{\overline{u}_p}{\overline{u}_p(0)}\right)\left(1-e^{-\frac{x}{\bar{l}_p(0)}}\right)\right)e^{\mathrm{i}\frac{\omega}{\overline{u}_g}x}\Bigg] \end{aligned} \tag{B.51}$$

This expression yields Equation (4.13) for $\overline{u}_p(0)=\overline{u}_g$.

Appendix C

Influence of the width $\delta\varphi_{PA}$ of the phase averaged windows on the phase-averaged velocity profiles

In the pulsed regime, the PDPA measurements of the gas velocity profiles at $z = 4$ mm are phase averaged for different phase windows $\delta\varphi_{PA}$ with $\varphi_{PA}(k) = k\pi/4$ and $k \in [0, 7]$. The results are shown in Figure C.1. Figure C.2 shows the number of particles N_p over which each point are phase-averaged for different $\delta\varphi_{PA}$. For $\delta\varphi_{PA} = 1^o$, velocity profiles have some irregularities due to the insufficient number of particles ($N_p \approx 100 - 200$) over which phase averages are performed. From $\delta\varphi_{PA} = 5^o$ to $\delta\varphi_{PA} = 22.5^o (= \pi/8)$, there are enough particles ($N_p \approx 1000 - 8000$) to have smooth velocity profiles which are insensitive to $\delta\varphi_{PA}$. For $\delta\varphi_{PA} > \varphi_{PA}(k)/2$, the phase averaged windows begin to overlap and the velocity profiles now depend on $\delta\varphi_{PA}$ as it can be seen for $\delta\varphi_{PA} = 45^o (= \pi/4)$. This analysis is also repeated for different heights z. The value of $\delta\varphi_{PA} = 5^o$ has been retained in Chapter 6 in order to guarantee the convergence of the velocity profiles and a good representation of the instantaneous fluctuations at $\varphi_{PA}(k)$.

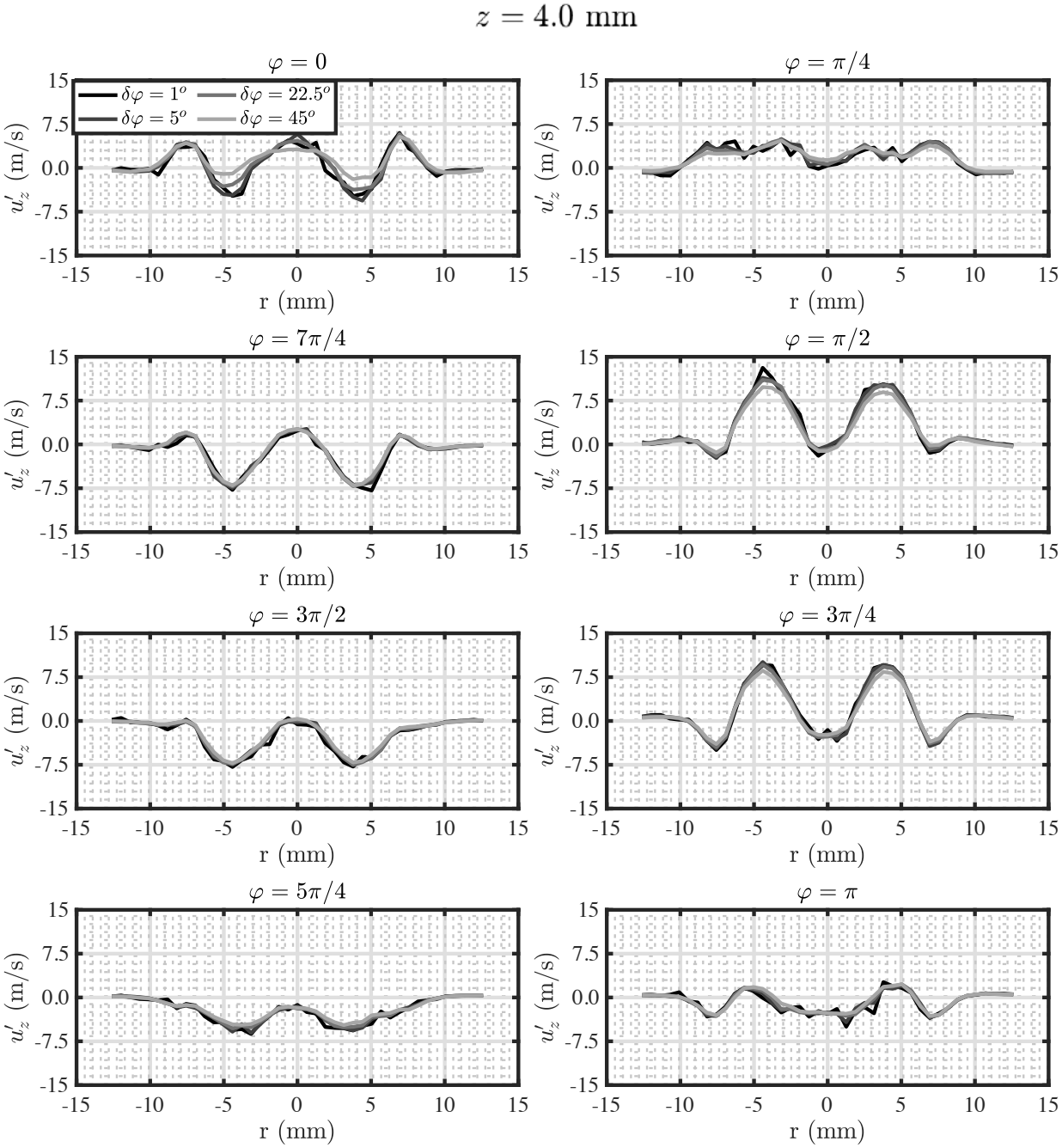

Figure C.1. – Phase-averaged axial velocity profiles of the gaseous phase at z = 4 mm for different width $\delta\varphi_{PA}$ of the phase averaged windows. The common reference for the phase φ is the phase of the acoustic velocity excitation at the combustion chamber backplane calculated with Equation (6.3).

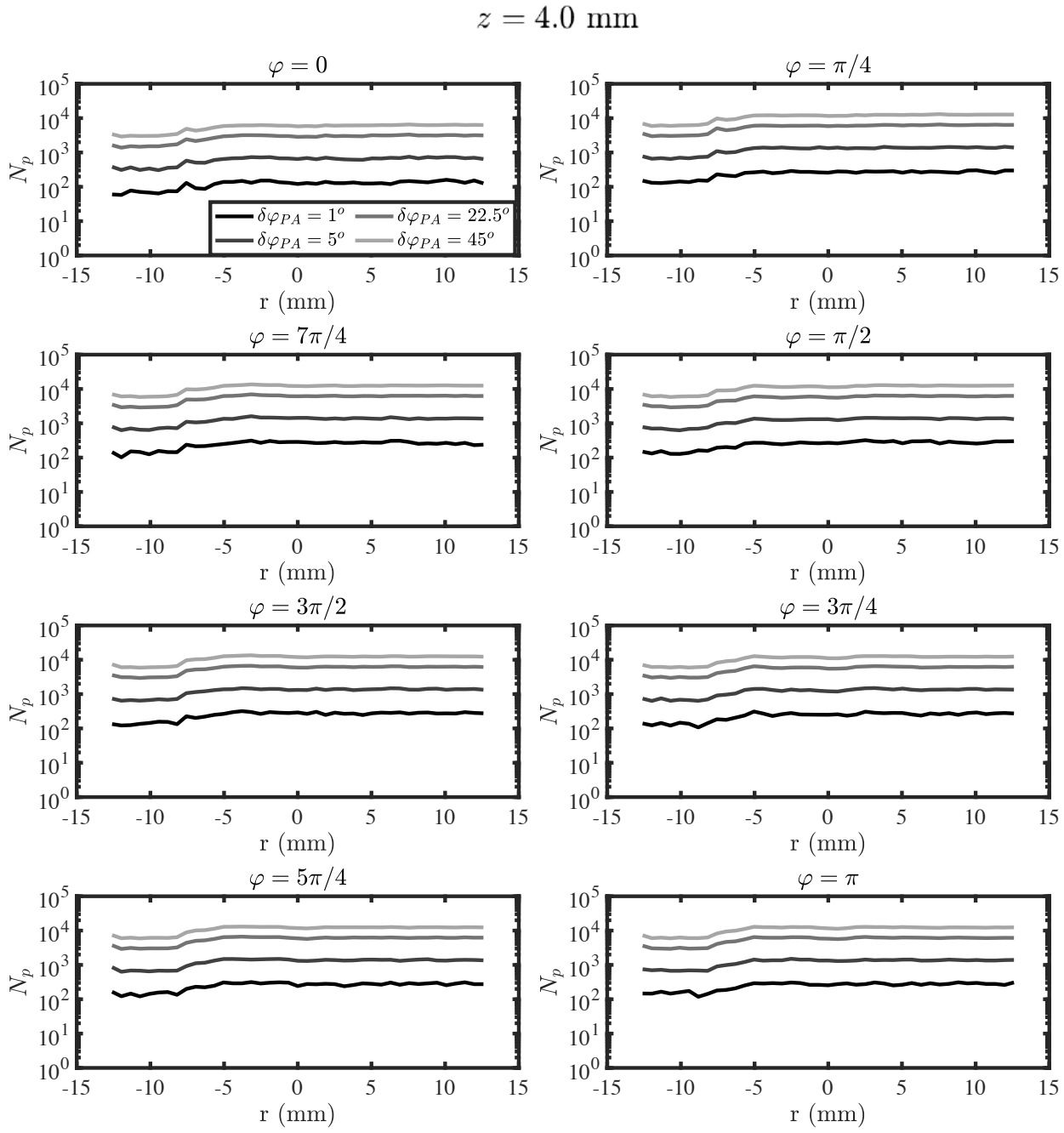

Figure C.2. – Number of particles N_p used to compute the phase-averaged axial velocity profiles of the gaseous phase at z = 4 mm for different width $\delta\varphi_{PA}$ of the phase averaged windows. The common reference for the phase φ is the phase of the acoustic velocity excitation at the combustion chamber backplane computed with Equation (6.3)

Appendix D

Relationship between power spectral densities and transfer functions

In this appendix, the relations used in Chapter 7 to compute the transfer functions with the CPSD and PSD of the recorded signals are detailed. The experimental transfer function $\mathscr{U}$ is defined as:

$$\mathscr{U} = \frac{\tilde{u}_3/\overline{u}_3}{\tilde{u}_2/\overline{u}_2} \tag{D.1}$$

where $\tilde{u}_2/\overline{u}_2$ and $\tilde{u}_3/\overline{u}_3$ are the relative velocity fluctuations recorded respectively by HW2 and HW3. The gain and phase of $\mathscr{U}$ are determined as follows:

$$|\mathscr{U}| = \frac{\overline{u}_2}{\overline{u}_3}\left(\frac{\tilde{u}_3\tilde{u}_3^*}{\tilde{u}_2\tilde{u}_2^*}\right)^{1/2} \tag{D.2}$$

$$\angle\mathscr{U} = \arg\left[\frac{\tilde{u}_3\tilde{u}_2^*}{\overline{u}_2\overline{u}_3}\right] \tag{D.3}$$

When attempting to compute $\mathscr{U}$ from the reconstructed velocity u_3 from the Equations (7.5)-(7.3), one needs to determine the terms $\tilde{u}_3\tilde{u}_3^*$ and $\tilde{u}_3\tilde{u}_2^*$ from the upstream recorded signals u_2 and p_2':

$$\tilde{u}_3\tilde{u}_3^* = K^2\left[|\tilde{\mathcal{T}}(2,1)|^2\tilde{p}_2\tilde{p}_2^* + |\tilde{\mathcal{T}}(2,2)|^2\tilde{u}_2\tilde{u}_2^* + 2\mathrm{Re}\left(\tilde{\mathcal{T}}(2,1)\tilde{\mathcal{T}}(2,2)^*\tilde{p}_2\tilde{u}_2^*\right)\right] \tag{D.4}$$

$$\tilde{u}_3\tilde{u}_2^* = K\left[\mathscr{T}(2,1)\tilde{p}_2\tilde{u}_2^* + \mathscr{T}(2,2)\tilde{u}_2\tilde{u}_2^*\right] \tag{D.5}$$

The gain G and the phase φ_F of the FTF $\mathscr{F}$ can now be deduced. Using the reconstructed velocity transfer function $\mathscr{U}$, $\mathscr{F}$ can be expressed as:

$$\frac{\tilde{\dot{Q}}/\overline{\dot{Q}}}{\tilde{u}_3/\overline{u}_3} = \left(\frac{\tilde{\dot{Q}}/\overline{\dot{Q}}}{\tilde{u}_2/\overline{u}_2}\right)\mathscr{U}^{-1} \tag{D.6}$$

where G and φ_F are determined as follows:

$$G = \left(\frac{\tilde{\dot{Q}}\tilde{\dot{Q}}^*/\overline{\dot{Q}}^2}{\tilde{u}_2\tilde{u}_2^*/\overline{u}_2^2}\right)^{1/2}|\mathscr{U}|^{-1} \tag{D.7}$$

and

$$\varphi_F = \arg\left[\frac{\tilde{\dot{Q}}}{\overline{\dot{Q}}}\frac{\tilde{u}_2^*}{\overline{u}_2}\right] - \angle\mathscr{U} \tag{D.8}$$

Hence, $\tilde{\dot{Q}}\tilde{\dot{Q}}^*/\overline{\dot{Q}}^2$ and $\dot{Q}\tilde{u}_2^*\overline{\dot{Q}}\overline{u}_2$ need to be determined. As shown in Section 7.4.2, $\tilde{\dot{Q}}/\overline{\dot{Q}}$ can be expressed as a function of light intensity fluctuations $\tilde{I}/\overline{I}$ and velocity fluctuations $\tilde{u}_3/\overline{u}_3$:

$$\frac{\tilde{\dot{Q}}}{\overline{\dot{Q}}} = A\left(\frac{\tilde{I}}{\overline{I}} + B\frac{\tilde{u}_3}{\overline{u}_3}\right) \tag{D.9}$$

with:

$$A = \frac{\overline{\dot{Q}} - \dot{Q}_0}{\overline{\dot{Q}}} \text{ and } B = -\beta\frac{\tilde{\Phi}/\overline{\Phi}}{\tilde{u}_3/\overline{u}_3}\frac{\overline{\Phi}}{\overline{\Phi} - \Phi_0} \tag{D.10}$$

where the expression of $(\tilde{\Phi}/\overline{\Phi})/(\tilde{u}_3/\overline{u}_3)$ depends on the assumption made on the fuel-air injection as explained in Section 7.4.2. One then has:

$$\frac{\tilde{\dot{Q}}\tilde{\dot{Q}}^*}{\overline{\dot{Q}}^2} = A^2\left(\frac{\tilde{I}\tilde{I}^*}{\overline{I}^2} + |B|^2\frac{\tilde{u}_3\tilde{u}_3^*}{\overline{u}_3^2} + 2\mathrm{Re}\left(B\frac{\tilde{u}_3}{\overline{u}_3}\frac{\tilde{I}^*}{\overline{I}}\right)\right) \tag{D.11}$$

with

$$\frac{\tilde{u}_3}{\overline{u}_3}\frac{\tilde{I}^*}{\overline{I}} = K\left[\tilde{\mathcal{T}}(2,1)\frac{\tilde{p}_2}{\overline{u}_3}\frac{\tilde{I}^*}{\overline{I}} + \tilde{\mathcal{T}}(2,2)\frac{\tilde{u}_2}{\overline{u}_3}\frac{\tilde{I}^*}{\overline{I}}\right] \tag{D.12}$$

and

$$\frac{\tilde{\dot{Q}}}{\overline{\dot{Q}}}\frac{\tilde{u}_2^*}{\overline{u}_2} = A\left(\frac{\tilde{I}}{\overline{I}}\frac{\tilde{u}_2^*}{\overline{u}_2} + B\frac{\tilde{u}_3}{\overline{u}_3}\frac{\tilde{u}_2^*}{\overline{u}_2}\right) \tag{D.13}$$

Appendix E

Evolution of the OH* signal in quasi-steady conditions

The relationship between I and $\dot{Q}$ empirically determined in Chapter 7, is examined at constant $\dot{Q}$ for different Φ and, in a second step, at constant equivalence ratio Φ for different $\dot{Q}$. The results are shown in Figure E.1. For the lean operating conditions considered, the signal intensity I decreases when Φ increases with a concave evolution at constant $\dot{Q}$. The signal intensity I is also found to be proportional to $\dot{Q}$ at constant Φ.

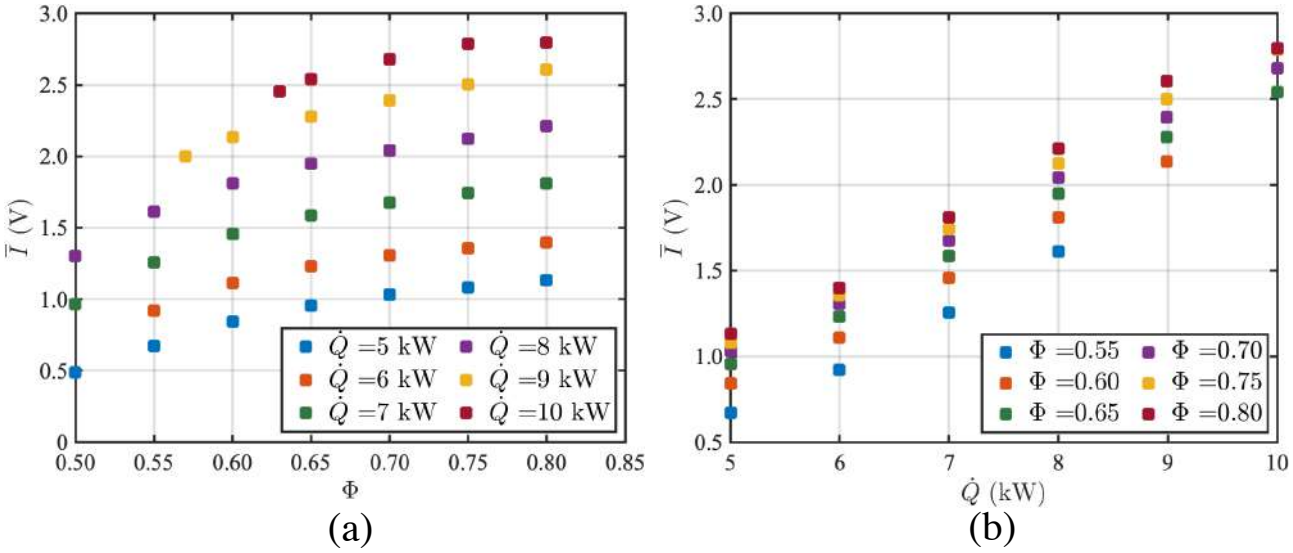

Figure E.1. – OH* light intensity recorded by PM (a) for different thermal powers $\dot{Q}$ as a function of equivalence ratio Φ, and (b) for a different equivalence ratios Φ when varying the thermal power $\dot{Q}$.

Appendix F

EMOOTION Probe: a new probe to detect combustion instabilities

F.1. Presentation of the probe

The luminosity emitted by an unsteady flame gives valuable information about the combustion dynamics, especially when combined with other measurements. The austrian company Combustion Bay One (CBOne) has developed an optical probe combined with a pressure probe that could be easily implemented inside a combustion chamber. A collaborative project has begun with CBOne in order to monitor the TALISMAN test rig with their new probe named "Emootion" shown in Figure F.1. It consists of a combination of 4 air-cooled photodiodes (RGB and White) surrounding a fast pressure transducer into a single and compact cylinder device designed to perform optic-acoustic monitoring in pressurised combustion chamber. THis sensor is made to infer the Rayleigh index and can be viewed as a Rayleigh Criterion Probe (RCP). More information about the probe and the different tests performed can be found in [301]. Already validated on their own air-propane premixed 2-stage burner reproducing a model power gas turbine, CBOne is willing to validate their technology on other burners. Reproducing a single sector of an annular combustor of aero-engine, the swirl-stabilized spray TALISMAN burner constitutes an opportunity for CBOne to push towards an application to aircraft engines.

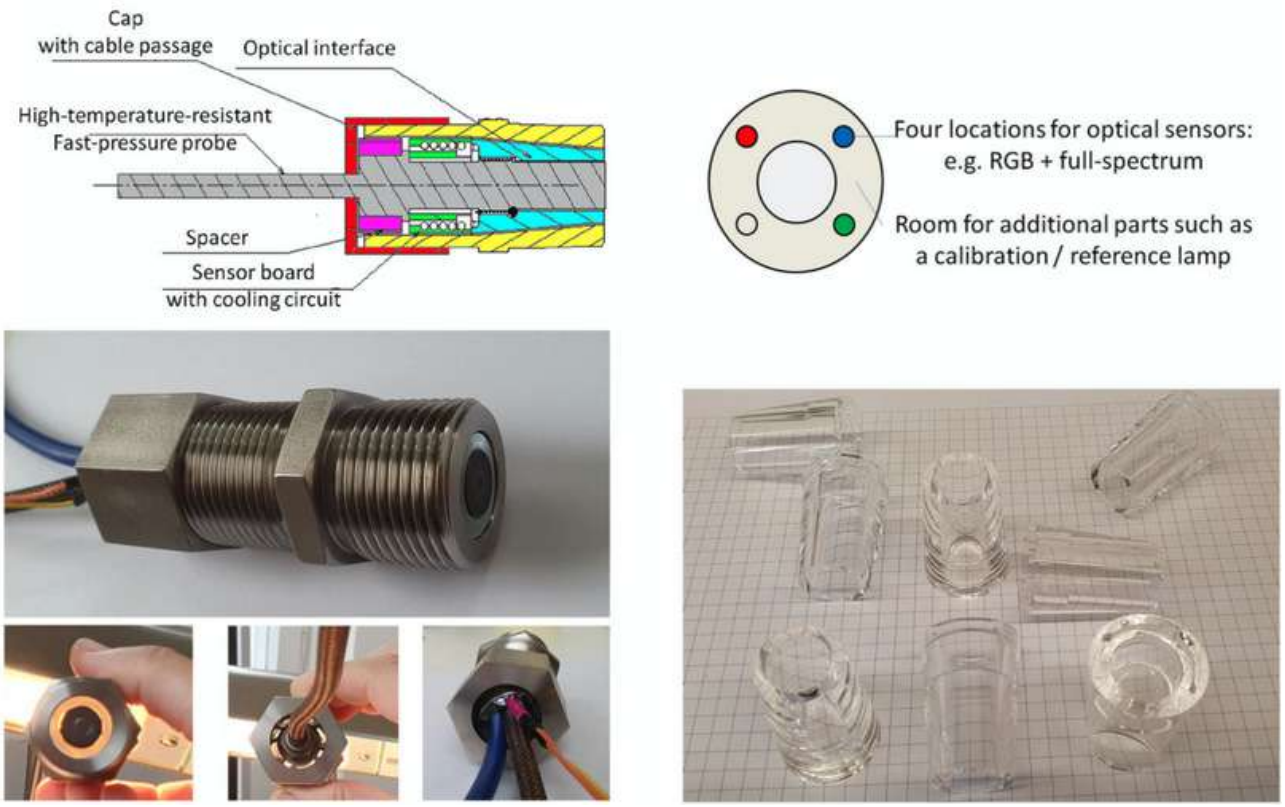

Figure F.1. – High-pressure, high-temperature-resistant Rayleigh Criterion Probe: (top) cutaway and principle including colour photodiodes arrangement and (bottom) pictures of the actual probe and details of the optical interface. Images from [301].

F.2. Implementation of the RCP on the TALISMAN burner

The design of the TALISMAN combustion chamber has been modified to insert conveniently the RCP probes. As shown in Figure F.2, they are mounted on the square chamber of configuration $\mathscr{C}_2$ described in Section 2.2.2. Two of the quartz walls of the square combustion chamber are replaced by a combination of two steel plates with a fiber glass gasket between them to lower the heat transfer towards the probe. Associated with a water cooling pipe wrapped around the sleeve where the probe is screwed into, the probes are protected from overheating. A hole is drilled in the wall and the sleeve carrying the probes is welded into it to provide an optical and acoustic access to the chamber.

Figure F.3 shows how the optimal length of the sleeve has been determined in order to guarantee the widest field of vision and omptimize the compactness of the device according to the view angle of the photodiodes (here 13°). Two RCP probes are necessary to capture the whole spray flame. They record the light originating respectively from the root and the tip of the flame. Their positions were determined for a truncated cone geometry of flame with an height of 50 mm, a root diameter of 25 mm and a tip diameter of 75 mm. To avoid Helmholtz resonances and hot dead gas pockets, the sleeves are filled with quartz glass hollow cylinders . The resonant frequencies were determined to be around 4000 Hz when the tube is filled with hot gases. The RCP at the lowest position records the light and pressure originating from the flame bottom. The upper RCP probe records the pressure and light originating from the tip of the flame. These two probes are mounted on opposite walls in order to capture the entire flame region.

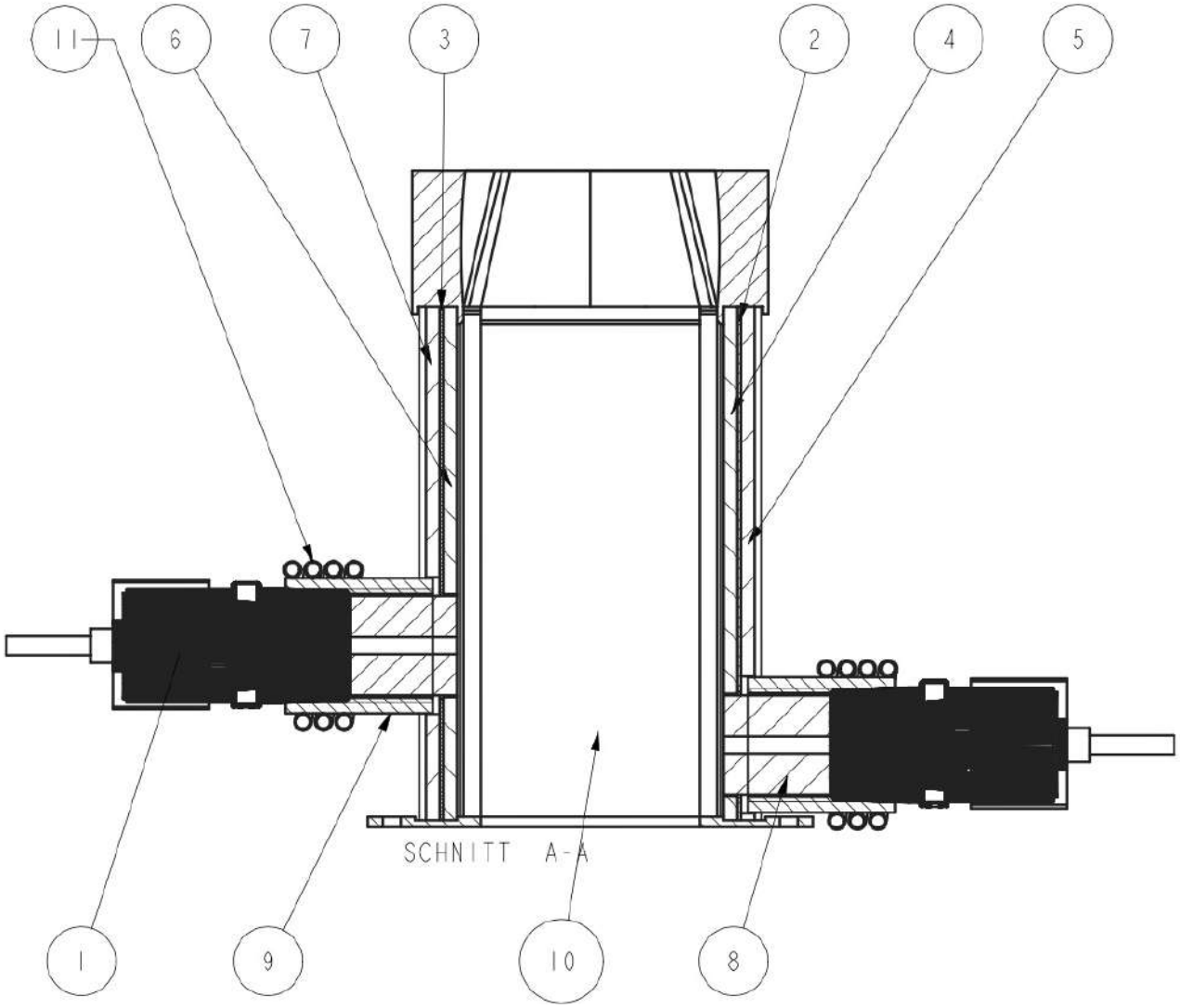

Figure F.2. – Technical drawing of the square combustion chamber of the TALISMAN setup instrumented with the EMOOTION probes (provided by CBOne).

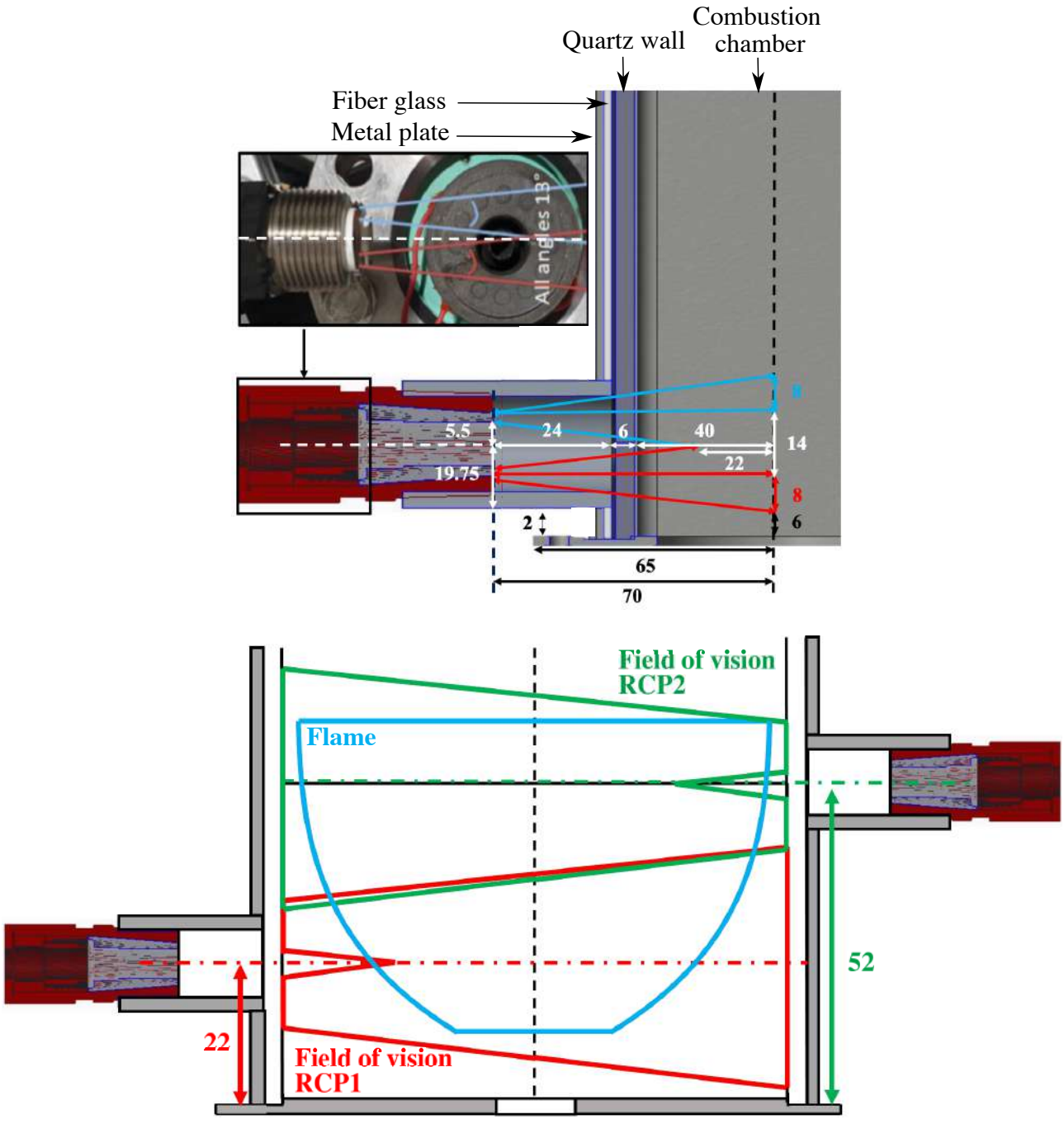

Figure F.3. – (Up) Field of view from a single RCP mounted on the sleeve with the dimensions retained for the set-up. (Bottom) Scaled representation of the whole field of view captured by the set of RCPs superposed to the region covered by the flame.

F.3. Results

Measurements are performed at $P = 7$ kW from $\Phi = 0.65$ to $\Phi = 0.80$. These conditions correspond to unstable points with a level of instability that progressively increases with the equivalence ratio. The acoustic and optical signals recorded by the RCPs are compared to the signals measured by a photomultiplier with an OH^* filter and with the microphone M3 mounted on a water-cooled waveguide. PSD of the different signals are shown in Figure F.4. No noticeable difference are detected when switching to the white, blue, red or green diode of the RCPs. This indicate that the air-fuel mixing is good enough to avoid the formation of soot by the flame. This is in agreement with the color of the flame which is mainly blue without red shades. The RCPs detect clearly the instability and, their signals have similar spectra as the ones detected by M3 and PM. The signals recorded by the RCPs are however slightly weaker due to the lower sensitivity of the RCP probes. They exhibit the same fundamental (230 Hz) and the same harmonic frequencies between all the probes. The width and the relative amplitude of the peaks compared to the background noise are also roughly the same. Nonetheless the background noise is higher for the RCP probes signals. The diode signals have a 50 Hz peak probably due to ground loops even when they are feeded with batteries. The source of the ground loop could not be identified. The pressure and the light signal measurements weakly differ here from RCP1 to RCP2.

F.4. Conclusions

RCPs have shown to have similar performances to detect and to characterize self-excited oscillations in the swirl spray TALISMAN setup. These results confirm the potential of RCPs to be used for online monitoring. For the next prototype of the Emootion probe, CBOne aims to have a transparent probe head of 8 mm, using miniature rapid probes (4 mm in diameter). The rest would remain similar, with at least one cooled photodiode on the probe.

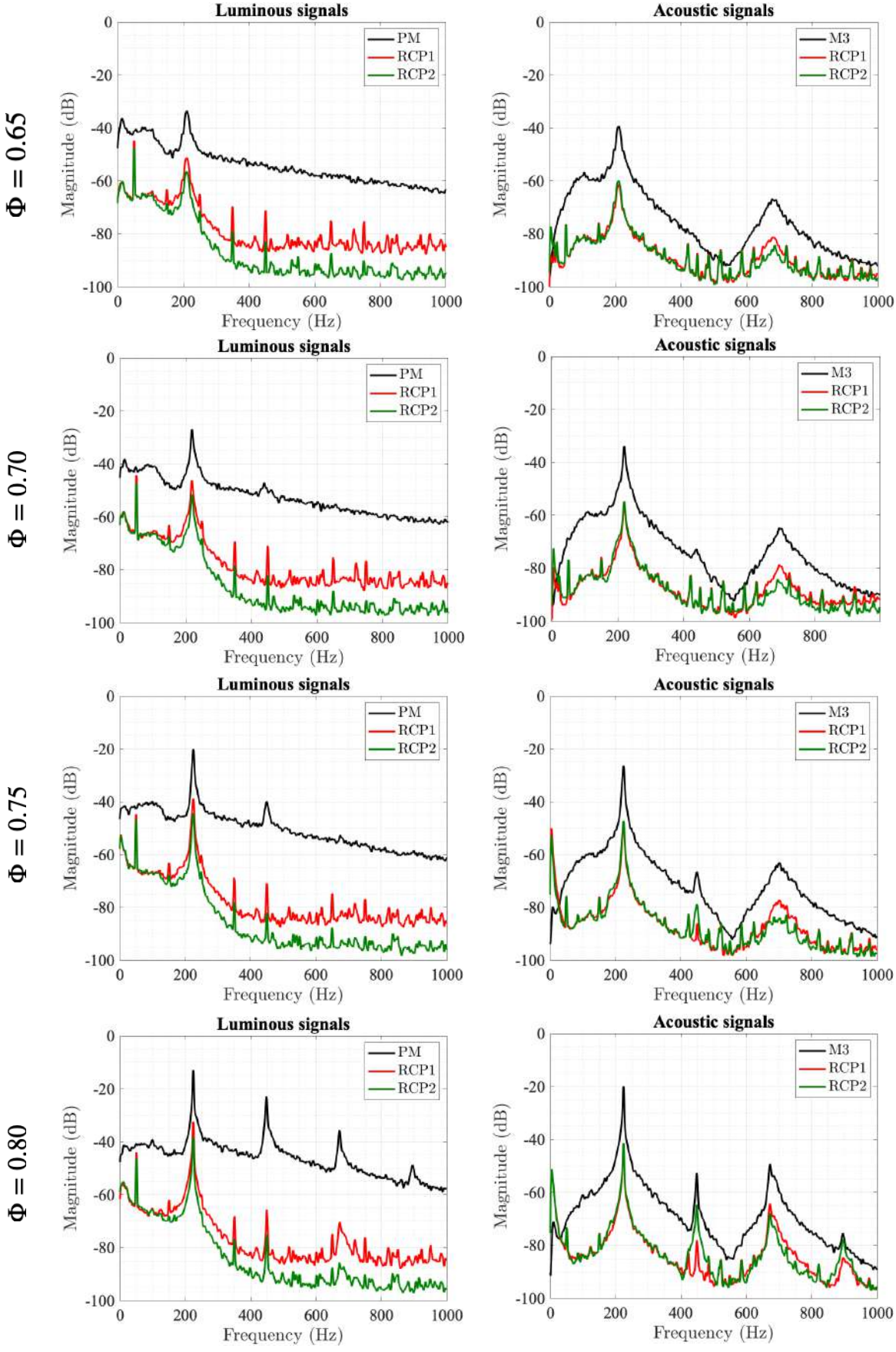

Figure F.4. – Power spectra of (left) the luminous signals and (right) the acoustic signals recorded by **M3**, **PM** and the RCPs for different equivalent ratios Φ and a fixed power of $P = 7$ kW.

Bibliography

[1] P. J. Crutzen, "Geology of mankind," Nature, vol. 415, pp. 23–23, 2002.

[2] C. Bonneuil and J.-B. Fressoz, L'événement Anthropocène: la Terre, l'histoire et nous. Paris, France: Points, 2013.

[3] A. Malm and A. Hornborg, "The geology of mankind? a critique of the anthropocene narrative," The Anthropocene Review, vol. 1, no. 1, pp. 62–69, 2014.

[4] J. Moore, Capitalism in the Web of Life: Ecology and the Accumulation of Capital. New-York, USA: Verso Books, 2015.

[5] A. D. Barnosky, E. A. Hadly, J. Bascompte, E. L. Berlow, J. H. Brown, M. Fortelius, W. M. Getz, J. Harte, A. Hastings, P. A. Marquet, et al., "Approaching a state shift in earth's biosphere," Nature, vol. 486, no. 7401, pp. 52–58, 2012.

[6] E. Wilson, L'avenir de la vie. Paris, France: Seuil, 2003.

[7] S. L. Pimm, C. N. Jenkins, R. Abell, T. M. Brooks, J. L. Gittleman, L. N. Joppa, P. H. Raven, C. M. Roberts, and J. O. Sexton, "The biodiversity of species and their rates of extinction, distribution, and protection," Science, vol. 344, no. 6187, p. 1246752, 2014.

[8] P. Forster, T. Storelvmo, K. Armour, W. Collins, J.-L. Dufresne, D. Frame, D. Lunt, T. Mauritsen, M. Palmer, M. Watanabe, M. Wild, and H. Zhang, The Earth's Energy Budget, Climate Feedbacks, and Climate Sensitivity, p. 923–1054. Cambridge, United Kingdom and New York, NY, USA: Cambridge University Press, 2021.

[9] J. Rockström, W. Steffen, K. Noone, Å. Persson, F. S. Chapin III, E. Lambin, T. M. Lenton, M. Scheffer, C. Folke, H. J. Schellnhuber, et al., "Planetary boundaries: exploring the safe operating space for humanity," Ecology and society, vol. 14, no. 2, 2009.

[10] L. Persson, B. Carney Almroth, C. Collins, S. Cornell, C. de Wit, M. Diamond, P. Fantke, M. Hassellöv, M. MacLeod, M. Ryberg, P. Jørgensen, P. Villarrubia-Gómez, Z. Wang, and M. Hauschild, "Outside the safe operating space of the planetary boundary for novel entities," Environmental Science & Technology, vol. 56, pp. 1510–1521, 01 2022.

[11] D. Lee, D. Fahey, A. Skowron, M. Allen, U. Burkhardt, Q. Chen, S. Doherty, S. Freeman, P. Forster, J. Fuglestvedt, A. Gettelman, R. De León, L. Lim, M. Lund, R. Millar, B. Owen, J. Penner, G. Pitari, M. Prather, R. Sausen, and L. Wilcox, "The contribution of global aviation to anthropogenic climate forcing for 2000 to 2018," Atmospheric Environment, vol. 244, p. 117834, 2021.

[12] S. Delbecq, J. Fontane, N. Gourdain, H. Mugnier, T. Planès, Simatos, and F., "Référentiel ISAE-SUPAERO aviation et climat," 2021.

[13] G. C. Oates, Aircraft propulsion systems technology and design. Washington, USA: AIAA, 1989.

[14] A. M. Mellor, Design of Modern Turbine Combustors. Cambridge, USA, London, UK, San Diego, USA and Oxford, UK: Academic Press, 1990.

[15] A. Lefebvre and D. Ballal, Gas Turbine Combustion: Alternative Fuels and Emissions, Third Edition. Boca Raton, USA: Taylor & Francis, 2010.

[16] J. D. Mattingly, W. H. Heiser, D. T. Pratt, K. M. Boyer, and B. A. Haven, Aircraft Engine Design, Third Edition. Washington, USA: AIAA, 2018.

[17] C. Soares, ed., Gas Turbine: A Handbook of Air, Land and Sea Applications. Oxford, UK: Butterworth-Heinemann, second edition ed., 2015.

[18] P. Palies, Stabilization and Dynamic of Premixed Swirling Flames. Cambridge, USA, London, UK, San Diego, USA and Oxford, UK: Academic Press, 2020.

[19] S. Blakey, L. Rye, and C. W. Wilson, "Aviation gas turbine alternative fuels: A review," Proceedings of the Combustion Institute, vol. 33, no. 2, pp. 2863–2885, 2011.

[20] J. Holladay, Z. Abdullah, and J. Heyne, "Sustainable aviation fuel: Review of technical pathways," 9 2020.

[21] S. S. Doliente, A. Narayan, J. F. D. Tapia, N. J. Samsatli, Y. Zhao, and S. Samsatli, "Bio-aviation fuel: a comprehensive review and analysis of the supply chain components," Frontiers in Energy Research, vol. 8, p. 110, 2020.

[22] A. Lefebvre and V. McDonell, Atomization and Sprays. Combustion (New York, N.Y. : 1989), Boca Raton, FL, USA: CRC Press, 2017.

[23] R. A. Dafsari, H. J. Lee, J. Han, D.-C. Park, and J. Lee, "Viscosity effect on the pressure swirl atomization of an alternative aviation fuel," Fuel, vol. 240, pp. 179–191, 2019.

[24] N. Syred and J. Beér, "Combustion in swirling flows: A review," Combustion and Flame, vol. 23, no. 2, pp. 143–201, 1974.

[25] O. Lucca-Negro and T. O'Doherty, "Vortex breakdown: a review," Progress in Energy and Combustion Science, vol. 27, no. 4, pp. 431–481, 2001.

[26] G. Vignat, D. Durox, and S. Candel, "The suitability of different swirl number definitions for describing swirl flows: Accurate, common and (over-) simplified formulations," Progress in Energy and Combustion Science, vol. 89, p. 100969, 2022.

[27] Y. Huang and V. Yang, "Dynamics and stability of lean-premixed swirl-stabilized combustion," Progress in Energy and Combustion Science, vol. 35, no. 4, pp. 293–364, 2009.

[28] R. Hadef and B. Lenze, "Measurements of droplets characteristics in a swirl-stabilized spray flame," Experimental Thermal and Fluid Science, vol. 30, no. 2, pp. 117–130, 2005.

[29] G. Eckel, J. Grohmann, L. Cantu, N. Slavinskaya, T. Kathrotia, M. Rachner, P. Le Clercq, W. Meier, and M. Aigner, "LES of a swirl-stabilized kerosene spray flame with a multi-component vaporization model and detailed chemistry," Combustion and Flame, vol. 207, pp. 134–152, 2019.

[30] J. Senoner, M. Sanjosé, T. Lederlin, F. Jaegle, M. García, E. Riber, B. Cuenot, L. Gicquel, H. Pitsch, and T. Poinsot, "Eulerian and Lagrangian large-eddy simulations of an evaporating two-phase flow," Comptes Rendus Mécanique, vol. 337, no. 6, pp. 458–468, 2009.

[31] M. Sanjosé, J. Senoner, F. Jaegle, B. Cuenot, S. Moreau, and T. Poinsot, "Fuel injection model for Euler–Euler and Euler–Lagrange large-eddy simulations of an evaporating spray inside an

aeronautical combustor," International Journal of Multiphase Flow, vol. 37, no. 5, pp. 514–529, 2011.

[32] D. G. Lilley, "Swirl flows in combustion: A review," AIAA Journal, vol. 15, no. 8, pp. 1063–1078, 1977.

[33] C. Edwards and R. Rudoff, "Structure of a swirl-stabilized spray flame by imaging, laser doppler velocimetry, and phase doppler anemometry," in Symposium (International) on Combustion, vol. 23, pp. 1353–1359, Elsevier, 1991.

[34] C. Presser, A. Gupta, and H. Semerjian, "Aerodynamic characteristics of swirling spray flames: Pressure-jet atomizer," Combustion and Flame, vol. 92, no. 1, pp. 25–44, 1993.

[35] D. L. Bulzan, "Structure of a swirl-stabilized combusting spray," Journal of Propulsion and Power, vol. 11, no. 6, pp. 1093–1102, 1995.

[36] V. Sankaran and S. Menon, "LES of spray combustion in swirling flows," Journal of Turbulence, vol. 3, p. 11, feb 2002.

[37] N. Rock, S. D. Stouffer, T. H. Hendershott, E. Corporan, and P. Wrzesinski, Characterization of Coherent Flow Structures in a Swirl-Stabilized Spray Combustor.

[38] S. Menon and R. Ranjan, Spray Combustion in Swirling Flow, p. 351–392. Cambridge, UK: Cambridge University Press, 2016.

[39] A. H. Lefebvre, "The Role of Fuel Preparation in Low-Emission Combustion," Journal of Engineering for Gas Turbines and Power, vol. 117, pp. 617–654, 10 1995.

[40] F. Ommi and M. Azimi, "Most effective combustion technologies for reducing nox emissions in aero gas turbines," The International Journal of Multiphysics, vol. 6, pp. 417–424, Dec. 2012.

[41] V. McDonell, "5 - lean combustion in gas turbines," in Lean Combustion (Second Edition) (D. Dunn-Rankin and P. Therkelsen, eds.), pp. 147–201, Boston, USA: Academic Press, second edition ed., 2016.

[42] Y. Liu, X. Sun, V. Sethi, D. Nalianda, Y.-G. Li, and L. Wang, "Review of modern low emissions combustion technologies for aero gas turbine engines," Progress in Aerospace Sciences, vol. 94, pp. 12–45, 2017.

[43] S. Mosier and R. Pierce, "Advanced combustion systems for stationary gas turbine engines. volume i. review and preliminary evaluation. final report december 1975-september 1976," tech. rep., Pratt and Whitney Aircraft Group, West Palm Beach, FL (USA). Government ..., 1980.

[44] K. M. Tacina, "Swirl-venturi lean direct injection combustion technology for low-nox aero gas turbine engines," in Spring Technology Meeting, Central States Section of the Combustion Institute, pp. 1–9, 2018.

[45] S. Samuelsen, Rich burn, quick-mix, lean burn (RQL) combustor, pp. 227–233. Morgantown, WV, USA: US Department of Energy, Office of Fossil Energy, National Energy Technology , 2006.

[46] M. Foust, D. Thomsen, R. Stickles, C. Cooper, and W. Dodds, "Development of the GE aviation low emissions taps combustor for next generation aircraft engines," in 50th AIAA Aerospace Sciences Meeting including the New Horizons Forum and Aerospace Exposition.

[47] S. M. Correa, "Power generation and aeropropulsion gas turbines: From combustion science to combustion technology," Symposium (International) on Combustion, vol. 27, no. 2, pp. 1793–1807, 1998.

[48] "Combustion instabilities in lean premixed systems," in Lean Combustion (Second Edition) (D. Dunn-Rankin and P. Therkelsen, eds.), pp. 231–259, Boston, USA: Academic Press, second edition ed., 2016.

[49] S. Candel, "Combustion dynamics and control: Progress and challenges," Proceedings of the Combustion Institute, vol. 29, no. 1, pp. 1–28, 2002.

[50] H. Mongia, T. Held, G. Hsiao, and R. Pandalai, "Challenges and Progress in Controlling Dynamics in Gas Turbine Combustors," Journal of Propulsion and Power, vol. 19, no. 5, pp. 822–829, 2003.

[51] T. C. Lieuwen and V. Yang, Combustion instabilities in gas turbine engines: operational experience, fundamental mechanisms, and modeling. Reston, VA, USA: American Institute of Aeronautics and Astronautics, 2005.

[52] T. Poinsot, "Prediction and control of combustion instabilities in real engines," Proceedings of the Combustion Institute, vol. 36, no. 1, pp. 1–28, 2017.

[53] C. Laurent, Low-order modeling and high-fidelity simulations for the prediction of combustion instabilities in liquid rocket engines and gas turbines. PhD thesis, 2020. Thèse de doctorat dirigée par Poinsot, Thierry et Gicquel, Laurent Energétique et Transferts Toulouse, INPT 2020, France.

[54] Rayleigh, "The explanation of certain acoustical phenomena1," Nature, vol. 18, no. 455, pp. 319–321, 1878.

[55] W. Polifke, C. Paschereit, and T. Sattelmayer, "A universaily applicable stability criterion for complex thermo-acoustic systems," pp. 455–460, 01 1997.

[56] F. Nicoud and T. Poinsot, "Thermoacoustic instabilities : Should the Rayleigh criterion be extended to include entropy changes?," Combustion and Flame, vol. 142, pp. 153–159, 2005.

[57] B.-T. Chu, "On the energy transfer to small disturbances in fluid flow (part i)," Acta Mechanica, vol. 1, no. 3, pp. 215–234, 1965.

[58] S. Ducruix, T. Schuller, D. Durox, and S. Candel, "Combustion dynamics and instabilities: Elementary coupling and driving mechanisms," Journal of Propulsion and Power, vol. 19, no. 5, pp. 722–734, 2003.

[59] L. de Goey, J. van Oijen, V. Kornilov, and J. ten Thije Boonkkamp, "Propagation, dynamics and control of laminar premixed flames," Proceedings of the Combustion Institute, vol. 33, no. 1, pp. 863–886, 2011.

[60] S. Candel, D. Durox, T. Schuller, J.-F. Bourgouin, and J. P. Moeck, "Dynamics of swirling flames," Annual Review of Fluid Mechanics, vol. 46, no. 1, pp. 147–173, 2014.

[61] J. O'Connior, V. Acharya, and T. Lieuwen, "Transverse combustion instabilities: Acoustic, fluid mechanic, and flame processes," Progress in Energy and Combustion Science, vol. 49, pp. 1–39, 2015.

[62] G. Vignat, D. Durox, T. Schuller, and S. Candel, "Combustion dynamics of annular systems," Combustion Science and Technology, vol. 192, no. 7, pp. 1358–1388, 2020.

[63] G. Vignat, Injection and combustion dynamics in swirled spray flames and azimuthal coupling in annular combustors. PhD thesis, Université Paris-Saclay, France, 2020.

[64] P. Gajan, F. Simon, M. Orain, and V. Bodoc, "Investigation and modeling of combustion instabilities in aero engines," Aerospace Lab, no. 11, pp. 1–12, 2016.

[65] S. Candel, D. Durox, S. Ducruix, A.-L. Birbaud, N. Noiray, and T. Schuller, "Flame dynamics and combustion noise: Progress and challenges," International Journal of Aeroacoustics, vol. 8, no. 1, pp. 1–56, 2009.

[66] I. Duran, S. Moreau, F. Nicoud, T. Livebardon, E. Bouty, and T. Poinsot, "Combustion noise in modern aero-engines," Aerospace Lab, no. 7, 2014.

[67] A. P. Dowling and Y. Mahmoudi, "Combustion noise," Proceedings of the Combustion Institute, vol. 35, no. 1, pp. 65–100, 2015.

[68] W. C. Strahle, "Combustion noise," Progress in Energy and Combustion Science, vol. 4, no. 3, pp. 157–176, 1978.

[69] D. G. Crighton, A. P. Dowling, J. Ffowcs-Williams, M. Heckl, F. Leppington, and J. F. Bartram, Modern methods in analytical acoustics lecture notes. Melville, NY, USA: Acoustical Society of America, 1992.

[70] P. Clavin and E. D. Siggia, "Turbulent premixed flames and sound generation," Combustion Science and Technology, vol. 78, no. 1-3, pp. 147–155, 1991.

[71] F. Nicoud, L. Benoit, C. Sensiau, and T. Poinsot, "Acoustic modes in combustors with complex impedances and multidimensional active flames," AIAA Journal, vol. 45, no. 2, pp. 426–441, 2007.

[72] F. Culick, "Nonlinear behavior of acoustic waves in combustion chambers—i," Acta Astronautica, vol. 3, no. 9, pp. 715–734, 1976.

[73] N. Kings and F. Bake, "Indirect combustion noise: Noise generation by accelerated vorticity in a nozzle flow," International Journal of Spray and Combustion Dynamics, vol. 2, no. 3, pp. 253–266, 2010.

[74] F. Marble and S. Candel, "Acoustic disturbance from gas non-uniformities convected through a nozzle," Journal of Sound and Vibration, vol. 55, no. 2, pp. 225–243, 1977.

[75] J. Keller, W. Egli, and J. Hellat, "Thermally induced low-frequency oscillations," Zeitschrift für angewandte Mathematik und Physik ZAMP, vol. 36, pp. 250–274, 1985.

[76] A. S. Morgans and I. Duran, "Entropy noise: A review of theory, progress and challenges," International Journal of Spray and Combustion Dynamics, vol. 8, no. 4, pp. 285–298, 2016.

[77] T. Poinsot and D. Veynante, Theoretical and Numerical Combustion. Philadelphia, PA, USA: R.T. Edwards Inc., 2005.

[78] F. Baillot, D. Durox, and R. Prud'homme, "Experimental and theoretical study of a premixed vibrating flame," Combustion and Flame, vol. 88, no. 2, pp. 149–168, 1992.

[79] T. Schuller, D. Durox, and S. Candel, "A unified model for the prediction of laminar flame transfer functions: comparisons between conical and v-flame dynamics," Combustion and Flame, vol. 134, no. 1, pp. 21 – 34, 2003.

[80] Preetham and T. Lieuwen, "Nonlinear flame-flow transfer function calculations: flow disturbance celerity effects," in 40th AIAA/ASME/SAE/ASEE Joint Propulsion Conference and Exhibit, no. 4035, 2004.

[81] D. Durox, T. Schuller, and S. Candel, "Combustion dynamics of inverted conical flames," Proceedings of the Combustion Institute, vol. 30, no. 2, pp. 1717–1724, 2005.

[82] P. Palies, D. Durox, T. Schuller, and S. Candel, "The combined dynamics of swirler and turbulent premixed swirling flames," Combustion and Flame, vol. 157, no. 9, pp. 1698–1717, 2010.

[83] P. Palies, D. Durox, T. Schuller, and S. Candel, "Nonlinear combustion instability analysis based on the flame describing function applied to turbulent premixed swirling flames," Combustion and Flame, vol. 158, no. 10, pp. 1980–1991, 2011.

[84] P. Palies, T. Schuller, D. Durox, and S. Candel, "Modeling of premixed swirling flames transfer functions," Proceedings of the Combustion Institute, vol. 33, no. 2, pp. 2967–2974, 2011.

[85] T. Saitoh and Y. Otsuka, "Unsteady behavior of diffusion flames and premixed flames for counter flow geometry," Combustion Science and Technology, vol. 12, no. 4-6, pp. 135–146, 1976.

[86] F. N. Egolfopoulos and C. S. Campbell, "Unsteady counterflowing strained diffusion flames: diffusion-limited frequency response," Journal of Fluid Mechanics, vol. 318, p. 1–29, 1996.

[87] T. Brown, R. Pitz, and C. Sung, "Oscillatory stretch effects on the structure and extinction of counterflow diffusion flames," Symposium (International) on Combustion, vol. 27, no. 1, pp. 703–710, 1998.

[88] P.-H. Renard, D. Thévenin, J. Rolon, and S. Candel, "Dynamics of flame/vortex interactions," Progress in Energy and Combustion Science, vol. 26, no. 3, pp. 225–282, 2000.

[89] E. Halle, O. Delabroy, F. Lacas, D. Veynante, and S. Candel, "Structure of an acoustically forced turbulent spray flame," Symposium (International) on Combustion, vol. 26, no. 1, pp. 1663 – 1670, 1996.

[90] F. E. Culick, "Combustion instabilities in liquid-fuelled propulsion systems," in AGARD Conference on Combustion instabilities in liquid-fuelled propulsion systems, Caltech, USA, 1988.

[91] M. Saito, M. Sato, and I. Suzuki, "Evaporation and combustion of a single fuel droplet in acoustic fields," Fuel, vol. 73, no. 3, pp. 349 – 353, 1994.

[92] M. Saito, M. Hoshikawa, and M. Sato, "Enhancement of evaporation/combustion rate coefficient of a single fuel droplet by acoustic oscillation," Fuel, vol. 75, no. 6, pp. 669 – 674, 1996.

[93] R. I. Sujith, G. A. Waldherr, J. I. Jagoda, and B. T. Zinn, "An Experimental Investigation of the Behavior of Droplets in Axial Acoustic Fields," Journal of Vibration and Acoustics, vol. 119, pp. 285–292, 07 1997.

[94] R. I. Sujith, G. A. Waldherr, J. I. Jagoda, and B. T. Zinn, "A Theoretical Investigation of the Behavior of Droplets in Axial Acoustic Fields," Journal of Vibration and Acoustics, vol. 121, pp. 286–294, 07 1999.

[95] R. I. Sujith, G. A. Waldherr, J. I. Jagoda, and B. T. Zinn, "Experimental investigation of the evaporation of droplets in axial acoustic fields," Journal of Propulsion and Power, vol. 16, no. 2, pp. 278–285, 2000.

[96] J. Carvalho, M. McQuay, and P. Gotaç, "The interaction of liquid reacting droplets with the pulsating flow in a rijke-tube combustor," Combustion and Flame, vol. 108, no. 1, pp. 87–103, 1997.

[97] Y. Méry, L. Hakim, P. Scouflaire, L. Vingert, S. Ducruix, and S. Candel, "Experimental investigation of cryogenic flame dynamics under transverse acoustic modulations," Comptes Rendus Mécanique, vol. 341, no. 1, pp. 100–109, 2013.

[98] T. Sattelmayer, M. Schmid, and M. Schulze, "Impact of injector mass flow fluctuations on combustion dynamics in liquid engines," Journal of Spacecraft and Rockets, vol. 52, no. 5, pp. 1417–1429, 2015.

[99] L. Hakim, T. Schmitt, S. Ducruix, and S. Candel, "Dynamics of a transcritical coaxial flame under a high-frequency transverse acoustic forcing: Influence of the modulation frequency on the flame response," Combustion and Flame, vol. 162, no. 10, pp. 3482–3502, 2015.

[100] A. Genot, S. Gallier, and T. Schuller, "Thermo-acoustic instabilities driven by fuel droplet lifetime oscillations," Proceedings of the Combustion Institute, vol. 37, no. 4, pp. 5359–5366, 2019.

[101] F. Giuliani, P. Gajan, O. Diers, and M. Ledoux, "Influence of pulsed entries on a spray generated by an air-blast injection device: An experimental analysis on combustion instability processes in aeroengines," Proceedings of the Combustion Institute, vol. 29, no. 1, pp. 91 – 98, 2002.

[102] P. Gajan, A. Strzelecki, B. Platet, R. Lecourt, and F. Giuliani, "Investigation of spray behavior downstream of an aeroengine injector with acoustic excitation," Journal of Propulsion and Power, vol. 23, no. 2, pp. 390–397, 2007.

[103] J. Eckstein, E. Freitag, C. Hirsch, and T. Sattelmayer, "Experimental Study on the Role of Entropy Waves in Low-Frequency Oscillations in a RQL Combustor," Journal of Engineering for Gas Turbines and Power, vol. 128, no. 2, pp. 264–270, 2006.

[104] M. de la Cruz García, E. Mastorakos, and A. Dowling, "Investigations on the self-excited oscillations in a kerosene spray flame," Combustion and Flame, vol. 156, no. 2, pp. 374 – 384, 2009.

[105] C. Pera and J. Reveillon, "Direct numerical simulation of spray flame/acoustic interactions," Proceedings of the Combustion Institute, vol. 31, no. 2, pp. 2283 – 2290, 2007.

[106] V. Fratalocchi and J. B. Kok, "Ethanol turbulent spray flame response to gas velocity modulation," Combustion Theory and Modelling, vol. 22, no. 1, pp. 91–109, 2018.

[107] F. Baillot, C. Patat, M. Cáceres, J.-B. Blaisot, and E. Domingues, "Saturation phenomenon of swirling spray flames at pressure antinodes of a transverse acoustic field," Proceedings of the Combustion Institute, vol. 38, no. 4, pp. 5987–5995, 2021.

[108] C. Patat, J.-B. Blaisot, E. Domingues, and F. Baillot, "Response of a spray of n-heptane or dodecane at an acoustic pressure antinode in reactive conditions," International Conference on Liquid Atomization and Spray Systems (ICLASS), vol. 1, 08 2021.

[109] C. Patat, F. Baillot, J.-B. Blaisot, and E. Domingues, "Responses of lean swirling spray flames to acoustic pressure and transverse velocity perturbations," in Symposium on Thermoacoustics in Combustion: Industry meets Academia (SoTiC 2021), (Munich, Germany), Sept. 2021.

[110] R. I. Sujith, "An experimental investigation of interaction of sprays with acoustic fields," Experiments in Fluids, vol. 38, no. 5, pp. 576–587, 2005.

[111] F. Baillot, J.-B. Blaisot, G. Boisdron, and C. Dumouchel, "Behavior of an air-assisted jet submitted to a transverse high-frequency acoustic field," Journal of Fluid Mechanics, vol. 640, pp. 305–342, 2009.

[112] J. Apeloig, F.-X. d'Herbigny, F. Simon, P. Gajan, M. Orain, and S. Roux, "Liquid-fuel behavior in an aeronautical injector submitted to thermoacoustic instabilities," Journal of Propulsion and Power, vol. 31, pp. 309–319, 2015.

[113] V. Bodoc, A. Desclaux, P. Gajan, F. Simon, and G. Illac, "Characterization of confined liquid jet injected into oscillating air crossflow," Flow, Turbulence and Combustion, vol. 104, pp. 1–18, 2020.

[114] E. L. Schiavo, D. Laera, E. Riber, L. Gicquel, and T. Poinsot, "On the impact of fuel injection angle in euler–lagrange large eddy simulations of swirling spray flames exhibiting thermoacoustic instabilities," Combustion and Flame, vol. 227, pp. 359–370, 2021.

[115] D. Katoshevski, T. Shakked, S. S. Sazhin, C. Crua, and M. R. Heikal, "Grouping and trapping of evaporating droplets in an oscillating gas flow," International Journal of Heat and Fluid Flow, vol. 29, no. 2, pp. 415–426, 2008.

[116] Q. Li and W. Yang, "Study on gas-droplet heat and mass transfers in oscillating flows," International Journal of Heat and Mass Transfer, vol. 126, pp. 52 – 60, 2018.

[117] J. Li, D. Yang, C. Luzzato, and A. S. Morgans, "Open source combustion instability low order simulator (oscilos-long) technical report," Imperial College London, London, UK, pp. 1–48, 2015.

[118] A. P. Dowling, "The calculation of thermoacoustic oscillations," Journal of Sound and Vibration, vol. 180, no. 4, pp. 557–581, 1995.

[119] W. Polifke, A. Poncet, C. Paschereit, and K. Döbbeling, "Reconstruction of acoustic transfer matrices by instationary computational fluid dynamics," Journal of Sound and Vibration, vol. 245, no. 3, pp. 483–510, 2001.

[120] R. Gaudron, Réponse acoustique de flammes prémélangées soumises à des ondes sonores harmoniques. PhD thesis, 2018. Thèse de doctorat dirigée par Schuller, Thierry et Mirat, Clément Combustion Université Paris-Saclay (ComUE) 2018, France.

[121] W. Polifke, Low-Order Analysis Tools for Aero- and Thermo-Acoustic Instabilities. Advances in Aero-Acoustics and Thermo-Acoustics. Von Karman Institute for Fluid Dynamics., Rhode-St-Genèse, Belgium, 11 2010.

[122] T. Sattelmayer, "Influence of the Combustor Aerodynamics on Combustion Instabilities From Equivalence Ratio Fluctuations ," Journal of Engineering for Gas Turbines and Power, vol. 125, pp. 11–19, 12 2002.

[123] T. Sattelmayer and W. Polifke, "Assessment of methods for the computation of the linear stability of combustors," Combustion Science and Technology, vol. 175, no. 3, pp. 453–476, 2003.

[124] W. Polifke, C. Paschereit, and K. Döbbeling, "Suppression of combustion instabilities through destructive interference of acoustic and entropy waves," in Sixth International Conference on Sound and Vibration, Copenhagen, Denmark, 01 1999.

[125] J.-F. Parmentier, P. Salas, P. Wolf, G. Staffelbach, F. Nicoud, and T. Poinsot, "A simple analytical model to study and control azimuthal instabilities in annular combustion chambers," Combustion and Flame, vol. 159, no. 7, pp. 2374–2387, 2012.

[126] M. Bauerheim, J.-F. Parmentier, P. Salas, F. Nicoud, and T. Poinsot, "An analytical model for azimuthal thermoacoustic modes in an annular chamber fed by an annular plenum," Combustion and Flame, vol. 161, no. 5, pp. 1374–1389, 2014.

[127] L. Crocco and S.-I. Cheng, "Theory of combustion instability in liquid propellant rocket motors," tech. rep., Princeton Univ NJ, USA, 1956.

[128] N. Noiray, D. Durox, S. T., and S. Candel, "A unified framework for nonlinear combustion instability analysis based on the flame describing function," Journal of Fluid Mechanics, vol. 615, p. 139–167, 2008.

[129] D. Durox, T. Schuller, N. Noiray, and S. Candel, "Experimental analysis of nonlinear flame transfer functions for different flame geometries," Proceedings of the Combustion Institute, vol. 32, no. 1, pp. 1391–1398, 2009.

[130] T. Schuller, T. Poinsot, and S. Candel, "Dynamics and control of premixed combustion systems based on flame transfer and describing functions," Journal of Fluid Mechanics, vol. 894, p. P1, 2020.

[131] W. Polifke, "Modeling and analysis of premixed flame dynamics by means of distributed time delays," Progress in Energy and Combustion Science, vol. 79, p. 100845, 2020.

[132] T. Lieuwen and B. T. Zinn, "The role of equivalence ratio oscillations in driving combustion instabilities in low nox gas turbines," Symposium (International) on Combustion, vol. 27, no. 2, pp. 1809 – 1816, 1998.

[133] A. Birbaud, S. Ducruix, D. Durox, and S. Candel, "The nonlinear response of inverted "v" flames to equivalence ratio nonuniformities," Combustion and Flame, vol. 154, no. 3, pp. 356 – 367, 2008.

[134] K. Truffin and T. Poinsot, "Comparison and extension of methods for acoustic identification of burners," Combustion and Flame, vol. 142, no. 4, pp. 388 – 400, 2005.

[135] R. Gaudron, M. Gatti, C. Mirat, and T. Schuller, "Flame describing functions of a confined premixed swirled combustor with upstream and downstream forcing," Journal of Engineering for Gas Turbines and Power, vol. 141, no. 5, p. 051016, 2018.

[136] J. Seume, N. Vortmeyer, W. Krause, J. Hermann, C.-C. Hantschk, P. Zangl, S. Gleis, D. Vortmeyer, and A. Orthmann, "Application of Active Combustion Instability Control to a Heavy Duty Gas Turbine," Journal of Engineering for Gas Turbines and Power, vol. 120, no. 4, pp. 721–726, 1998.

[137] K. McManus, T. Poinsot, and S. Candel, "A review of active control of combustion instabilities," Progress in Energy and Combustion Science, vol. 19, no. 1, pp. 1 – 29, 1993.

[138] D. W. Kendrick, T. J. Anderson, W. A. Sowa, and T. S. Snyder, "Acoustic Sensitivities of Lean-Premixed Fuel Injectors in a Single Nozzle Rig," Journal of Engineering for Gas Turbines and Power, vol. 121, no. 3, pp. 429–436, 1999.

[139] C. O. Paschereit, P. Flohr, H. Kno¨pfel, W. Geng, C. Steinbach, P. Stuber, K. Bengtsson, and E. Gutmark, "Combustion Control by Extended EV Burner Fuel Lance," in Turbo Expo: Power for Land, Sea, and Air, vol. Volume 1: Turbo Expo 2002, pp. 721–730, 06 2002.

[140] J. Moeck, D. Lacoste, C. Laux, and C. Paschereit, "Control of combustion dynamics in a swirl-stabilized combustor with nanosecond repetitively pulsed discharges," in 51st AIAA Aerospace Sciences Meeting including the New Horizons Forum and Aerospace Exposition.

[141] D. A. Lacoste, J. P. Moeck, D. Durox, C. O. Laux, and T. Schuller, "Effect of Nanosecond Repetitively Pulsed Discharges on the Dynamics of a Swirl-Stabilized Lean Premixed Flame," Journal of Engineering for Gas Turbines and Power, vol. 135, 08 2013.

[142] W. Kim, J. Snyder, and J. Cohen, "Plasma assisted combustor dynamics control," Proceedings of the Combustion Institute, vol. 35, no. 3, pp. 3479 – 3486, 2015.

[143] D. A. Lacoste, J. P. Moeck, W. L. Roberts, S. H. Chung, and M. S. Cha, "Analysis of the step responses of laminar premixed flames to forcing by non-thermal plasma," Proceedings of the Combustion Institute, vol. 36, no. 3, pp. 4145 – 4153, 2017.

[144] D. A. Lacoste, Y. Xiong, J. P. Moeck, S. H. Chung, W. L. Roberts, and M. S. Cha, "Transfer functions of laminar premixed flames subjected to forcing by acoustic waves, ac electric fields, and non-thermal plasma discharges," Proceedings of the Combustion Institute, vol. 36, no. 3, pp. 4183 – 4192, 2017.

[145] W. Kim and J. Cohen, "Plasma-assisted combustor dynamics control at realistic gas turbine conditions," Combustion Science and Technology, vol. 193, pp. 1–20, 10 2019.

[146] P. Berenbrink and S. Hoffmann, "Suppression of dynamic combustion instabilities by passive and active means," in Turbo Expo: Power for Land, Sea, and Air, vol. Volume 2: Coal, Biomass and Alternative Fuels; Combustion and Fuels; Oil and Gas Applications; Cycle Innovations, 2000.

[147] J. Hermann and S. Hoffmann, Implementation of Active Control in a Full-Scale Gas-Turbine Combustor, ch. 19, pp. 611–634. Reston, VA, USA: American Institute of Aeronautics and Astronautics, 2006.

[148] S. Kulkarni, C. F. Silva, and W. Polifke, "Response of spray number density and evaporation rate to velocity oscillations," International Journal of Spray and Combustion Dynamics, vol. 14, no. 1-2, pp. 107–117, 2022.

[149] C. Mirat, D. Durox, and T. Schuller, "Analysis of the Spray and Transfer Function of Swirling Spray Flames From a Multi-Jet Steam Assisted Liquid Fuel Injector," in Volume 4A: Combustion, Fuels and Emissions, Turbo Expo: Power for Land, Sea, and Air, 06 2014. V04AT04A008.

[150] C. Mirat, D. Durox, and T. Schuller, "Stability analysis of a swirl spray combustor based on flame

describing function," Proceedings of the Combustion Institute, vol. 35, no. 3, pp. 3291–3298, 2015.

[151] K. Prieur, Dynamique de la combustion dans un foyer annulaire multi-injecteurs diphasique. PhD thesis, Université Paris-Saclay, Paris, France, Dec. 2017.

[152] P. Rajendram Soundararajan, D. Durox, A. Renaud, G. Vignat, and S. Candel, "Swirler effects on combustion instabilities analyzed with measured fdfs, injector impedances and damping rates," Combustion and Flame, vol. 238, p. 111947, 2022.

[153] P. Rajendram Soundararajan, G. Vignat, D. Durox, A. Renaud, and S. Candel, "Do flame describing functions suitably represent combustion dynamics under self-sustained oscillations?," Journal of Sound and Vibration, vol. 534, p. 117034, 2022.

[154] P. Rajendram Soundararajan, D. Durox, A. Renaud, and S. Candel, "Impact of spray dynamics on combustion instabilities investigated by changing the atomizer recess in a swirl combustor," Combustion and Flame, vol. 252, p. 112757, 2023.

[155] J. Renner, M. March, T. A. Do, M. Merk, C. Hirsch, and T. Sattelmayer, "Flame transfer functions of the lean burnout zone of an rql combustion chamber - dynamic response to primary zone and mixing port velocity fluctuations," International Journal of Spray and Combustion Dynamics, vol. 0, no. 0, 2023.

[156] C. D. Slabaugh, A. C. Pratt, R. P. Lucht, S. E. Meyer, M. Benjamin, K. Lyle, and M. Kelsey, "The development of an optically accessible, high-power combustion test rig," Review of Scientific Instruments, vol. 85, no. 3, 2014.

[157] A. Brito Lopes, N. Emekwuru, and K. Joshi, "Are the available data from laboratory spray burners suitable for cfd modelling validations? a review," Energy Conversion and Management: X, vol. 16, p. 100289, 2022.

[158] A. Cochet, V. Bodoc, C. Brossard, O. Dessornes, C. Guin, R. Lecourt, M. Orain, and A. Vincent-Randonnier, "Onera test facilities for combustion in aero gas turbine engines, and associated optical diagnostics," Aerospace Lab, p. 16 pages, June 2016.

[159] F. Grisch, A. Boukhalfa, G. Cabot, B. Renou, and A. Vandel, "CORIA aeornautical combustion facilities and associated optical diagnostics," Aerospace Lab, no. 11, 2016.

[160] P. Rajendram Soundararajan, Investigation of combustion instabilities in annular combustors combining injector dynamics and flame describing functions determined in simplified configurations. Theses, Université Paris-Saclay, Paris, France, July 2022.

[161] G. Vignat, D. Durox, T. Schuller, and S. Candel, "Combustion dynamics of annular systems.," Combustion Science and Technology, vol. 192, no. 7, pp. 1358–1388, 2020.

[162] G. Oztarlik, Numerical and experimental investigations of combustion instabilities of swirled premixed methane-air flames with hydrogen addition. PhD thesis, 2020. Thèse de doctorat dirigée par Poinsot, Thierry et Selle, Laurent Dynamique des fluides Toulouse, INPT 2020, Toulouse, France.

[163] S. Marragou, H. Magnes, A. Aniello, L. Selle, T. Poinsot, and T. Schuller, "Experimental analysis and theoretical lift-off criterion for h2/air flames stabilized on a dual swirl injector," Proceedings of the Combustion Institute, vol. 39, no. 4, pp. 4345–4354, 2023.

[164] M. Ferand, T. Livebardon, M. Sanjosé, and S. Moreau, "Numerical prediction of far-field combustion noise from aeronautical engines," Acoustics, vol. 1, 2019.

[165] G. Comte-Bellot, "Hot-wire anemometry," Annual Review of Fluid Mechanics, vol. 8, no. 1, pp. 209–231, 1976.

[166] I. Hurle, R. Price, T. M. Sugden, and A. Thomas, "Sound emission from open turbulent premixed flames," Proceedings of the Royal Society of London. Series A. Mathematical and Physical Sciences, vol. 303, no. 1475, pp. 409–427, 1968.

[167] P. Rajendram Soundararajan, D. Durox, A. Renaud, G. Vignat, and S. Candel, "Swirler effects on combustion instabilities analyzed with measured fdfs, injector impedances and damping rates," Combustion and Flame, vol. 238, p. 111947, 2022.

[168] H. Albrecht, N. Damaschke, M. Borys, and C. Tropea, Laser Doppler and Phase Doppler Measurement Techniques. Experimental Fluid Mechanics, Springer Berlin Heidelberg, 2013.

[169] A. Yule, C. AhSeng, P. Felton, A. Ungut, and N. Chigier, "A laser tomographic investigation of liquid fuel sprays," Symposium (International) on Combustion, vol. 18, no. 1, pp. 1501–1510, 1981.

[170] P. Sagaut and Y.-T. Lee, "Large eddy simulation for incompressible flows: An introduction. scientific computation series," Applied Mechanics Reviews, vol. 55, pp. 115–, 11 2002.

[171] T. Schonfeld and M. Rudgyard, "Steady and unsteady flow simulations using the hybrid flow solver avbp," AIAA Journal, vol. 37, no. 11, pp. 1378–1385, 1999.

[172] N. Gourdain, L. Gicquel, M. Montagnac, O. Vermorel, M. Gazaix, G. Staffelbach, M. Garcia, J.-F. Boussuge, and T. Poinsot, "High performance parallel computing of flows in complex geometries: I. methods," Computational Science & Discovery, vol. 2, p. 015003, nov 2009.

[173] N. Gourdain, L. Gicquel, G. Staffelbach, O. Vermorel, F. Duchaine, J.-F. Boussuge, and T. Poinsot, "High performance parallel computing of flows in complex geometries: Ii. applications," Computational Science & Discovery, vol. 2, p. 015004, nov 2009.

[174] D. Paulhiac, Modélisation de la combustion d'un spray dans un brûleur aéronautique. PhD thesis, École doctorale Mécanique, énergétique, génie civil et procédés, Toulouse, 2015.

[175] P. Lax, "Systems of conservation laws," tech. rep., Los Alamos Scientific Laboratory of the University of California, 1959.

[176] H. Toda, O. Cabrit, G. Balarac, S. Bose, J. Lee, H. Choi, and N. Franck, "A subgrid-scale model based on singular values for les in complex geometries," Proc. Summer Program, 2010.

[177] F. Nicoud, H. B. Toda, O. Cabrit, S. Bose, and J. Lee, "Using singular values to build a subgrid-scale model for large eddy simulations," Physics of Fluids, vol. 23, no. 8, p. 085106, 2011.

[178] L. Schiller, "A drag coefficient correlation," Zeit. Ver. Deutsch. Ing., vol. 77, pp. 318–320, 1933.

[179] B. Abramzon and W. Sirignano, "Droplet vaporization model for spray combustion calculations," International Journal of Heat and Mass Transfer, vol. 32, no. 9, pp. 1605 – 1618, 1989.

[180] T. J. Poinsot and S. K. Lele, "Boundary conditions for direct simulations of compressible viscous flows," Journal of Computational Physics, vol. 101, no. 1, pp. 104–129, 1992.

[181] N. Rizk and A. Lefebvre, "Internal flow characteristics of simplex swirl atomizers," Journal of Propulsion and Power, vol. 1, no. 3, pp. 193–199, 1985.

[182] M. Q. McQuay and R. K. Dubey, "The interaction of well-characterized, longitudinal acoustic waves with a nonreacting spray," Atomization and Sprays, vol. 8, no. 4, pp. 419–437, 1998.

[183] R. K. Gurubaran and R. Sujith, "An experimental investigation of evaporative sprays in axial acoustic fields," in 44th AIAA/ASME/SAE/ASEE Joint Propulsion Conference and Exhibit, no. 2008-4769, 2008.

[184] R. K. Gurubaran and R. I. Sujith, "Dynamics of spray – swirl – acoustics interactions," International Journal of Spray and Combustion Dynamics, vol. 3, no. 1, pp. 1–22, 2011.

[185] M. Zhu, A. Dowling, and K. Bray, "Self-excited oscillations in combustors with spray atomizers," Journal of Engineering for Gas Turbines and Power, vol. 123, pp. 779–786, 2001.

[186] D. Katoshevski, M. Ruzal, T. Shakked, and E. Sher, "Particle grouping, a new method for reducing emission of submicron particles from diesel engines," Fuel, vol. 89, no. 9, pp. 2411–2416, 2010.

[187] L. Freret, C. Lacour, S. de Chaisemartin, S. Ducruix, D. Durox, F. Laurent, and M. Massot, "Pulsated free jets with polydisperse spray injection: Experiments and numerical simulations," Proceedings of the Combustion Institute, vol. 32, no. 2, pp. 2215–2222, 2009.

[188] C. Lacour, D. Durox, S. Ducruix, and M. Massot, "Interaction of a polydisperse spray with vortices," Experiments in Fluids, vol. 51, pp. 295–311, 08 2011.

[189] D. Katoshevski, "Characteristics of spray grouping/non-grouping behavior," Aerosol and Air Quality Research, vol. 6, pp. 54–66, 01 2006.

[190] D. Katoshevski, T. Shakked, and S. S. Sazhin, "Particle grouping in standing and moving wave velocity fields," International Journal of Engineering Systems Modelling and Simulation, vol. 2, no. 3, p. 177, 2010.

[191] P. S. Mahapatra, A. Mukhopadhyay, and M. V. Panchagnula, "Dispersion of polydisperse droplets in a pulsating flow field," Procedia IUTAM, vol. 15, pp. 242 – 248, 2015.

[192] J. Achury and W. Polifke, "Modulation of spray droplet number density and size distribution by an acoustic field," The Journal of Computational Multiphase Flows, vol. 9, no. 1, pp. 32–46, 2017.

[193] Q. Li, G. Lei, and W. Yang, "Study on the clustering of dispersed particles in an oscillating flow field," Powder Technology, vol. 311, pp. 167 – 174, 2017.

[194] A. K. Gupta, S. B. Chen, L. E. Yu, A. Prhashanna, and D. Katoshevski, "CFD study on particle grouping under an oscillatory flow in a wavy duct," Separation and Purification Technology, vol. 213, pp. 303–313, 2018.

[195] Q. Li, F. Dong, and P. Liu, "A numerical study on the acoustic forcing of a laminar premixed saturated spray flame," Journal of Thermal Analysis and Calorimetry, vol. 139, no. 4, pp. 2899–2912, 2020.

[196] R. Gurubaran and R. Sujith, "An experimental investigation of non-evaporative sprays in axial

acoustic fields," in 44th AIAA/ASME/SAE/ASEE Joint Propulsion Conference and Exhibit, no. 2008-1046, (Hartford,CT), 07 2008.

[197] W. Jones, A. Marquis, and K. Vogiatzaki, "Large-eddy simulation of spray combustion in a gas turbine combustor," Combustion and Flame, vol. 161, pp. 222–239, 2014.

[198] F. Shum-Kivan, J. Marrero Santiago, A. Verdier, E. Riber, B. Renou, G. Cabot, and B. Cuenot, "Experimental and numerical analysis of a turbulent spray flame structure," Proceedings of the Combustion Institute, vol. 36, no. 2, pp. 2567–2575, 2017.

[199] L. Guedot, G. Lartigue, and V. Moureau, "Modeling and analysis of the interactions of coherent structures with a spray flame in a swirl burner," in Turbulence and Interactions: Proceedings of the TI 2015 Conference, June 11-14, 2015, Cargèse, Corsica, France 4, pp. 15–26, Springer, 2018.

[200] G. Vignat, E. Lo Schiavo, D. Laera, A. Renaud, L. Gicquel, D. Durox, and S. Candel, "Dynamics of spray and swirling flame under acoustic oscillations : A joint experimental and les investigation," Proceedings of the Combustion Institute, vol. 38, no. 4, pp. 6015–6024, 2021.

[201] E. Lo Schiavo, D. Laera, E. Riber, L. Gicquel, and T. Poinsot, "Effects of liquid fuel/wall interaction on thermoacoustic instabilities in swirling spray flames," Combustion and Flame, vol. 219, pp. 86–101, 2020.

[202] R. I. Sujith, G. A. Waldherr, J. I. Jagoda, and B. T. Zinn, "A Theoretical Investigation of the Behavior of Droplets in Axial Acoustic Fields," Journal of Vibration and Acoustics, vol. 121, pp. 286–294, 07 1999.

[203] M. R. Maxey and J. J. Riley, "Equation of motion for a small rigid sphere in a nonuniform flow," The Physics of Fluids, vol. 26, pp. 883–889, 04 1983.

[204] A. T. HjelmfeltJr. and L. F. Mockros, "Motion of discrete particles in a turbulent fluid," Flow Turbulence and Combustion, vol. 16, pp. 149–161, 1966.

[205] C. Crowe, M. Sommerfeld, and Y. Tsuji, Multiphase Flows with Droplets and Particles. Boca Raton, FL, USA: CRC Press, 1998.

[206] A. Kaufmann, Vers la simulation des grandes échelles en formulation Euler-Euler des écoulements réactifs diphasiques. PhD thesis, Institut National Polytechnique de Toulouse, 2004.

[207] J. Dormand and P. Prince, "A family of embedded runge-kutta formulae," Journal of Computational and Applied Mathematics, vol. 6, no. 1, pp. 19–26, 1980.

[208] P. Welch, "The use of fast fourier transform for the estimation of power spectra: a method based on time averaging over short, modified periodograms," IEEE Transactions on audio and electroacoustics, vol. 15, no. 2, pp. 70–73, 1967.

[209] M. Ishii and T. Hibiki, Thermo-fluid dynamics of two-phase flow. New York, NY, USA: Springer Science & Business Media, 2010.

[210] C. Morel, Mathematical Modeling of Disperse Two-Phase Flows. Cham, Switzerland: Springer International Publishing, 2015.

[211] H. Bruce Stewart and B. Wendroff, "Two-phase flow: Models and methods," Journal of Computational Physics, vol. 56, no. 3, pp. 363–409, 1984.

[212] J. Stuhmiller, "The influence of interfacial pressure forces on the character of two-phase flow model equations," International Journal of Multiphase Flow, vol. 3, no. 6, pp. 551–560, 1977.

[213] M. Ndjinga, "Influence of interfacial pressure on the hyperbolicity of the two-fluid model," Comptes Rendus Mathematique, vol. 344, no. 6, pp. 407–412, 2007.

[214] T. Gallouët, J.-M. Herard, and N. Seguin, "Numerical modeling of two-phase flows using the two-fluid two-pressure approach," Mathematical Models and Methods in Applied Sciences, vol. 14, pp. 663–700, 2004.

[215] O. Simonin, "Continuum modelling of dispersed two-phase flows," in Lecture series-von Karman Institute for fluid dynamics, vol. 2, pp. K1–K47, Von Karman Institute, Belgium, 1996.

[216] P. Février, O. Simonin, and K. D. Squires, "Partitioning of particle velocities in gas–solid turbulent flows into a continuous field and a spatially uncorrelated random distribution: theoretical formalism and numerical study," Journal of Fluid Mechanics, vol. 533, pp. 1–46, 2005.

[217] O. Simonin, L. I. Zaichik, V. M. Alipchenkov, and P. Février, "Connection between two statistical approaches for the modelling of particle velocity and concentration distributions in turbulent flow: The mesoscopic eulerian formalism and the two-point probability density function method," Physics of Fluids, vol. 18, no. 12, p. 125107, 2006.

[218] A. Kaufmann, M. Mathieu, O. Simonin, and J. Helie, "Comparison between Lagrangian and mesoscopic eulerian modelling approaches for inertial particles suspended in decaying isotropic turbulence," Journal of Computational Physics, vol. 227, pp. 6448–6472, 06 2008.

[219] F. Laurent and M. Massot, "Multi-fluid modelling of laminar polydisperse spray flames: origin, assumptions and comparison of sectional and sampling methods," Combustion theory and modelling, vol. 5, no. 4, pp. 537–572, 2001.

[220] A. Vié, Simulation aux grandes échelles d'écoulements diphasiques turbulents à phase liquide dispersée. Theses, Institut National Polytechnique de Toulouse - INPT, Toulouse, France, Dec. 2010.

[221] A. Vié, S. Jay, C. Benedicte, and M. Massot, "Accounting for polydispersion in the eulerian large eddy simulation of the two-phase flow in an aeronautical-type burner," Flow, Turbulence and Combustion, vol. 90, 04 2013.

[222] O. Simonin, P. Février, and J. Laviéville, "On the spatial distribution of heavy-particle velocities in turbulent flow: from continuous field to particulate chaos," Journal of Turbulence, vol. 3, p. N40, 2002.

[223] S. Sazhin, T. Shakked, V. Sobolev, and D. Katoshevski, "Particle grouping in oscillating flows," European Journal of Mechanics - B/Fluids, vol. 27, no. 2, pp. 131 – 149, 2008.

[224] B. Chu, "On the energy transfer to small disturbances in fluid flow (part i)," Acta Mechanica, vol. 1, pp. 215–234, 1965.

[225] K. W. Thompson, "Time dependent boundary conditions for hyperbolic systemsf," Journal of Computational Physics, vol. 68, no. 1, pp. 1–24, 1987.

[226] B. Cuenot, R. Vicquelin, E. Riber, V. Moureau, G. Lartigue, A. Figuer, Y. Mery, J. Lamouroux, S. Richard, L. Gicquel, et al., "Advanced simulation of aeronautical combustors," Aerospace Lab, no. 11, pp. 9–pages, 2016.

[227] M. Boileau, S. Pascaud, R. Eleonore, C. Benedicte, G. L.Y.M., T. Poinsot, and M. Cazalens, "Investigation of two-fluid methods for large eddy simulation of spray combustion in gas turbines," Flow, Turbulence and Combustion, vol. 80, pp. 291–321, 04 2008.

[228] W. Jones, A. Marquis, and K. Vogiatzaki, "Large-eddy simulation of spray combustion in a gas turbine combustor," Combustion and Flame, vol. 161, no. 1, pp. 222–239, 2014.

[229] D. Paulhiac, B. Cuenot, E. Riber, L. Esclapez, and S. Richard, "Analysis of the spray flame structure in a lab-scale burner using large eddy simulation and discrete particle simulation," Combustion and Flame, vol. 212, pp. 25–38, 2020.

[230] S. Tachibana, K. Saito, T. Yamamoto, M. Makida, T. Kitano, and R. Kurose, "Experimental and numerical investigation of thermo-acoustic instability in a liquid-fuel aero-engine combustor at elevated pressure: Validity of large-eddy simulation of spray combustion," Combustion and Flame, vol. 162, no. 6, pp. 2621–2637, 2015.

[231] W. Konrad, N. Brehm, F. Kameier, C. Freeman, and I. J. Day, "Combustion Instability Investigations on the BR710 Jet Engine," Journal of Engineering for Gas Turbines and Power, vol. 120, pp. 34–40, 01 1998.

[232] K. Prieur, D. Durox, J. Beaunier, T. Schuller, and S. Candel, "Ignition dynamics in an annular combustor for liquid spray and premixed gaseous injection," Proceedings of the Combustion Institute, vol. 36, no. 3, pp. 3717–3724, 2017.

[233] S. Subramaniam, "Lagrangian–eulerian methods for multiphase flows," Progress in Energy and Combustion Science, vol. 39, no. 2, pp. 215–245, 2013.

[234] A. D. Gosman and E. loannides, "Aspects of computer simulation of liquid-fueled combustors," Journal of Energy, vol. 7, no. 6, pp. 482–490, 1983.

[235] P. Jenny, D. Roekaerts, and N. Beishuizen, "Modeling of turbulent dilute spray combustion," Progress in Energy and Combustion Science, vol. 38, no. 6, pp. 846–887, 2012.

[236] K. Warncke, S. Gepperth, B. Sauer, A. Sadiki, J. Janicka, R. Koch, and H.-J. Bauer, "Experimental and numerical investigation of the primary breakup of an airblasted liquid sheet," International Journal of Multiphase Flow, vol. 91, pp. 208–224, 2017.

[237] C. Guillamon, R. Janodet, L. Voivenel, R. Mercier, and V. Moureau, "Building Lagrangian injectors from resolved primary atomization simulations. application to jet in crossflow fuel injection," International Conference on Liquid Atomization and Spray Systems (ICLASS), vol. 1, 08 2021.

[238] J. Carmona, N. Odier, O. Desjardins, B. Cuenot, A. Misdariis, and A. Cayre, "A comparative study of direct numerical simulation and experimental results on a prefilming airblast atomization configuration," Atomization and Sprays, vol. 31, no. 8, 2021.

[239] R. Janodet, C. Guillamon, V. Moureau, R. Mercier, G. Lartigue, P. Bénard, T. Ménard, and A. Berlemont, "A massively parallel accurate conservative level set algorithm for simulating turbulent atomization on adaptive unstructured grids," Journal of Computational Physics, vol. 458, p. 111075, 02 2022.

[240] G. Chaussonnet, O. Vermorel, E. Riber, and B. Cuenot, "A new phenomenological model to

predict drop size distribution in large-eddy simulations of airblast atomizers," International Journal of Multiphase Flow, vol. 80, pp. 29–42, 2016.

[241] N. C. W. Treleaven, D. Laera, J. Carmona, N. Odier, Y. Gentil, J. Dombard, G. Daviller, L. Gicquel, and T. Poinsot, "Coupling of Combustion Simulation with Atomisation and Filming Models for LES in Swirled Spray Flames," Flow, Turbulence and Combustion, vol. 109, no. 3, pp. 759–789, 2022.

[242] T. Lancien, K. Prieur, D. Durox, S. Candel, and R. Vicquelin, "Large Eddy Simulation of Light-Round in an Annular Combustor With Liquid Spray Injection and Comparison With Experiments," Journal of Engineering for Gas Turbines and Power, vol. 140, 10 2017.

[243] K. Töpperwien, F. Collin-Bastiani, E. Riber, B. Cuenot, G. Vignat, K. Prieur, D. Durox, S. Candel, and R. Vicquelin, "Large-Eddy Simulation of Flame Dynamics During the Ignition of a Swirling Injector Unit and Comparison With Experiments," Journal of Engineering for Gas Turbines and Power, vol. 143, no. 2, 2021.

[244] J. Su, A. Barker, A. Garmory, and J. Carrotte, "Spray Response to Acoustic Forcing of a Multi-Passage Lean-Burn Aero-Engine Fuel Injector," in Turbo Expo: Power for Land, Sea, and Air, vol. Volume 4A: Combustion, Fuels, and Emissions, 06 2018.

[245] P. Vesilind, "The rosin-rammler particle size distribution," Resource Recovery and Conservation, vol. 5, no. 3, pp. 275–277, 1980.

[246] M. Alderliesten, "Mean particle diameters. part vii. the rosin-rammler size distribution: Physical and mathematical properties and relationships to moment-ratio defined mean particle diameters," Particle & Particle Systems Characterization, vol. 30, no. 3, pp. 244–257, 2013.

[247] G. Daviller, M. Brebion, P. Xavier, G. Staffelbach, J.-D. Müller, and T. Poinsot, "A mesh adaptation strategy to predict pressure losses in les of swirled flows," Flow, Turbulence and Combustion, vol. 99, pp. 93–118, 2017.

[248] W. Polifke, A. Fischer, and T. Sattelmayer, "Instability of a premix burner with nonmonotonic pressure drop characteristic," J. Eng. Gas Turbines Power, vol. 125, no. 1, pp. 20–27, 2003.

[249] G. Vignat, D. Durox, K. Prieur, and S. Candel, "An experimental study into the effect of injector pressure loss on self-sustained combustion instabilities in a swirled spray burner," Proceedings of the Combustion Institute, vol. 37, no. 4, pp. 5205–5213, 2019.

[250] P. Kowalczuk and J. Drzymala, "Physical meaning of the sauter mean diameter of spherical particulate matter," Particulate Science and Technology, vol. 34, pp. 645–647, 10 2015.

[251] N. Otsu, "A threshold selection method from gray-level histograms," IEEE Transactions on Systems, Man, and Cybernetics, vol. 9, no. 1, pp. 62–66, 1979.

[252] A. Dowling, "The calculation of thermoacoustic oscillations," Journal of Sound and Vibration, vol. 180, no. 4, pp. 557–581, 1995.

[253] M. R. Bothien, N. Noiray, and B. Schuermans, "Analysis of azimuthal thermo-acoustic modes in annular gas turbine combustion chambers," Journal of Engineering for Gas Turbines and Power, vol. 137, no. 6, 2015.

[254] J. Eckstein and T. Sattelmayer, "Low-order modeling of low-frequency combustion instabilities in aeroengines," Journal of propulsion and power, vol. 22, no. 2, pp. 425–432, 2006.

[255] A. Andreini, B. Facchini, A. Giusti, and F. Turrini, "Assessment of flame transfer function formulations for the thermoacoustic analysis of lean burn aero-engine combustors," Energy Procedia, vol. 45, pp. 1422–1431, 2014. ATI 2013 - 68th Conference of the Italian Thermal Machines Engineering Association.

[256] A. Dowling., "A kinematic model of a ducted flame," Journal of Fluid Mechanics, vol. 394, p. 51–72, 1999.

[257] T. Yi and D. Santavicca, "Flame transfer functions and their applications to combustion analysis and control," in Proceedings of the ASME Turbo Expo, vol. 1, pp. 757–766, 01 2009.

[258] T. Yi and D. A. Santavicca, "Forced flame response of turbulent liquid-fueled lean-direct-injection combustion to fuel modulations," Journal of Propulsion and Power, vol. 25, no. 6, pp. 1259–1271, 2009.

[259] W. Polifke and C. Lawn, "On the low-frequency limit of flame transfer functions," Combustion and Flame, vol. 151, no. 3, pp. 437 – 451, 2007.

[260] A. Innocenti, A. Andreini, B. Facchini, and A. Peschiulli, "Numerical analysis of the dynamic flame response of a spray flame for aero-engine applications," International Journal of Spray and Combustion Dynamics, vol. 9, no. 4, pp. 310–329, 2017.

[261] J. Gikadi, Prediction of Acoustic Modes in Combustors using Linearized Navier-Stokes Equations in Frequency Space. PhD thesis, München, Technische Universität München, Diss., 2014, 2014.

[262] T. Schuller, S. Marragou, G. Oztarlik, T. Poinsot, and L. Selle, "Influence of hydrogen content and injection scheme on the describing function of swirled flames," Combustion and Flame, vol. 240, p. 111974, 2022.

[263] J. Kuhlmann, S. Marragou, I. Boxx, T. Schuller, and W. Polifke, "LES-based prediction of technically premixed flame dynamics and comparison with perfectly premixed mode," Physics of Fluids, vol. 34, 08 2022.

[264] A. Blonde, B. Schuermans, K. Pandey, and N. Noiray, "Effect of hydrogen enrichment on transfer matrices of fully and technically premixed swirled flames," in Proceedings of the ASME Turbo Expo, 06 2023. GT2023-101500.

[265] M. Cerna and A. F. Harvey, "The fundamentals of FFT-based signal analysis and measurement," tech. rep., Application Note 041, National Instruments, 2000.

[266] A. Hirschberg, Introduction to aero-acoustics of internal flows. Von Karman Institute, Brussels, Belgium, 2009.

[267] H. Levine and J. Schwinger, "On the radiation of sound from an unflanged circular pipe," Phys. Rev., vol. 73, pp. 383–406, Feb 1948.

[268] R. Gaudron, M. Gatti, C. Mirat, and T. Schuller, "Impact of the acoustic forcing level on the transfer matrix of a turbulent swirling combustor with and without flame," Flow Turbulence and Combustion, vol. 103, p. 751–771, 09 2019.

[269] C. O. Paschereit and W. Polifke, "Investigation of the Thermoacoustic Characteristics of a Lean Premixed Gas Turbine Burner," in Turbo Expo: Power for Land, Sea, and Air, vol. Volume 3: Coal, Biomass and Alternative Fuels; Combustion and Fuels; Oil and Gas Applications; Cycle Innovations, 06 1998. 98-GT-582.

[270] V. Latour, P. Rajendram Soundararajan, D. Durox, A. Renaud, and S. Candel, "Assessing transfer matrix models and measurements using acoustic energy conservation principle," in Proceedings of the ASME Turbo Expo, 2023. GT2023-102035.

[271] B. Higgins, M. McQuay, F. Lacas, and S. Candel, "An experimental study on the effect of pressure and strain rate on CH chemiluminescence of premixed fuel-lean methane/air flames," Fuel, vol. 80, no. 11, pp. 1583–1591, 2001.

[272] B. Higgins, M. McQuay, F. Lacas, J. Rolon, N. Darabiha, and S. Candel, "Systematic measurements of OH chemiluminescence for fuel-lean, high-pressure, premixed, laminar flames," Fuel, vol. 80, no. 1, pp. 67–74, 2001.

[273] B. Schuermans, F. Guethe, and W. Mohr, "Optical Transfer Function Measurements for Technically Premixed Flames," Journal of Engineering for Gas Turbines and Power, vol. 132, 05 2010.

[274] K. Prieur, D. Durox, G. Vignat, T. Schuller, and S. Candel, "Experimental determinations of Flame Describing Functions of swirling spray flames," in Colloque INCA, (Châteaufort, France), Oct. 2017.

[275] S. Brohez, C. Delvosalle, and G. Marlair, "A two-thermocouples probe for radiation corrections of measured temperatures in compartment fires," Fire Safety Journal, vol. 39, no. 5, pp. 399–411, 2004.

[276] K. Benson, L. Tozzi, E. Van Dyne, and J. Barrett, "Method and apparatus for detecting combustion instability in continuous combustion systems," Apr. 17 2006. US Patent 7,096,722.

[277] T. Lieuwen, "Systems and methods for detection of combustor stability margin," Mar. 20 2007. US Patent 27,194,382 B2.

[278] P. Hoehne and F. Schroer, "Pressure-measuring device and pressure-measuring method for a turbomachine," 2014. US Patent S 2013/0139578.

[279] T. Lieuwen, "Online Combustor Stability Margin Assessment Using Dynamic Pressure Data ," Journal of Engineering for Gas Turbines and Power, vol. 127, pp. 478–482, 06 2005.

[280] T. Yi and E. J. Gutmark, "Online prediction of the onset of combustion instability based on the computation of damping ratios," Journal of Sound and Vibration, vol. 310, no. 1, pp. 442 – 447, 2008.

[281] M. P. Juniper and R. Sujith, "Sensitivity and nonlinearity of thermoacoustic oscillations," Annual Review of Fluid Mechanics, vol. 50, no. 1, pp. 661–689, 2018.

[282] H. Gotoda, H. Nikimoto, T. Miyano, and S. Tachibana, "Dynamic properties of combustion instability in a lean premixed gas-turbine combustor," Chaos: An Interdisciplinary Journal of Nonlinear Science, vol. 21, no. 013124, 2011.

[283] V. Nair and R. I. Sujith, "Identifying homoclinic orbits in the dynamics of intermittent signals through recurrence quantification," Chaos: An Interdisciplinary Journal of Nonlinear Science, vol. 23, no. 3, p. 033136, 2013.

[284] K. Kashinath, I. C. Waugh, and M. P. Juniper, "Nonlinear self-excited thermoacoustic oscillations of a ducted premixed flame: bifurcations and routes to chaos," Journal of Fluid Mechanics, vol. 761, p. 399–430, 2014.

[285] Y. Okuno, M. Small, and H. Gotoda, "Dynamics of self-excited thermoacoustic instability in a combustion system: Pseudo-periodic and high-dimensional nature," Chaos: An Interdisciplinary Journal of Nonlinear Science, vol. 25, no. 4, p. 043107, 2015.

[286] V. Nair and R. Sujith, "Multifractality in combustion noise: predicting an impending combustion instability," Journal of Fluid Mechanics, vol. 747, p. 635–655, 2014.

[287] R. Sujith and V. R. Unni, "Dynamical systems and complex systems theory to study unsteady combustion," Proceedings of the Combustion Institute, vol. 38, no. 3, pp. 3445–3462, 2021.

[288] F. Boudy, D. Durox, T. Schuller, and S. Candel, "Nonlinear Flame Describing Function Analysis of Galloping Limit Cycles Featuring Chaotic States in Premixed Combustors," in Turbo Expo: Power for Land, Sea, and Air, vol. Volume 2: Combustion, Fuels and Emissions, Parts A and B, pp. 713–724, 2012.

[289] V. Nair, G. Thampi, S. Karuppusamy, S. Gopalan, and R. I. Sujith, "Loss of chaos in combustion noise as a precursor of impending combustion instability," International Journal of Spray and Combustion Dynamics, vol. 5, no. 4, pp. 273–290, 2013.

[290] J. Y. Chung and D. A. Blaser, "Transfer function method of measuring in-duct acoustic properties. I. theory," The Journal of the Acoustical Society of America, vol. 68, no. 3, pp. 907–913, 1980.

[291] J. Y. Chung and D. A. Blaser, "Transfer function method of measuring in-duct acoustic properties. II. experiment," The Journal of the Acoustical Society of America, vol. 68, no. 3, pp. 914–921, 1980.

[292] S. Nair and T. Lieuwen, "Acoustic detection of blowout in premixed flames," Journal of Propulsion and Power, vol. 21, no. 1, pp. 32–39, 2005.

[293] V. Nair, G. Thampi, and R. Sujith, "Intermittency route to thermoacoustic instability in turbulent combustors," Journal of Fluid Mechanics, vol. 756, p. 470–487, 2014.

[294] V. Nair and R. Sujith, "A reduced-order model for the onset of combustion instability: Physical mechanisms for intermittency and precursors," Proceedings of the Combustion Institute, vol. 35, no. 3, pp. 3193 – 3200, 2015.

[295] M. Murugesan and R. Sujith, "Combustion noise is scale-free: transition from scale-free to order at the onset of thermoacoustic instability," Journal of Fluid Mechanics, vol. 772, p. 225–245, 2015.

[296] F. Nicoud and T. Poinsot, "Thermoacoustic instabilities: Should the rayleigh criterion be extended to include entropy changes ?," Combustion and Flame, vol. 142, no. 1, pp. 153–159, 2005.

[297] G. Oztarlik, L. Selle, T. Poinsot, and T. Schuller, "Suppression of instabilities of swirled premixed flames with minimal secondary hydrogen injection," Combustion and Flame, vol. 214, pp. 266–276, 2020.

[298] A. Cellier, C. Lapeyre, G. Öztarlik, T. Poinsot, T. Schuller, and L. Selle, "Detection of precursors of combustion instability using convolutional recurrent neural networks," Combustion and Flame, vol. 233, p. 111558, 2021.

[299] W. T. Chung, K. S. Jung, J. H. Chen, and M. Ihme, "Blastnet: A call for community-involved

big data in combustion machine learning," Applications in Energy and Combustion Science, vol. 12, p. 100087, 2022.

[300] A. Couzinet, Approche PDF jointe fluide-particule pour la modélisation des écoulements turbulents diphasiques anisothermes. PhD thesis, 2008. Thèse de doctorat dirigée par Simonin, Olivier et Bédat, Benoît, INPT, Toulouse, France.

[301] F. Giuliani, L. Andracher, V. Moosbrugger, N. Paulitsch, and A. Hofer, "Combined optic-acoustic monitoring of combustion in a gas turbine," International Journal of Turbomachinery, Propulsion and Power, vol. 5, no. 3, 2020.